

Multispectral Luminescence Studies: Methodological Developments and Applications

A thesis submitted in partial fulfilment of

the requirements for the degree of

Doctor of Philosophy

by

Monika Devi

(Roll No. 18330013)

Under the supervision of

Dr. Naveen Chauhan

Associate Professor

Atomic, Molecular, and Optical Physics Division

Physical Research Laboratory, Ahmedabad, India



DISCIPLINE OF PHYSICS

INDIAN INSTITUTE OF TECHNOLOGY GANDHINAGAR

2023

Dedicated to
my Family,
my Gurus
and
my Friends

Declaration

I declare that this thesis report represents my own ideas in my own words and I have included others ideas with appropriate citations of original sources. I also declare that I have followed all principles of academic honesty and integrity and have not misrepresented or fabricated or falsified any idea/fact/source/data in my submission. I understand that any violation of the above can cause disciplinary action by the Institute and can also evoke penal action from the sources which have thus not been properly cited or from whom proper permission has not been taken when needed.

Monika Devi

(Roll No.: 18330013)

Date:



Department of Physics
Indian Institute of Technology, Gandhinagar
Gandhinagar, Gujarat-382355

CERTIFICATE

It is certified that the work contained in the thesis titled “**Multispectral Luminescence Studies: Methodological Developments and Applications**” by **Ms. Monika Devi** (Roll no: 18330013) has been carried out under my supervision and that this work has not been submitted elsewhere for a degree.

Dr. Naveen Chauhan
(Thesis Supervisor)
Associate Professor,
Atomic Molecular and Optical Physics Division,
Physical Research Laboratory,
Ahmedabad 380009,

Date:

India.

Acknowledgements

I would like to express my deepest gratitude and appreciation to the individuals who have supported and contributed to the completion of this PhD thesis.

I extend my sincere thanks to Physical Research Laboratory (PRL), Ahmedabad for resources, facilities, and research opportunities that enabled me to pursue my doctoral studies. I am grateful for the intellectual environment and the stimulating academic atmosphere that fostered my personal and professional development.

First and foremost, I would like to extend my heartfelt appreciation to my supervisor, Dr. Naveen Chauhan. His invaluable guidance, expertise, and unwavering support throughout this journey have been instrumental in shaping this thesis and my overall academic growth. I am truly grateful for their mentorship and dedication. I am truly fortunate to have had such an exceptional mentor who not only shared their expertise but also inspired and encouraged me to push the boundaries of my research.

I am profoundly grateful for the guidance and support I have received from Prof. Ashok Kumar Singhvi, whom I consider not only a mentor but also a grandfather figure. His vast knowledge has enriched my understanding of the subject matter. His dedication to academic excellence has inspired me to strive for the highest standards in my work. His kindness, wisdom, and generosity have left an indelible mark on my heart. I would also like to extend my heartfelt thanks to Anita Singhvi ma'am for her warm hospitality, who nourished my body and soul with her delicious food. Her motivation during my hard times has helped me a lot. My stay at their home was one of the best days of my Ph.D. journey.

I am indebted to the members of my doctoral research committee Dr. Amzad H. Laskar, Dr. S. Vijayan, Dr. Bhala Sivaraman, for their insightful feedback and valuable suggestions that significantly enhanced the quality of this research work.

I thank Prof. A.D. Shukla, Dr. Deepak Panda, and Yash for their help in using the Scanning electron microscope, this helps to complete my research work on time. I sincerely thank Dr. Morthekai for all the fruitful discussions that have enriched my knowledge of the subject significantly. Thanks to Dr. Shubra Sharma and Dr. Navin Juyal for the help in the field and for teaching me some aspects of Himalayan geology. I thank Hareesh and Sachin Joshi for helping me in the research in the early days of Ph.D.

I would like to acknowledge the contributions of my colleagues Dr. Kartika, Dr. Rahul Kaushal, Dr. Sukumar Parida, Santunu and Malika, whose discussions, insights, and collaborative efforts have enriched my understanding and expanded the scope of my research. My special thanks to Dr. Sukumar (office mate) for helping in thesis formatting and for providing moral support. I sincerely thank Debashis, Sanjit, Santunu, Malika, Dr. Priyank, Dr. Sukumar, and Dr. Kartika for proofreading the thesis.

I am immensely grateful to my friends Namita, Yash, Meghna, Deepak, Sidharatha, Shreya, Deepak Rai, Daya, Deva, Sanjit, Anju, Akanksha, Arijit, Anupam, Sunil, Yogesh, Pranav, Vikas, Binal, Sandeep, Supriya, Nabo and Naval for all the crazy talks and laughs. Meghna's friendship has been a true blessing and an essential part of this Ph.D. journey, and I cannot imagine having come this far without her by my side. I thank Namita and Yash for always helping me, listening to me and all the fun that we have shared together. I thank Siddhartha (crime partner) and Shreya for making me laugh and being there in my hard times. I thank Deva for all the childish fights, helping me in hard times, and in thesis formatting. I thank Ayushi for her patience during late-night study sessions. I extend a special thanks to Raza for the delightful talks and laughter shared during tea and ice cream times.

I thank my seniors cum friends like Priyank, Abdur, Harish, Surendra, Sana, Sushree, and Sandeep. I sincerely thank my seniors Raja ji, Partha, Shivani, Ankit, Abhay, and Milan for their friendly support and making this journey truly enjoyable. I thank all my lovely juniors Somu, Vineet, Birendra, Goldy, Maity, Komal, Aakash, Kamran, Debashis, Guru and Dharmendra. Throughout the Ph.D. journey, Priyank has been my pillar of strength, offering unwavering and emotional support, especially when I faced health issues. Being a senior in academics, he has been a constant source of inspiration and motivation for my work. I am excited to embark on new adventures together beyond the completion of this Ph.D. thesis.

I am deeply grateful for the role of sports in enriching my Ph.D. journey. I am grateful for the role that sports played in providing balance, resilience, and rejuvenation throughout this process. I also want to acknowledge the friendships I developed through sports. I want to express my sincere thanks to the dispensary, cleaning staff, and canteen personnel for providing healthy and comfortable environment and making Ph.D. journey enjoyable.

To my beloved grandmother and parents, I extend my heartfelt thanks for their unconditional love, encouragement, tireless support, and sacrifices. Their prayers have been a source of immense strength throughout this journey. It's their hard work and prayers that I am here writing my doctoral thesis. I thank my two younger brothers Ankush and Anmol, for their love and support.

In conclusion, this thesis would not have been possible without the collective support and collaboration of numerous individuals. I am truly humbled and privileged to have had the opportunity to work with such remarkable individuals. It is not possible to write everyone's name who have contributed to the thesis. Thank you all for your invaluable contributions, encouragement, and support.

To myself, I say thank you for embracing the challenges, for growing through the difficulties, and for emerging as a more resilient individual. Cheers to me!!

Monika Devi

Abstract

The present study attempts to understand the insights of the luminescence mechanism of feldspar and its application for radiation dosimetry and dating. Luminescence dating relies on the principle that natural minerals, such as quartz and feldspar, accumulate charges (electrons and holes) in crystal defect sites, which are stored for short time periods of a few seconds to a geologically significant time period of millions of years. On stimulation, the trapped charges radiatively recombine at appropriate lattice defects and result in stimulated emission of luminescence proportional to stored charges.

Among the two most widely used minerals, quartz and feldspar, the former has been most widely used for dating purposes because of well characterised luminescence properties and the non-fading nature of the signal. Over the past decade, luminescence dating using feldspar has been studied extensively due to its higher luminescence sensitivity and saturation dose (~1200 Gy), which is approximately five times higher compared to quartz. This offers the potential to increase the range of luminescence dating up to millions of years. Its use has, however, been limited due to anomalous fading of luminescence signal, which is athermal loss of signal in addition to that predicted by the thermal kinetic considerations. The present thesis encompasses a comprehensive exploration of the various spectral regions of feldspar, assessing their athermal stability through different stimulations and emissions wavelength bands. The luminescence production mechanism of feldspar is complex due to its complex defect structure and has not yet been fully understood. The current understanding of the feldspar luminescence mechanism is based on a single principal trap, also known as a dosimetric trap.

This thesis rigorously investigated aspects associated with the mechanism of luminescence in feldspar and studied the traps and recombination centres responsible for luminescence in feldspar. The athermal stability of luminescence signals in different spectral regions of feldspar was explored using multispectral stimulation and emission combination studies. Among all signals, the post violet IR stimulated luminescence (pVIRSL) signal resulted in the lowest average fading value of $0.0 \pm 0.1\%$ per decade, indicating that the signal originates from stable electron and recombination centres. The TL and OSL experiments suggest that pVIRSL is a recuperated signal arising from the eviction of charges from deep

traps by violet stimulation and their recapture by the IR trap. The study showed the role of deep traps present beneath the principal trap in pVIRSL luminescence emission.

Further, the newly identified pVIRSL signal was characterised for its dosimetric properties. An optimized single aliquot regenerative dose protocol for the pVIRSL (pVIR-SAR) protocol was developed for the estimation of equivalent doses. The proposed protocol fulfils all the essential criteria for the use of a SAR protocol, such as rapid bleaching (<10% of the equivalent dose in 60 min of daylight exposure), recuperation <5%, reproducibility within 10%, and dose recovery within 10%. The pVIR-SAR protocol was tested for several K-feldspar samples from varied depositional environments with age ranges between 6 to 286 ka. The obtained ages were consistent with the expected ages.

The pVIR-SAR enabled the dating of polymineral fine- and coarse-grain samples, as violet stimulation bleaches signal from quartz and permits probing of pVIRSL signal from feldspar. Therefore, the protocol offers the advantage of dating unseparated samples as well as samples where feldspar cannot be fully separated from quartz, like in the case of polymineral fine grains and samples of small quantities used for rock surface exposure dating. The applicability of the pVIR-SAR protocol for such samples was explored. The ages obtained from polymineral fine and coarse grain samples, which include volcanic ash, pottery, and fluvial samples, were consistent with geological reasoning and available age controls. The work suggests that mineral separation can be avoided if pVIR-SAR is used for dating. A notable result obtained through the pVIR-SAR dating of fine-grained materials is its potential suitability as an alternative method for samples with low sensitivity quartz and poorly bleachable feldspar signal. Such samples are often encountered in glaciated terrains such as the Himalayas and Antarctica.

Additionally, this thesis examines the application of pVIRSL and IRSL for luminescence dating of old exposed rock surfaces (> 1 ka), shedding light on its utility in glacial studies and paleo-climate research. Theoretical modeling has suggested that the rock surface exposure dating technique could potentially be applied to rocks up to 1 million years old. However, in practice, the technique has yielded reliable ages primarily for younger samples (<1 ka). For older rock samples, underestimation in the ages are reported. The same is observed for the samples collected from old glacially polished samples for the present thesis work. Therefore, possible reasons for such a large discordance, including the role of desert varnish and structural micro-cracks inside the rocks that modify the

apparent transparency of the sample and luminescence depth profiles, are explored and discussed. SEM-EDS analysis showed the presence of desert varnish and cracks in the rock samples. The sample used for calibration of the model, however, had no desert varnish or cracks, indicating that the parameters derived from the calibration sample were not suitable for estimating the ages of the unknown age samples. It also highlights prospects for refining luminescence dating techniques and addressing the complexities associated with surface exposure dating of polished rock samples.

In conclusion, the thesis work contributes to the advancement of luminescence dating by expanding our understanding of feldspar luminescence and offering a viable alternative for dating various geological materials. It also sheds light on the challenges and complexities associated with dating exposed rock surfaces, highlighting the need for continued refinement of luminescence dating techniques in these contexts.

Keywords: Luminescence; radiation dosimetry; luminescence dating; quartz; feldspar; stimulated emission; anomalous fading; spectral regions; dosimetric trap; multispectral; polymineral samples; rock surface exposure dating; desert varnish; microfractures.

Table of Contents

Acknowledgements.....	ix
Abstract.....	xiii
Table of Contents.....	xvii
List of Figures.....	xxi
List of Tables.....	xxix
Abbreviations.....	xxxiii
Chapter 1 Introduction.....	1
1.1 Introduction.....	1
1.1.1 Luminescence.....	2
1.1.2 Thermoluminescence (TL).....	5
1.1.3 Optically stimulated luminescence (OSL).....	6
1.1.4 Natural phosphors/dosimeters.....	7
1.1.5 Luminescence for geological dating.....	17
1.1.6 Challenges.....	26
1.1.7 Objectives of the present thesis.....	28
1.1.8 Thesis outline.....	29
Chapter 2 Instrumentation and Experimental Methods.....	33
2.1 Introduction.....	33
2.2 Instruments.....	33
2.2.1 TL/OSL reader equipped with detection and stimulation head (DASH) system 34	
2.2.2 High purity Germanium (HPGe) detector.....	38
2.3 Petrological Analysis.....	39
2.3.1 X-ray diffraction (XRD).....	40

2.3.2 Scanning electron microscopy with Energy dispersive spectroscopy (SEM-EDS).....	40
2.4 Luminescence Dating: Experimental Methods	41
2.4.1 Sample collection.....	41
2.4.2 Sample preparation	42
2.5 Methodology	46
2.5.1 Dose estimation.....	46
2.5.2 Anomalous fading	52
2.5.3 Measurement of the dose rate	55
Chapter 3 Multispectral Studies in K-Feldspar	59
3.1 Introduction.....	59
3.2 Samples	60
3.3 Measurements	62
3.4 Results and Discussion	66
3.4.1 Single stimulations.....	66
3.4.2 Double stimulations	68
3.4.3 Fading rate of pVIRSL signal for natural samples	72
3.5 Summary	74
Chapter 4 Post Violet-Infrared Stimulated Luminescence (pVIRSL) Dating Protocol ...	77
4.1 Introduction.....	77
4.2 Samples	77
4.3 Measurements	78
4.4 Results and Discussion	81
4.4.1 Source traps and pVIRSL mechanism	81
4.4.2 Mechanism for pVIRSL.....	89
4.4.3 Dating using pVIRSL	91

4.5 pVIRSL Single Aliquot Regenerative Dose (pVIR-SAR) Protocol	97
4.5.1 Repeatability and sensitivity changes	97
4.5.2 Residual doses of the pVIRSL	99
4.5.3 Dose recovery	100
4.5.4 Athermal stability of the pVIRSL	100
4.5.5 Saturation dose	101
4.5.6 Comparison with expected ages	101
4.6 Luminescence Mechanism of the Optimized Parameter pVIRSL at 200 °C	105
4.7 Conclusions	107
Chapter 5 Application of pVIR-SAR Protocol for Polymineral Natural Samples	109
5.1 Introduction	109
5.2 Samples	110
5.3 Methodology	112
5.4 Results and Discussion	113
5.4.1 Quartz and sodium feldspar contamination	113
5.4.2 Luminescence characteristics and dose determination	114
5.4.3 Residual dose	116
5.4.4 Dose recovery	117
5.4.5 Athermal Fading	117
5.4.6 Dose rate determination	122
5.5 Age Determination from Polymineral Fine- and Coarse-grain Fractions	125
5.5.1 Fine grains	125
5.5.2 Coarse grains: Fluvial samples	128

5.6 Conclusions.....	130
Chapter 6 An Attempt to Date Glacially Polished Samples using Luminescence Surface Exposure Dating.....	133
6.1 Introduction.....	133
6.2 Sample and Methodology	134
6.3 Measurement Protocols.....	135
6.4 Results and Discussion	137
6.4.1 Estimation of attenuation coefficient and detrapping rate	137
6.4.2 IRSL depth profiles.....	138
6.4.3 pVIRSL depth profiles.....	142
6.4.4 Scanning electron microscope with energy dispersive X-ray spectroscopy (SEM-EDS).....	144
6.5 Conclusion	147
Chapter 7 Summary and Future Prospect.....	149
7.1 Summary.....	149
7.2 Future Outlook	153
Bibliography	157
List of Publications	173
Publications Attached with Thesis.....	176

List of Figures

Fig. 1.1: a) Band model for a pure crystal. b) Band model for crystals with trace impurities. Due to impurities and defects crystals have localized energy levels within the forbidden gap. The ionizing radiations excite the electrons from the valence band to the conduction. Some of the electrons are trapped in the localized energy levels. c) The trapped electrons are excited using external stimulation and recombine with holes, resulting in the emission of light from the crystal, known as luminescence. 4

Fig. 1.2: a) TL glow of quartz recorded in the UV window recorded up to 500 °C at a heating rate of 2 °C/s. b) OSL decay curve of quartz with blue stimulation and detection in UV window. 6

Fig. 1.3: a) TL glow of potassium feldspar (KF) recorded in the blue window. b) IRSL decay curve of KF detected in blue window. 8

Fig. 1.4: Band model for K-feldspar luminescence (Redrawn after Jain et al. (2011)). Transition 1 is representing the resonating transition from principal trap (dosimetric trap) of feldspar. Transition 2 is non-resonating transition to the conduction band from high energy stimulations, e.g., blue (~2.63 eV) and violet (~3.06 eV). Transition 3 is recapture from the excited state of principal trap to the ground state. Transition 4 is representing the direct recombination of electron and hole due to quantum mechanical tunnelling. 10

Fig. 1.5: Modified band model for K-feldspar from Kumar et al., (2020) and Jain et al., (2011). 11

Fig. 1.6: Escape routes from a trap; a) athermal tunnelling; b) thermal assisted tunnelling; c, d) thermal eviction. 15

Fig. 1.7: Decay chain of ^{40}K , ^{238}U and ^{232}Th nuclides. 18

Fig. 1.8: Variation of luminescence signal in nature. After crystallization, minerals inside the rock store the energy in the form of electrons from the surrounding radioactive elements. The stored energy is released by daylight exposure. After the burial, crystal again starts to accumulate dose from ambient radioactivity. The timing of the burial event can be estimated by collecting samples. 19

Fig. 1.9: Variation of luminescence profile with depth at different exposure times (graph taken from Sohbaty et al, (2012a)). 26

Fig. 2.1: a) The setup used to perform experiments was ‘The Risø TL/OSL Reader’ and b) schematic of measurement system in TL/OSL reader. 34

Fig. 2.2: Different excitation and detection windows a) Emission characteristics of the stimulation LEDs and violet laser diode. Stimulations were carried out using 850 nm IR, 525 nm green, 470 nm blue LEDs, and 405 nm violet laser. b) Transmission characteristics of three different detection filter combinations. Detection were appropriately made through 260-400 nm [U-340 (Broad-UV)], 327-353 nm [U-340 + brightline 340/26 (Narrow-UV)], and 320–520 nm [BG-39 + BG-3 (blue)] transmission windows. (Emission data of LEDs were taken from the Risø product catalogue 1811a. The data on transmission spectra of different filters were taken from <https://hoyaoptics.com/wp-content/uploads/2019/10/U340.pdf>). 37

Fig. 2.3: Block diagram of HPGe detector. 39

Fig. 2.4: Map of India showing the geological locations of all samples used in Thesis. 43

Fig. 2.5: Sample preparation steps for SEM-EDS measurements. 46

Fig. 2.6: a) Single aliquot regenerative dose (SAR) protocol for equivalent dose estimation. b) D_e value estimation using SAR protocol. 47

Fig. 2.7: Fading rate (g-value) measurements for a sample. 53

Fig. 3.1: The XRD spectrum of museum KF sample (microcline). 61

Fig. 3.2: Thermoluminescence glow curves of a) KF, b) NaF, c) PRL2, and d) PRL0 recorded in open window (BG39, 3 mm; transmission range: 330-650 nm), blue, broad-UV, and narrow-UV detection window (Table 3.2). 63

Fig. 3.3: Methodology for the measurement of fading rates [g_{2days} (% per decade)] for single (a) and double stimulation (b) experiments. * IRSL measurements post green, post blue, and post violet stimulation were carried out with the sample at 100°C to get a good signal to noise ratio. 65

Fig. 3.4: Average fading rates [g_{AV} (% per decade)] for single stimulation and detection combinations for the PRL0 sample. The x-axis represents the stimulations, and the pattern of the bar represents the detection window. The height of the bar (y-axis) is the g_{AV} -values. 67

Fig. 3.5: Average fading rates [g_{AV} (% per decade)] for double stimulation and detection combinations for PRL0 sample. The x-axis represents the stimulations, and the pattern of the bar represents the detection window. The height of the bar (y-axis) is the g_{AV} -values. Double stimulation yielded lower fading rates for each second stimulation. The minimum fading ($g_{min} = 0.0 \pm 0.1\%$ per decade) was obtained in the post violet IRSL (pVIRSL) signal.

69

Fig. 3.6: The double stimulation decay curves for both stimulations. Decay curves for a) GSL and IRSL post green, b) BSL and IRSL post blue, c) VSL and IRSL post violet, and d) IRSL and IRSL post IR. The signal intensities are different because detection were made in the different windows viz., violet stimulation is recorded in the narrow UV window, both green and blue are in the broad UV window and IR stimulation is recorded in the blue window. The optical decay curves for all stimulations measured after ~20 Gy beta dose, and preheat of 250 °C for 60 s. All the stimulations were carried out at 50 °C temperature and power normalised.

70

Fig. 3.7: Ratio of IRSL2 to IRSL1 signals as a function of optical bleach energy. The IRSL1 was measured without any optical bleach, and IRSL2 was measured after the optical bleach with IR, green, blue, and violet stimulations. All the stimulations were carried out at 50 °C temperature. A maximum signal is obtained in the IRSL after the green stimulation. The IRSL signal starts to decrease with an increase in the energy of optical bleach. All the applied stimulations were power normalised.

71

Fig. 3.8: Fading rate [g_{2days} (% per decade)] results for PRL0 for pVIRSL signal. a) Normalised intensity is constant with delay and hence gives near zero fading rate, b) g_{2days} values for all aliquots are near to the zero line and result in an average fading value near to zero.

72

Fig. 3.9: Fading rate (g_{2days}) measurements for a single aliquot of each sample. The normalised intensities are constant with delay time for the KF, PRL1, PRL2, PRL3, and PRL4 samples.

73

Fig. 3.10: Average fading rates [g_{AV} (% per decade)] of pVIRSL signal for all samples. The x-axis represents the sample code. The g_{AV} -values are near zero for KF, PRL1, PRL2, PRL3, and PRL4, and for one sample (PRL5, $D_e = 237 \pm 23$ Gy) g_{AV} -value is $3.4 \pm 0.6\%$ per decade.

74

Fig. 4.1: Intergrated TL intensity (integrated whole glow curve) intensity variation for repeated five cycles. 78

Fig. 4.2: a) Measurement protocol to explore the relative intensity of pVIRSL compared to IRSL for KF sample. b) IRSL decay curves recorded before (IRSL1) and after (IRSL2) violet stimulation. The signal of IRSL2 is about an order of magnitude smaller than IRSL1. The inset shows the normalised IRSL intensities for IRSL1 and IRSL2. 81

Fig. 4.3: a) TL glow curve of KF feldspar sample after irradiation of 20 Gy. b) Measurements carried out to explore the TL emissions after the repeated violet stimulation without any additional dose of the KF sample. c) The background subtracted TL glow curves are recorded in the blue window. Inset in the figure shows the variation of the integrated intensity of TL peak at 130 °C (integrated from 120 to 140 °C) and 380 °C (integrated from 370 to 390 °C) with cycle number. All these measurements were carried out in an nitrogen environment. 82

Fig. 4.4: TL glow peaks were recorded after violet stimulation following variable annealing temperatures ranging from 450 to 800 °C. 83

Fig. 4.5: a) The measurement protocol to estimate the population of recombination centres emitting in BUUV and blue window. b) The background subtracted TL glow curves of in blue window before and after the violet stimulation. c) The background subtracted TL glow curves of in BUUV window before and after the violet stimulation. All glow curves were measured in same aliquot. * represents TL measurement in blue and BUUV window. All these measurements were carried out under nitrogen environment. 84

Fig. 4.6: a) Measurement protocol to record decay curves in IRSL, GSL, and BSL after violet stimulation. * and \$ represent detection in blue and BUUV, respectively. b) The post violet - IR, -green, and -blue stimulated decay curves in the blue and BUUV detection window. The stimulation treatments and detection window are mentioned in the legend as (simulation (detection window)). c) Measurements carried out to explore the IRSL emissions after the repeated violet stimulation without any additional dose. d) IRSL signal obtained after repetitive violet light stimulation. The IRSL signal intensity is obtained by subtracting the last 2 s signal from the initial 2 s. 85

Fig. 4.7: a) VSL signal is only observed for cycle-1. VSL decreases with repeated cycles and a background level was obtained after three cycles. 86

Fig. 4.8: a) Sequence used to explore the origin of IRSL signal after the violet stimulation of KF sample. The temperature of both violet stimulation and cut-heat was varied simultaneously. b) Measurements carried out to explore the origin of IRSL signal. Both a) and b) sequences are performed on the same and single aliquot. c) Variation of IRSL and pVIRSL with different cut-heat and violet stimulation temperatures. The IRSL is obtained by subtracting the last 2 s background from initial 2 s signal. IRSL signal was normalised with respect to its maximum value. To test any sensitivity change, data for IR 50 °C after all measurements is also presented. 88

Fig. 4.9: Variation of VSL decay curves with increase in stimulation temperature after 20 Gy dose and preheat of 250 °C for 60 s for KF sample. 89

Fig. 4.10: Band model for post violet IRSL signal (modified after Jain et al., 2011). Transition-1 represents the excitation, recombination, and recapture pathway of violet stimulation. Electrons from deep reservoir traps are excited using violet stimulation. The excited electrons go to the conduction band, and some are recaptured to the unoccupied states of the principal trap. These recaptured charges are further probed using IR stimulation (Transition-2) and resulted in pVIRSL in the blue window. (For interpretation of the references to colour in this figure legend, the reader is referred to the Web version of this article.) 90

Fig. 4.11: a) Measurement protocol to test the bleachability of pVIRSL signal in the reader at the variable temperature of violet and IR stimulation (bleaching step). b) Percentage of residual pVIRSL signal ($pVIRSL_2/pVIRSL_1$; test dose normalised) at variable elevated temperature of violet and IR bleaching for MHK-07-07 sample. Each data point represents a single aliquot with natural dose. At illumination temperature 350 °C, the residual pVIRSL signal is 4.5%. 91

Fig. 4.12: a) DRC constructed using pVIR-SAR protocol (Table 4.3, Protocol A) for MHK-07-07 sample. The D_e , recycling ratio and recuperation are 50 ± 2 Gy, 1.06 ± 0.04 , and $12.0 \pm 0.5\%$, respectively. b) DRC constructed using pVIR-SAR protocol (Table 3, Protocol B) for the MHK-07-07 sample. The D_e , recycling ratio and recuperation are 52 ± 2 Gy, 1.02 ± 0.03 , and $4.1 \pm 0.1\%$, respectively. 92

Fig. 4.13: a) Variation of recuperation for pVIR-SAR with IRSL stimulation temperature of the MHK-07-07 sample. Recuperation is <5% for pVIRSL at 200 °C. b) D_e plateau with preheat temperature for PRL2 sample. Here, D_e at each preheat temperature is the mean of

three aliquots. All D_e values fall within 5% of each other in the preheat temperature range of 220 to 260 °C. 94

Fig. 4.14: Test dose dependency of dose for MHK-07-07 (a, b) and RTP-18-02 (c, d). At each test dose, D_e is an average of at least three aliquots. Test doses were varied from approximately 5 to 90% of the expected dose. Dose recovery ratios at variable test doses for MHK-07-07 and RTP-18-02 samples are shown in the inset of (a) and (c). 95

Fig. 4.15: T_x/T_n ratio and DRC for low (~15% of expected dose) and high (~55% of expected dose) test doses of HMP-18-5: a) The ratio of test dose signal from regenerative to natural doses recorded during construction of the DRC for low test doses. b) The ratio of test dose signal from regenerative to natural doses recorded for high test doses. c) DRC constructed at low test doses. The natural normalised intensity lies in the saturation region. d) DRC constructed at high test doses. The natural normalised intensity lies below the saturation region, and the obtained D_e is 580 ± 29 Gy. 96

Fig. 4.16: a) Ratio of regeneration dose net pVIRSL signal (L_x : initial signal minus background) to test dose signal (T_x : initial signal minus background) is plotted against measurement cycle number for the RSN-01-17. 98

Fig. 4.17: Bleaching curves for a MHK-07-07 sample under UV filtered sun-lamp light and natural daylight exposure. Each point is an average of three aliquots. The pVIRSL signal reaches the residual level in ~60 min and ~100 min under daylight and solar lamp light exposure, respectively. For clarity data for the initial two hours is shown in the inset. 99

Fig. 4.18: Fading rate [g (% per decade)] results for RSN-01-17 sample for pVIRSL at 200 °C. 101

Fig. 4.19: Sensitivity corrected DRC constructed using pVIR-SAR protocol (Table 4.3, Protocol B) for MHD-02-17 sample along with the natural intensity. The single saturating exponential function as in analyst was used for the fitting. The recycling ratio and recuperation are 1.00 ± 0.05 and $2.6 \pm 0.1\%$, respectively. The estimated D_e is 640 ± 32 Gy, and saturation dose ($2D_0$) is 970 ± 23 Gy. 102

Fig. 4.20: Ages obtained using pVIR-SAR protocol with the ages constraint using BSL-SAR and pIRIR-SAR. 103

Fig. 5.1: a) Weight normalised shine down curves of pVIRSL from potassium feldspar (KF), sodium feldspar (NaF), quartz and empty disc are shown. b) Normalised luminescence intensity variation with delay time in NaF. 114

Fig. 5.2: pVIRSL decay curves, dose response curves and variation of normalised intensity with delay time for all volcanic samples named PRL23-01, PRL23-02, and PRL23-03. 115

Fig. 5.3: The pVIRSL decay curves, dose response curves, and variation of normalised intensity with delay time for all pottery fine grain samples named PRL23-04, PRL23-05, PRL23-06, and PRL23-07. 116

Fig. 5.4: The pVIRSL decay curves, dose response curves and variation of normalised intensity with delay time for fine grain fluvial samples named PRL23-10 and PRL23-11. 117

Fig. 5.5: Normalised intensity with delay time for fine grain PRL23-08 and PRL23-09 sample. 118

Fig. 5.6: Average fading rate values for all fine grain polymineralic samples. Fading corrections in ages for fading rates less than one were not made (Buylaert et al. 2012). 122

Fig. 5.7: Alpha efficiency of all samples. 124

Fig. 5.8: a) OSL sampling of PRL23-03 volcanic ash sampling site. b) Zoomed view of deposited volcanic ash layer. The thickness of ash layer is ~30 cm. A sphere of radius 30 cm is considered for volumetric corrections for dose deposited by gamma radiations. 125

Fig. 5.9: Polymineralic fine grain pVIR ages plotted against the IR and pIRIR ages. The black lines represent the 20% uncertainty. 127

Fig. 5.10: Comparison of coarse and fine grain pVIR and pIRIR ages with the expected ages (quartz ages) of fluvial samples. The black lines represent the 20% uncertainty. 130

Fig. 6.1: a) Bedrock surface having striations and chatter marks. b) Sample collected from the glacially polished bedrock surface. c) Polished bedrock surface having desert varnish and d) sample collected for calibration with a known age (~15 yrs). 134

Fig. 6.2: Procedure followed for sample preparation for rock surface exposure dating. 135

Fig. 6.3: Fading rate measurements for IR signal for TRTX-cal sample. The weighted mean of the fading rate is $0.8 \pm 0.8\%$ /decade. 137

Fig. 6.4: Estimation of parameters such as $\sigma\phi_0$ and μ for the calibration sample TRTX-Cal of known age of 15 yrs for depth profiles for both IR (a and b) and pVIR (c and d) signals for first and second order kinetics. Normalization was done using the average luminescence derived from the five deepest depth L_n/T_n values, which were in saturation. 139

Fig. 6.5: Exposure ages estimated using first order kinetics for IR data for TRTX-1, TRTX-2B, TRTX-3B, and TRTX-4A 140

Fig. 6.6: Exposure ages estimated using second order kinetics for IR data for TRTX-1, TRTX-2B, TRTX-3B, and TRTX-4A. The potential cause for these substantial uncertainties may be attributed to data scatter. 141

Fig. 6.7: Exposure ages estimated using first order kinetics for pVIR data for TRTX-1, TRTX-2B, TRTX-3B, and TRTX-4A. 142

Fig. 6.8: Exposure ages estimated using second order kinetics for pVIR data for TRTX-1, TRTX-2B, TRTX-3B, and TRTX-4A. 143

Fig. 6.9: Field Photograph of the Study Area: Nubra Valley, Tirith, Ladakh, India ($34^{\circ} 34' 05.2''$ N, $77^{\circ} 37' 09.7''$ E). Desert varnish is prominently observed on all rock formations. 145

Fig. 6.10: Variation of a) FeO and b) MnO with depth of the rock sample for unknown age (TRTX-3B) and calibration sample (TRTX-cal). 145

Fig. 6.11: Scanning electron microscope images of the calibration sample and TRTX-4A sample. No microfractures were observed in the calibration samples whereas fractures of thickness of a few micrometers were observed in TRTX-4A samples. 146

List of Tables

Table 1.1: Summary table of the excited state energy, sub-conduction band-tail width (i.e., Urbach width, E_u), and width of the band-tail states, which are accessible from the ground state of the defect (ΔE) and optical trap depth reported in the previously published studies. Here, potassium feldspar and sodium feldspar are named as KF and NaF, respectively	12
Table 2.1: Parameters of the BSL-SAR protocol (Murray and Wintle, 2000).	49
Table 2.2: Parameters of the IR-SAR protocol (Wallinga et al., 2000).	49
Table 2.3: Parameters of the pIRIR-SAR protocol (Buylaert et al., 2009).	50
Table 2.4: Number of α , β particle, and γ rays emitted and average energy per decay and average dose per decay deposited by radioactive nuclides present in the sediment.	56
Table 3.1: List of samples used and their location, depositional environment, and equivalent doses.	61
Table 3.2: Stimulation and detection spectral region combinations used for fading rate measurements along with their estimated average fading rates [g_{AV} (% per decade)] for single stimulation experiments.	64
Table 3.3: Combinations of stimulation and detection windows used for double stimulation experiments along with the measured g_{AV} -values. The double stimulation experiment comprised sequential stimulation by two wavelengths: stimulation-1 and stimulation-2.	66
Table 3.4: Observed g_{AV} -values for all samples. Here Q and F represents quartz and feldspar, respectively. The paleodoses were estimated using the independently existing protocols such as BSL-SAR and pIRIR-SAR.	73
Table 4.1: List of samples along with geological location and history, and age controls. In the table NCF-refers to natural correction factor.	79
Table 4.2: Dose rate details of all samples.	80
Table 4.3: Parameters for preliminary pVIR-SAR protocol (A). Parameters for optimized pVIR-SAR protocol (B) for the equivalent dose estimation. The text in bold are optimized parameters.	93

Table 4.4: Variation of saturation dose ($2D_0$) with test dose (% of expected doses) for pVIR-SAR protocol for MHK-07-07 and RTP-18-02 sample. 97

Table 4.5: Protocol used to explore the L_x and T_x correlation for the RSN-01-17 sample. * represents the doses given to RSN-01-17. 98

Table 4.6: Saturation doses ($2D_0$) estimated using pVIR-SAR protocol for all samples. 102

Table 4.7: Estimated D_e , fading value, recuperation, residual dose, and dose recovery ratio for all samples using the optimized pVIR-SAR protocol. Recuperation observed in all the samples is <5% except for PRL0 (young sample) where it is less than 10%. * represents the fading uncorrected feldspar doses and ages, + represents the quartz converted feldspar doses, and \$ represents the quartz D_e values and dose rates. 104

Table 4.8: D_e values, fading values, residual doses, and dose recovery ratios for all samples using the pIRIR-SAR protocol. Recuperation in all the samples was <5%. The D_e values are the residual subtracted and fading corrected. * represents the fading corrected feldspar doses and ages. 105

Table 4.9: Protocol used to quantify the IRSL from principal trap contributing to the pVIRSL. 106

Table 4.10: Results of quantification of the IRSL from principal trap contributing to the pVIRSL. 106

Table 5.1: List of samples along with geological location, expected age, and age controls. Here CG and FG stands for coarse and fine grains, respectively. FG and CG represents the fine and coarse grains, respectively. All IR50 and pIRIR measurements were made on feldspar. 111

Table 5.2: Estimated D_e values, fading value, recuperation, residual dose, and dose recovery ratio for all samples using pVIR-SAR, IR and pIRIR protocol. Recuperation observed in all the samples is <5%. The D_e values are corrected for fading, wherever applicable. The residual doses are subtracted from both estimated doses from natural sample and recovered doses from given dose for dose recovery test. Here \$ represents the ages estimated using IR-SAR protocol. 119

Table 5.3: Dose rate details of all samples. 120

Table 6.1: Protocol for measuring luminescence depth profiles for pIRIRSL and pVIRSL signals. 136

Table 6.2: Exposure ages of all samples for IRSL and pVIRSL for both first order and second kinetics. 141

Abbreviations

BBR	Black Body Radiations
BSL	Blue Stimulated Luminescence
BUV	Broad Ultra-Violet
CAM	Central Age Model
CB	Conduction Band
CL	Cathodoluminescence
CR	Cosmic Rays
CWOSL	Continuous Wave Optical Stimulated Luminescence
De	Equivalent dose
DRC	Dose Response Curve
DRc	Dose Rate Calculator
FOK	First Order Kinetics
FMM	Finite Mixture Model
GOK	General Order Kinetics
HPGe	High Purity Germanium Detector
IR	Infrared
IR-PL	Infrared Photoluminescence
IR-RL	Infrared Radioluminescence
IRSL	Infrared Stimulated Luminescence
KF	Potassium Feldspar
LED	Light Emitting Diode
LET	Linear Energy Transfer
LMOSL	Linearly Modulated Optical Stimulated Luminescence
LRSED	Luminescence Rock Surface Exposure Dating
MAAD	Multiple Aliquot Additive Dose
MAM	Minimum Age Model
MET-pIRIRSL	Multiple Elevated Temperature post Infrared Infrared Stimulated Luminescence
NaF	Sodium Feldspar
NUV	Narrow Ultra-Violet

OSL	Optically Stimulated Luminescence
PAD	Phonon Assisted Diffusion
pIRIR	Post Infrared Infrared
pIRIRSL	Post Infrared Infrared Stimulated Luminescence
POSL	Pulsed Optical Stimulated Luminescence
pVIR	Post Violet Infrared
pVIRSL	Post Violet Infrared Stimulated Luminescence
PL	Photoluminescence
PMT	Photomultiplier Tube
PTTL	Photo-transferred Thermoluminescence
SAR	Single Aliquot Regenerative
SEM-EDS	Scanning Electron Microscope with Energy Dispersive Spectroscopy
TL	Thermoluminescence
UV	Ultra-Violet
VB	Valence Band
XRD	X-Ray Diffraction
YTT	Youngest Toba Tuff

Chapter 1

Introduction

1.1 Introduction

The concerns of climatic changes are constantly raising due to excessively increasing artificial interferences. With limited instrumental and historic records available about the formation and evolution of sustainable earth surface processes, studies of past climatic and tectonic variabilities have become crucial for determining future climatic perspectives. Such studies have the potential to inform about the natural and temporal variability of Earth forming processes so that the amplitude of more recent human impact can be understood and controlled for future courses. Studies of the past comprise a) the use of proxy that inform on the amplitude of relevant geological processes and b) analysis of samples for their chronology. Several naturally occurring radioisotopes are used for establishing chronologies, such as radiocarbon and uranium series. The present study deals with the use of mineral luminescence and its use as a natural radiation dosimeter.

After the successful identification of luminescence phenomenon and establishment of its theoretical framework, efforts were initiated to assess its potential for dosimetric purposes. In the late 1940s, Daniels and co-workers were the pioneers in proposing the utilization of TL for quantitatively measuring radiation exposure. Initially, their primary focus was on investigating TL properties in alkali halides and geological specimens (McKinlay, 1981). Daniels et al. (1953) suggested the feasibility of TL dating for ceramics, but it was not until 1959 that the full potential of this technique was recognized (Kennedy, 1959). During the 1960s and 1970s, TL was developed for archaeological dating, notably in Oxford by Aitken et al. (1964) and Aitken et al. (1968).

A major breakthrough occurred when Huntley et al. (1985) reported the discovery of optically stimulated luminescence (OSL) in quartz. This achievement involved the use of green light to stimulate luminescence emission from quartz in the ultraviolet (UV) range. The introduction of optical stimulation for stimulating optically sensitive, photo-bleachable

luminescent signals of ubiquitous minerals quartz, feldspars and many others, opened up new avenues for dating the most recent depositional events of nearly all types of quaternary sediments. These sediments are exposed to daylight during the weathering of their parent rock and undergo multiple episodes of transport, and lose their geologically acquired luminescence. On burial, a build-up of luminescence signal begins due to irradiation of the ambient radiation environment, which enables their dating (Aitken, 1998; Rhodes, 2011; Murray et al., 2021).

Hütt et al. (1988) pioneered the use of infrared stimulation to stimulate luminescence in K-feldspars. Over the past two decades, luminescence dating has emerged as an important chronological tool to establish the timing of archaeological and geological events through its wide ability to provide deposition age of associated sediments (Murray et al., 2021; Singhvi et al., 2022; Akhilesh et al., 2018; Anil et al., 2023, 2022; Bailiff, 2022). The sensitivity of mineral luminescence permits it to cover an age range extending from a few years to several hundred thousand years (Ollerhead et al., 1994; Morthekai et al., 2015).

Luminescence dating relies on the principle that the natural ubiquitous minerals such as quartz and feldspar have the ability to cumulatively record and store the record of their irradiation from the ionizing radiation over long geological time periods. They do so through the accumulation of charges (electrons or holes) in their crystal defects (also termed traps) due to the decay of naturally occurring radioactive isotopes in the surrounding environment. Billion-year half-life of natural isotopes ensures that the radiation flux due to their decay remains constant over million-year timescales.

This chapter provides a brief introduction to luminescence, its production mechanism, and application in burial and surface exposure dating, the current status and challenges in the feldspar dating along with the objectives of the present work.

1.1.1 Luminescence

Luminescence is the light emitted by an insulator without the need for high temperatures, unlike incandescence. This arises from the exposure of crystals by ionizing radiation that causes ionization and release of free charges in the lattice. A minor fraction of these free charges are trapped in defects deficient in charges. The mean residence time of these charges ranges from a few seconds to billions of years (Aitken, 1985). This, on account of the life-time of the electron trapping centre being $\tau \geq 10^{-8}$ s, is known as phosphorescence (Garlick, 1949). Phosphorescence is subdivided as a) short delay ($\tau < 10^{-4}$ s) and b) long

delay ($\tau > 10^{-4}$ s) phosphorescence (McKeever, 1985). This thesis deals with the long delay of phosphorescence in natural minerals. The stored charges can be stimulated by many ways. The luminescence processes are termed based on the mode of stimulation, such as photoluminescence (PL: stimulation by photon absorption), cathodoluminescence (CL; stimulation by electron bombardment), electroluminescence (EL; stimulation by electric current), thermoluminescence (TL; material is stimulated by heating) and optically stimulation luminescence (OSL; stimulation by optical light).

This thesis deals with the TL and OSL of natural minerals.

1.1.1.1 Luminescence mechanism: Band model of solids

Most of the minerals are insulators with a wide band gap of 8-10 eV. The luminescence mechanism in such cases is explained using the band theory of solids (Fig. 1.1). In an isolated atom, electrons are restricted to sets of discrete energy levels. In the solid, the atoms are closer and influence each other. The wave functions of the electrons overlap and result in the formation of energy bands. The band formed from electron filled energy levels is known as valence band (VB), and the band formed from empty energy levels is known as conduction band (CB). The VB and CB are separated by a forbidden gap (E_g). This configuration exists for ideal pure crystals. However, in reality, the crystals have defects and impurities which could be both intrinsic and extrinsic, such as interstitial, substitutional, Schottky and Frankel defects. In naturally occurring crystals, during crystallization, some of the ions of crystals can be replaced with the impurities present in the magma. The nature of the impurity incorporated depends upon its ionic radii, density, concentration, and the chemical and thermal environment existing during crystallization. The defect and impurities break the periodicity of the crystal structure and form the localized energy states within the forbidden gap, as shown in Fig. (1.1a). These impurities can have an attractive potential for certain charge carriers and can retain the charge carriers depending on the charge environment, acting as traps for the charges. These states are thus known as 'traps' and can either capture a hole (known as a hole trap) or an electron (electron trap) depending on charge vacancy. Conventionally, electron traps lie above the Fermi level, and hole traps lie below the Fermi level.

In natural sediments, ionizing radiations (α , β , and γ) having energy of order of MeV are decay products from surrounding long lived radioactive materials such as Uranium (U), Thorium (Th), and Potassium (K). These interact with the crystal, resulting in the creation

of electron and hole pairs (Fig. 1.1b). A large fraction of these electrons recombine with the holes within 10^{-8} s, resulting in fluorescence. A fraction of electrons and holes are captured in the lattice defects. These captured charges are stable depending upon the life time of the trap, which depends upon the ionization state of impurity and strength of attractive potential, i.e., binding energy, also known as trap depth (E). The life time (τ) of charge in a trap is given by

$$\tau = s^{-1} \exp\left(\frac{E}{kT}\right) \quad (1.1)$$

Where s is the attempt to escape frequency ($\sim 10^{15} \text{ s}^{-1}$), k is the Boltzmann constant and T is the ambient temperature. Life time τ can vary from a few seconds to 10^9 years (Singhvi and Wagner, 1986) and is dependent on the ambient temperature. Typical trap depths range from 0 to 2 eV (Aitken, 1985). Traps with a lifetime of more than a hundred million years are of interest for geological and archaeological dating. Charges from traps with low life times (few hundred years or less) lose electrons on storage over long geological times. Therefore, charges from these traps are emptied by a suitable preheating.

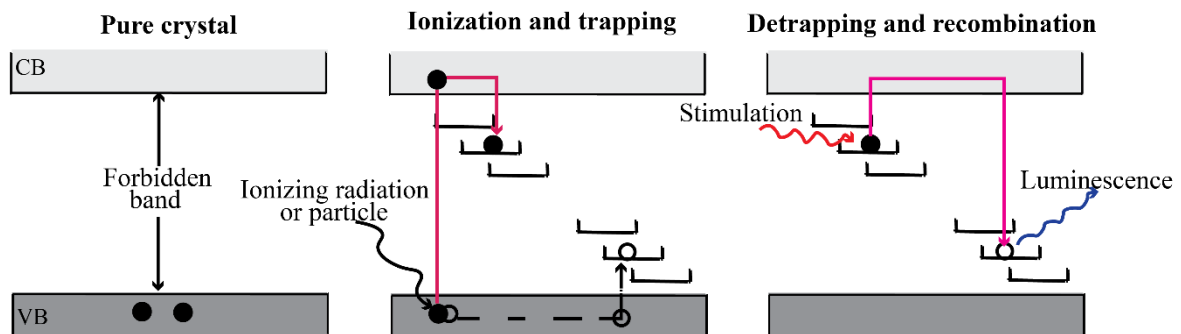


Fig. 1.1: a) Band model for a pure crystal. b) Band model for crystals with trace impurities. Due to impurities and defects crystals have localized energy levels within the forbidden gap. The ionizing radiations excite the electrons from the valence band to the conduction. Some of the electrons are trapped in the localized energy levels. c) The trapped electrons are excited using external stimulation and recombine with holes, resulting in the emission of light from the crystal, known as luminescence.

On stimulation with heat or light, the trapped electrons are evicted and raised to CB (Fig. 1.1c). Some of the electrons in CB radiatively recombine with the holes at a defect state (called recombination centre). It is noteworthy that stability of trapped charges depends on the lifetime of the electron trap whereas the spectrum of emitted light is characteristic of the recombination centre. The intensity of emitted light is proportional to the rate of detrapping of electrons on stimulations (Nambi, 1977) and is given below:

$$I = C \frac{dn}{dt} \quad (1.2)$$

Where I is the luminescence intensity, n is the number of trapped electrons at time t , and C is the proportionality constant.

1.1.2 Thermoluminescence (TL)

Thermoluminescence (TL) is obtained by heating the crystal at a constant rate, and the resulting curve is known as a glow curve. TL glow curve comprises different peaks of each trap, and are termed as the glow peaks. The peak temperature of the glow peak is related to the energy depth of trap. These glow peaks provide the trap distribution of the crystal (Urbach, 1930). Garlick and Gibson (1948) and Randall and Wilkins (1945a, 1945b) established a relationship between the trap depth and TL peak. Randall and Wilkins (1945a, 1945b) computed this relationship using the first-order kinetics theory, considering that on detrapping, an electron can only recombine with hole and give luminescence. Garlick and Gibson (1948) developed a formalism for second-order kinetics, which considered the retrapping of detrapped charges.

The first order kinetics equation is

$$I = n_0 s \exp\left(-\frac{E}{kT}\right) \exp\left[-\left(\frac{s}{\beta}\right) \int_{T_0}^T \exp\left(\frac{E}{kT}\right) dT\right] \quad (1.3)$$

and the second order kinetics equation is

$$I = n_0^2 s \exp\left(-\frac{E}{kT}\right) / N \left[1 + (n_0 s / N \beta) \int_{T_0}^T \exp\left(-\frac{E}{kT}\right) dT\right]^2 \quad (1.4)$$

where I is the intensity, n_0 is the initial concentration of the traps, E is the trap depth, k is the Boltzmann constant, T is the absolute temperature, N is the concentration of empty traps, and β represents the heating rate.

The TL glow curve for quartz in the UV window recorded up to 500 °C at a heating rate of 2 °C/s, is shown in Fig. 1.2a. The TL glow curve of feldspar in the blue detection window,

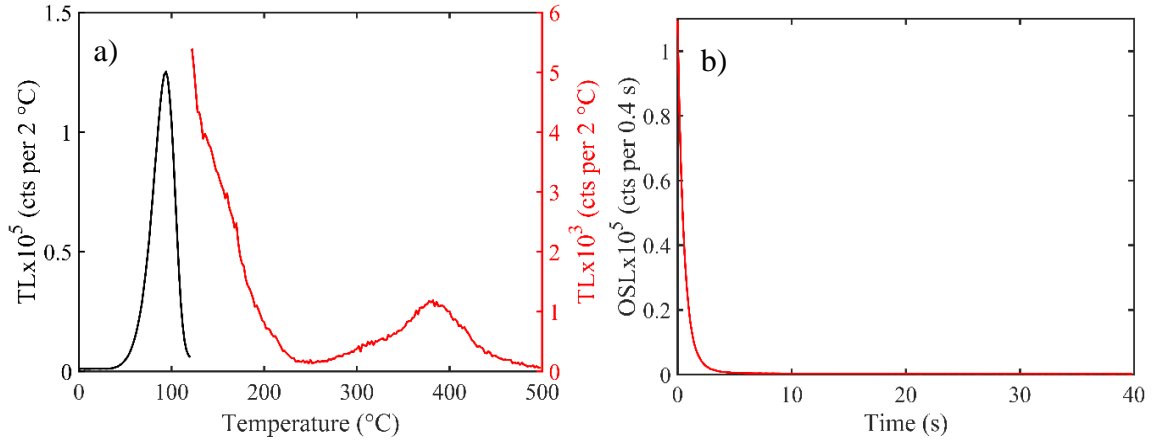


Fig. 1.2: a) TL glow of quartz recorded in the UV window recorded up to 500 °C at a heating rate of 2 °C/s. b) OSL decay curve of quartz with blue stimulation and detection in UV window.

is shown in Fig. 1.3a. TL is useful to estimate the kinetic parameters of the traps, such as trap depth, order of kinetics, and attempt to escape frequency.

1.1.3 Optically stimulated luminescence (OSL)

OSL is obtained by stimulating the crystal with photons in the UV-visible-IR energy region, the basic mechanism of which is depicted in Fig. 1.1. When the energy of a photon exceeds the trap depth, it results in the ejection of electrons from their bound states, facilitating their transition to the conduction band. Subsequently, some of these freed electrons recombine with holes, emitting a luminescence signal. The intensity of OSL depends on the intensity of the stimulation light (ϕ) and photo-ionization of the trap (σ) as

$$I = \frac{dn}{dt} \propto \phi\sigma(\lambda) \quad (1.5)$$

Where I is the OSL intensity, n is the number of trapped electrons at a time t . The photo-ionization cross-section is a function of incident wavelength (λ). On stimulation, the concentration of trapped electrons decreases exponentially, hence the OSL. The OSL decay curve for quartz with blue stimulation and UV detection window is shown in Fig. 1.2b. OSL can be stimulated in several ways such as continuous wave OSL (CWOSL), pulsed OSL (POS�), linearly modulated OSL (LMOSL) based on if the stimulation intensity remains constant or is pulsed or increased with time in a programmed manner. These help understand the different properties of the traps and their usages in dating.

1.1.4 Natural phosphors/dosimeters

Most applications of luminescence dating use two ubiquitous minerals, quartz and feldspar. These minerals cover around 60% of the earth's crust. Other minerals such as calcium carbonate (CaCO_3), gypsum ($\text{CaSO}_4 \cdot 2\text{H}_2\text{O}$), olivine, zircon, biotite, and others are also explored for specific locales.

1.1.4.1 Quartz

Quartz is one of the most abundant minerals comprising approximately 12% of the Earth's crust by volume. It is widely distributed and found in various rock types, including igneous, metamorphic, and sedimentary. For dating, most of the studies so far have used quartz due to its robust luminescence properties in respect to its stability and ease of bleachability. Quartz has a stable OSL signal, and it offers several advantages over the other minerals. Quartz is resistant to weathering. Therefore, it is more likely to be present in the sediment samples (Wintle and Murray, 2006). The daylight exposure time required to remove electrons from the defects present within quartz is small (1–100 s) compared to K-feldspars (several hours (Li and Li, 2014)). Therefore, there is usually no past remnant OSL signal present in quartz. The OSL decay curve for quartz is shown in Fig. 1.2b. Quartz exhibits spectral emission in the range of 290 nm to 700 nm, spanning from ultraviolet to visible wavelengths (Krbetschek et al., 1997 and references therein). The OSL decay of quartz comprises of 3 to 7 components, and the fast component is most used to measure the radiation doses up to 150–200 Gy (Chawla et al., 1998). Beyond this, the growth of luminescence with dose exhibits a saturation (Aitken, 1985; Wintle and Murray, 2006).

1.1.4.2 Feldspar

Feldspar minerals account for approximately 60% of the Earth's crust. Different types of feldspar present are potassium feldspar (KAlSi_3O_8), sodium feldspar ($\text{NaAlSi}_3\text{O}_8$), and plagioclase feldspar, which is a solid solution series between the sodium and the calcium feldspar ($\text{CaAl}_2\text{Si}_2\text{O}_8$). Feldspars are important constituents of different rock types, including igneous, sedimentary, and metamorphic. For luminescence dating, K-feldspar is widely used because of the following reasons:

1. The luminescence intensity of K-feldspar saturates at several fold higher radiation dose (~1200 Gy; Buylaert et al., 2012) than those for quartz (150–200 Gy (Chawla et al., 1998)).

2. The luminescence sensitivity (luminescence/dose/weight) of feldspar is high due to its inherent impurities and defects (Pye et al., 1995).
3. Its internal radioactivity of ^{40}K and ^{87}Rb , makes it suitable for dating younger samples and provides additional means to check the robustness of ages (Li et al., 2007b).
4. Another advantage of using feldspar is its sensitivity to IR stimulation. This removes the need for a rigorous mineral separation, as most other minerals are not sensitive to IR stimulation (Hütt et al., 1988).

These attributes of feldspars offer the potential to increase the range of luminescence dating from a few years to around a Ma (Ollerhead et al., 1994; Morthekai et al., 2015). Its use has, however, been limited due to anomalous fading (Huntley and Lamothe, 2001): the athermal loss of luminescence signal in addition to that predicted by the kinetic considerations. This loss of luminescence signal is attributed to the quantum mechanical tunnelling effect (Jain and Ankjærgaard, 2011; Visocekas, 1979). The TL and IRSL decay curve detected in the blue window of potassium feldspar is shown in Fig. 1.3a and 1.3b.

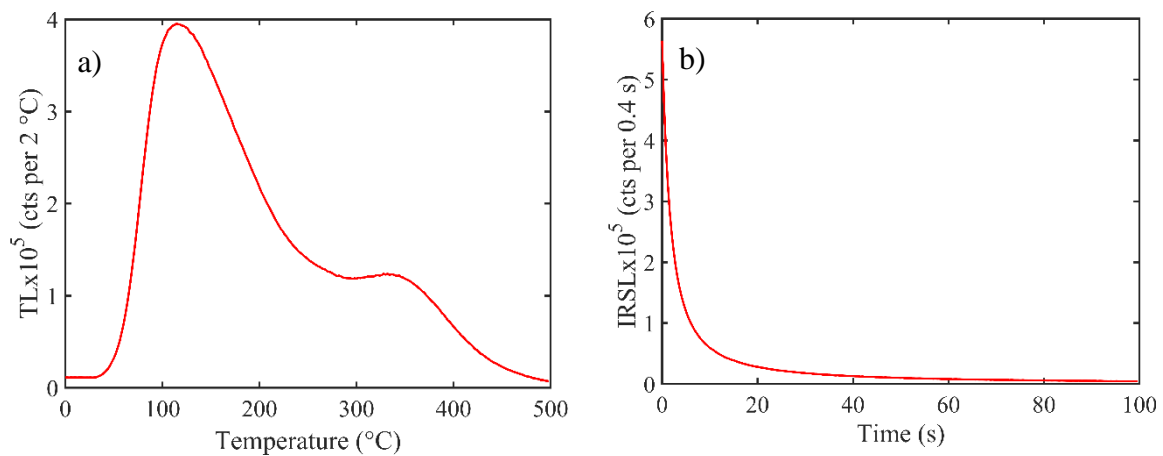


Fig. 1.3: a) TL glow of potassium feldspar (KF) recorded in the blue window. b) IRSL decay curve of KF detected in blue window.

1.1.4.2.1 Crystal structure

Feldspar crystal lattice consists of (Al, Si)O₄ tetrahedra connected to four other similar tetrahedrons through shared oxygen ions at their vertices. These lead to a continuous, interconnected structure. The framework has four tetrahedral positions (two each of T1 and T2) occupied by Si⁴⁺ or Al³⁺. A significant number of the large cations (primarily K⁺, Na⁺, and Ca²⁺) occupy cavities in the framework termed as M-sites, resulting in a net negative

charge (Deer et al., 2013). Typically, feldspars contain three end members with distinct cations at the M-sites: KAlSi_3O_8 (K-feldspar), $\text{NaAlSi}_3\text{O}_8$ (Na-feldspar), and $\text{CaAl}_2\text{Si}_2\text{O}_8$ (Ca-feldspar).

1.1.4.2.2 Band model of feldspar

The IRSL production of feldspar was explained using the two stage excitation model by Hütt et al. (1988), given that the excitation energy of IR (1.44 eV) is lower than the estimated trap depth (~2-2.5 eV). The IR stimulation excites the electrons from the ground state of the trap to its excited state at 1.44 eV. The excited electrons are thermally assisted to reach the conduction band and thereafter recombine with holes to give the IRSL. Poolton et al. (2002a) reported the existence of localised states below the conduction band and attributed them to structural disorders, different bond angles, thermal vibrations, and random distribution of impurities. These states are known as band-tail states. The band model for feldspar luminescence production was refined by Jain et al. (2011) based on a single trap (also known as a principal trap) and spatially distributed recombination centers (Fig. 1.4). The excited state of the principal trap overlaps with the band-tail states, facilitating the transfer of excited-state electrons to the band tails through phonon-assisted diffusion (PAD). This process leads to recombination with holes in the recombination centers, resulting in luminescence. The IRSL is a consequence of the recombination of electrons and holes in close proximity to each other.

Further using low temperature Infrared-Photoluminescence (IRPL) excitation-emission spectroscopy, Kumar et al. (2020) elucidated the nature of the principal trap of potassium rich feldspar through two distinct trapping centres, emitting IRPL at 1.31 eV and 1.41 eV. These trapping centres have different thermal stabilities and different ground and excited state energies, but their dose response curves (DRC) and relaxation times are identical. Based on their IRPL data, they suggested that these are the manifestation of the same centre but with a in slightly different crystal field environments. They reported there are atleast three resonating peaks, namely peak 1, peak 2, and peak 3, for each centre (Fig. 1.5). Peak 1 and 3 are the excited states of the trap, which exist below and above the conduction band. Peak 2 represents the transition to CB edge, which is the trap depth of the principal trap (Kumar et al., 2020).

In the past, there have been theoretical and experimental studies to understand the luminescence mechanism of potassium feldspar. The optical trap depth for the principal

trap is in the range of 2.0 to 2.5 eV (Hütt et al., 1988; Kumar et al., 2020; Riedesel et al., 2019, 2021). Energies of the first excited state, sub-conduction band-tail widths (i.e., Urbach width, E_u) and the width of the band tail states accessible from the ground state (ΔE) ranges from 1.44 to 1.48 eV (Hütt et al., 1988; Riedesel et al., 2019), 0.26 to 0.81 eV (Poolton et al., 2009; Riedesel et al., 2019) and 0.16 to 0.46 eV (Poolton et al., 2009; Riedesel et al., 2019), respectively (Table 1.1). Feldspar exhibit spectral emissions in the range of 280 nm to 860 nm, spanning from ultraviolet to near-infrared wavelengths (Krbetschek et al., 1997 and references therein).

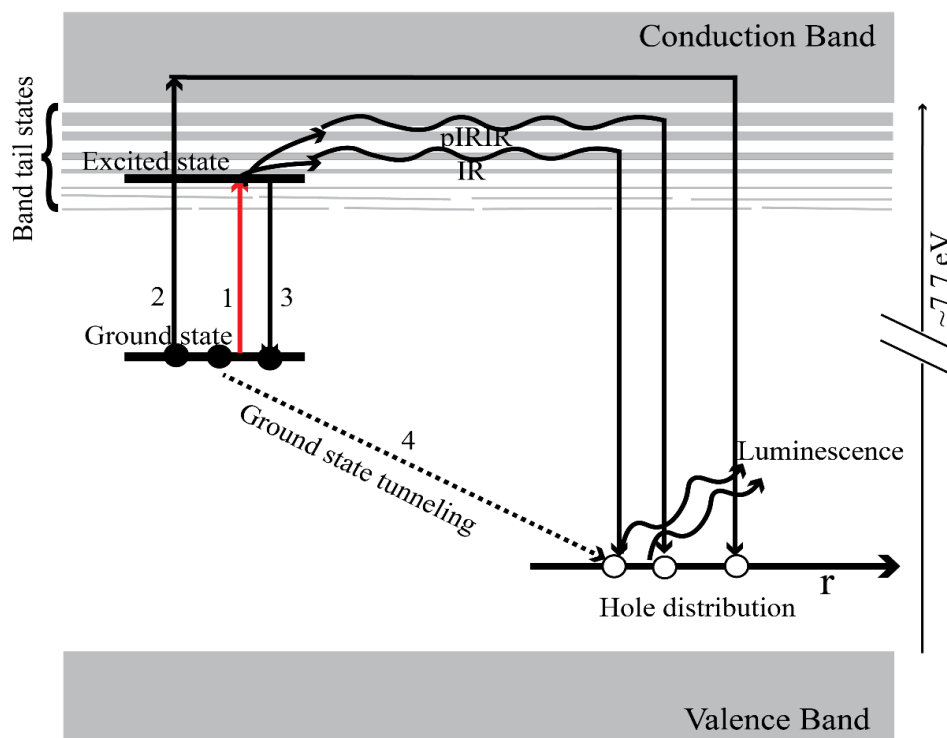


Fig. 1.4: Band model for K-feldspar luminescence (Redrawn after Jain et al. (2011)). Transition 1 is representing the resonating transition from principal trap (dosimetric trap) of feldspar. Transition 2 is non-resonating transition to the conduction band from high energy stimulations, e.g., blue (~2.63 eV) and violet (~3.06 eV). Transition 3 is recapture from the excited state of principal trap to the ground state. Transition 4 is representing the direct recombination of electron and hole due to quantum mechanical tunnelling.

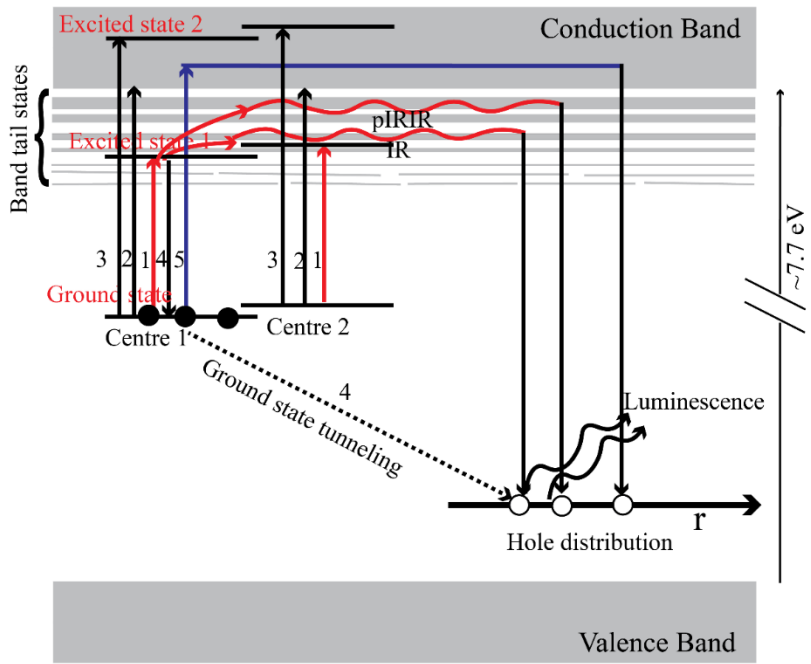


Fig. 1.5: Modified band model for K-feldspar from Kumar et al., (2020) and Jain et al., (2011).

Table 1.1: Summary table of the excited state energy, sub-conduction band-tail width (i.e., Urbach width, E_u), and width of the band-tail states, which are accessible from the ground state of the defect (ΔE) and optical trap depth reported in the previously published studies. Here, potassium feldspar and sodium feldspar are named as KF and NaF, respectively

Method	Mineral	Excited state energy (eV)	Band tails width (eV)		Optical trap depth (eV)	References
			E_u (eV)	ΔE (eV)		
Optical excitation or the relationship between optical and thermal activation energies	Microcline	~1.45			~2.25	Hütt et al., 1988
Photostimulated luminescence excitation spectroscopy	KF				<2.5	Clark and Sanderson, 1994
Estimated based on hydrogenic nature of the trap	KF	1.44				Poolton et al., 1995b
IR stimulation spectroscopy	NaF and microcline	~1.48 and ~1.47				Godfrey-Smith and Cada, 1996
Estimated based on hydrogenic nature of the trap	NaF and KF	1.48			1.97 (NaF) and 1.99 (KF)	Poolton et al., 2002a,b
Correlation between the shape and intensity of the OSL signals or OSL excitation spectroscopy	Wide range of Feldspar	1.44–1.45			>2.5	Baril and Huntley, 2003
Fitting of excitation spectra (photo-transferred OSL and TL) measured at 10 K (E_u) Fitting the non-resonant rising continuum excitation spectrum at 300, 200, 100 and 10 K (ΔE)	NaF and KF		NaF: 0.28 and 0.32 0.67 and 0.54	NaF: 0.12-0.09 KF: 0.30 to 0.16	2.0-2.5	Poolton et al., 2009
Time-resolved OSL	Orthoclase				> 2.4	Jain et al., 2011
Red-IR spectroscopy	Orthoclase	1.44-1.47				Andersen et al., 2012

Fitting of excitation spectra at 10 K using an equation for the photoionization cross-section of a deep defect	NaF and KF			0.18 and 0.23	~2.1 (NaF) and >2.5 (KF)	Kars et al., 2013
IR-Photoluminescence excitation spectra at 7, 100 and 295 K	Oligoclase		0.32			Prasad et al., 2016
IR-Photoluminescence excitation spectra at 295 K	KF and NaF		0.29–0.51			Prasad et al., 2018
Fitting of excitation spectra at 10 K using an equation for the photoionization cross-section of a deep defect	Feldspar (Irrespective of chemical composition)	1.44	0.26 to 0.81	0.21- 0.46	~2.04	Riedesel et al., 2019
IR-Photoluminescence excitation spectra at cryogenic temperature	Feldspar				IRPL _{1.30} 1.90 to 2.21 IRPL _{1.41} 2.15 to 2.38	Kumar et al., 2020a
IR-Photoluminescence excitation spectra at 7 K	Feldspar				IRPL _{1.30} 2.04 to 2.20 IRPL _{1.41} 2.16 to 2.46	Riedesel et al., 2021

*IRPL_{1.30} and IRPL_{1.41} mean photo-luminescence spectra are detected in 1.30 eV and 1.41 eV, respectively.

1.1.4.2.3 Anomalous fading

A key impediment in the routine use of feldspar for dating of samples has been the presence of anomalous fading, which limits its usage. Wintle (1973) detected this for the first time in volcanic feldspars. Anomalous fading is the athermal loss of luminescence signal in addition to that predicted by the kinetic considerations (Aitken, 1985; Spooner, 1992, 1994; Wintle, 1973; Visocekas, 1979). Thus, signals that are expected to be stable over geological timescales decay over days and weeks. The fading leads to an underestimation of age.

When an electron is trapped in a potential of finite depth, then according to quantum mechanics, there is a finite probability of escape of electron from the potential well via tunnelling. It loses its luminescence over time even at very low temperatures (~77 K). There are several possible ways of tunnelling in feldspar as shown in Fig. 1.6. Transition *a* represents direct tunnelling from trap to hole centre without any thermal assistance and hence called athermal or anomalous fading. In transition *b*, trapped electron will get finite temperature and then tunnel to hole centre. Similarly, in *c* and *d* transitions, electrons will get thermal energy and will go either to the hole centre or the conduction band. All these possibilities of tunnelling ultimately lead to a decrease in luminescence signal. Quantum tunneling depends on the distances between the trap centers and the recombination centers. The probability of tunneling increases if the trap centres and recombination centres are near to each other and vice versa. As feldspar has many impurities, therefore, electron and hole centres are closely spaced, resulting in the direct recombination of electrons and holes (Visocekas, 1985). The tunneling probability or transmission coefficient is given by the following equation (Griffiths, 1995):

$$T = \frac{16E}{V} \left(1 - \frac{E}{V}\right) e^{\left(-2W \left(\frac{\sqrt{2m(V-E)}}{\hbar}\right)\right)} \quad (1.6)$$

Eq. 1.6 can be expressed in a simplified form as

$$T \propto \exp(-\alpha W) \quad (1.7)$$

Where 'E' is the energy of the incident particle, 'V' is the potential height, 'W' is the distance between the electron and hole, and 'α' is a constant. For randomly distributed

defects, a range of tunneling probabilities can arise. Eq. 1.7 indicates that quantum tunneling probability is dependent on the distance between the donor (electron) and the acceptor (hole) and it decreases as distance increases. Therefore, tunneling begins with the proximal donor-acceptor pairs, and as time progresses, the distant pairs recombine (Poolton, 1994). The rate of recombination of electron and hole is inversely proportional to time elapsed (t) after the irradiation. The light intensity observed after the recombination of electron hole pairs is termed as ‘afterglow intensity’ and is given below (Huntley and Lamothe, 2001) as

$$\text{After glow intensity} \propto (t)^{-1} \quad (1.8)$$

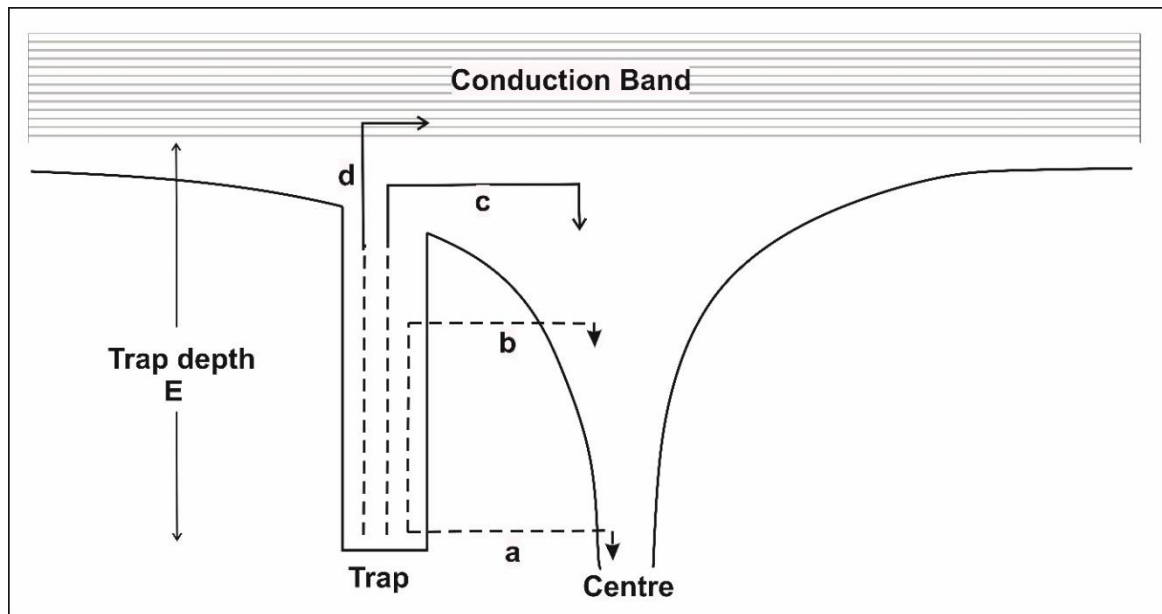


Fig. 1.6: Escape routes from a trap; a) athermal tunnelling; b) thermal assisted tunnelling; c, d) thermal eviction.

Integration of the above suggest that the intensity depends on the logarithm of time. The relationship between intensity and time elapsed after radiation can be given as (Huntley and Lamothe, 2001):

$$I = I_c \left[1 - \left(\frac{g}{100} \right) \log \left(\frac{t}{t_c} \right) \right] \quad (1.9)$$

Where ' t_c ' is any characteristic time and ' I_c ' is the intensity measurement at that time. ' t ' is the delay time since irradiation and ' I ' is the delayed intensity. ' g ' is the fading rate and is the fractional decrease in the intensity from t_c to $10t_c$. The unit of ' g ' is in percentage per decade (% per decade). The g -value can be estimated from the slope of graph plotted between delayed intensity and delay time on semi-logarithmic scale (Eq. 1.9).

Two approaches are most widely used to correct or circumvent the athermal fading. These include

- a) laboratory estimation of the fading rate with samples stored for various delay times and correcting the measured ages considering fading rates (Huntley and Lamothe, 2001; Auclair et al., 2003)
- b) probing the stable (deeper) traps that are not faded in nature (Buylaert et al., 2011, 2012; Biswas et al., 2012; Morthekai et al., 2015).

The fading corrected ages using Huntley and Lamothe's prescriptions are restricted to the linear portion of the dose response curve (DRC) and therefore are limited to an age range of 20 to 50 ka (Huntley and Lamothe, 2001). For older samples, further corrections were made by Huntley (2006) and Kars and Wallinga (2009). These fading correction methods lead to higher uncertainty in the age calculations. In addition, models for fading correction assume that the fading rates estimated over laboratory time scales can be extrapolated to geological time scales. However, this assumption is questioned several times and is difficult to test in laboratory conditions (Li and Li, 2014).

In the second approach, luminescence signals from stable recombination centres are measured. As suggested signals may come from the distal pairs which comparatively have a larger tunnelling life time and therefore show lower fading rates (Jain et al., 2015; Poolton, 1994). Such signals have been variously probed e.g., a) post-IR IRSL (pIRIRSL; Buylaert et al., 2009; 2011, 2012; Biswas et al., 2013; Thomsen et al., 2008), b) multiple elevated temperatures pIRIRSL (MET-pIRIRSL; Li and Li, 2011), c) thermally redistributed IRSL (RD-IRSL; Morthekai et al., 2015), d) infrared photoluminescence (IR-PL; Kumar et al., 2018; Prasad et al., 2017a) and e) infrared and blue light stimulated photo-transferred thermoluminescence (PTTL; Kalita and Chithambo, 2021; 2022). The pIRIRSL signal is widely used for luminescence dating as high temperature IR stimulation (225 and 290 °C) measured after IR 50 °C bleach, yields negligible or low fading rates (Biswas et al., 2012; Buylaert et al., 2011, 2012; Morthekai et al., 2015).

IRPL also offers a good prospect to probe non-fading emission from the IR traps in feldspar (Prasad et al., 2017; Kumar et al., 2020) and is suggested to be a promising signal. The PTTL signal induced by blue and infrared lights shows negligible anomalous fading (Kalita and Chithambo, 2021). Currently, both IR-PL and PTTL methods are being refined, since, they offer prospects for obtaining stable luminescence signals from feldspar (Kalita and Chithambo, 2022; Kumar et al., 2021; Prasad et al., 2017a).

1.1.5 Luminescence for geological dating

Luminescence has been used for the determination of burial age and exposure ages of the associated geological events. The events that can be dated using luminescence are: a) last heating events (pottery, bricks, volcanic ash, and fire events, etc.), b) recent daylight exposed events (sediments transported by water, wind, glacier, debris, and rock exposed by deglaciation), and c) crystallization events (gypsum, carbonates, salts and volcanic ashes, etc.).

1.1.5.1 Burial age determination

Luminescence dating is now an established tool to date buried sediment, and the event dated is the most recent burial event. In sediments, minerals like quartz and feldspar are surrounded by ambient radioactive nuclides (U, Th, and K). These nuclides emit alpha (α), beta (β), and gamma (γ) radiations having energy of the order of MeV. Along with these radiations, there is also a small contribution from cosmic rays (CR). These ionizing radiations interact with the minerals, create the electron-hole pairs in the crystal, and deposit their energy in the form of trapped charges. The energy deposited per unit mass is known as dose (Units Gray: Gy = Joule/Kg). The charges captured in the traps having life time greater than Ma are used for luminescence dating.

On thermal and optical stimulation, charges in traps are de-trapped and recombine with holes to give luminescence. The luminescence intensity (photons/s) is proportional to the number of trapped charges, which in turn is proportional to the radiation dose acquired by the crystal and the surrounding radiations during its burial. Therefore, by estimating the luminescence intensity, the dose acquired by the crystal can be estimated. The half-lives of radioactive nuclides are of the order of 10^9 years (Ga) (Aitken, 1985). Therefore, for million years timescale, the decay of these nuclides is negligible, giving a constant rate of deposition of energy. This is called dose rate and is normally expressed as Gy/ka, i.e., energy deposited per thousand years. The decay series of these radioactive nuclides is

shown in Fig. 1.7. There is also a small contribution from ^{87}Rb and cosmic rays, which should be added while estimating the dose rates. In addition to dose rate contribution to minerals from the surrounding sediments, the radioactivity present inside the minerals also contributes significantly for the coarse grains ($>90\ \mu\text{m}$). For quartz, internal radioactivity contribution is negligible (Murray and Roberts, 1997), however for K-feldspar, the internal radioactivity is 14% due to the inherent ^{40}K isotope and it can contribute up to a few percent of the total dose rate (Mejdahl, 1987). The radioactive nuclides emit α -particles, β -particles, and γ -radiations. The α -particles deposit their energy in the crystal through ionization and excitation, resulting in generation of electrons, which further deposit energy. These are heavy mass particles and, hence, travel in straight paths. These particles have +2 charge, and hence have high linear energy transfer (LET). A large number of electron-hole pair are generated along their straight path, resulting in saturation to the available traps. Most of the charges are lost and dissipate their energy in the heating of the crystal. Therefore, the luminescence generation efficiency of α -particles is lower and needs to be considered during the dose rate estimations. The β -particles interact with orbital electrons through coulomb interaction and by ionization. These particles travel in scattered paths and hence deposit the energy uniformly in the crystals. The γ -radiations are neutral and interact with matter by the photoelectric effect, Compton scattering and pair production, and further deposit their energy similar to the β -particle. In addition to these, very high cosmic particles ($> \text{GeV}$) can enter into the earth's atmosphere. Most of them are absorbed in the atmosphere. However, secondary cosmic particles, such as soft electromagnetic radiations and muons reach the earth's surface. These particles interact with matter and hence deposit the dose in

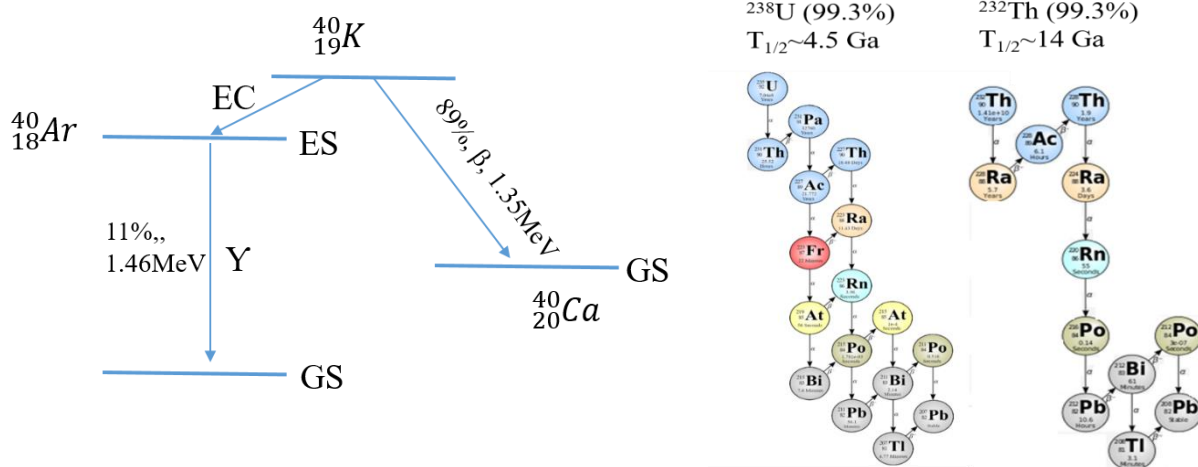


Fig. 1.7: Decay chain of ^{40}K , ^{238}U and ^{232}Th nuclides.

the minerals. Therefore, their contribution to the total dose rate needs to be estimated considering their dependency on latitude and geographical latitude.

The dose rate is calculated by estimating the concentration of radioactive nuclides in the sample, their stopping powers, and the concentration of their daughter products. The contribution from cosmic rays is derived from known fluxes, burial depth, latitude, and altitude (Prescott and Hutton, 1994). Estimating both dose and dose rate enables the estimation of time (age) of irradiation of the sample as:

$$\text{Age (ka)} = \frac{\text{Equivalent dose (D}_e\text{)}}{\text{Dose rate (D}_r\text{)}} \quad (1.10)$$

Here, the equivalent dose (D_e) is the dose absorbed from laboratory beta radiations that induces the same luminescence intensity as that from the dose absorbed in nature. The dose rate (D_r) is the dose deposited by unit time. The unit of dose is Gy, and the dose rate is expressed as Gy/ka. Age is generally reported in kilo years (ka) or years (a).

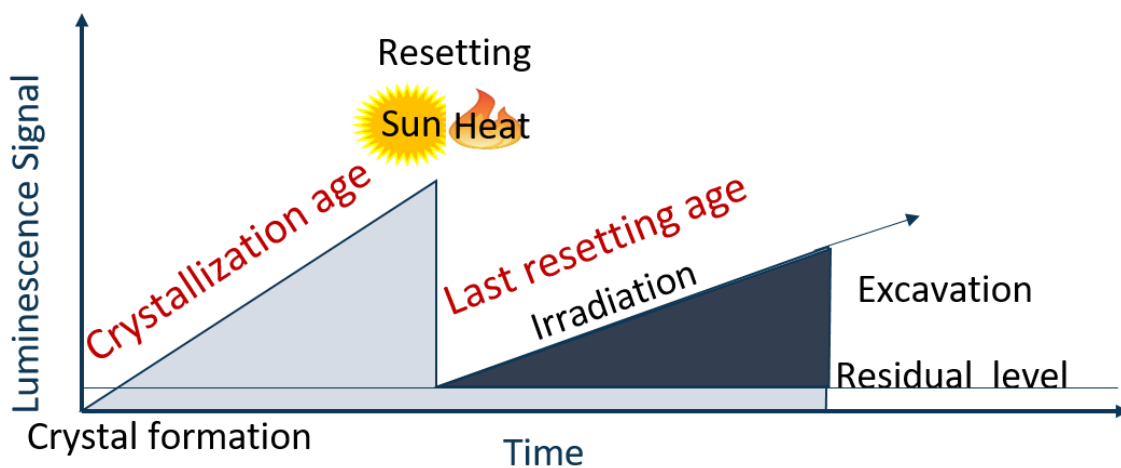


Fig. 1.8: Variation of luminescence signal in nature. After crystallization, minerals inside the rock store the energy in the form of electrons from the surrounding radioactive elements. The stored energy is released by daylight exposure. After the burial, crystal again starts to accumulate dose from ambient radioactivity. The timing of the burial event can be estimated by collecting samples.

Fig. 1.8 shows the variation of luminescence signal in nature. After the crystallization of the sample, minerals start to acquire dose from the surrounding radioactive nuclides. The signal increases till saturation/equilibrium as the burial time increases. At saturation/equilibrium, the signal becomes constant because the traps cannot be filled any further, and it remains so till exposure to either daylight or heating to few hundred °C takes

place. During weathering, erosion and transport, mineral grains constituting sediment are exposed to daylight, and this bleached the geological signal to a near zero residual level (beyond which the signal cannot be bleached). If sample gets buried again luminescence acquisition begins again due to irradiation from its ambient radioactivity. This dose accumulation continues till excavation. There can be multiple cycles of exposure (resetting) and burial (dose accumulation) of the sample during its journey in nature. Generally, the last burial event can be dated using the luminescence dating technique (Fig. 1.8). Therefore, this technique provides the estimate of the time elapsed since the sediments were last exposed to the sun.

In the laboratory, by estimating the dose accumulated and the rate of deposition of the dose (dose rate), the age of the last burial event can be estimated. For older samples near saturation/equilibrium, a minimum age can only be estimated. Reliable depositional ages were obtained for a wide variety of sediments from a few years old to several hundred thousand years (Ollerhead et al., 1994; Mortheikai et al., 2015). Murray et al. (2021) provide a compilation of all the ages with controls and show that luminescence can provide reliable ages.

1.1.5.2 Exposure age determination: Rock surface dating

Luminescence rock surface exposure dating (LRSED) is a method used to estimate the time since when a rock surface has been exposed to daylight. This technique utilizes the luminescence properties of minerals present in rocks to estimate the duration of their exposure to daylight. LRSED has emerged as a valuable tool for investigating the age of geological and archaeological events and processes.

Exposure of a rock surface to daylight bleaches the daylight luminescence signal immediately on the surface. The rate of bleaching depends on the flux and energy of the daylight exposure. The daylight flux on the surface decreases exponentially with depth as per the Lambert-Beer law. Thus, the rate of resetting in the interior progressively becomes slower. As a result, the residual luminescence increases with depth and reaches saturation, where the daylight cannot reach further (Sohbati et al., 2011). The profile follows the sigmoidal function with depth, and this profile penetrates deeper into the rock with time. The light penetration depth and, thus, the resetting depth depends on rock type, radioactivity content, and duration of daylight exposure. As radioactivity content and type

of rock do not change, the duration of exposure time of the rock surface can be estimated from the dose depth relation of the sigmoidal profile (Sohbati et al., 2011).

Over the past few years, studies on the use of OSL to date rock surfaces have increased, due to the possibility of its varied applications in archaeology, geomorphology and tectonics, as it can help date rock falls, landslides and glacial events, and enable the understanding of long term evolution of landscapes. In archaeological sciences, it enables the dating of rock art, stone gargoyles or lithic implement's features. This method provides valuable insights to elucidate the manner in which people have used the landscape and how it has evolved over time. In geology, the ice rock surfaces polished by ice movements and boulders deposited as glacial moraines during glacial advancements, help in studying the glacial cover over the region and thence used for paleoclimatic studies. Further gravels or boulders deposited during extreme flood events can help us develop the flooding history of the region.

Conventionally, the exposure dating is done using cosmogenic radioactive nuclides (CRN) (Lal, 1991), and attempts are being made using LRSED technique to establish the same. The former technique is based on the production of radionuclides from cosmic rays, and is based on the concentration of these nuclides. It gives the time since when rock has been exposed to the cosmic rays. The latter approach requires the resetting of the luminescence signal with the exposure time of the rock, and is based on the depth of resetting. It gives the exposure time of the rocks. Theoretically, LRSED technique appears to be much simpler and effective than CRN, as the sample is still preserved after the measurements. However, the technique is still in a developmental stage, and a lot more needs to be done to achieve the practical applicability of the technique. LRSED mainly uses the OSL and the IRSL for dating, due to their rapid bleachability than the TL signal (Liritzis and Galloway, 1999). LRSED offers following additional advantages over CRN dating method:

1. Study of multiple events of exposure and burial
2. Estimation of erosion rates
3. Applicability to estimate exposure times on non-terrestrial bodies for in situ measurements.

In luminescence based dating of rock surface, multiple sequential events to daylight exposure can be detected and dated by plotting the optical luminescence signals as a function of depth into rock surfaces. In geology, it can tell events of glaciation and

deglaciation from a single piece of rock provided not much erosion has occurred. In archaeology, this method informs about the burial/used events the stone tools faced and the manner of their use (Galganic et al., 2018; Freiesleben et al., 2015).

LRSED is used to quantify the erosion rates of the rocks. Erosion rate can be estimated using luminescence surface exposure dating and cosmogenic radionuclide method. The cosmogenic radionuclide method is less sensitive to erosion as the mean free path for cosmic rays is 50 cm. In contrast, the luminescence signal is sensitive to incident daylight and depth. The absorption mean free path of sun-light is on the scale of mm (Sohbati et al., 2012b). Therefore, any loss in the rock surface due to erosion can be detected from the luminescence depth profile provided that an independent age of the same event is available. The erosion of the earth surface is caused by a combination of physical, chemical and biological weathering. These weathering products are removed by aeolian and fluvial processes. Erosion rates and timings of such events on spatial and temporal scale determine the contribution of each process and hence, understanding of the evolution of landscape (Sohbati et al., 2018).

In addition to the above, LRSED has the potential to provide luminescence based exposure ages for lunar, planetary, and asteroid surfaces (Sohbati et al., 2012a). This helps for understanding the evolution of modern surfaces. For instance, Martian surfaces exhibit a lot of aeolian, fluvial and volcanic events. For such surfaces, crater density method is used to find the age. This technique has an uncertainty of ~1 Ma. Therefore, for events of age within million years, OSL surface exposure technique provides a viable method for in-situ measurements of time scales of surface processes operating on Mars. Use of the CRN dating technique is not possible for non-terrestrial bodies due to a long chemical procedure, precise sample preparation requirements, and incapability to transport the accelerator mass spectrometer (AMS) system to such bodies (Sohbati et al., 2012a).

The luminescence rock surface dating method has also been used to estimate the burial ages of the gravels deposited by tsunamis and glaciers etc. (Galganic et al., 2018; Jenkins et al., 2018). In the luminescence sediment dating, there is always an assumption that the sample is bleached prior to burial. This assumption can directly be tested on the burial rocks by selecting the suitable surface (Galganic et al., 2018; Jenkins et al., 2018).

The use of LRSED was first explored on freshly excavated marble objects using thermoluminescence (TL), but the results showed overestimation in the ages (Polikreti et

al., 2003). This discrepancy was attributed to residual TL signal persisting after prolonged exposure to daylight, which additionally limited its use for the young samples (Liritzis & Galloway, 1999). In those days, optical bleaching of luminescence was not well known. Development of sediment TL dating and then of the optically stimulated luminescence (OSL) made it possible to examine only the optically sensitive signal, which paved the way to date exposure of rock surfaces (Greilich & Wagner, 2005; Habermann et al., 2000; Vafiadou et al., 2007). The most promising outcomes were obtained from the use of OSL and IRSL signals from quartz and feldspar for surface exposure studies, respectively (Greilich & Wagner, 2005; Sohbaty et al., 2012a, 2012b, 2015; Vafiadou et al., 2007). Luminescence measurements are conducted on polymineral samples as limited quantity of samples are available from the slices. The OSL (blue stimulation) stimulates both quartz and feldspar. However, the IRSL stimulates only feldspar luminescence, which is intrinsically more sensitive than quartz (Baril and Huntley, 2003). Therefore, recent studies have used IRSL for surface exposure studies (Freiesleben et al., 2015; Meyer et al., 2018; Sohbaty et al., 2018)-

1.1.5.2.1 Models for OSL and IRSL dating

Previous studies have made significant developments in the LRSED (Freiesleben et al., 2015; Meyer et al., 2018; Sohbaty et al., 2011, 2018 and references therein). A kinematic model to describe the resetting of luminescence with depth and as a function of time, was developed by Sohbaty et al., 2011. The LRSED is based on the resetting of charges in the presence of natural daylight. When rocks are buried beneath the Earth's surface, they are shielded from the daylight. During this burial, minerals in the rocks, such as quartz and feldspar, accumulate energy from ionizing radiation in the environment, primarily from radioactive isotopes (such as U, Th, and K) present in the surrounding sediments. If the rock is buried and shielded from the sun for millions of years, the electrons trapped in the minerals are in the field saturation due to finite trapping capacity. When the rock is exposed at the Earth's surface due to erosion or other geological processes such as exhumation and fracture, it is subjected to the daylight. The photons from the daylight provide an external energy source that can stimulate the trapped electrons present within the minerals. The population of the trapped electrons begins to deplete as the daylight exposure bleaches the light-sensitive traps to a near zero residual value. The detrapping rate of electrons decreases with depth because of attenuation of daylight flux with depth, which follows Beer-Lambert's law, i.e.,

$$I_x = I_s e^{-\mu x} \quad (1.11)$$

Where μ is the attenuation coefficient, I_s and I_x is the daylight intensity at surface and at depth x . Attenuation coefficient defines the slope of the profile and hence, depth and exposure age. The rate of change of population of electrons at any depth and time depends on two effects: a) eviction of electrons due to daylight exposure, b) filling of electrons at the trapping centres due to ambient environment of ionizing radiations. Therefore, the residual luminescence forms a sigmoidal profile with depth, and it travels deeper and deeper into the rock as the time progresses until the time, where the electron de-trapping rate and the electron trapping rate become equal.

The instantaneous concentration of electrons n (mm^{-3}) at depth x (mm) and time t (ka) is (Sohbati et al., 2012a):

$$\frac{dn(x, t)}{dt} = (N - n(x, t))F(x) - n(x, t)E(x) \quad (1.12)$$

Where N is the concentration of electron traps and $E(x)$ and $F(x)$ are the de-trapping and trapping rates, respectively. $E(x)$ decreases with depth due to the attenuation of daylight intensity as:

$$E(x) = \sigma \phi_o e^{-\mu(\lambda)x} \quad (1.13)$$

Where $\sigma \phi_o$ represents the de-trapping rate at the surface of the rock. The de-trapping rate defines the rate at which a photon can eject the electron from the trap. This de-trapping rate decreases with depth, according to Beer Lambert's law.

The coefficient $F(x)$ in Eq. 1.12 is the trapping rate constant:

$$F(x) = \frac{D_r}{D_o} \quad (1.14)$$

Where D_r (Dose rate; Gy/ka) is the dose rate and D_o (Gy) is an intrinsic property of the dosimeter, which characterise the dose rate for any dosimeter. The dose rate can be estimated from the concentration of U, Th, and K, and D_o can be calculated from the laboratory generated dose response curve (DRC) of the sample.

Integration of Eq. 1.12 with time yields

$$n(x) = \frac{[n_i(x)E(x) - F(x)(N - n_i(x))]e^{-(E(x)+F(x))t} + F(x)N}{E(x) + F(x)} \quad (1.15)$$

Here, $n_i(x)$ is the initial concentration of trapped electrons. For terrestrial bodies, electron trapping rate is negligible during daylight exposure (Sohbati et al., 2011). Therefore, $F(x)$ is negligible compared to $E(x)$, and hence, can be neglected. If the rock is buried and shielded from the sun for millions of years, the trapped electrons in the minerals are in the field saturation; hence the initial concentration ($n_i(x)$) is maximum (N). For the terrestrial rock surface dating, Sohbati et al. (2012b) developed a model describing the resetting of luminescence profile with depth in rocks during daylight exposure. In this model, trap filling rate was not considered as it is negligible compared to de-trapping rate due to daylight flux.

This case is for glacially exposed bedrocks, rock fall events, landslides, and fault movement. Here $n_i = N$, so Eq. 1.15 modifies as:

$$n(x) = NE(x)e^{-(E(x))t} \quad (1.16)$$

The luminescence intensity is proportional to the concentration of trapped electrons. By using the value of $E(x)$ from Eq. 1.13, the above equation can be written as:

$$L_x = L_0 e^{-\sigma\phi_0 t e^{-\mu x}} \quad (1.17)$$

Where t is the exposure time, L_0 and L_x are the luminescence intensity at saturation and at depth x , respectively. This equation represents luminescence depth profile inside rock surface. The variation of normalised residual luminescence profile with depth is shown in Fig. 1.9, fitted with Eq. 1.17. The point of inflection of the luminescence profile is known as bleaching depth (x_{ip}) and is used to estimate the exposure time as:

$$\tau = \frac{1}{\sigma\phi_0} e^{\mu x_{ip}} \quad (1.18)$$

The age model takes cognizance of a) the optical attenuation coefficient of the rocks, b) daylight photon flux at the surface of the rock, c) the photoionization cross-section of the electrons and d) charge trapping probability. The model assumed that the optical attenuation coefficient is wavelength independent and the daylight flux is independent of wavelength. In addition, the trapping probability is negligible compared to detrapping and hence, neglected for terrestrial samples (Sohbati et al., 2012a).

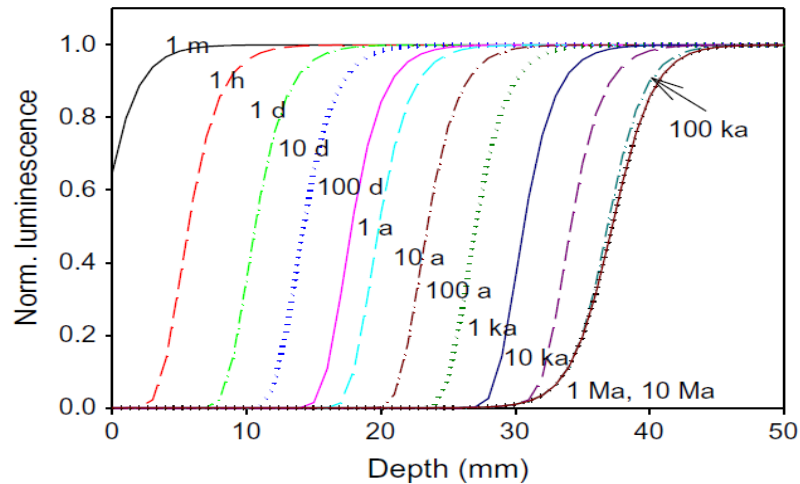


Fig. 1.9: Variation of luminescence profile with depth at different exposure times (graph taken from Sohbaty et al, (2012a).

1.1.6 Challenges

1.1.6.1 Burial dating

Luminescence signals from K-feldspar are prone to anomalous fading and can lead to underestimation in ages if not properly accounted. Various correction methods, such as measurement of the fading rate or employing correction models, are employed to mitigate this issue, but it remains a challenge to accurately quantify and correct for the anomalous fading in K-feldspar luminescence dating. Therefore, pIRIR-SAR protocol, which probes the signal with minimal fading of K-feldspar, is a valuable technique for estimating the age of sedimentary deposits. Li et al. (2011) reported that with the increase in stimulation temperature of IRSL, the bleaching rate and the dose saturation limit decrease. Therefore, high stimulation temperature IRSL probes the slowly bleachable charges, which gives high residual doses even after several hours to tens of hours of exposure to unfiltered daylight for pIRIR-SAR (Duller, 1991; Liu et al., 2016; Yi et al., 2016; Colarossi et al., 2018; Li and Li, 2011; Li et al., 2014b). The residual dose is subtracted from the estimated dose to obtain the actual dose. However, it has been found that residual dose subtraction leads to the underestimation of the true D_e values (Li et al., 2013).

In the past, there have been many attempts, both theoretical and experimental, to understand the luminescence mechanism of K-feldspar, which has enriched our understanding significantly. Most studies use the blue detection window (320-520 nm) to measure the IRSL. Other emission bands of K-feldspar have also been explored (e.g., Biswas et al.,

2013; Duller, 1997; Jain and Singhvi, 2001; Kalita and Chithambo, 2022; Kumar et al., 2020; Thomsen et al., 2008), but their use in routine dating has been limited. Therefore, other spectral regions of feldspar need to be explored for their athermal stability. Further, the dosimetric properties of the use of stable signal, need to be explored for their use in luminescence dating.

1.1.6.2 Rock surface exposure dating

Luminescence rock surface exposure dating (LRSED) technique is in a developmental stage. LRSED technique is mainly based on luminescence depth model fitting (Eq. 1.17) and is highly sensitive to attenuation coefficient and de-trapping rate. The luminescence depth model has some assumptions, a) trap filling rate is negligible during daylight, b) the attenuation coefficient is independent of wavelength and depth, and c) $\sigma\phi_0$ is independent of wavelength. The first assumption is only valid under the low dose rate environments. Using a correlation between μ from direct measurement and μ estimated from the fitting of IR at 50 °C and pIRIR at 225 °C profile, Ou et al. (2018) reported that μ is different for both IR at 50 °C and pIRIR at 225 °C signal. Previous studies have estimated $\sigma\phi_0$ only for IR at 50 °C signal not for pIRIR at 225 °C .

For fitting of the data, previous studies (e.g., Freiesleben et al., 2015; Sohbaty et al., 2012b) used first order kinetics (FOK) for data fitting of IRSL of feldspar. This assumption is true for quartz but not for feldspar. In feldspar, retrapping of the charges to the principal trap is observed (Bailiff and Poolton, 1991). In feldspar, there is a certain probability that an electron from the conduction band can become trapped again in the electron trapping centres, and this process is known as retrapping. The recent studies by Freiesleben et al. (2022) and Biswas et al. (2023) have suggested the use of general order kinetics (GOK) for feldspar as it incorporates the retrapping of charges.

To estimate the parameters (μ , $\sigma\phi_0$) of the luminescence depth profile model, two methods have been used a) using the first principle and b) calibration with a known age sample. The parameters estimated from the first principle were not physically realistic, particularly for $\sigma\phi_0$ (Sohbaty et al., 2011). In the second approach, calibration of the model with a known age sample was used for the estimation of the parameters. A calibration sample is a sample with a known age collected from the site of sampling. This sample is used to determine model parameters such as the detrapping rate and attenuation coefficient of the rock samples. These estimated parameters were then used to find the unknown ages of samples,

provided both samples have the same geological conditions, i.e., lithology, compositions, and opacity. This technique gives reliable ages for younger samples (< 1 ka). The theoretical modelling has suggested that LRSED can potentially be used for samples up to 1 Ma (Sohbati et al., 2012a). However, studies are limited for older samples due to the difficulties in finding suitable calibration samples, and underestimation in the exposure ages has been reported (Galganic et al., 2018; Freiseleben et al., 2023). The mineralogical composition of the rock can significantly affect the luminescence depth profile (Meyer et al., 2018). Hence, in heterogeneous rocks, a slight change in depth can considerably change the calculated ages. Very recently, Andričević et al. (2023) reported that cracks observed in the rocks significantly affect the light flux. Several other geological factors, such as desert varnish (an orange-yellow to black coating on exposed rock surfaces) and erosion, can significantly affect the luminescence depth profile. All these parameters need to be considered in the experimental and model fitting approaches for the application of older samples.

1.1.7 Objectives of the present thesis

This thesis focuses on using multispectral luminescence studies to circumvent the athermal fading issue in the K-feldspar and its implication for robust dating protocol and rock surface exposure dating.

The objectives of the thesis were:

1. Investigation of different spectral regions of feldspar to explore low fading signals.
2. Development of dating protocols for signals identified with minimum fading for routine dating.
3. Establishing rock surface dating methodology and carrying out a comparative study of new and previously used signals to explore the potential of applicability of luminescence surface exposure dating for glacially polished samples.

Due to the potential of K-feldspar to increase the luminescence dating limit, this thesis explored several possible combinations of stimulation wavelengths and detection windows in order to identify the optimum configurations that could provide a signal with minimal athermal fading. The post violet infrared stimulated luminescence (pVIRSL; IRSL at 100 °C after violet bleach at 50 °C) has a near zero fading. Therefore, the thesis developed the single aliquot regenerative dose protocol for pVIRSL (pVIR-SAR) and explored the

mechanism for the pVIRSL. In the pVIR-SAR, the violet stimulation bleached signal from other minerals such as quartz, and hence the followed photo-transferred IRSL yielded signal only from feldspar. The protocol thus offers the advantage of dating the particular samples where feldspar cannot be fully separated from quartz, i.e., when feldspar is present in quartz as inclusion, polymineralic fine grains, and a small amount of sample (e.g., rock surface exposure studies). Therefore, the thesis explores the applicability of pVIR-SAR for samples of such kinds. The final objective of the thesis is to explore the potential applicability of LRSED for old glacially polished samples with desert varnish. The effect of desert varnish is studied on the samples and the challenges faced in dating them were explored. The suitability of existing methods for rock surface dating, their limitations, and geological factors affecting the luminescence depth profiles along with the model fitting parameters are explored and discussed.

1.1.8 Thesis outline

During my doctoral research, the mechanism of luminescence in feldspar was investigated, and the traps and recombination centres responsible for luminescence in feldspar were studied. It was established that post-violet IR stimulated luminescence (pVIRSL) is non-fading and has desirable luminescence properties for dating applications. Furthermore, a single aliquot regenerative dose protocol for pVIRSL (pVIR-SAR) was developed and its applicability to museum samples, natural specimens, and polymineral samples was demonstrated. Additionally, the potential of IRSL and pVIRSL (new signal) for surface exposure dating of glacially polished rocks from the Himalaya was examined.

The thesis comprises of seven chapters, which details the background of the work, the experimental techniques pursued, characterization of the new signal, and development of pVIR-SAR protocol and its performance and application for luminescence of surface exposure dating. The following provides the chapter-wise outline and the content of individual chapters.

Chapter 1: Introduction

The chapter discusses the motivation, objective, and outlines the structure of this thesis. It introduces the basics of luminescence and its mechanism using the band model and then discusses the applications of luminescence in archaeological and geological sample dating using quartz and feldspar. The use of luminescence for sediments and exposed rock surfaces dating is then discussed.

Chapter 2: Experimental Details and Methodology

This chapter discusses the instrumentation techniques for luminescence dosimetry and dating. The system used for dosimetry in this thesis comprised of commercial Risø TL/OSL readers with a detection and stimulation head (DASH) comprising of a software controlled facility for the use of light emitting diodes (LEDs) emitting in various spectral regions and an automated detection filter changer assembly (Lapp et al., 2015). Further, the chapter details the laboratory procedures followed for sample preparations along with different types of protocols used for measurements. This includes a methodology for fading rate estimation and measurement protocol for the estimation of annual dose using a high purity germanium (HPGe) detector. The chapter also discusses different analytical techniques, such as Electron Dispersive Spectroscopy-Scanning Electron Microscope (EDS-SEM), and X-ray Diffraction (XRD) used for mineralogical/petrological analysis.

Chapter 3: Multispectral Studies in K-Feldspar

This chapter discusses the experimental results of fading rates using varying combinations of single and double stimulations and luminescence detection windows. The chapter reports athermal fading rates in K-feldspar grains extracted from sediments of varied ages, depositional environments and provenances. Multiple combinations of stimulation and emission spectral regions helped to identify an optimum combination that provided a luminescence signal (pVIRSL) with minimal athermal fading. The stimulation wavelengths were infrared (855 ± 33 nm), green (525 ± 30 nm), blue (470 ± 20 nm), and violet (405 ± 15 nm), and detection windows comprised of broad-UV (260–400 nm), narrow-UV (327–353 nm), and blue (320–520 nm). Athermal fading rates using both single stimulation and sequential double stimulation combinations were measured. For single stimulation, the average fading rates (g_{AV}) ranged from 6.6 to 7.9% per decade. Sequential double stimulation comprising post green-blue (pGB), post blue-violet (pBV), post blue-IR (pBIR), and post violet-IR (pVIR) gave fading rates ranging from 2.0 to 0.0% per decade. The minimum fading rate value of $g_{AV} = 0.0 \pm 0.1\%$ per decade was obtained for post Violet Infrared stimulation, which is a new signal for dating the sediments. These results are discussed in detail in this chapter. The results in this chapter were published in *Radiation Measurements* DOI: <https://doi.org/10.1016/j.radmeas.2022.106804>.

Chapter 4: Post Violet-Infrared Stimulated Luminescence (pVIRSL) Dating Protocol

This chapter explored the mechanism and suitability of the post violet IRSL (pVIRSL) signal for dating applications. Experiments to explore the source traps responsible for the pVIRSL signal, the electron transfer processes, and the nature of recombination centres, were conducted. An optimized Single Aliquot Regeneration dose protocol using pVIRSL was developed and its successful application was demonstrated on samples with varied age ranges and depositional environments.

Results obtained in this chapter suggest that pVIRSL is a recuperated signal arising from the eviction of charges from deep traps by violet stimulation following their recapture by the IR trap. The methods, therefore, probe the deep traps through a charge transfer process. The pVIRSL fulfils all the criteria for the use of a SAR protocol, i.e., rapid bleaching (< 10% in 60 min of daylight exposure), recuperation (<5%), reproducibility (within 10%), and dose recovery (within 10%). A post violet IR single aliquot regenerative dose (pVIR-SAR) protocol was tested for several K-feldspar samples from varied depositional environments and ages in the range of 6-286 ka. The results accorded with the independent ages.

This work is published in *Quaternary Geochronology*. DOI: <https://doi.org/10.1016/j.quageo.2023.101487>.

Chapter 5: Application of pVIR-SAR Protocol for Polyminerall Natural Samples

This chapter discusses the potential of pVIR-SAR protocol for polyminerall fine-grained and coarse-grained samples. The pVIR-SAR enables the dating of polyminerall samples, as violet stimulation bleaches signal from quartz and permits probing of pVIRSL signal from feldspar. The protocol therefore, offers the advantage of dating the samples where feldspar cannot be fully separated from quartz, i.e., when feldspar is present in quartz as inclusion or polyminerall fine grains, and minute quantities of sample is available for the rock surface exposure dating. The applicability of pVIR-SAR for samples from such cases was explored. Use of pVIR-SAR protocol on varied samples, provided ages of dating polyminerall fine-grained and coarse-grained sediments from 2 ka to ~68 ka. These ages were consistent with geological reasoning and available age controls. The work suggests that mineral separation can be dispensed if pVIRSL is used for measurements of sediments and rock samples.

This study also investigated the bleaching behaviour of different grain size for fluvial samples and their impact on the precision of age. Results demonstrate that coarse grain

feldspars exhibit poor bleachability and can lead to overestimation of ages. Further, for the fluvial samples, analysis of polymineral fine-grain samples using both pVIR-SAR and pIRIR-SAR reasonably accorded with an expected error of 10% or 20% in the obtained ages. Thus, it is suggested that the use of pVIRSL will be valuable for samples where quartz grains have low sensitivity and feldspars show inadequate bleachability, as is the case for samples from the Himalaya and Antarctica.

The work presented in this chapter will be submitted shortly as Devi et al. (in preparation).

Chapter 6: An Attempt to Date Glacially Polished Samples using Luminescence Surface Exposure Dating

This chapter discusses the results of studies examining the potential use of rock surface dating to glacially polished samples with age controls (Ganju et al., 2018). The results brought to the fore possible complications that may arise in this application. In this study, the sensitivity of the model to different parameters was examined, and the results obtained were different from the expected ages. Possible reasons for such a discordance were examined. These included the role of desert varnish and structural micro-cracks inside the rocks that modify the apparent transparency of the sample and luminescence depth profiles. Scanning electron microscope with electron dispersive spectroscopy (SEM-EDS) analysis showed the presence of desert varnish and cracks in the rock samples. The calibration sample, however, had no desert varnish or cracks, suggesting that the parameters estimated from the calibration sample could not be used for age estimations. A survey of potential factors that could be affecting the depth profile of luminescence signal for the dating is discussed.

The work presented in this chapter is being prepared for publication and will be submitted as Devi et al.

Chapter 7: Summary and Future Prospects

This chapter summarizes the results presented in all the chapters discussed earlier and provides few suggestions for future studies.

Chapter 2

Instrumentation and Experimental Methods

2.1 Introduction

In Chapter 1, we discussed the mechanism of luminescence and its use in dosimetry and dating. The current chapter serves as a bridge between the theoretical concepts discussed in the first chapter and the practical aspects of luminescence dating. In this Chapter, an overview of different instruments used to measure dose and dose rates is provided. The working principle of a TL/OSL reader for the measurement of equivalent dose is discussed, along with the details of a high purity germanium (HPGe) detector for the measurement of the concentration of radioactive nuclides. Additionally, the principles of X-ray diffraction (XRD) and scanning electron microscope with electron dispersive microscopy (SEM-EDS) used for mineralogical and petrological studies are discussed. The chapter also discusses the sampling methodology and the chemical treatments for extraction of minerals (both fine and coarse grains) of interest. Detailed discussions on the methodologies for dose and dose rate estimations are presented. Methodologies used to estimate fading rates and various corrections applied in luminescence ages are discussed.

2.2 Instruments

To estimate luminescence ages, the following instruments are used:

1. TL/OSL reader for the measurement of equivalent doses.
2. HPGe detector for the measurement of concentration of natural radioelements.

2.2.1 TL/OSL reader equipped with detection and stimulation head (DASH) system

The thermoluminescence/optically stimulated luminescence (TL/OSL) reader is cardinal to the measurement of the luminescence signals emitted by the sample. All luminescence measurements were carried out in ‘Risø TL/OSL DA-20 Readers’. This system comprises three units: a) the TL/OSL reader unit, b) a controller that interfaces the TL/OSL reader with a PC, and c) a PC equipped with the required software programs, viz., the sequence editor and the control program (Fig. 2.1a). The TL/OSL reader comprises three parts: stimulation unit, light detection unit, and irradiation unit. The reader contains a software controlled system known as detection and stimulation head (DASH) (Lapp et al., 2015). DASH comprises the facility to change stimulation LEDs and detection filters through a software driven control. The software permits the choice of sequence, preheat and irradiation in a desired sequence. A schematic of the luminescence measurement system in the reader is shown in Fig. 2.1b. The system allows 48 samples to be analyzed multiple times in varied ways within a single run.

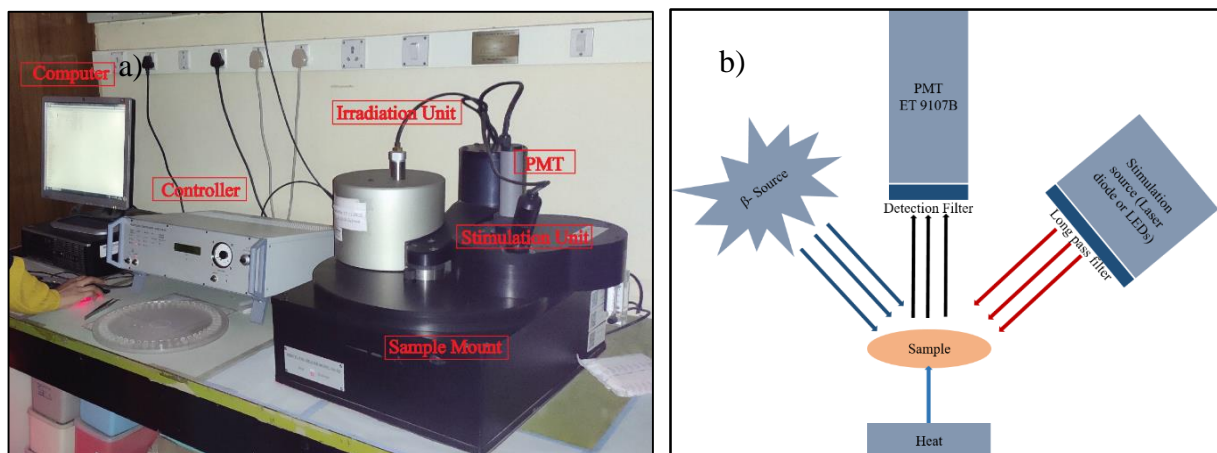


Fig. 2.1: a) The setup used to perform experiments was ‘The Risø TL/OSL Reader’ and b) schematic of measurement system in TL/OSL reader.

2.2.1.1 Stimulation

The TL/OSL reader provides controlled and reproducible heating (for TL) and controlled exposure to light (for OSL) of a sample. The stimulation system consists of two units: a) Heating and b) Light stimulation.

2.2.1.1.1 Heating system

The heating system comprises a Kanthal or Nichrome heating plate, universally used for resistive heating. In the Risø reader, the heating element has two functions: a) lifting the sample into the measurement position and b) heating the sample. Typically, this heating system can heat to 700 °C at predefined software controlled heating rates in the range of 0.2 to 10 °C/s. In order to reduce the thermal delay between the transfers of heat from the heater plate to the aliquot to grains, a heating rate was kept at 2 °C/s. The heat transfer was further facilitated by continuously flowing ultrapure nitrogen. To ensure accurate temperature control, a Chromel-Alumel thermocouple based feedback loop was employed that controlled the heating at a desired rate. This system enabled a reproducible heating rate to within 1%. The temperature is increased at a constant rate.

2.2.1.1.2 Light stimulation system

The light stimulation system provides a controlled and reproducible optical stimulation to the sample. The stimulation system includes light-emitting diodes (LEDs) and laser diodes that provide the required optical stimulation. The choice of a light source depends on the specific needs of the research and the sample being analyzed. Typically, for the stimulation of quartz, blue LEDs emitting at around 470 nm and green laser light from Nd:YAG sources at 525 nm were employed. For feldspars, infrared LEDs emitting at either 880 nm or 930 nm were used.

The automated DASH system comprises four different stimulations: IR (855 ± 33 nm), Green (525 ± 30 nm), Blue (470 ± 20 nm), and Violet (405 ± 15 nm). The emission spectra of each stimulation source are shown in Fig. 2.2a. Long-pass filters are employed in front of each LED to reduce the incidence of directly scattered stimulation light from reaching the light detection system. The filters used in front of LEDs are a) GG420 in front of blue LEDs, b) GG475 in front of green LEDs, c) RG780 in front of IR LEDs, and d) AHF F49-402 and ITOS GG395 in front of violet laser diode.

The light stimulation system offers the following operating modes:

1. Continuous wave (CW) mode with an intensity range of 0-100%.
2. Linear modulated (LM) mode with an intensity range of 0-100%.
3. Pulsed (POSL) mode with adjustable on/off times starting from 5 μ s with a 0.1 μ s resolution.

In this thesis, blue stimulation was applied for quartz, while IR, green, blue and violet stimulations were employed for feldspar. All stimulations were used in continuous wave mode, and the light intensity remained constant during and between repeated measurements.

2.2.1.2 Detection unit

The detection unit measures the luminescence emitted by a sample. The reader is equipped with photomultiplier tube (PMT) with a suitable combination of detection filters provided in DASH to measure luminescence from the irradiated sample. The TL/OSL reader has a blue/UV sensitive quartz window bialkali PMT (ET 9107B) with spectral response in near UV to red wavelength region (160-630 nm). The PMT has a maximum detection efficiency between 200 and 400 nm. The PMT is operated in photon-counting mode to provide an improved signal to noise ratio. Photons striking the photocathode are converted to electrons that interact with dynodes, and secondary electrons are generated. The PMT multiplies the photon received to provide a measurable signal. To discriminate the stimulation light entering the PMT, optical filters are used in front of the PMT. The intensity of the stimulation light is approximately 18 orders of magnitude greater than the emitted luminescence (Riso TL/OSL reader manual). To effectively measure the emitted luminescence, it is necessary to employ detection filters to block any scattered stimulation light from reaching the PMT. Additionally, it is essential to ensure a clear separation between the spectrum of stimulation and detection windows. The filters employed were Hoya U-340, Schott BG3, Schott BG39, and Semrock Brightline HC 340/26 nm. These filters are used in combination as 260-400 nm (Hoya U-340 (broad-UV)), 327-353 nm (Hoya U-340 + Semrock Brightline HC 340/26 (Narrow-UV)), and 320-520 nm (Schott BG-39 + Schott BG-3 (Blue)). Transmission spectra of the detection filters are shown in Fig. 2.2b. An automated DASH system incorporates a filter changer, enabling the seamless switching of stimulation filters (with 4x4 filter combinations available) within a measurement sequence. The detection filter changer comprises two filter changer wheels, each capable of holding up to four detection filters, allowing for a maximum of 16 filter combinations to be used in any given measurement sequence. The filter changer facilitates the automatic choice of detection filters throughout a measurement sequence. These detection filter changers accommodate individual or stacks of filters, with a maximum thickness of 7.5 mm and a diameter of 25 mm.

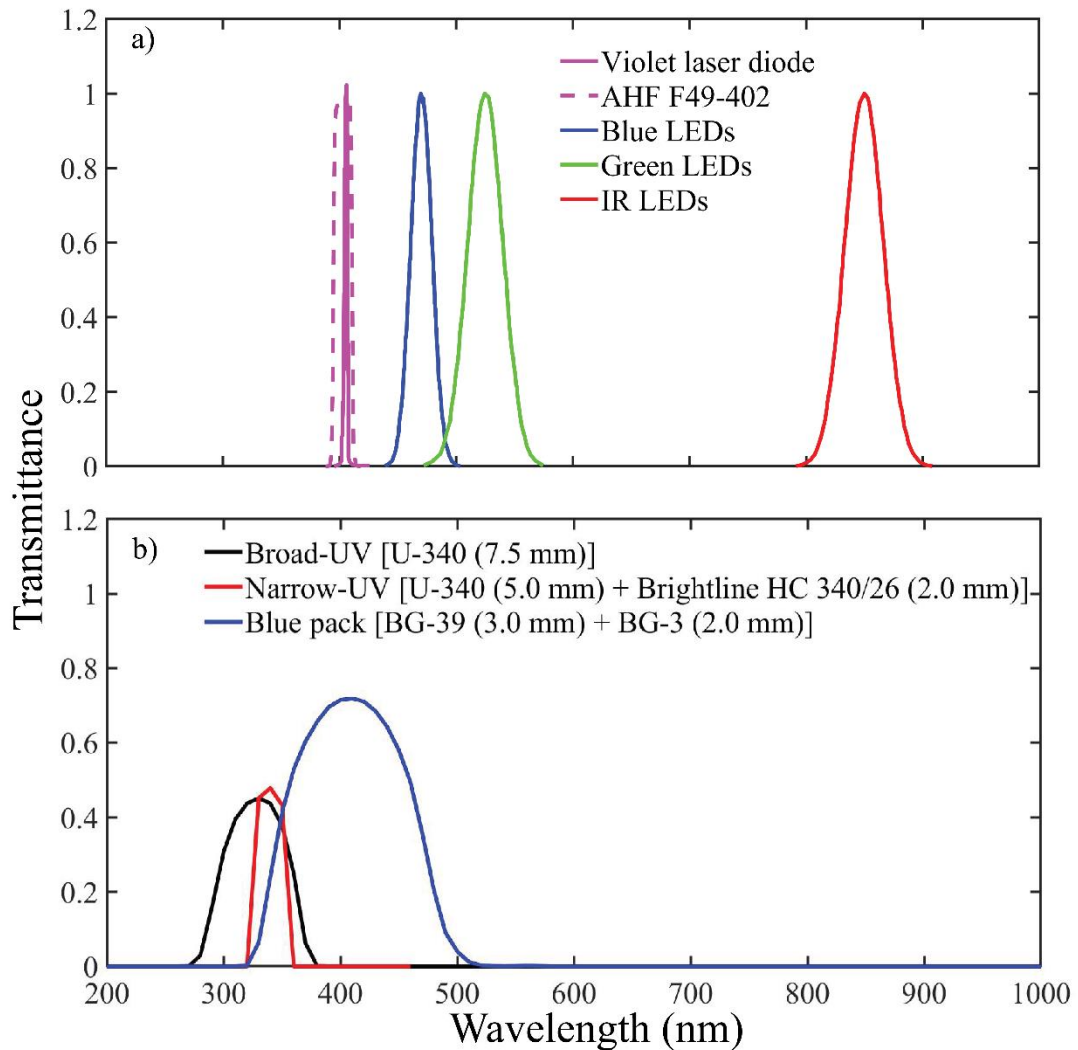


Fig. 2.2: Different excitation and detection windows a) Emission characteristics of the stimulation LEDs and violet laser diode. Stimulations were carried out using 850 nm IR, 525 nm green, 470 nm blue LEDs, and 405 nm violet laser. b) Transmission characteristics of three different detection filter combinations. Detection were appropriately made through 260-400 nm [U-340 (Broad-UV)], 327-353 nm [U-340 + brightline 340/26 (Narrow-UV)], and 320–520 nm [BG-39 + BG-3 (blue)] transmission windows. (Emission data of LEDs were taken from the Risø product catalogue 1811a. The data on transmission spectra of different filters were taken from <https://hoyaoptics.com/wp-content/uploads/2019/10/U340.pdf>).

2.2.1.3 Irradiation Unit

The irradiation unit in a TL/OSL reader irradiates samples through a beta source in a controlled manner. Risø TL/OSL reader is equipped with a ceramic $^{90}\text{Sr}/^{90}\text{Y}$ beta source (end point energy of 2.27 eV) having a half-life of 28.5 years. The long half-life and compactness of the beta source enable ease of its use. The dose rate calibration of the

system is done using a calibration quartz sample supplied by Risø National Laboratory, Technical University of Denmark, Denmark. A 0.125 mm thick beryllium window between the irradiator and the measurement chamber is used to serve as a vacuum seal for the measurement chamber. The current dose rate for quartz coarse grains (90-150 μm) of the source is 0.094 Gy/s on a stainless steel disc. Similarly, the beta source is calibrated for fine grain (4-11 μm) measurements on aluminum discs, and the corresponding dose rate is 0.065 Gy/s.

For alpha efficiency measurements, a six seater alpha irradiator with ^{241}Am alpha source having a half-life of 432.6 years is used. ^{241}Am exhibits a combination of alpha and gamma emissions. The primary alpha energy is 5.49 MeV, constituting 85.1% of its emissions, while the dominant gamma energy is 59 keV. Because the alpha particles emitted by ^{241}Am have a short range ($\sim 20 \mu\text{m}$), all the measurements were made in vacuum to reduce the attenuation of alpha particle energy from the air (Singhvi and Aitken, 1978).

2.2.2 High purity Germanium (HPGe) detector

High purity Germanium (HPGe) detector was used to estimate the concentration of radioactive nuclides present in the sediment sample, which is used for the estimation of dose rate. HPGe contains a particle detection and counting system. HPGe is a high resolution semiconductor diode featuring a p-i-n structure based gamma spectrometer. In this configuration, the intrinsic (I) region within the detector is responsive to ionizing radiations (gamma rays). These are manufactured from ultrapure germanium (impurity concentration $\sim 10^{10}$ atoms/cm³) and have depletion depths of several centimetres. If the remaining low-level impurities are acceptors, the electrical properties of the semiconductor are mildly p-type. Alternatively, if donor impurities remain, then n-types is the result. Generally, for gamma spectrometry HPGe detectors in coaxial shape are preferred as they provide large active volumes (up to 800 cm³) (Knoll, 2010). Electrodes are created on the surface of the germanium crystal. For coaxial detectors, a central p-type electrode is formed, surrounded by n-type outer electrode. The HPGe detectors are fabricated from P-type germanium with an outer contact of diffused Li and an inner contact of ion-implanted boron. HPGe detectors are typically operated at cryogenic temperatures, usually around 77 K, using liquid nitrogen. To reduce background radiation interference, HPGe detectors are housed within lead shields.

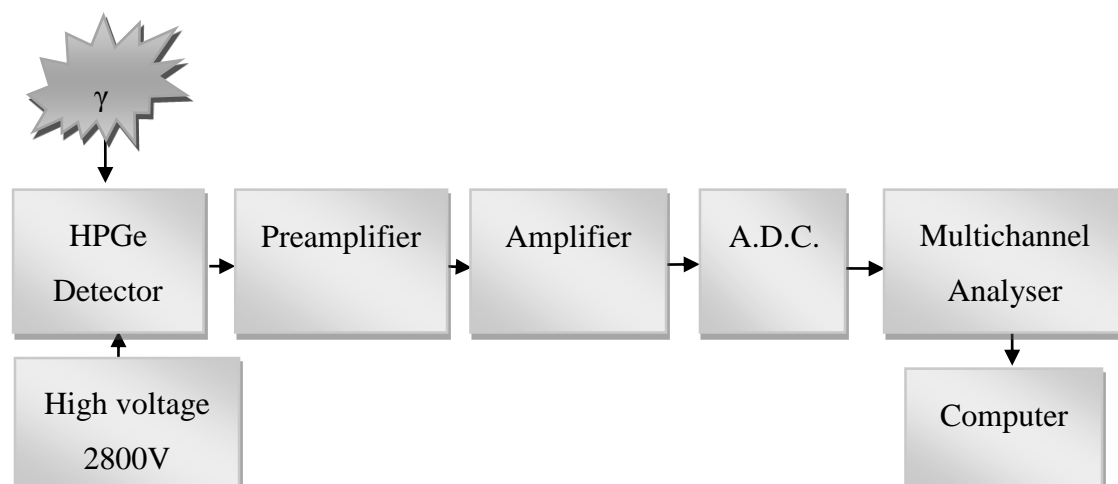


Fig. 2.3: Block diagram of HPGe detector.

The working schematic of HPGe is shown in Fig. 2.3. As photons interact with the material within this depleted volume, they generate charge carriers, which include holes and electrons. The applied high electric field (reverse bias) allows the electrons and holes to move in opposite directions toward the respective electrodes. The electrodes are connected to a preamplifier, which amplifies the electrical signals. The amplified signal is further processed by pulse shaping electronics, which is then sent to a spectroscopy amplifier that amplifies the pulses and filters out unwanted noise. Signals are sent to a multichannel analyser, which digitizes the pulse amplitudes and assigns them to specific energy bins. It creates a histogram of pulse amplitudes, generating an energy spectrum that represents the distribution of gamma ray energies. To identify and quantify the radioactive isotopes in a sample, the energy spectrum is compared to calibration standards. By comparing the intensities of the gamma ray peaks from the sample to the intensities of the corresponding peaks in the calibration spectrum, the concentrations of radioactive isotopes in the sample are estimated.

2.3 Petrological Analysis

Petrological analysis is essential to reveal the mineral constituents of rocks, which help to determine the types and relative proportions of minerals present. In the present thesis, samples were characterised using X-ray diffraction (XRD) and scanning electron microscope with electron dispersive microscopy (SEM-EDS). This detailed analysis with XRD and SEM-EDS helps us better understand the minerals in the rock samples. The details of the instruments are provided below:

2.3.1 X-ray diffraction (XRD)

X-ray diffraction (XRD) technique is used to determine the atomic arrangement in the crystalline materials and hence identify a mineral or compound based on lattice structure. The XRD measurements were carried out at Physical Research Laboratory, Ahmedabad. It is based on the principle that when X-rays interact with the crystal lattice of the sample, they undergo scattering at specific angles due to interactions with the atoms in the crystal lattice. The scattered X-rays interfere with each other, creating a diffraction pattern, consisting of peaks at various angles. These peaks correspond to the crystallographic planes and lattice spacing of the minerals present in the sample. The scattered waves interfere constructively if the Bragg's law is satisfied:

$$n\lambda = 2d \sin(\theta), \quad (2.1)$$

where n is an integer (the order of the diffraction peak), λ is the wavelength of the X-rays, d is the distance between adjacent crystal lattice planes, and θ is the angle between the incident X-ray beam and the crystal lattice plane. A detector in the XRD instrument records the diffraction pattern produced by the sample. The positions and intensities of the diffraction peaks are used to identify the minerals present in the sample. The diffraction pattern also provides information about the crystal structure and lattice parameters.

In the present thesis, XRD technique was used to characterize the type of feldspars. The sample was powdered to a grain size of less than 10 μm for better resolution, and about 600 mg of powdered sample was used for measurements. The sample was evenly distributed onto a thin flat plate sample holder. The sample holder was placed in the XRD instrument's sample chamber, and measurements were made.

2.3.2 Scanning electron microscopy with Energy dispersive spectroscopy (SEM-EDS)

Scanning electron microscopy (SEM) is used to determine the mineral compositions and high resolution images of rock samples used for surface exposure studies. The SEM-EDS measurements were carried out at Physical Research Laboratory, Ahmedabad. It involves the interaction of a focused high energy electron beam (a few hundred eV to tens of keV) with the sample to produce images with high resolution. An electron gun (tungsten filament) produces a narrow and coherent electron beam accelerated by applying a high voltage, typically in the range of a few kilovolts to several tens of kilovolts.

Electromagnetic lenses focus and shape the electron beam to a few nanometres to tens of nanometres in diameter. When the electrons interact with the sample, secondary electrons are emitted from the surface of the sample due to inelastic scattering and are the primary source of image formation in SEM. The emitted secondary electrons are collected using the semiconductor detectors. These signals are amplified and converted into electrical signals and are fed into a computer, which processes the signals to generate a visual representation of the sample surface and is used for surface imaging. SEM with Energy Dispersive Spectroscopy (EDS) facility provides information about the elemental composition of a sample, which is useful for material characterization. When the high-energy electron beam from the SEM interacts with the atoms in the sample, it causes the inner-shell electrons of the atoms to be ionized. The outer-shell electrons transition to the inner-shell vacancies, releasing energy in the form of characteristic X-rays. The X-rays emitted by the sample have characteristic energies specific to the elements present in the sample. The solid-state detector (lithium-drifted silicon detector) produces the electrical pulses corresponding to each emitted X-rays. The energy information collected from the X-rays is used to generate an energy spectrum. Each peak corresponds to a specific element present in the sample. To determine the elemental composition quantitatively, the intensities of the X-ray peaks are typically calibrated using standards of known composition. This calibration allows for the calculation of the concentration or weight percent of the elements present in the sample.

2.4 Luminescence Dating: Experimental Methods

As discussed in Chapter 1, when the minerals are buried and shielded from light, they begin to accumulate dose from the ambient radioactivity. The rate of deposition of dose is determined by the surrounding radioactive materials. By measuring the accumulated dose and dose rate, the burial age of the sample or event can be calculated. Sediment materials, such as sand, silt, and clay from the Quaternary period (the past ~2.6 million years), and archaeological artefacts, such as ceramics and pottery, are commonly studied using luminescence dating.

2.4.1 Sample collection

In luminescence dating, the selection of samples and collection procedures is most important. Sedimentary deposits were carefully chosen to prevent the mixing of different layers, reducing the risk of contamination from multiple geological or archaeological

events. This careful process aims to maintain the order of sediment layers and ensure that luminescence signals from samples truly represent their unique deposition history. Ideally, the samples with specific grain sizes, ranging from 4 to 11 μm for fine-grain and 90 to 150 μm for coarse-grain, were preferred for the multigrain aliquot measurements. Sampling is carried out under conditions of reduced ambient illumination, specifically in dim lighting or within the spectral range of red light. To prevent any exposure to daylight, stainless steel or aluminium light-tight pipes were used for the sample collection. Latitude, longitude, elevation, and sample depth were noted precisely for each sample to estimate the cosmic ray's contribution to dose rate, a crucial factor in accurate age determination.

2.4.2 Sample preparation

In the thesis, various samples, including sedimentary, fluvial clay, volcanic ash, pottery, brick, and rock samples were utilized. The Indian map showing the geological locations of the all samples used in thesis is shown in Fig. 2.4. The selected samples encompassed geographical locations across India. More details about the samples are provided in the individual chapters. The sedimentary, fluvial clay, and volcanic ash samples were collected using stainless steel pipes and opened under subdued red light (Chandel et al., 2006). The top and bottom ~3 cm portion of sample of the pipe, which may have been accidentally exposed to sun-light, was used for moisture content and radioactivity measurements. The water content of the sample was measured immediately after the sample pipe was opened to avoid any moisture loss caused by exposure to the air. To determine the water content, the weight of the sample, both as received and in saturation, was measured, then the same sample was dried and weighed. For radioactivity measurements, the sample was dried and pulverized to talcum powder size. The powdered sample was sealed in an airtight holder for more than three weeks to establish equilibrium in the radioactive decay series of ^{238}U and ^{232}Th . Following this, the sealed sample was used for the estimation of the concentration of radioactive elements present in the sediment. Radioactivity concentration was measured in the High Purity Germanium (HPGe) detector. The standard used for calibration is reported by Shukla et al. (2002).

A sediment sample in the interior of the stainless steel pipe was used for equivalent dose measurements. Sample pre-treatment comprised a reaction with 1N HCl for 30 min and 30% H_2O_2 for one day to remove the carbonates and organic matter, respectively. These carbonates and organic materials were expected to be post depositional and could result in

spurious signals during the thermal and optical measurements. The following chemical reaction takes place in the procedure:



Depending on the availability of grain sizes, we have used two grain size fractions, viz., coarse grains (90-150 μm) and fine grains (4-11 μm). The detailed sample preparation process for these two fractions is discussed below:

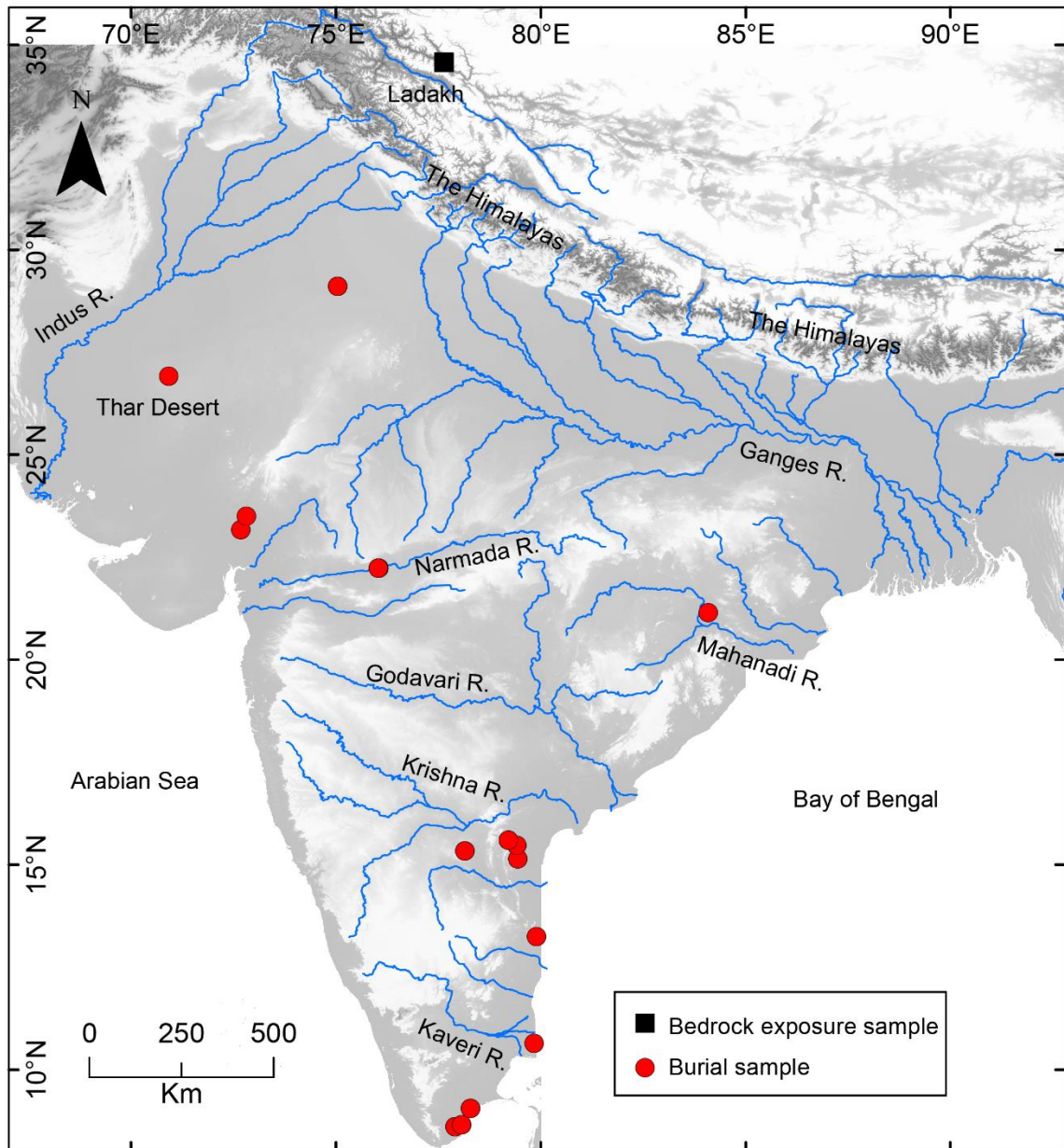


Fig. 2.4: Map of India showing the geological locations of all samples used in Thesis.

2.4.2.1 Coarse grain

To obtain the coarse grains of size 90-150 μm , the sample was dry sieved after the removal of carbonates and organic material from the sample. The obtained grains were treated with 10% hydrofluoric (HF) acid for 10 min to remove any iron coating from the sample and remove the alpha irradiated skin from feldspar (Goedicke, 1984). To dissolve the fluorides precipitated during HF treatment, the sample was treated with 12N HCl for 30 min. The iron coating facilitated the separation of quartz and feldspar. While quartz is diamagnetic, the presence of the Fe coating makes it behave as paramagnetic. The quartz and K-feldspar grains were separated using Frantz® magnetic separator at magnetic fields of ~ 7 and ~ 18 kGauss (Porat et al., 2015). Some samples were separated using sodium polytungstate ($\rho = 2.65 \text{ g/cm}^3$ for quartz and $\rho = 2.58 \text{ g/cm}^3$ for feldspar) and these samples underwent HF treatment only after the separation process. The quartz and feldspar grains were etched with 40% HF acid for 80 min and 10 min, respectively (Goedicke, 1984). Again, 12N HCl treatment was provided for 30 min to dissolve the insoluble fluorides. Quartz purity was tested using IR stimulation. The sample with an OSL IR depletion ratio within 10% of unity was considered for quartz measurements (Duller, 2003). The obtained quartz and feldspar samples were mounted on the stainless steel discs using silicon spray and used for luminescence measurements.

2.4.2.2 Fine grains

For brick, pottery, and volcanic ash samples, 4 to 11 μm (fine grains) grain size was used. For pottery and brick, the upper few millimetre of outer skin, which may have been exposed to daylight, was removed and used for dose rate measurements. The interior was used for the equivalent dose estimation. After the removal of carbonates and organic material, the sample was treated with 0.01N sodium oxalate solution to deflocculate the fine grain size particles, which may have coagulated due to static charges. The desired grain size of 4 to 11 μm was obtained using the Stokes Law. The sample solution was added in the 6 cm column of alcohol, and grains present in the suspension were obtained using gravity settling for 1.5 min. The obtained grains have size of less than 11 μm . Further, this solution was mixed with alcohol in the 6 cm column, and the sample obtained from the bottom part of the column solution after the gravity settling for 15 min contained the fine grains with size 4 to 11 μm . To make a single layer of the sample on a clean aluminium disc, we mixed the solution with alcohol until it became translucent. The 1 ml solution of sample and 1 ml

alcohol was added in the glass vial of diameter 1 cm, this vial also contained aluminium disc. The sample was dried in the oven at a temperature of 45 °C for 2-3 days. The luminescence signal was measured from the polymineral sample due to the difficulty in the separation of minerals from fine grain size samples. Therefore, IRSL was used for feldspar measurements as only feldspar responds to IR stimulation (Hütt et al., 1988).

2.4.2.3 Rock surface exposure dating

To determine the ages of exposed rock surfaces using luminescence dating, samples from the Nubra Valley in Ladakh, Himalaya were collected. These rock samples were wrapped in aluminium foil immediately after collection in the field to shield them from exposure to light. Samples were prepared for measurements under the red subdued light. The cores were extracted, leaving a 3 cm distance from the edges of the rock samples, in order to prevent contamination from the light-exposed surfaces. Using a water-cooled diamond-tipped core drill, the cylindrical cores with a diameter of 10 mm and a length of approximately ~30 mm were extracted from the rock samples. These cores were then sliced into pieces ~1.0 mm thick using a water-cooled diamond wafer saw which itself was 300 µm thick. This resulted in a net slice spacing of about 1.3 mm. The slices were crushed in alcohol to prevent luminescence loss due to heating. The grains of size 90-150 µm were then treated with 10% HF for 10 min to remove the alpha irradiated surface layer, weathering products, and Fe-coatings. HF etching was followed by a treatment with 37% HCl for 30 min to convert the fluorides into water soluble chlorides and were washed. The sample was dried at 45 °C and used for luminescence measurements. The dried samples were then placed on the stainless-steel discs using the silicon oil and mounted in the TL/OSL reader for the measurements.

2.4.2.4 Sample preparation for SEM-EDS measurements

The sample preparation steps for SEM-EDS measurements are shown in Fig. 2.5. Cores of diameter 1 cm and length 2 cm were drilled from the rocks and placed into aluminium holders of 2.5 cm diameter. A solution of epoxy and hardener, mixed with Milli-Q water at a ratio of 20 parts epoxy to 9 parts hardener, was poured into the moulds containing the cores and left overnight to settle. The sample was gently removed using alcohol, and its surface was polished using fine-grained sandpaper grade. To achieve the desired level of surface quality, the polished samples underwent a series of polishing steps using different polishing clothes with varying abrasiveness starting from 3 µm to 0.25 µm. Each polishing step lasted for 3 hours. This process continued until the surface was shiny and reflective.

Finally, all the polished samples were cleaned in Milli-Q water for 10 min in an ultrasonic bath to remove any contaminants from the epoxy. To avoid charging effects during imaging, a 25 μm thick gold coating was applied using vacuum evaporation.

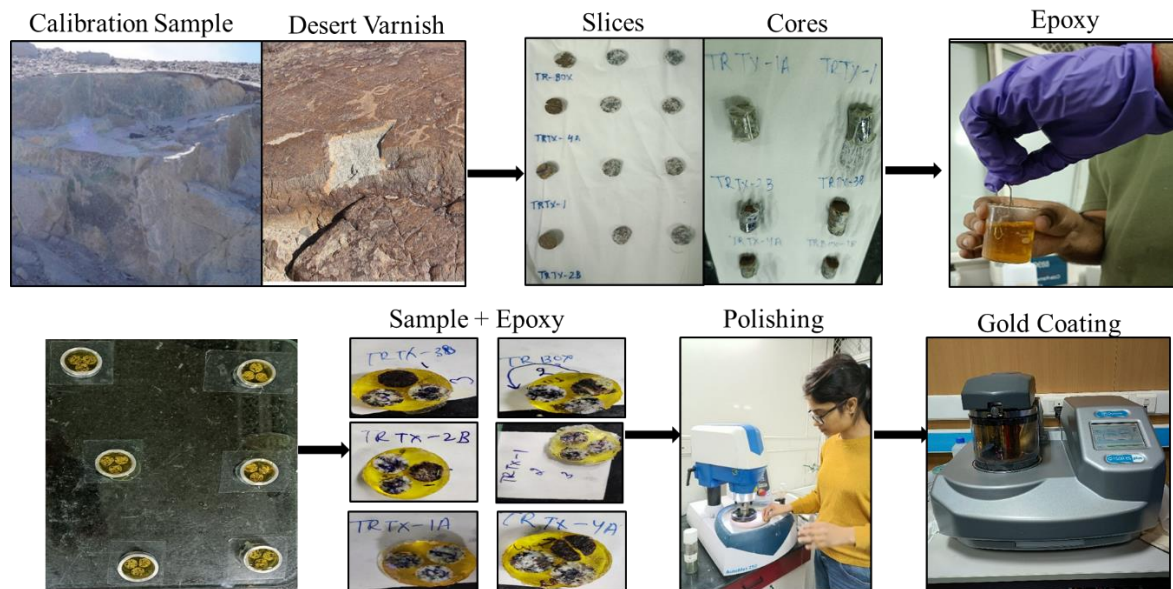


Fig. 2.5: Sample preparation steps for SEM-EDS measurements.

2.5 Methodology

Luminescence measurements were carried out in a commercial Risø-TL/OSL DA-20 reader with a DASH system comprising a set of stimulation LEDs and detection filters (Bøtter-Jensen et al., 2010; Lapp et al., 2015). Details of stimulation and detection windows are presented in subsection 2.2.1.

2.5.1 Dose estimation

The equivalent dose (D_e) is the laboratory beta dose, which induces a signal intensity in the sample similar to that of the sample as received (natural signal). Methods for D_e estimation can broadly be classified into two categories: a) the additive dose and b) the regenerative dose methods. The multiple aliquot additive dose (MAAD) method uses several identical aliquots of the same sample (Aitken, 1985; Singhvi and Wagner, 1986; Ward et al., 2003). In order to obtain an equivalent dose, these aliquots are divided into several identical aliquots and given known laboratory doses in addition to natural doses ranging from zero, β_1 , β_2 , β_3 ... β_N . A growth curve is constructed by plotting the luminescence signal against the applied doses. The D_e value is determined by analysing the

growth and extrapolating it to the negative x-axis. Various normalization methods were used for normalization between aliquots.

Single aliquot regenerative dose (SAR) protocol is widely used for D_e estimation (Murray and Wintle, 2000). It involves multiple measurements on the same aliquot with due care for changes in luminescence sensitivity. The SAR protocol is the preferred approach because it allows for the exploration of various heterogeneities within samples, thereby enabling more precise age estimation and enhanced accuracy. In this thesis, SAR protocol is used.

2.5.1.1 A single aliquot regenerative dose (SAR) protocol

SAR method was suggested by Murray and Roberts (1997) and later improved by Murray and Wintle (2000). A visual depiction of the steps followed in SAR protocol is displayed in Fig. 2.6a. In SAR protocol, D_e is estimated on a single aliquot with the assumption that the luminescence behaviour during laboratory and in nature is similar and any change in luminescence response during measurement can be corrected using test dose normalisation. In SAR protocol, natural intensity of samples is recorded, and then, a dose response curve

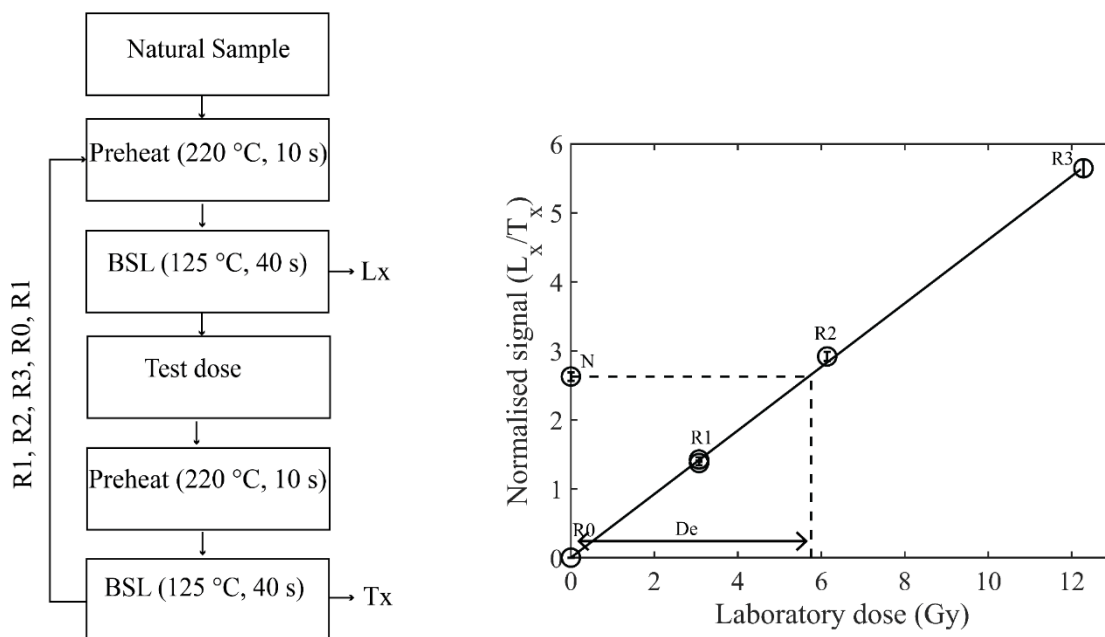


Fig. 2.6: a) Single aliquot regenerative dose (SAR) protocol for equivalent dose estimation. b) D_e value estimation using SAR protocol.

is constructed using regenerative doses in incremental order (Fig. 2.6b). The D_e is estimated by interpolating the natural luminescence of the sample to the regeneration growth curve

generated through a cycle of measurements. A preheat is applied before every regenerative dose to remove the charges that are not stable during their geological antiquity and their lifetimes are less than or nearly same of age of the sample (Roberts et al., 1994; Murray and Wintle, 1999). The preheat temperature is determined using preheat plateau test (Murray and Wintle, 2000). In the preheat plateau tests, the SAR doses are estimated using different preheat temperatures and the estimated doses are plotted with preheat temperature. The region of temperatures where the plateau of doses occurs is used as for preheat temperature. Any change in luminescence sensitivity during the repeated cycles of preheating, optical stimulation, and irradiation is corrected using a test dose after each regeneration dose. It is assumed that any sensitivity change during the repeated measurement cycles gets reflected in the test dose luminescence. Therefore, normalising the luminescence signal with the test dose signal corrects it for any sensitivity change occurring during measurements.

Dose response curves are constructed by using three doses for regeneration. Two additional doses are given to test for the robustness of the correction procedure of the SAR protocol. An identical regeneration dose is administered twice to assess the validity of sensitivity correction through a test dose. This is referred to as the recycling ratio, which should ideally lie within 10% of unity (Murray and Wintle, 2000). In the second test, the thermal transfer of charges is tested by administering a zero regeneration dose. The ratio of luminescence signal at zero dose to natural dose gives the amount of thermal transfer and is known as recuperation, and it should be less than 5% (Murray and Wintle, 2000).

D_e measurement steps using SAR protocol for blue stimulated luminescence (BSL-SAR), IRSL (IR-SAR), and post IR IRSL (pIRIR-SAR) are shown in Tables 2.1, 2.2, and 2.3, respectively. The exact procedures for D_e measurements for different samples are provided in the relevant section.

2.5.1.2 Natural correction factor (NCF)

The SAR protocol addresses the sensitivity changes that occur during each regeneration cycle of the measurement. However, when measuring natural OSL, sensitivity fluctuations can be problematic. The standard SAR protocol works well if both the OSL measurement and the consecutive test dose OSL are conducted under identical sensitivity conditions or if they experience the same level of sensitivity change during these two consecutive measurements within each cycle. However, natural OSL is typically measured under

laboratory sensitivity conditions, while immediate test dose OSL is measured under controlled laboratory conditions. In this modified protocol, Singhvi et al. (2010) introduced an adapted SAR protocol known as NCF-SAR. This modified protocol involves additional steps, such as measuring the sensitivity of the 110 °C peak both before and after the natural OSL measurement following a test dose. The ratio of two TL peaks (after/before) is then multiplied by the intensity of natural OSL (L_n/T_n). Subsequently, the modified sensitivity-corrected natural point is interpolated on the regeneration growth curve to determine the D_e . Further details of the protocol can be found in Singhvi et al. (2011) and Chauhan et al. (2015).

Table 2.1: Parameters of the BSL-SAR protocol (Murray and Wintle, 2000).

Step	Treatment	Observed measurement
1	Natural signal	
2	Preheat, 10 s at 220 °C	Removes thermally unstable signal
3	Blue stimulation, 40 s at 125 °C	L_x (measured luminescence)
4	Test dose	
5	Preheat, 10 s at 220 °C	Removes thermally unstable signal
6	Blue stimulation, 40 s at 125 °C	T_x (measured test dose luminescence)
7	Blue stimulation, 100 s at 200 °C	Bleach
8	Give dose and return to step 2	

Table 2.2: Parameters of the IR-SAR protocol (Wallinga et al., 2000).

Step	Treatment	Observed measurement
1	Natural signal	
2	Preheat, 60 s at 250 °C	Removes thermally unstable signal
3	IR stimulation, 100 s at 50 °C	L_x (measured luminescence)
4	Test dose	
5	Preheat, 60 s at 250 °C	Removes thermally unstable signal
6	IR stimulation, 100 s at 50 °C	T_x (measured test dose luminescence)
7	IR stimulation, 200 s at 100 °C	Bleach
8	Give dose and return to step 2	

Table 2.3: Parameters of the pIRIR-SAR protocol (Buylaert et al., 2009).

Step	Treatment	Observed measurement
1	Natural signal	
2	Preheat, 60 s at 320 °C	Removes thermally unstable signal
3	IR stimulation, 100 s at 50 °C	
4	IR stimulation, 100 s at 290 °C	L_x (measured luminescence)
5	Test dose	
6	Preheat, 60 s at 320 °C	Removes thermally unstable signal
7	IR stimulation, 100 s at 50 °C	
8	IR stimulation, 100 s at 290 °C	T_x (measured test dose luminescence)
9	IR stimulation, 200 s at 325 °C	Bleach
10	Give dose and return to step 2	

2.5.1.3 Dose Distribution Analysis

In the SAR protocol, each aliquot gives a value of D_e . Each individual grain within a sample can have a distinct exposure history to natural radiation and daylight. Therefore, analysis of several single aliquots from the same sample provides a spectrum of D_e values. The variation in D_e could be because of the heterogeneous distribution of ^{40}K radioactive isotopes, variable bleachability of grains before deposition, and measurement uncertainty (Mayya et al., 2006; Chauhan et al., 2021). Statistical models are then employed to calculate representative D_e values, and these are:

1. Common age model

Common age model estimates a common (average) age for all the samples, assuming that they were exposed to similar environmental conditions and received the same dose (Galbraith et al., 1999). This model relies on the theoretical premise that samples within the same context would have the same age.

2. Central age model (CAM)

The CAM employs the weighted mean as a measure of central tendency to compute a representative D_e value (Galbraith et al., 1999). In this model, the true D_e values of individual aliquot, δ_i (for a grain i with estimated D_e is δ_i) are not equal, but are a random sample from a normal distribution with mean δ and standard deviation σ . The spread in the dose could be due to beta heterogeneity. The spread due to both causes can be considered to be σ and the experimental error ϵ , which is normally distributed.

If ϵ is normally distributed, it follows that δ_i is also normally distributed with mean δ and σ , which can be estimated by standard maximum likelihood methods. The maximum likelihood estimates are denoted by $\hat{\delta}$ and $\hat{\sigma}$. The values of δ and σ satisfy the equations:

$$\delta = \frac{\sum_{i=1}^n w_i \hat{\delta}_i}{\sum_{i=1}^n w_i} \quad (2.2)$$

and,

$$\sum_{i=1}^n w_i^2 (\delta - \hat{\delta})^2 = \sum_{i=1}^n w_i, \quad (2.3)$$

where $w_i = 1/(\sigma^2 + s_i^2)$; s_i is standard error.

In this thesis, the central age model is used for D_e estimation because only samples that should have been well-bleached were used.

3. Minimum age model (MAM)

In cases involving partially bleached samples, the minimum age model (MAM) is a preferred method for estimating D_e values. It assumes that in an ensemble of D_e values, the minimum D_e would correspond to those aliquots/grains that would have been bleached well (Bailey and Arnold, 2006). MAM identifies the minimum age estimate within a set of statistically plausible ages by considering the minimum luminescence signal (Galbraith et al., 1999). MAM extracts D_e values from a truncated normal distribution, with the lower truncation point corresponding to the D_e values of most bleached grains.

4. Finite mixture model (FMM)

The finite mixture model (FMM) is based on the premise that the D_e distribution comprises many components, each with a normal distribution, depending on the population of grains with varying doses (Galbraith and Green, 1990). The model considers the existence of several grain populations within a single sample. It statistically fits the dose distribution by combining numerous Gaussian functions, and it calculates the proportion of grains that contribute to a dose value based on these functions. Through this process, it estimates the true burial dose value.

2.5.2 Anomalous fading

As discussed in Chapter 1, two approaches are used to account for athermal fading. These include (a) laboratory estimation of the fading rate (g -value) and correction of the measured ages for fading (Auclair et al., 2003; Huntley and Lamothe, 2001; Kars et al., 2008), and (b) probing of traps and recombination centres that are less prone to fading (Buylaert et al., 2011, 2012; Krbetschek and Trautmann, 2000; Prasad et al., 2017; Zink and Visocekas, 1997).

2.5.2.1 Correction procedure: Huntley and Lamothe (2001)

The Huntley and Lamothe (2001) model characterises athermal fading over time and corrects the ages for it in feldspar minerals. They suggest that the athermal fading rate (g -value) can be estimated using the following equation:

$$I = I_c \left[1 - \frac{g}{100} \log_{10} \left(\frac{t}{t_c} \right) \right] \quad (2.4)$$

where I is OSL intensity measured at time t , t is the delay time, t_c is characteristic time, and I_c is the intensity when $t = t_c$ and g -values are normalised to a $t_c = 2$ days. Athermal fading rates are determined by analysing the slope of the semi-logarithmic graph between luminescence intensity and time delays (Auclair et al., 2003) (Fig. 2.7). The procedure involves the following sequence, daylight of blue light optical bleaching to minimize residual, a laboratory beta dose closer to the equivalent doses, preheat, and measurement of OSL intensity for multiple time delays, ranging from a few minutes to several days. A test dose is administered after each regenerative dose to normalise the signal for all samples. During analysis, photon counts from the first 2.40 s are taken as the signal, while photon counts in the final 20 s of the decay curve are the background. Following method outlined

in Huntley and Lamothe (2001), this fading rate is then used to calculate the true age of the sample using the following equation:

$$\frac{T_f}{T} = 1 - \frac{g}{230} \left[\ln\left(\frac{T}{t_c}\right) - 1 \right] \quad (2.5)$$

Here T_f is the faded age, and T is the true age. Faded age is the age estimated using equivalent doses, and these are corrected for fading using g values.

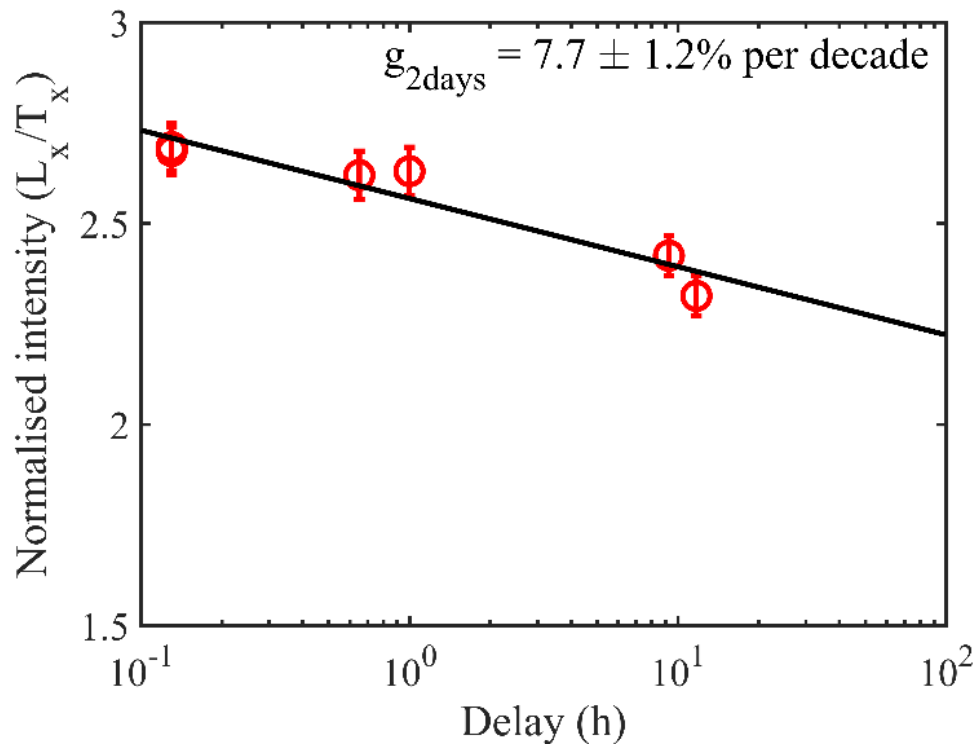


Fig. 2.7: Fading rate (g -value) measurements for a sample.

2.5.2.2 Correction procedure: Kars and Wallinga (2009) model

For older samples, prescriptions by Huntley (2006), Kars et al. (2008), and Kars and Wallinga (2009) are used, which use a power-law dependence of athermal fading with time. Kars and Wallinga, (2009) model assume that recombination centres are randomly distributed with a density ρ and electrons can tunnel only to their nearest recombination centre (Huntley, 2006). They developed a relationship:

$$I = I_0 e^{-\rho \ln(1.8st)^3} \quad (2.6)$$

where I and I_0 are the luminescence intensities at time t and immediately after irradiation, i.e., $t = 0$ and ρ' is the fading parameter related to the number density of luminescence centres in the crystal, and s is the attempt to escape frequency, assumed as $3.0 \times 10^{15} \text{ s}^{-1}$ (Huntley, 2006). The measurement process involves measuring the natural luminescence signal and constructing a dose response curve (DRC). Each regenerated OSL is adjusted for fading during laboratory irradiation considering irradiation source dose rate and corrected time. This corrected time is calculated as 0.5 times the regeneration beta dose exposure time plus the time delay between irradiation and prompt measurements. The corrected DRC is fitted to a single saturating exponential function to determine the saturating limit (I_0) and the onset of saturation (D_0). Further, a DRC is constructed assuming a natural dose rate, with I_0 considered as the limit for the OSL. The natural normalised OSL intensity is interpolated on the simulated DRC, which is representative of DRC during natural irradiation.

2.5.2.3 Probing non-fading signal

Models used to correct for fading assume that the rates of fading estimated in a laboratory setting can be extended to geological timescales. Nevertheless, this assumption has faced scrutiny from various researchers (Li and Li, 2014). The next approach attempts to isolate luminescence signals with low or minimal athermal loss of charges.

Production of the IRSL signal in feldspar was explained using donor-acceptor model (Poolton, 1994), which states that electron tunnelling occurs from the excited state of the IRSL trap at 1.4 eV. Extending previous studies by Visocekas (1985), Jain et al. (2011) suggested a mechanism of K-feldspar luminescence that involves a trap and spatially distributed recombination centers. The excited state of the trap overlaps with the band tail states beneath the conduction band. Stimulation with IR (1.44 eV) moves charges from the ground state of the trap through a resonant excitation to an excited state; thereafter, these charges are thermally assisted to the band tail states to recombine, resulting in IRSL. IRSL in K-feldspar depends on the tunnelling probability from the excited state which decreases exponentially with increasing donor-acceptor distance (Hütt et al., 1988; Jain et al., 2015; Poolton, 1994). Therefore, during IRSL, proximal charge pairs are consumed first, and distal ones are accessed later. Luminescence from the distal pairs has a large tunnelling life-time and, therefore, has lower fading rates (Jain et al., 2015; Poolton, 1994). Such signals have been variously probed, e.g., a) post-IR IRSL (pIRIRSL; Buylaert et al., 2009;

2011, 2012; Biswas et al., 2013; Thomsen et al., 2008) and other methods discussed briefly in the chapter 1. Using spectroscopic measurements, Andersen et al. (2012) suggested that both IRSL and pIRIRSL arise from the same trap and that the pIRIRSL results from the recombination of distant charge pairs. Most widely used protocol is pIRIR-SAR for K-feldspar dating as described in Table 2.3 (Buylaert et al., 2009).

In the thesis, multiple combinations of stimulation wavelengths and detection windows were explored to identify the optimum configurations that could provide a signal with minimal athermal fading. Details of the experiment conducted and the obtained results are discussed in Chapter 3.

2.5.3 Measurement of the dose rate

Dose rate is the rate of energy deposited per unit mass in natural minerals by ionizing radiations emitted by radioactive nuclides such as ^{238}U , ^{235}U , ^{232}Th , and ^{40}K present in the surrounding sediment. The number of particles emitted by these nuclides and the average dose deposited per year are shown in Table 2.4.

The total dose rate is given below:

$$\dot{D} = a\dot{D}_\alpha + \dot{D}_\beta + \dot{D}_\gamma + \dot{D}_{CR}$$

Here \dot{D}_{CR} is the dose rate contribution by cosmic rays and a is the alpha efficiency of luminescence production per unit Gy by α dose with respect to the β dose. The a -values were estimated using the relations given in Aitken (1985, pp. 308-317) and is given below:

$$a = \frac{D_\beta}{13sT_\alpha}, \quad (2.7)$$

where D_β is the beta equivalent dose, which produces same amount of luminescence as produced by the alpha dose in T_α minutes and s is the source strength. The a -value is important to consider for dose rates where the grain size is smaller than the range of α -particles such as fine-grains (4-11 μm).

Along with these factors, the moisture content of soil also needs to be considered for dose rate estimations. The water in the void spaces in sediment attenuates the ionizing radiations coming from radioactive nuclides. Therefore, corrections in the dose rate are required, and the corrections in the dose rates are made using the following equations (Zimmerman, 1971):

$$\dot{D}_\alpha = \frac{\dot{D}_{\alpha,\text{dry}}}{1 + 1.5 WF} \quad (2.8)$$

$$\dot{D}_\beta = \frac{\dot{D}_{\beta,\text{dry}}}{1 + 1.25 WF} \quad (2.9)$$

$$\dot{D}_\gamma = \frac{\dot{D}_{\gamma,\text{dry}}}{1 + 1.14 W_1 F} \quad (2.10)$$

Here, W and W_1 is the saturation water content of the sample and soil, respectively. F is the average soil water content as a fraction of saturation water content.

Table 2.4: Number of α , β particle, and γ rays emitted and average energy per decay and average dose per decay deposited by radioactive nuclides present in the sediment.

Radio nuclide	Decay particle	Average energy per decay (MeV)				Average dose per decay (Gy/Ka)			
		α	β	γ	Total	α	β	γ	Total
^{238}U	8 α , 6 β and γ	42.7	2.28	1.78	46.76	2.68	0.14	0.11	2.94
^{235}U	7 α , 4 β and γ	41.1	1.27	0.67	43.04	16.60	0.52	0.27	17.38
^{232}Th	6 α , 4 β and γ	35.7	1.33	2.32	39.35	0.73	0.03	0.05	0.81
^{40}K	89% β and 11% γ		0.50	0.15	0.61		0.78	0.24	1.02

While estimating the dose rates, it is assumed that radioactive nuclides are secular equilibrium throughout their burial means that the activity of all daughter products are the same. However, if any member of the radioactive series is lost, such as Radon which is gaseous and can escape out of the system, disequilibrium can take place. To measure the extent of disequilibrium in radioactive series, all radioactivity measurements were made in the high resolution HPGe detector. All the samples used in the thesis showed equilibrium.

The dose rates are calculated using the standard assumption of infinite matrix assumption in offline Dose Rate calculator (DRc) software (Tsokolas et al. 2016). The conversion factors used in DRc software are those published by Guérin et al. (2011). The a-value and beta attenuation factors were estimated using Guérin and Mercier (2012) and Nathan and Mauz (2008), respectively. The dose rate assumed internal potassium (^{40}K) of $12.5 \pm 0.5\%$ (Huntley and Baril, 1997) and 400 ± 100 ppm Rubidium (^{87}Rb) (Huntley and Hancock, 2001). The cosmic ray contribution to dose rate was estimated according to Prescott and Hutton (1994).

Chapter 3

Multispectral Studies in K- Feldspar

3.1 Introduction

As discussed in Chapter 1, K-feldspar has a higher saturation dose, and thereby offers the prospects of dating samples up to a few millions of years. However, athermal fading that leads to an underestimation of the age (Spooner, 1994; Visocekas, 1985; Wintle, 1973) and is attributed to quantum mechanical tunnelling of the charges leading to loss of luminescence signal, hence restricts its applicability (Aitken, 1985; Jain and Ankjærgaard, 2011; Poolton et al., 2002a, 2002b; Visocekas, 1979). As discussed in Chapter 2, two approaches are used to circumvent the effect of athermal fading. In the first approach, the fading correction models assume that the fading rates estimated over laboratory time scales can be extrapolated to geological time scales. However, this assumption has been challenged by various researchers and is challenging to validate experimentally (Li and Li, 2014).

The second approach attempts to isolate stable luminescence signals having low or minimal athermal fading. As discussed in Chapter 1, many signals have been reported with low fading rates (< 5% per decade). Among them all, pIRIR signal is widely used feldspar dating. In the pIRIR technique, luminescence signals with IR stimulation at higher temperatures (150 to 290 °C) are measured after an IR 50 °C stimulation (Buckland et al., 2019; Buylaert et al., 2009; Jain and Ankjærgaard, 2011; Reimann et al., 2011, 2012; Thomsen et al., 2008). The MET-pIRIR protocol uses the premise that the fading rate of feldspar can be progressively reduced using multiple IR stimulations with increasing stimulation temperature from 50 to 250 °C (Li and Li, 2011). In both protocols, the IRSL at elevated temperatures shows lower athermal fading (Buylaert et al., 2012; Li and Li, 2011; Thiel et al., 2011). Previous studies also reported that the elevated temperature pIRIR and MET-pIRIR signals are harder to bleach than the IRSL (50 °C) signal, which can result

in the overestimation of ages (Buylaert et al., 2012; Li et al., 2014; Poolton et al., 2002a). Mortheikai et al. (2015) proposed that distant pairs can be redistributed by a thermal treatment, and such re-distributed trapped electrons can be accessed through IRSL measurements at 320 °C. The IR-PL and PTTL methods are also being developed as these show the promise for a non-fading luminescence signal. Other efforts included optimization of the detection window to identify more stable signals, such as red TL emissions (Biswas et al., 2013; Fattahi and Stokes, 2003; Zink and Visocekas, 1997). The red thermoluminescence emission (590-750 nm) has low fading and higher saturation dose as compared to that for conventional blue (360-590 nm) TL emission (Fattahi and Stokes, 2000, 2003; Zink and Visocekas, 1997).

The charges in distant donor-acceptor recombination pairs are expected to be more athermally stable. Sequential stimulation by increasing energies can probe the luminescence from the distant donor-acceptor pairs, hence can result in lower fading rates. Additionally, the use of different detection wavelengths also offers another opportunity to access the more stable emissions (i.e., recombination centres). In this chapter, we explore the multiple combinations of stimulation and emission spectral regions to identify an optimum combination that provides a luminescence signal with minimal athermal fading. Stimulation wavelengths used were IR (855 ± 33 nm), Green (525 ± 30 nm), Blue (470 ± 20 nm), and Violet (405 ± 15 nm), and detection windows were broad-UV (260-400 nm), narrow-UV (327-353 nm), and blue (320–520 nm) (Fig. 2.2). We report athermal fading rates in feldspar grains extracted from sediments of varied ages and provenances.

3.2 Samples

A total six potassium-rich feldspar samples from sediments with diverse depositional histories and provenances were investigated. These samples belong to aeolian and fluvial deposits. Table 3.1 provides the list of samples used and their depositional environments. The equivalent doses (D_e) of the samples investigated ranged from 10 Gy to 240 Gy. These D_e -values were estimated using the existing protocols, such as blue light stimulated luminescence SAR (BSL-SAR) of quartz and pIRIR (50, 290 °C)-SAR for feldspar (Table 2.1 and 2.3). In addition, a museum specimen of potassium feldspar (KF: microcline), whose mineralogy was confirmed using XRD technique, was investigated (Fig. 3.1). We carried out detailed investigations of fading rates for all stimulation and detection combinations on PRL0 sample due to its higher luminescence sensitivity and sufficient

amount of sample available. Thereafter the optimized combination of spectral windows with minimal fading rate was used to measure the fading rates for other geological samples with varying ages from different depositional environments. By testing the applicability of optimized combination with minimal fading on these samples, we tested the universality of the signal for minimal fading and how its luminescence properties change with varying ages and provenances.

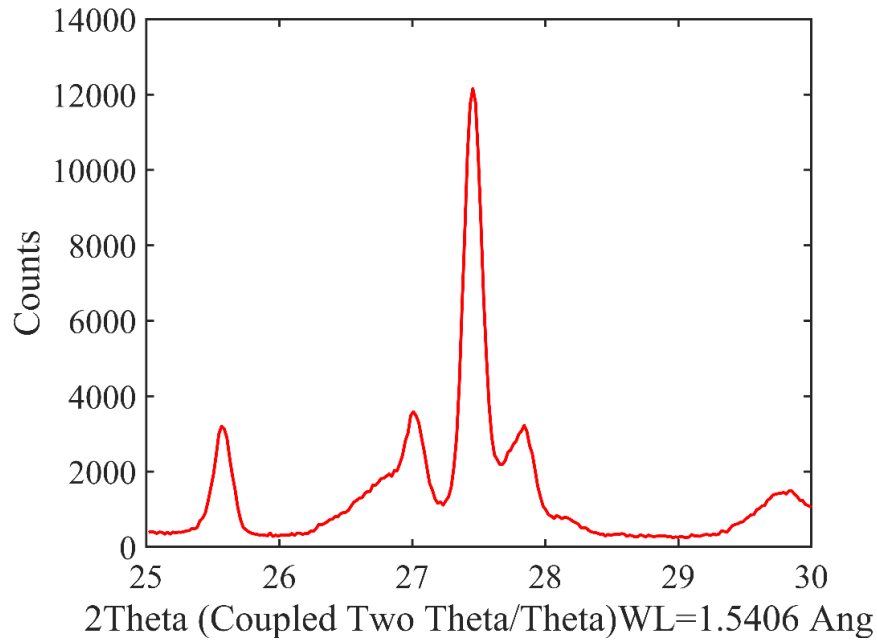


Fig. 3.1: The XRD spectrum of museum KF sample (microcline).

Table 3.1: List of samples used and their location, depositional environment, and equivalent doses.

Sample code	Location	Depositional environment	D _e (Gy)	Protocol
KF	-	Museum sample	-	-
PRL0	Tamil Nadu	Fluvial	11.1 ± 0.3	Quartz NCF-SAR
PRL1	Rajasthan (Thar desert)	Aeolian	15 ± 1	Feldspar pIRIR
PRL2	Narmada valley	Fluvial	36.0 ± 0.1	Quartz SAR OS�
PRL3	Odisha	Fluvial	77 ± 3	Quartz SAR OS�
PRL4	Andhra Pradesh	Fluvial	217 ± 3	Feldspar pIRIR
PRL5	Chennai (Attirampakkam)	Fluvial	237 ± 23	Feldspar pIRIR

3.3 Measurements

The coarse grain potassium feldspar grains were extracted using the methodology discussed in Chapter 2 (subsection 2.4.2). To explore the athermal stability of different spectral regions of feldspar, different combinations of stimulation and detection windows were made. The details of the stimulation sources and detection windows are provided in subsection 2.2.1. The combinations were made such that there is no overlap between the transmission of stimulation and the detection filter. Following this, the IR stimulation was detected in both Broad-UV and blue windows. The green and blue stimulations were detected in both Broad-UV and Narrow-UV, whereas violet stimulation was only detected in Narrow-UV. Table 3.2 summarizes the different combinations of stimulation and detection windows considered for investigations.

Experiments were conducted to assess the emission of the samples in different detection windows, namely the open window (BG39, 3 mm; transmission range: 330-650 nm), blue, broad-UV, and narrow-UV detection windows (Fig. 2.2). All TL measurements in different detection windows were carried out on the same aliquot after approximately 1 Gy dose for each sample. Fig. 3.2 shows that luminescence is emitted in variable wavelengths which can be observed via different optical transmission filters. For samples KF and PRL2, the maximum emission of TL is around 100 °C for all detection windows (Fig. 3.2a and c). In case of samples NaF and PRL0, the maximum TL emission is near 100 °C in the blue window but it is between 250 and 280 °C in the broad-UV and narrow-UV windows (Fig. 3.2b and d). The results indicate that signal from specific recombination centres can be picked up using particular detection windows for exploring their athermal behaviour. Therefore, further experiments were conducted to characterise the athermal behaviour of luminescence emission from different detection windows.

For fading measurements, a laboratory dose equivalent to the paleodose was administered after the samples bleaching in the TL/OSL reader. The samples were bleached with the stimulation wavelength for which the fading rates were to be estimated. The bleaching temperature was kept 50 °C higher than the stimulation temperature used for fading rate estimations to ensure that the traps corresponding to each stimulation were emptied out. After irradiation, the sample was preheated to 250 °C for a duration of 60 s. The OSL signal from the sample was then measured at various time intervals, ranging from a few minutes to several days. To ensure accurate measurements, a test dose was given following each

regenerative dose. The g-values (% per decade) were measured from the slope of a plot between delayed luminescence intensities and delay times on a logarithmic scale (Auclair et al., 2003). Fig. 3.3(a, b) provides a generalized measurement sequence. The average fading rate [g_{AV} (% per decade)] is a mean of fading values on 15 aliquots. Photon counts from the initial 2.40 s were used as the signal, and the normalized averaged photon counts during the final 20 s of the stimulation were taken as the background. This process was adopted for all fading measurements for all different combinations of stimulation and detection windows.

The fading rate measurements were carried out using both single stimulation and double stimulation experiments to identify the combination with minimal athermal fading. The stimulation and detection combinations used in the fading rate measurements of the single stimulation experiments are listed in Table 3.2. For ease of understanding, a given stimulation and detection combination is written as [stimulation, detection]. The

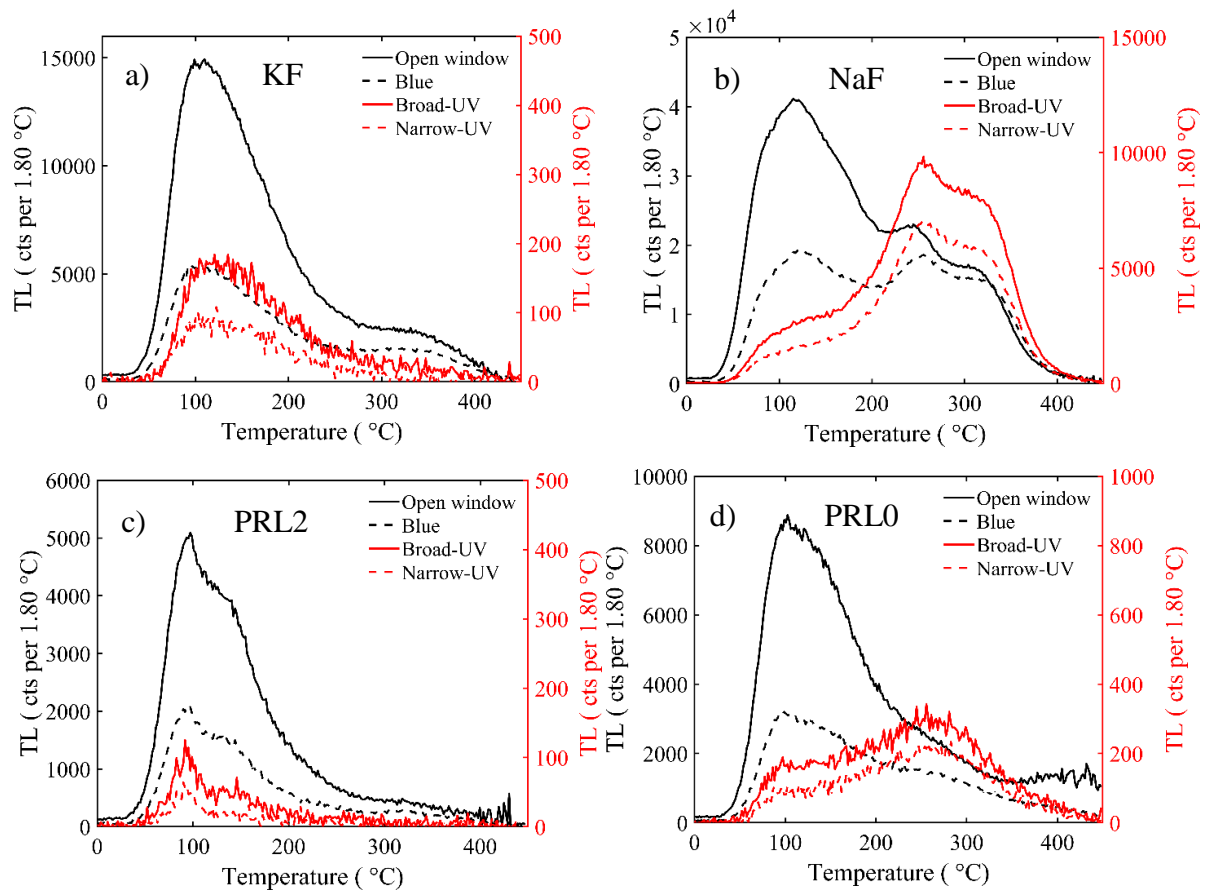


Fig. 3.2: Thermoluminescence glow curves of a) KF, b) NaF, c) PRL2, and d) PRL0 recorded in open window (BG39, 3 mm; transmission range: 330-650 nm), blue, broad-UV, and narrow-UV detection window (Table 3.2).

measurement sequence for single stimulation experiments is shown in Fig. 3.3a. Following the results from the single stimulation, the double stimulation fading measurements were carried out. In the double stimulation experiments, the successive stimulation of sample aliquots by two different sources was provided and named stimulations-1 and 2, as shown in Fig. 3.3b. The purpose of the double stimulation experiments was to first deplete the proximal charge pairs using stimulation-1, then subsequent stimulation-2 probes the distant charge pairs and hence will result in lower fading rates. In the double stimulation experiments, the first five fading measurements were carried out by applying stimulations in the increasing order of their excitation energies (IR-green, IR-blue, IR-violet, green-blue, and blue-violet). The subsequent three experiments were performed using stimulation in a decreasing order of their excitation energies (green-IR, blue-IR, and violet-IR). The measurement combinations for double stimulations are provided in Table 3.3.

Table 3.2: Stimulation and detection spectral region combinations used for fading rate measurements along with their estimated average fading rates [g_{AV} (% per decade)] for single stimulation experiments.

Sr. no.	Stimulation	Stimulation wavelength (nm)	Detection (Filter name)	Transmission range (nm)	g_{AV} (% per decade)
1	Infrared	855 ± 33	Hoya U-340 (Broad-UV)	260–400 nm	7.5 ± 0.3
			BG-39 +BG-3 (Blue)	320–520 nm	6.9 ± 0.3
2	Green	525 ± 30	Hoya U-340 (Broad-UV)	260–400 nm	7.9 ± 0.3
			Brightline (FF-340/26) + U-340 filter (Narrow-UV)	327–353 nm	7.4 ± 0.5
3	Blue	470 ± 20	Hoya U-340 (Broad-UV)	260–400 nm	7.0 ± 0.3
			Brightline (FF-340/26) + Hoya U-340 (Narrow-UV)	327–353 nm	6.7 ± 0.5
4	Violet	405 ± 15	Brightline (FF-340/26) + Hoya U-340 (Narrow-UV)	327–353 nm	6.6 ± 0.5

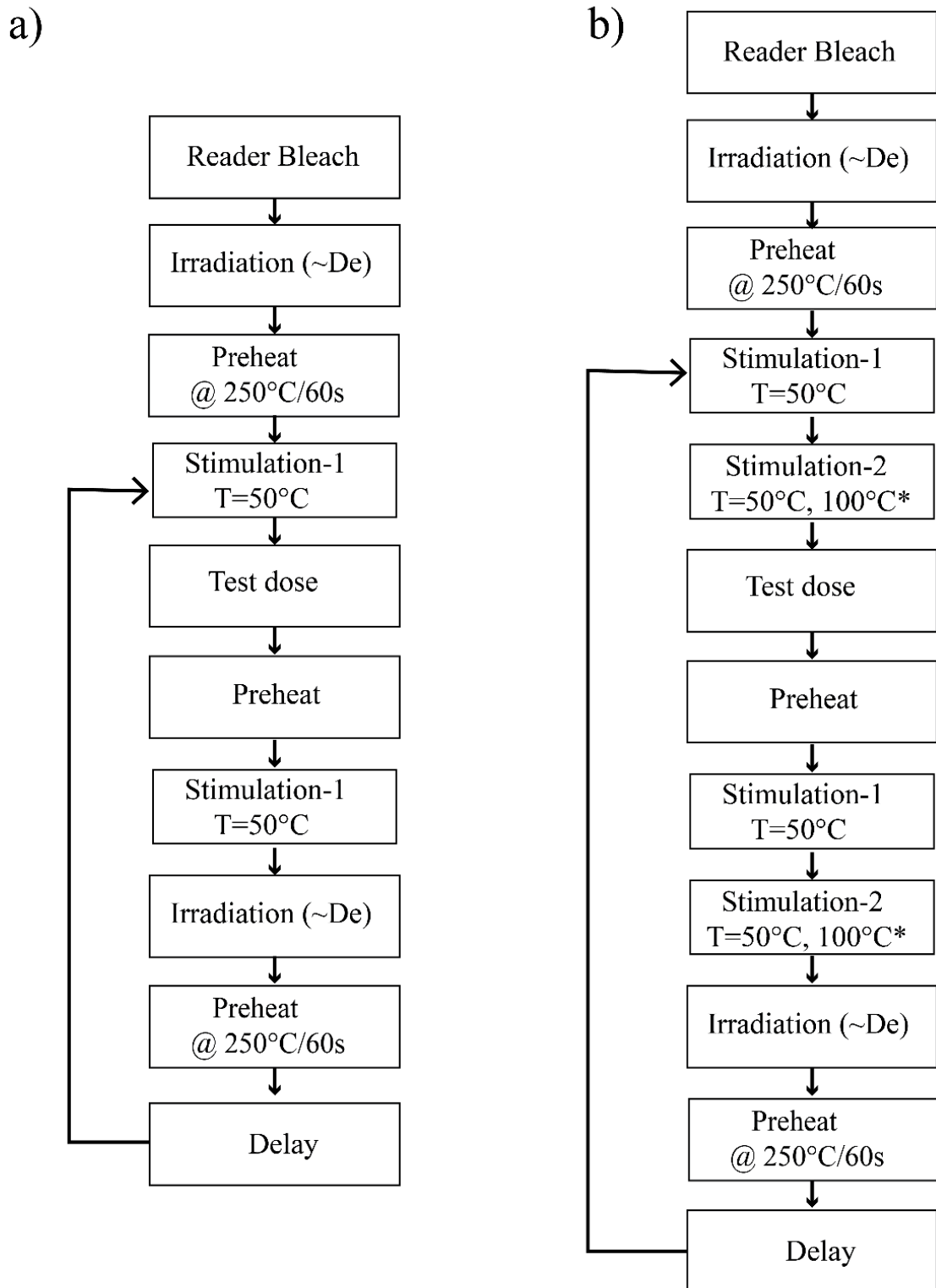


Fig. 3.3: Methodology for the measurement of fading rates [g_{2days} (% per decade)] for single (a) and double stimulation (b) experiments. * IRSL measurements post green, post blue, and post violet stimulation were carried out with the sample at 100 °C to get a good signal to noise ratio.

Table 3.3: Combinations of stimulation and detection windows used for double stimulation experiments along with the measured g_{AV} -values. The double stimulation experiment comprised sequential stimulation by two wavelengths: stimulation-1 and stimulation-2.

Sr. no.	Stimulation	Detection	g_{AV} (% per decade)	Stimulation	Detection	g_{AV} (% per decade)
	Stimulation-1			Stimulation-2		
1	IR	Blue	7.0 ± 0.2	Green	Narrow-UV	2.3 ± 0.2
2	IR	Blue	7.1 ± 0.1	Blue	Narrow-UV	3.2 ± 0.2
3	IR	Blue	5.7 ± 0.1	Violet	Narrow-UV	4.0 ± 0.4
4	Green	Narrow UV	7.8 ± 0.2	Blue	Narrow-UV	1.1 ± 0.1
5	Blue	Narrow UV	7.3 ± 0.3	Violet	Blue	1.3 ± 0.2
6	Green	Narrow UV	8.2 ± 0.3	IR	Blue	2.9 ± 0.2
7	Blue	Narrow UV	7.9 ± 0.2	IR	Blue	2.0 ± 0.2
8	Violet	Narrow UV	6.1 ± 0.2	IR	Blue	0.0 ± 0.1

3.4 Results and Discussion

3.4.1 Single stimulations

The fading rates corresponding to each stimulation with allowed detection window were measured. The average fading rates (g_{AV}) for each single stimulation measurement are presented in Table 3.2 and shown in Fig. 3.4. Fading rates for all the stimulation and detection combinations lie between 6.6 to 7.9% per decade. These results demonstrate that the fading rates for all the stimulation and detection combinations were high and similar (~7% per decade). The green (~2.3 eV), blue (~2.6 eV), and violet (~3.1 eV) excitation energies are equal to or higher than optical trap depth of the principal trap of feldspar which lies between 2.0 and 2.5 eV (Hütt et al., 1988; Kumar et al., 2020; Riedesel et al., 2019, 2021). This leads to a direct transfer of charges from the ground state of principal traps to the conduction band in case of green, blue and violet stimulation. However, the energy of IR is ~1.4 eV and lower than the optical trap depth (Jain and Ankjærgaard, 2011).

Therefore, the IR stimulation transfers the electrons to the first excited state of the principal trap due to resonance excitation (Hütt et al., 1988), and thereafter the electrons further move to the band tail states of feldspar. Low mobility of electrons in the band tail states facilitates the proximal donor-acceptor recombination (Jain and Ankjærgaard, 2011). Due to high mobility of electrons in the conduction band, electrons will also recombine with the distant holes; therefore, it is expected that green, blue, and violet stimulated luminescence will show lower fading rates than IR stimulation. However, the similarity of fading rates for the single stimulation and detection combinations indicate that either similar types of traps and recombination centres are involved in the luminescence production or a population of the proximal donor-acceptor (unstable) pairs is significantly higher than distant donor-acceptor (stable) pairs. Therefore, the population of unstable charges dominating the luminescence signal resulted from all stimulation and detection combinations.

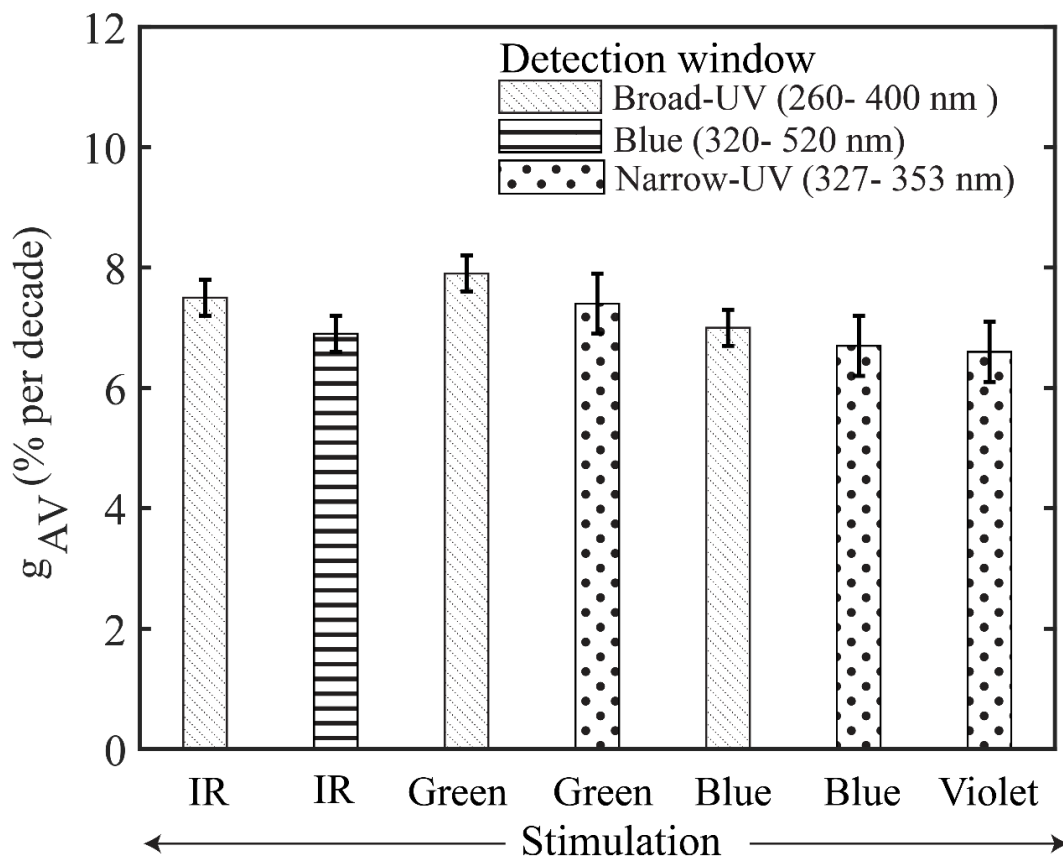


Fig. 3.4: Average fading rates [g_{AV} (% per decade)] for single stimulation and detection combinations for the PRL0 sample. The x-axis represents the stimulations, and the pattern of the bar represents the detection window. The height of the bar (y-axis) is the g_{AV} -values.

An intriguing observation of the study was the progressive decrease in fading rates from broad-UV to narrow-UV, and finally to blue detection window for the same stimulation, as illustrated in Fig. 3.4. These results accord with Thomsen et al. (2008) and Clarke et al. (1997). The results indicate that the charges resulting in luminescence in broad-UV are more closely spaced than that emitting in blue window. Further, lower fading rates for narrow-UV compared to broad-UV indicate that the charges stored in recombination centres, which emit in the lower UV wavelengths, fade more. Following the lower fading results for blue and narrow-UV detection windows from single stimulation experiment results, these were considered for estimating fading rates for double stimulation experiments.

3.4.2 Double stimulations

Considering the results from signal stimulation experiments, further attempts were to separate the stable component of the luminescence signal from the unstable component using double stimulation experiments. Table 3.3 and Fig. 3.5 provide the g_{AV} -values for each double stimulation and detection combination.

The results from double stimulation experiments showed that fading rates for stimulation-2 were significantly lower as compared to that through stimulation-1 (Fig. 3.5). These results indicate that the nearest donor-acceptor pairs are consumed using the low energy stimulation-1 for IR-green, IR-blue, IR-violet, green-blue, and blue-violet. Therefore, the distant donor-acceptor pair participates in the luminescence signal of stimulation-2 and yields low fading rates. These results accord with the donor-acceptor model, which states that the initial IRSL signal arises from the proximal donor-acceptor recombination pairs, and the latter IRSL signal originates from distant pairs (Jain et al., 2015; Poolton, 1994). Hence, the luminescence signal following the IR stimulation originates from the distant pairs, resulting in lower fading rates.

It is also noteworthy when stimulations were applied in the increasing order of energies, i.e., for IR-green, IR-blue, IR-violet, green-blue, and blue-violet, the fading rates for stimulation-2 were higher for higher excitation energy ($violet_{gAV} > blue_{gAV} > green_{gAV}$) (Fig. 3.5). The possible reason for the increase in fading rates could be the recapture of electrons from the high energy stimulation-2 to the ground state of the principal trap (Jain and Ankjærgaard, 2011; Kumar et al., 2020) and the instability of charges in recombination centres emitting in the UV window (Clarke and Rendell, 1997; Thomsen et al., 2008).

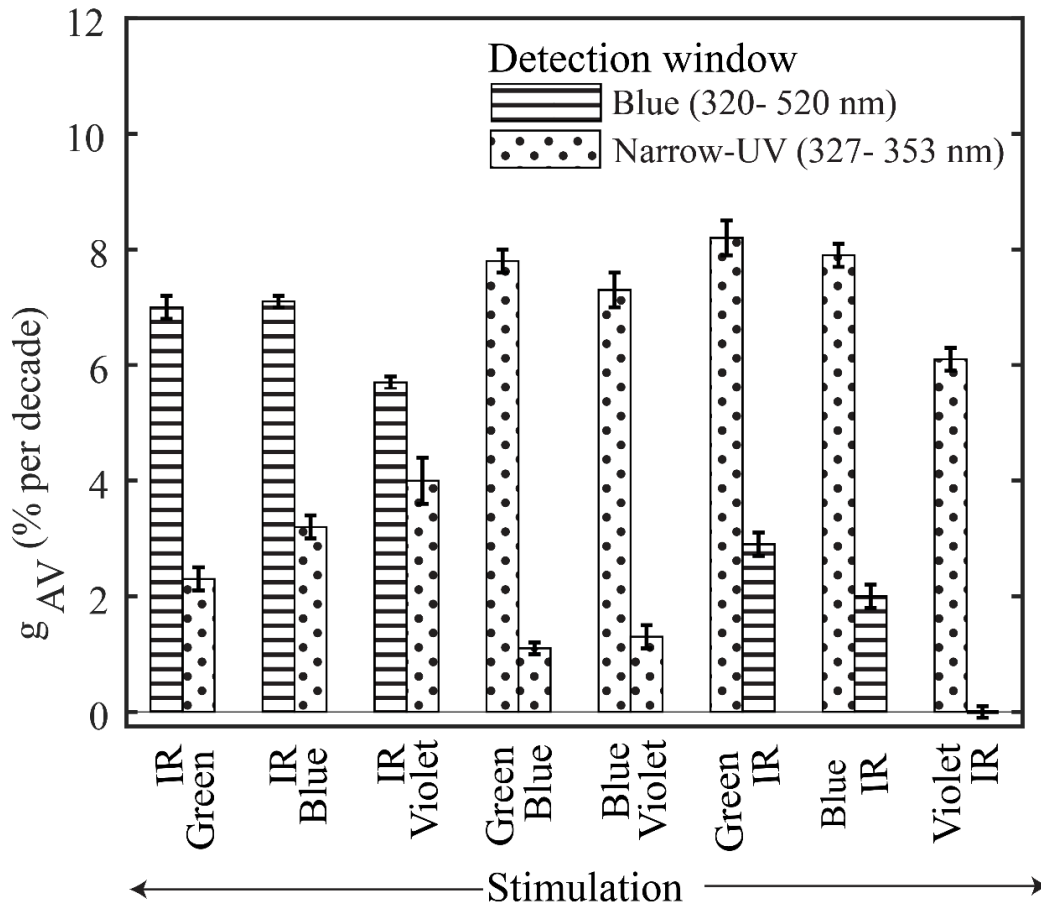


Fig. 3.5: Average fading rates [g_{AV} (% per decade)] for double stimulation and detection combinations for PRL0 sample. The x-axis represents the stimulations, and the pattern of the bar represents the detection window. The height of the bar (y-axis) is the g_{AV} -values. Double stimulation yielded lower fading rates for each second stimulation. The minimum fading ($g_{min} = 0.0 \pm 0.1\%$ per decade) was obtained in the post violet IRSL (pVIRSL) signal.

Recaptured electrons from the green, blue, and violet stimulation participate in the next fading measurement along with charges generated from the fresh irradiation during the fading measurements. Hence, an increased population of charges participates in the fading, and the probability of quantum mechanical tunnelling from the ground state also increases, resulting in a higher fading rate of high stimulation energies. Another possible reason for an increase in fading rate could be instability of UV centres as stimulation-2 is detected in the narrow-UV window in all the cases. Higher excitation energies transport a significantly greater proportion of electrons (20% at room temperature) to the conduction band (Jain and Ankjærgaard, 2011). Hence, more UV emitting centres participate in the luminescence of

higher excitation energies and lead to an increase in the fading rates. These observations need further exploration.

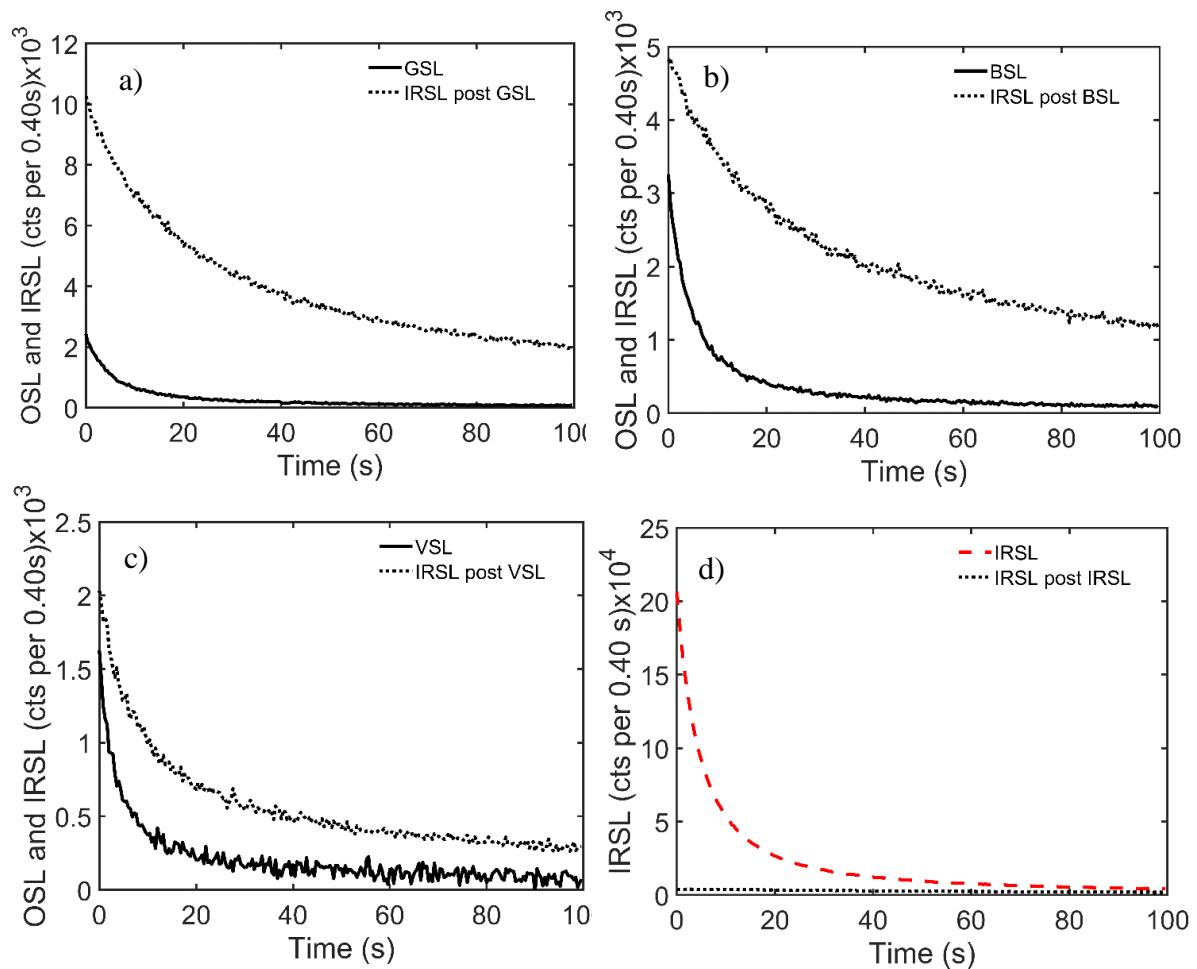


Fig. 3.6: The double stimulation decay curves for both stimulations. Decay curves for a) GSL and IRSL post green, b) BSL and IRSL post blue, c) VSL and IRSL post violet, and d) IRSL and IRSL post IR. The signal intensities are different because detection were made in the different windows viz., violet stimulation is recorded in the narrow UV window, both green and blue are in the broad UV window and IR stimulation is recorded in the blue window. The optical decay curves for all stimulations measured after ~ 20 Gy beta dose, and preheat of 250°C for 60 s. All the stimulations were carried out at 50°C temperature and power normalised.

A significant signal in IRSL after green-, blue-, and violet stimulation was observed. Optical decay curves for all stimulations are shown in Fig. 3.6. Fig. 3.7 provides the ratio of IRSL signal for the sample as received (IRSL1) and IRSL post green, blue, violet, and IR stimulation (IRSL2). It is noteworthy that IRSL2 was an order of magnitude lower after the green bleach, whereas the IR signal was reduced by two orders of magnitude after the

blue and violet bleaching. On the contrary, only a slow decaying portion of the IRSL signal was obtained after IR bleach. This finding is particularly intriguing because it contradicts

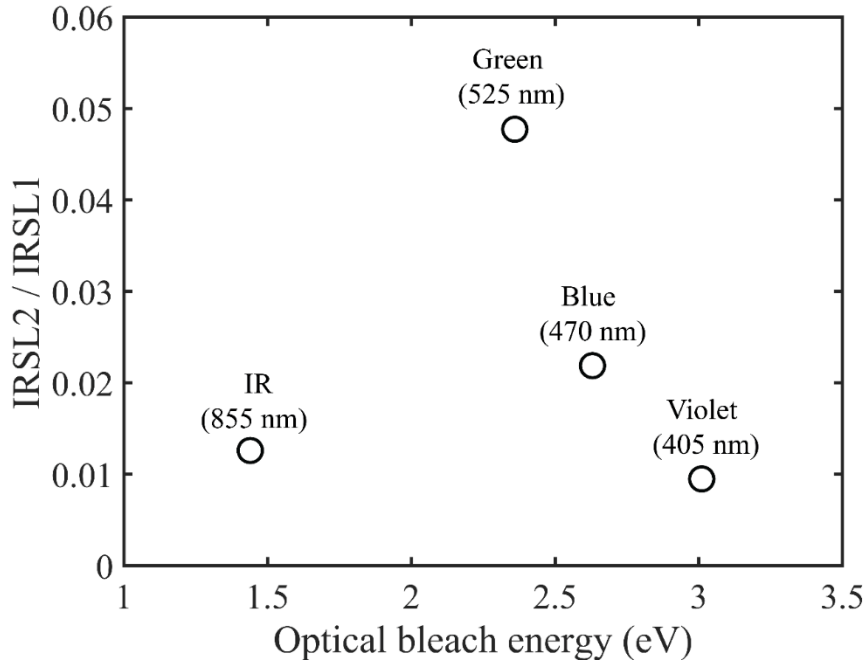


Fig. 3.7: Ratio of IRSL2 to IRSL1 signals as a function of optical bleach energy. The IRSL1 was measured without any optical bleach, and IRSL2 was measured after the optical bleach with IR, green, blue, and violet stimulations. All the stimulations were carried out at 50 °C temperature. A maximum signal is obtained in the IRSL after the green stimulation. The IRSL signal starts to decrease with an increase in the energy of optical bleach. All the applied stimulations were power normalised.

the expected outcome. Typically, after optical bleaching of a sample using higher energies, the generation of IRSL signal is not anticipated. This is suggestive of retrapping of charges from the conduction band to the ground state of the principal trap (Jain and Ankjærgaard, 2011; Kumar et al., 2020). These retrapped charges then provide luminescence in stimulation-2, i.e., IRSL in the blue window. Other possible reason for the IRSL2 signal could be the existence of at least two types of traps (Ditlefsen and Huntley, 1994; G.A.T. Duller, 1993; Jain and Singhvi, 2001) or multiple traps (Biswas et al., 2018; Ditlefsen and Huntley, 1994; Jain and Singhvi, 2001; Morthekai et al., 2015). Further, the fading rates of above mentioned IRSL signals, i.e., green-IR, blue-IR, and violet-IR were measured, and lower fading rates were obtained for each IRSL (Fig. 3.5). The fading rate of IRSL (blue detection window) was 2.9 ± 0.2 and 2.0 ± 0.2 after green and blue stimulation, respectively (Table 3.3). A more noteworthy observation is that IRSL (blue detection window) after

violet stimulation (pVIRSL) gave a $g_{AV} = 0.0 \pm 0.1\%$ per decade which is near zero (Fig. 3.5). The sensitivity corrected intensity remained constant with delay time for the pVIRSL signal (Fig. 3.8a). Fading rates [$g_{2\text{days}} (t_c = 2 \text{ days})$] for 15 aliquots were found to be in the range of -0.7 to 1.1% per decade (Fig. 3.8b). These results suggest that the pVIRSL signal results from the stable electron trapping and recombination centres. A decrease in the fading rate for stimulation-2 (IRSL) with an increase in the excitation energy of stimulation-1 (green-IR, blue-IR, and violet-IR) could be due to the fact that higher energy of stimulation-1 leads to the participation of a larger number of distant donor-acceptor pairs participating in the IRSL signal of stimulation-2. As the energy of violet light is highest among all the excitations used, the resulting pVIRSL signal comes from the distant donor-acceptor pairs and yields zero fading.

3.4.3 Fading rate of pVIRSL signal for natural samples

We further conducted testing of the pVIRSL signal on different geological samples as detailed in Table 3.1. Typical g_{AV} -values for these samples were near zero, as illustrated in Fig. 3.9 and 3.10 and summarized in Table 3.4. However, we encountered an intriguing exception in one sample named PRL5, which had an equivalent dose of $237 \pm 23 \text{ Gy}$. For this sample, the average fading rate was approximately $3.4 \pm 0.6\%$ per decade, as depicted in Fig 3.9 and reported in Table 3.4.

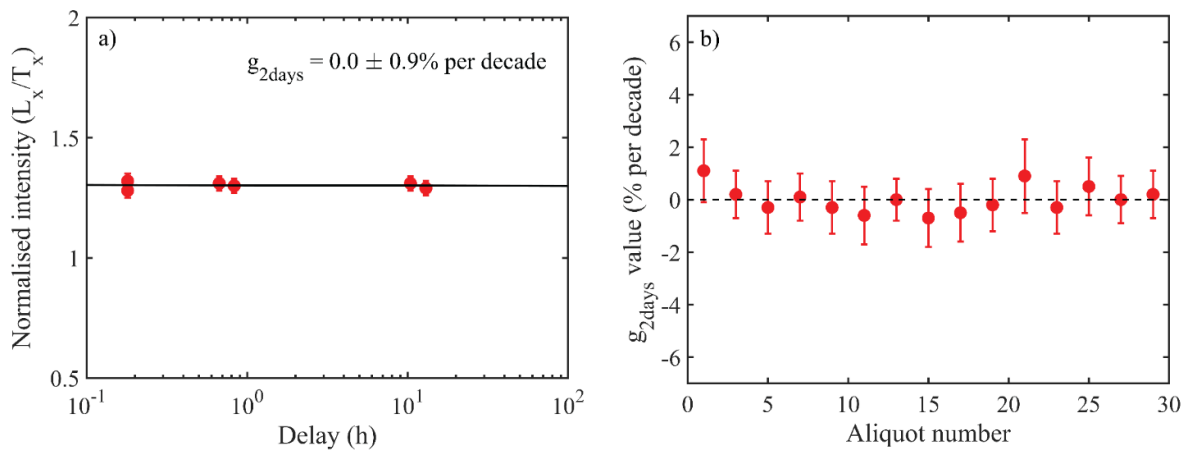


Fig. 3.8: Fading rate [$g_{2\text{days}}$ (% per decade)] results for PRL0 for pVIRSL signal. a) Normalised intensity is constant with delay and hence gives near zero fading rate, b) $g_{2\text{days}}$ values for all aliquots are near to the zero line and result in an average fading value near to zero.

At the present moment, it will be difficult to specify the reason for this high value, and it needs to be explored more. Nevertheless, the results obtained from most of the geological samples, as well as controlled museum samples, are quite promising. These findings

suggest the potential for the development of a pVIRSL protocol suitable for routine measurements, allowing us to obtain ages with minimal athermal fading effects.

Table 3.4: Observed g_{AV} -values for all samples. Here Q and F represents quartz and feldspar, respectively. The paleodoses were estimated using the independently existing protocols such as BSL-SAR and pIRIR-SAR.

No.	Sample code	Known D_e (Gy)	g_{AV} (% per decade)
1	KF	0 (F)	-0.7 ± 0.1
2	PRL0	11.1 ± 0.3 (Q)	0.0 ± 0.1
3	PRL1	15 ± 1 (F)	-1.2 ± 0.3
4	PRL2	36.0 ± 0.1 (Q)	-0.2 ± 0.2
5	PRL3	77 ± 3 (Q)	0.1 ± 0.1
6	PRL4	217 ± 3 (F)	-0.1 ± 0.7
7	PRL5	237 ± 23 (F)	3.4 ± 0.6

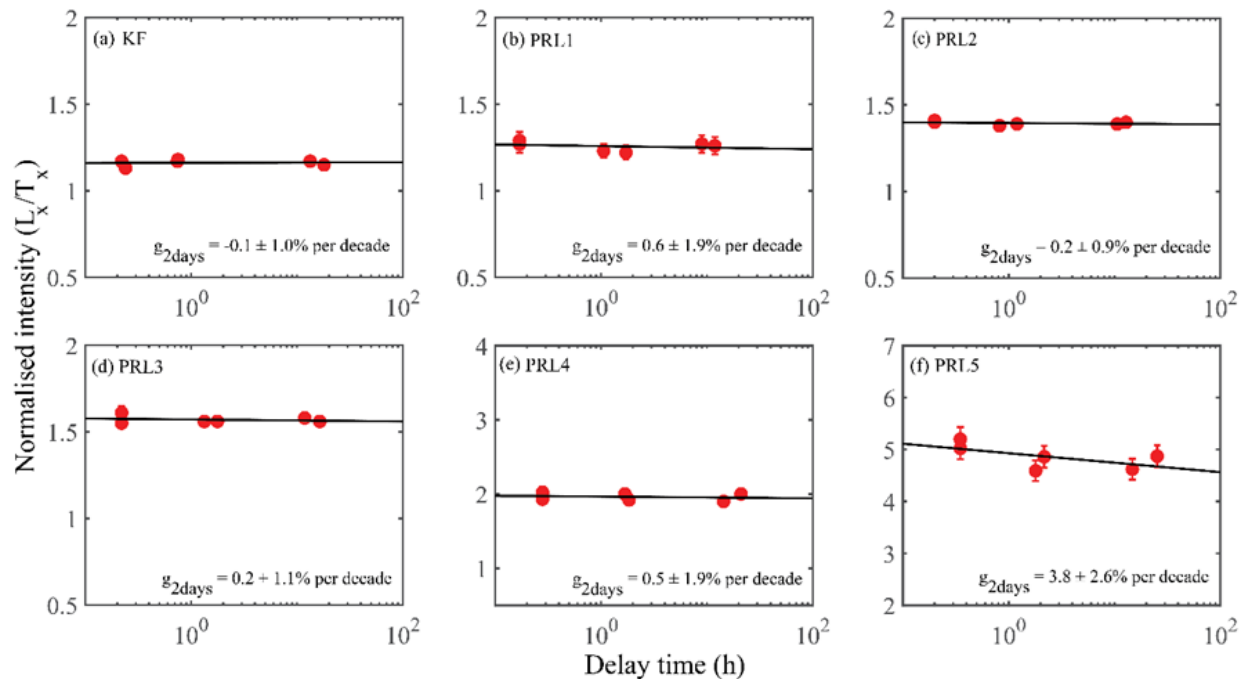


Fig. 3.9: Fading rate (g_{2days}) measurements for a single aliquot of each sample. The normalised intensities are constant with delay time for the KF, PRL1, PRL2, PRL3, and PRL4 samples.

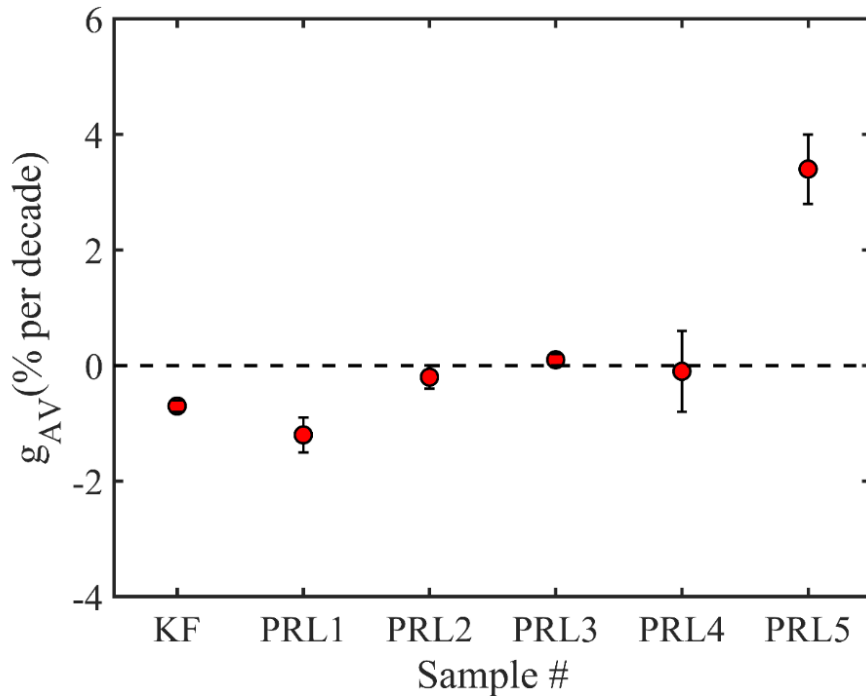


Fig. 3.10: Average fading rates [g_{AV} (% per decade)] of pVIRSL signal for all samples. The x-axis represents the sample code. The g_{AV} -values are near zero for KF, PRL1, PRL2, PRL3, and PRL4, and for one sample (PRL5, $D_e = 237 \pm 23$ Gy) g_{AV} -value is $3.4 \pm 0.6\%$ per decade.

3.5 Summary

In this study, the different spectral regions of potassium feldspar were explored for their athermal stability and an attempt to probe the non-fading traps using multispectral luminescence studies is made. Athermal fading rates were estimated for both single and sequential double stimulation combinations. Key findings of the study are as follows:

1. Single stimulations using infrared, green, blue, and violet light all resulted in similar fading rates, approximately around 7% per decade.
2. Fading rates varied depending on the detection wavelength, with broad-UV emissions exhibiting higher fading rates, followed by narrow-UV, and the blue window showing the least fading rates.
3. In the double stimulations, the fading rates for the second stimulation were significantly reduced (Fig. 3.5). This suggests that the initial stimulation consumed the nearest donor-acceptor recombination population, and the second stimulation probed more distant pairs.

4. When both stimulations were applied with increasing order of energies (e.g., IR-green, IR-blue, IR-violet, green-blue, and blue-violet), the fading rates for each second stimulation increased with an increase in the excitation energy of the second stimulation (Fig. 3.5). The possible reason could be the recapture of electrons from the high energy stimulation (Jain and Ankjærgaard, 2011; Kumar et al., 2020) and the instability of recombination centres emitting in the UV window (Clarke and Rendell, 1997; Thomsen et al., 2008). These observations need further investigation and can hint towards a new understanding of the feldspar luminescence production mechanism.
5. A significant signal in IRSL post green, blue, and violet light stimulations was observed. The obtained IRSL signal exhibits low fading rates. The possible reason might be that with an increase in the energy of stimulation-1, more distant donor-acceptor pairs participate in the IRSL signal of stimulation-2.
6. The minimum fading rate value ($g_{AV} = 0.0 \pm 0.1\%$ per decade) was obtained for pVIR stimulation, and this highlights it as a potential candidate for dating natural sediments such that the tedium and time of fading measurements can be minimized.
7. The pVIRSL signal gave near zero fading rates for several geological samples used in the study. However, one sample named PRL5 exhibited an average fading rate of $3.4 \pm 0.6\%$ per decade, the cause of which remains to be understood.
8. These findings provide valuable insights into the behaviour of luminescence signals in geological samples, shedding light on their fading characteristics. Further experiments on the suitability for dating and the dose-response of the pVIRSL signal are reported in Chapter 4.

Chapter 4

Post Violet-Infrared Stimulated Luminescence (pVIRSL) Dating Protocol

4.1 Introduction

Chapter 3 discussed multispectral luminescence studies of K-feldspars and compared athermal fading rates for different luminescence signals. The measurements using varied combinations of stimulation and detection wavelengths suggested that post-violet-infrared stimulated luminescence (pVIRSL: IRSL at 100 °C after a violet bleach at 50 °C) of K-feldspars, generally has a near zero athermal fading rate. The present chapter is dedicated to the understanding of pVIRSL luminescence mechanism and its properties relevant to dating application. Further, an optimized post violet IR single aliquot regenerative dose (pVIR-SAR) protocol was developed and tested for seven K-feldspar samples from varied depositional environments with ages ranging from 6 ka to 286 ka.

4.2 Samples

In this study, investigations were conducted on seven samples with known ages collected from various depositional environments. Feldspar grains were extracted from the natural sedimentary samples using the sample preparation procedure discussed in Chapter 2 (subsection 2.4.2). Samples from both fluvial and aeolian deposits were used. These samples covered a wide range ages, spanning from 6 ka to 286 ka, with corresponding estimated equivalent doses ranging from 11 Gy to more than 956 Gy. The expected ages of these samples were determined using well established quartz BSL-SAR (Table 2.1) and K-feldspar pIRIR-SAR (Table 2.3) techniques. The expected ages, geological locations and

depositional environments of all the samples are provided in Table 4.1. Dose rate details are provided in Table 4.2. Sample RTP-18-02, had an additional age control as it was collected from the bottom layer of the Youngest Toba Tuff (YTT) deposit, which had been securely dated to approximately 75 ka using K-Ar and pIRIR-SAR dating methods (Ninkovich et al., 1978; Anil et al., 2023). An aeolian surface samples (DH1) was used to test the bleachability of pVIRSL signal natural daylight exposure. Furthermore, to gain insights into the mechanisms underlying the pVIRSL signal, experiments were conducted using a museum specimen of potassium feldspar (KF). As discussed in Chapter 3, XRD analysis confirmed it to be a microcline.

4.3 Measurements

As discussed in Chapter 3, a significant signal was observed during IR stimulation applied after high energy green, blue and violet stimulations. Among these signals, IRSL observed after violet stimulation originated from stable charges, hence resulted in near zero fading. The current study aimed to investigate the characteristics and behaviour of the pVIRSL signal and its use in dosimetry. To understand the source of the pVIRSL signal, the luminescence mechanism, and its suitability for routine dating, sequential laboratory experiments were conducted. To understand the mechanism of pVIRSL, all measurements were made on the KF sample. Inter aliquot variability was minimized by stabilizing the sensitivity through five repeated cycles of dose (~20 Gy) followed by TL glows to 500 °C. The TL reproducibility was within 1% (Fig. 4.1). Two such sensitized aliquots were used for subsequent experiments in sections 4.4.1.1 and 4.4.1.2. The measurement conditions

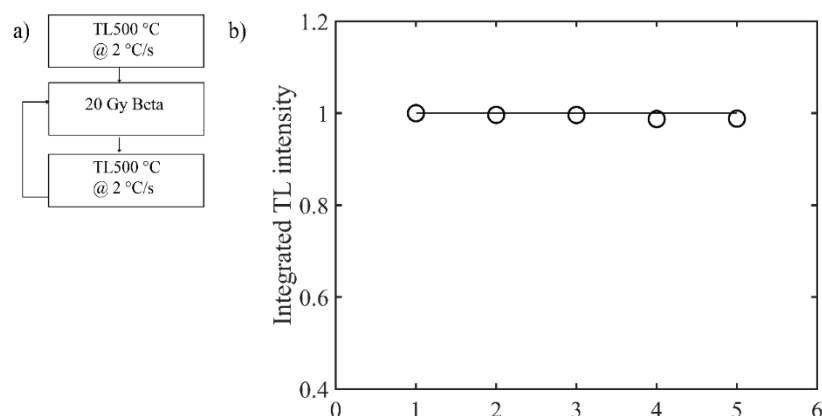


Fig. 4.1: Integrated TL intensity (integrated whole glow curve) intensity variation for repeated five cycles.

were VSL and IRSL at 50 °C, a uniform test dose of 20 Gy. The TL glows to 500 °C at 2 °C/s, and preheat of 250 °C for 60 s was detected in the blue window. The choice of luminescence measurements at 50 °C was to minimize any thermal effects due to temperature.

Table 4.1: List of samples along with geological location and history, and age controls. In the table NCF-refers to natural correction factor.

Sr no	Sample code	Location Latitude Longitude	Depositional history	Expected age (ka)	Age controls	Reference
1	KF	-	Museum	-		(Devi et al., 2022)
2	DH1	Rajasthan (26 47'59.20" N, 72 18' 42.00" E)	Aeolian	Zero age (surface sample)		This study
3	PRL0	Tamil Nadu (10° 38' 5.388" N, 79° 49' 45.012" E)	Fluvial	6 ± 1	Quartz NCFBSL-SAR	This study
4	PRL2	Narmada valley (22° 13' 44" N 76° 01' 36" E)	Fluvial	25 ± 2	Quartz BSL-SAR	(Mishra et al., 2013)
5	MHK-07-07	Narmada valley (22° 13' 44" N 76° 01' 36" E)	Fluvial	31 ± 3	Quartz BSL-SAR	(Mishra et al., 2013)
6	RTP-18-2	Andhra Pradesh (15.590630°N, 79.194290° E)	Fluvial	76 ± 6*	pIRIR-SAR Feldspar	(Anil et al., 2023) (Ninkovich et al., 1978)
7	RSN-01-17	Raisan (23° 9' 59.4" N, 72° 39' 38.16" E)	Fluvial	129 ± 16*	pIRIR-SAR Feldspar	This study
8	HMP-18-5	Andhra Pradesh (15° 27' 56.9016" N, 79° 23' 59.0388" E)	Fluvial (archaeological)	>247 ± 32*	pIRIR-SAR Feldspar	(Anil et al., 2022)
9	MHD-02-17	Mahudi (23° 30' 0" N, 72° 47' 60" E)	Fluvial	>286 ± 13*	pIRIR-SAR Feldspar	This study

*The ages are fading corrected.

Table 4.2: Dose rate details of all samples.

Sample	U (ppm)	Th (ppm)	K (%)	Dose rate* (Gy/ka)	Water content (%)	Depth (cm)
PRL0	0.76 ± 0.15	3.08 ± 0.53	1.79 ± 0.19	1.66 ± 0.12 [§]	15	1200
PRL2	1.98 ± 0.37	3.82 ± 1.26	0.83 ± 0.08	1.43 ± 0.14 [§]	15	190
MHK-07-07	2.05 ± 0.70	3.90 ± 1.28	0.87 ± 0.07	1.39 ± 0.18 [§]	15	950
RTP-18-02	2.6 ± 0.6	11.7 ± 2.2	1.40 ± 0.09	3.07 ± 0.21	20	110
RSN-01-17	6.46 ± 0.11	20.24 ± 0.50	0.91 ± 0.05	3.97 ± 0.16	15	67
HMP-18-5	1.9 ± 0.4	8.2 ± 1.4	0.50 ± 0.06	2.07 ± 0.12	17	260
MHD-02-17	2.73 ± 0.04	14.05 ± 0.28	1.49 ± 0.03	3.35 ± 0.15	15	81

[§] are dose rate calculated for quartz. *Dose rates are calculated using standard infinite matrix assumption using offline Dose Rate calculator (DRc; Tsokolas et al., 2016). The conversion factors used in DRc software are by Guérin et al. (2011). The *a*-value and beta attenuation factors were estimated using Guérin and Mercier (2012) and Nathan and Mauz (2008), respectively.

The experiments were categorised as follows:

1. Identification of source traps

In this experiment, attempts were made to identify and characterize the traps responsible for producing pVIRSL signal in feldspar. Understanding the nature of traps is crucial for understanding the luminescence mechanism and stability of the signal.

2. Mechanism of charge transfer

The experiments were conducted to understand the mechanism through which charges are transferred in the IR traps after violet stimulation and how they get trapped in the IR traps.

3. Dosimetry and dating parameters of pVIRSL

This category is concerned with assessing the dosimetric properties of the pVIRSL signal, including its bleachability, recuperation, and reproducibility. These parameters are critical for using the pVIRSL signal in dating applications.

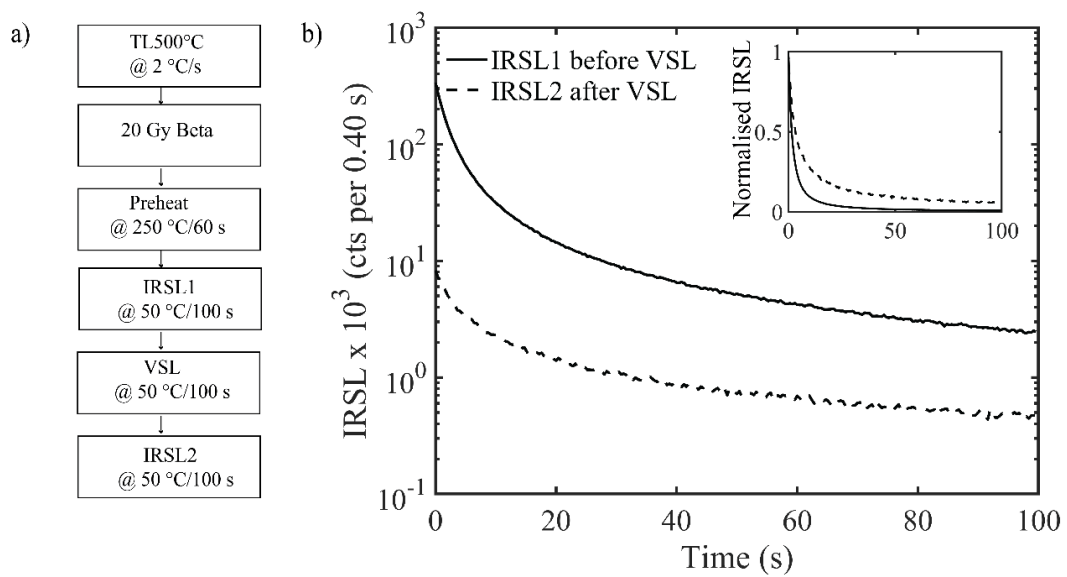


Fig. 4.2: a) Measurement protocol to explore the relative intensity of pVIRSL compared to IRSL for KF sample. b) IRSL decay curves recorded before (IRSL1) and after (IRSL2) violet stimulation. The signal of IRSL2 is about an order of magnitude smaller than IRSL1. The inset shows the normalised IRSL intensities for IRSL1 and IRSL2.

4.4 Results and Discussion

4.4.1 Source traps and pVIRSL mechanism

4.4.1.1 Post violet TL/IRSL measurements

To quantify the IRSL signal obtained after the violet stimulation, experiment mentioned in Fig. 4.2a was conducted. After irradiation and preheat, IRSL was recorded before (IRSL1) and after (IRSL2) the violet stimulation. The results are shown in Fig. 4.2b. The initial part of decay curve of post violet IRSL2 increased threefold compared to end of decay curve of IRSL1. Therefore, experiments were carried out to understand the production mechanism of pVIRSL. TL glow curve of the KF sample was recorded with 20 Gy dose and it comprises two peaks at 130 °C and 380 °C (Fig. 4.3a). The measurements for identifying the source traps for pVIRSL were carried out following the sequence detailed in the protocol in Fig. 4.3b. After irradiation, all the traps were emptied out using thermal stimulation up to 500 °C. Following this, TL was recorded after repeated five cycles of violet stimulation without any additional dose and named pVTL- i , where i is the cycle number. Fig. 4.3c provides the results and shows TL glow curves recorded after a 500 °C TL wash and a violet stimulation step. The result suggests photo-transfer of charges from

traps $> 500\text{ }^{\circ}\text{C}$ to shallower traps at $130\text{ }^{\circ}\text{C}$ and $380\text{ }^{\circ}\text{C}$. Repetitive VSL and TL measurement without intervening irradiation, produced a finite TL, suggestive of deep reservoir traps supplying charges for each post violet TL (pVTL). Inset of Fig. 4.3c plots the integrated intensity of PTTL glow peaks at $130\text{ }^{\circ}\text{C}$ (integration from 120 to $140\text{ }^{\circ}\text{C}$) and $380\text{ }^{\circ}\text{C}$ (integration from 370 to $390\text{ }^{\circ}\text{C}$) with the repeated cycles of violet stimulation. The data showed the depletion in PTTL for repetitive VSL and TL measurements, but still signal was obtained after multiple cycles, indicating that charges from deep traps were not depleted during repetitions.

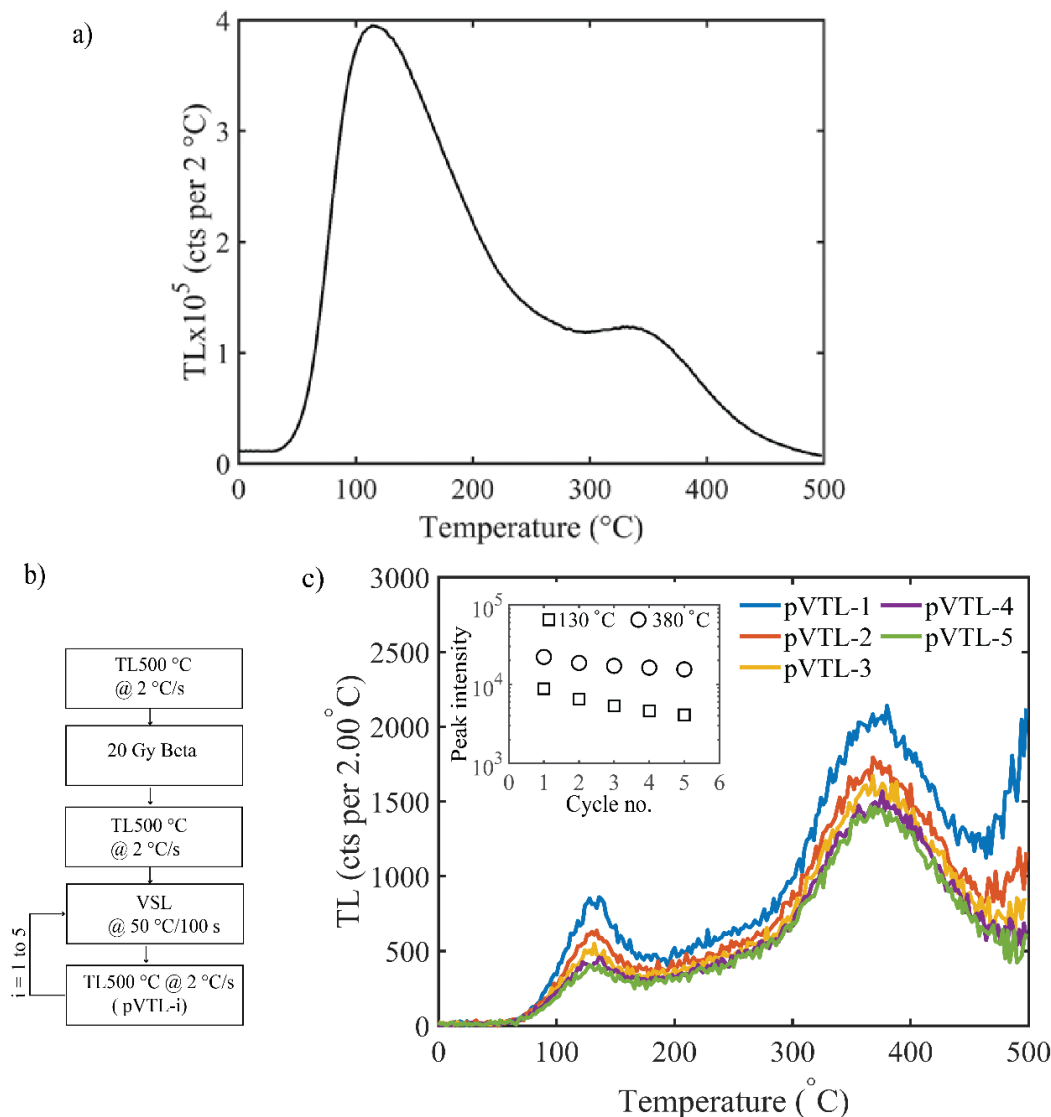


Fig. 4.3: a) TL glow curve of KF feldspar sample after irradiation of 20 Gy. b) Measurements carried out to explore the TL emissions after the repeated violet stimulation without any additional dose of the KF sample. c) The background subtracted TL glow curves are recorded in the blue window. Inset in the figure shows the variation of the integrated intensity of TL peak at $130\text{ }^{\circ}\text{C}$

(integrated from 120 to 140 °C) and 380 °C (integrated from 370 to 390 °C) with cycle number. All these measurements were carried out in a nitrogen environment.

Further, an experiment was conducted to determine the upper bound of temperature range up to which violet stimulation can affect. In our standard TL OSL reader, it is not possible to stimulate the samples to very high temperature, so the experiments were conducted in external muffle furnace with controlled temperature. All measurements were carried on a single aliquot. In this experiment, the sample was initially irradiated with a dose of nearly 20 Gy, then annealed at temperatures ranging from 450 to 800 °C. Subsequently, violet stimulation at 50 °C was applied for 100 seconds, and the corresponding photo transferred signal was recorded using TL in the blue window up to 450 °C. The results showed a decrease in the photo transfer of charges with increasing annealing temperatures, with negligible photo transfer observed at 800 °C (Fig. 4.4). This indicates that violet stimulation accesses TL traps below 800 °C and suggests the upper limit of TL peaks accessible by violet stimulation at 50 °C.

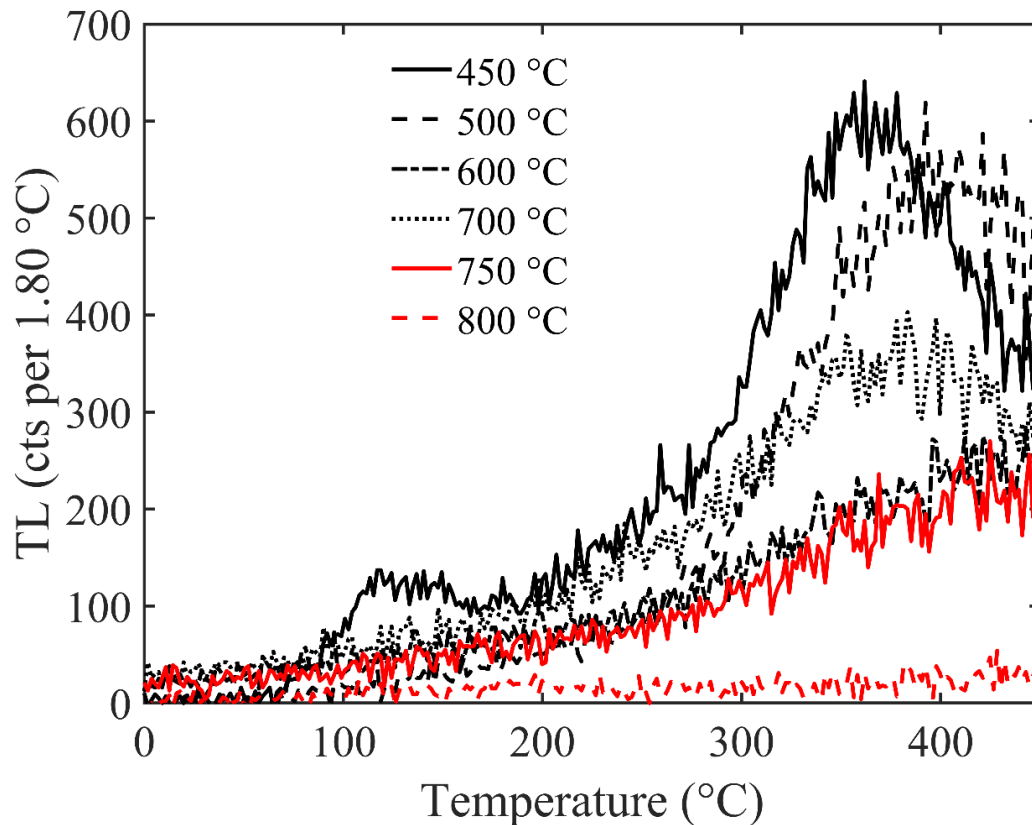


Fig. 4.4: TL glow peaks were recorded after violet stimulation following variable annealing temperatures ranging from 450 to 800 °C.

Further, to observe the luminescence from the photo-transferred charges, two types of experiment were conducted, a) the recombination centres remaining in broad-UV (BUV) and blue window after the violet stimulation and b) different stimulations viz. IR, green, and blue were recorded after the violet stimulation (pVIRSL, pVGSL, and pVBSL) in the allowed detection windows. For the first experiment, the recombination centres left in BUV

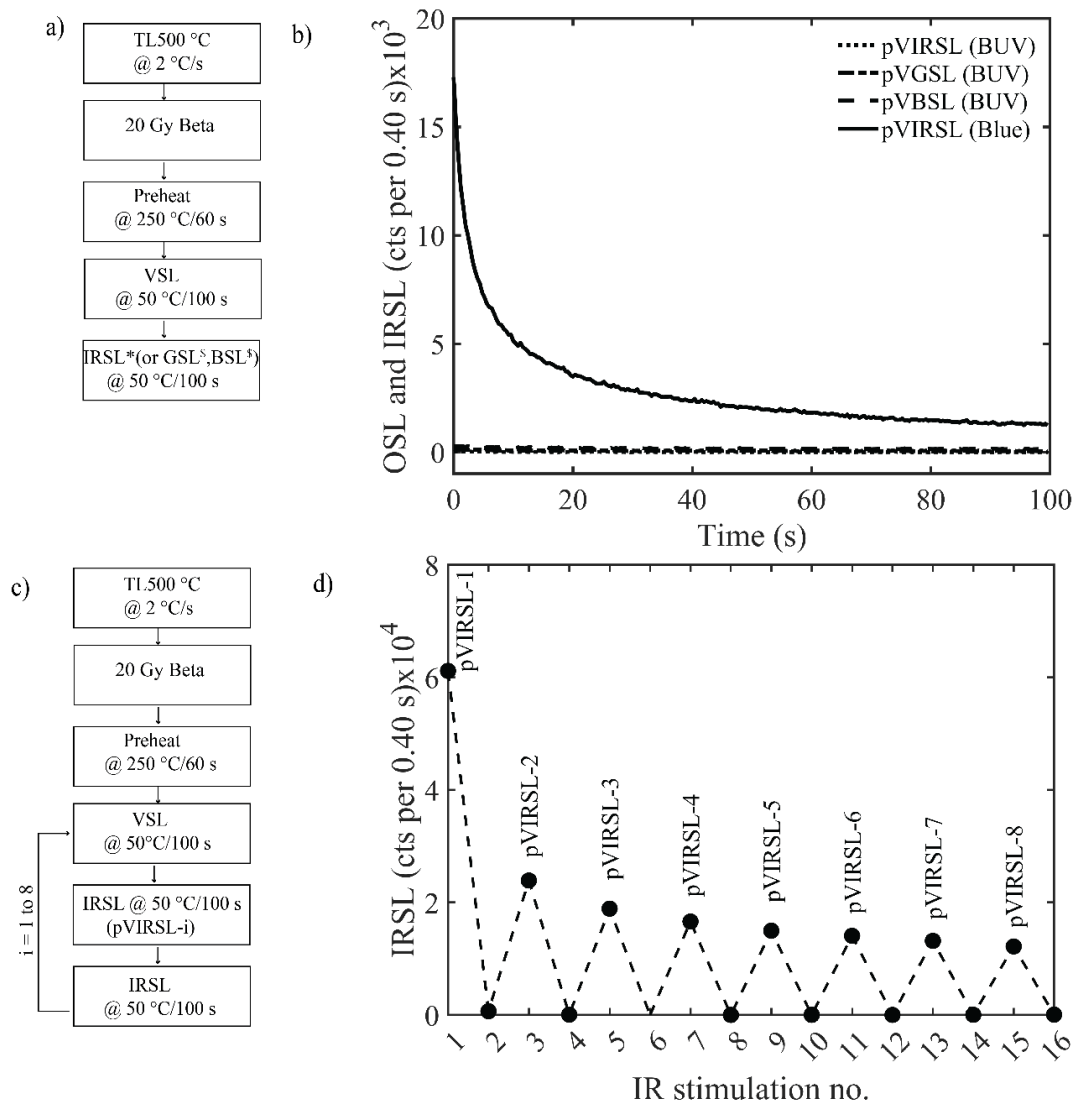


Fig. 4.5: a) The measurement protocol to estimate the population of recombination centres emitting in BUV and blue window. b) The background subtracted TL glow curves of in blue window before and after the violet stimulation. c) The background subtracted TL glow curves of in BUV window before and after the violet stimulation. All glow curves were measured in same aliquot. * represents TL measurement in blue and BUV window. All these measurements were carried out under nitrogen environment.

and blue window were observed using the protocol mentioned in Fig. 4.5a. The TL (500°C) glow curves were recorded in the BUUV and blue window after irradiation, preheat, and violet stimulation. The same procedure was repeated without violet stimulation. Fig. 4.5b and c compare the results of pVTL intensity in broad-UV and blue detection windows.

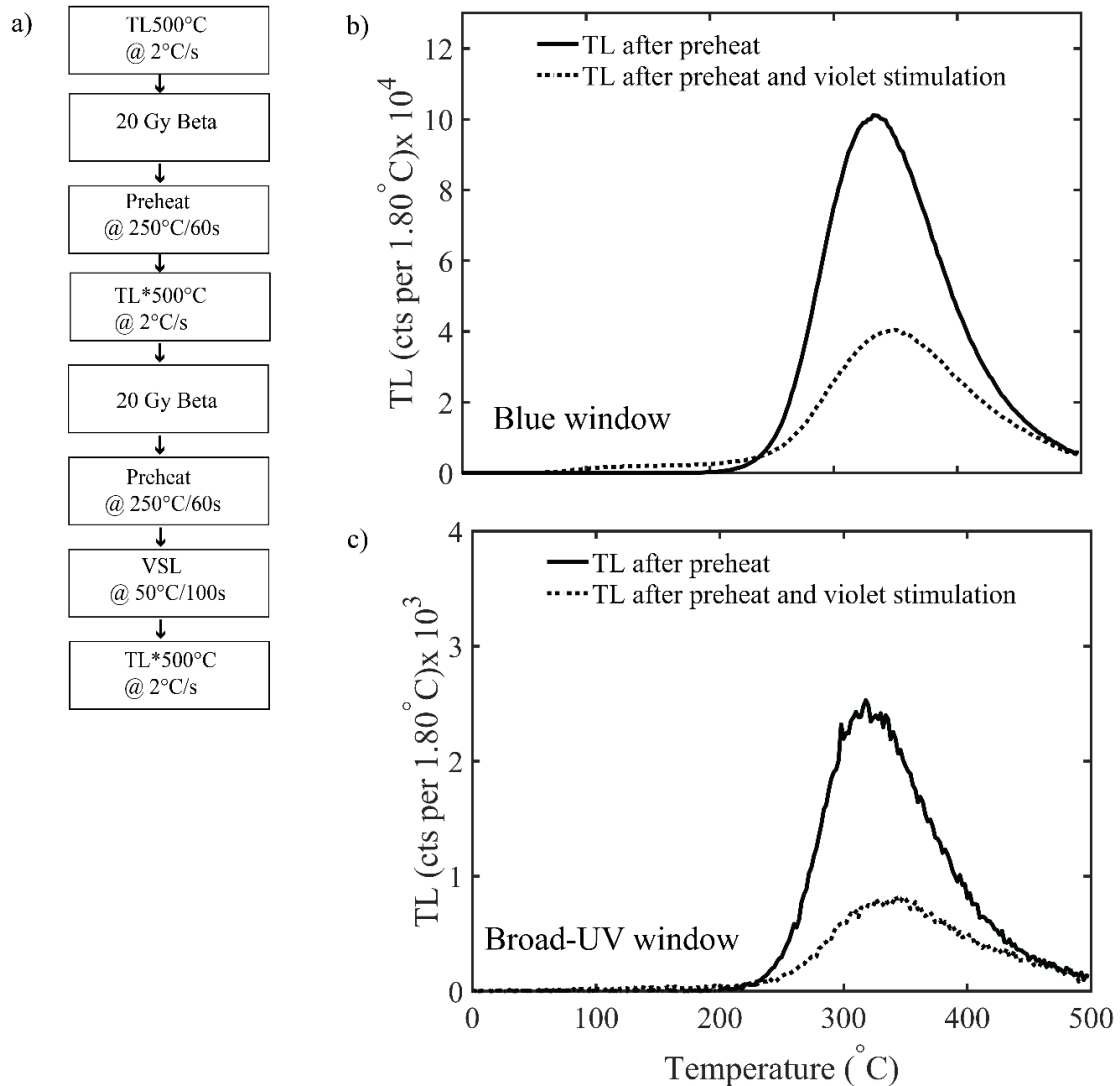


Fig. 4.6: a) Measurement protocol to record decay curves in IRSL, GSL, and BSL after violet stimulation. * and \$ represent detection in blue and BUUV, respectively. b) The post violet - IR, - green, and -blue stimulated decay curves in the blue and BUUV detection window. The stimulation treatments and detection window are mentioned in the legend as (simulation (detection window)). c) Measurements carried out to explore the IRSL emissions after the repeated violet stimulation without any additional dose. d) IRSL signal obtained after repetitive violet light stimulation. The IRSL signal intensity is obtained by subtracting the last 2 s signal from the initial 2 s.

The TL in a blue window is approximately two orders of magnitudes higher than centres emitting in the BUV window. During violet stimulation, about 80% of centres emitting in both broad-UV and blue windows were consumed. This resulted in a further reduction of BUV centres (Fig. 4.5b and c), hence a small population of recombination centres emitting in BUV was left after the violet stimulation. For the second experiment, the different stimulations were applied to probe the photo-transferred charges. The pVIRSL signal was observed in both BUV and blue window, whereas the pVGSL and pVBSL were detected

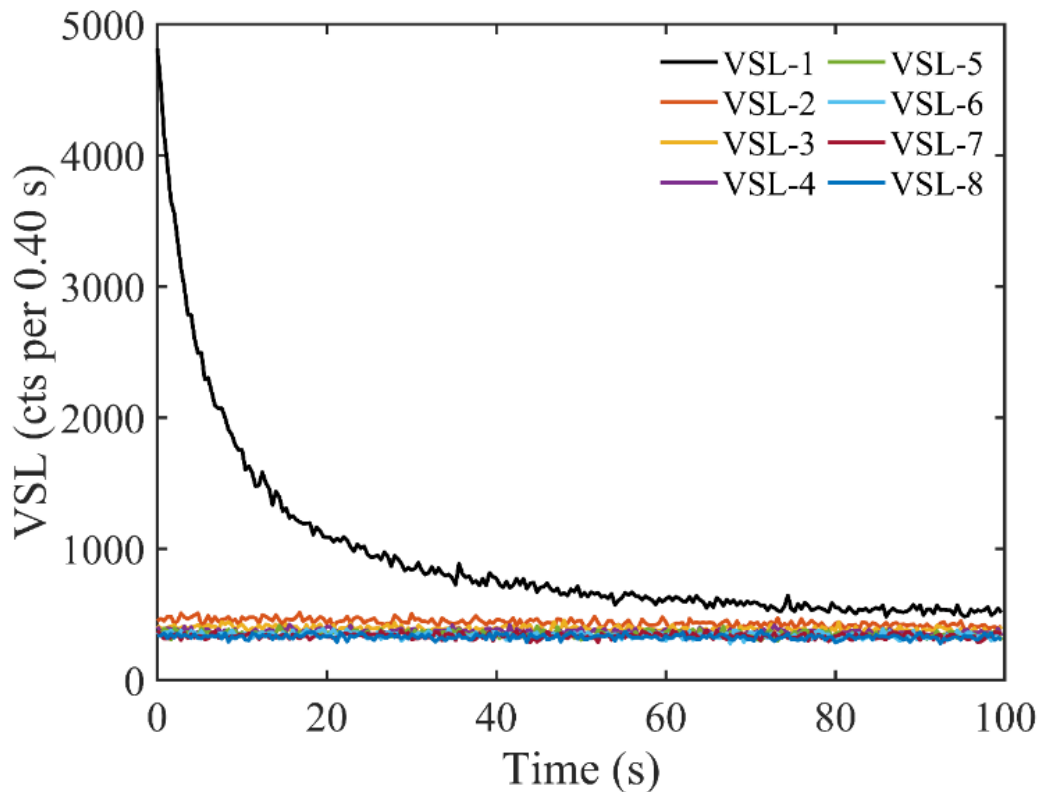


Fig. 4.7: a) VSL signal is only observed for cycle-1. VSL decreases with repeated cycles and a background level was obtained after three cycles.

only in the BUV window because of overlapping transmission with blue window. Fig. 4.6b shows pVIRSL, pVGSL, pVBSL decay curves in the BUV and blue detection window. The luminescence detected in BUV window from all stimulations after violet, i.e., pVIRSL, pVGSL, and pVBSL, were near the background. This observation was supported by results shown in Fig. 4.5b that all the recombination centres in the BUV window were consumed during violet stimulation. Therefore, further measurements were carried out using blue detection window of pVIR stimulation. The pVIRSL detected in the blue detection window yielded a luminescence signal (Fig. 4.6b) as sufficient recombination centres emitting in

the blue window were left after the violet stimulation (Fig. 4.5c). Therefore, any detection made in the BUV window resulted in near background luminescence.

The possibility of photo-transfer of charges by violet stimulation to IR light sensitive traps was also examined using the protocol in Fig. 4.6c. The IRSL was measured after the violet stimulation repeatedly for eight times without any intervening radiation dose. In each cycles, IRSL was followed by another IR treatment, to check that IRSL signal has reached to the background level. The results of this experiment are shown in Fig. 4.6d. Over 20% IRSL following repeated violet stimulations and without any intervening radiation dose was seen (Fig. 4.6d). At the end of each violet and IR stimulation, the IRSL was reduced to the background level as it can be seen from Fig. 4.6d. Repeated pVIRSL followed a trend similar to repeated pVTL i.e., the IRSL signal intensity decreased with repetitive cycles to an asymptotic value of about 20% of their initial value. VSL decay curves after each repeated cycle are also shown in Fig. 4.7 and it can be seen that after the third cycle, VSL residual was near background levels. These results are also supported by the above observation, shown in Fig. 4.5b that recombination centres emitting in the narrow-UV window get consumed during the violet stimulation. The signal in IRSL after repeated cycles of violet stimulation indicates that electrons from deep reservoir traps were still being photo-transferred to IR traps (Fig. 4.6d).

4.4.1.2 Source of post violet IRSL (pVIRSL) signal

As shown in Fig. 4.3c, the pVTL glow curve comprised TL glow peaks at 130 and 380 °C. Relation between pVTL and pVIRSL was examined through violet stimulation at increasing stimulation temperatures and cut-heats. The measurement protocol is shown in Fig. 4.8a. IRSL at 50 °C was measured after each violet stimulation and cut heat. The IRSL intensities were normalised to the IRSL after preheat, violet stimulation, and a cut-heat, both at 50 °C. The sample was monitored for any sensitivity change by repeating first measurement step after all cycles, and no sensitivity change was observed. Fig. 4.8c provides normalized IRSL with increasing cut-heats after a violet exposure. The pVIRSL decreased by about 20% from 50 °C to 100 °C, followed by an increase of 15% up to 250 °C violet stimulation and cut-heat. At cut heat of 500 °C, it reached 0.3% of the initial (Fig. 7c). The initial decrease (up to 100 °C) is possibly due to decrease in phosphorescence from glow peaks below 130 °C. An increase in IRSL up to 250 °C temperature of violet stimulation and cut-heat suggests the increased photo-transfer of charges to IR traps during

the violet stimulation. It can be seen from Fig. 4.9 that the slow component of the VSL decay curve increases with stimulation temperature due to an increase in thermal assistance at high temperatures. Consequently, charges recaptured in IRSL traps increase and lead to higher IRSL. Stimulation temperatures greater than 250 °C start depleting TL peaks sensitive to IR light, leading to a decrease in IRSL (Fig. 4.8c).

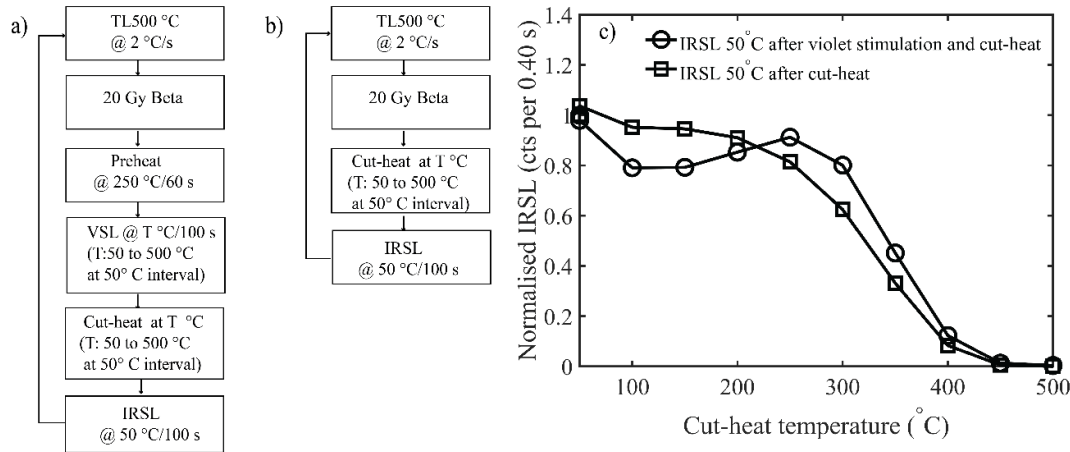


Fig. 4.8: a) Sequence used to explore the origin of IRSL signal after the violet stimulation of KF sample. The temperature of both violet stimulation and cut-heat was varied simultaneously. b) Measurements carried out to explore the origin of IRSL signal. Both a) and b) sequences are performed on the same and single aliquot. c) Variation of IRSL and pVIRSL with different cut-heat and violet stimulation temperatures. The IRSL is obtained by subtracting the last 2 s background from initial 2 s signal. IRSL signal was normalised with respect to its maximum value. To test any sensitivity change, data for IR 50 °C after all measurements is also presented.

For reference, the variation of conventional IRSL with varying cut-heat temperatures was also explored using the protocol in Fig. 4.8b. The variation of normalised IRSL with cut-heat temperatures is shown in Fig. 4.8c. IRSL shows a very gradual decrease (~10%) up to the cut-heat of 100 °C and nearly constant up to 200 °C. A faster decrease thereafter up to 500 °C and reduces to 0.01% of the initial value at 500 °C. Most of the decrease in the IRSL occurs between 250 and 400 °C, indicating that it is more associated with a broad TL peak at 300 to 350 °C, which is consistent with the observation from Li and Li (2011). A rapid decrease of IRSL with increasing cut-heats and violet stimulation temperature after 250 °C suggests the depletion of charges during thermal treatment that provides IRSL.

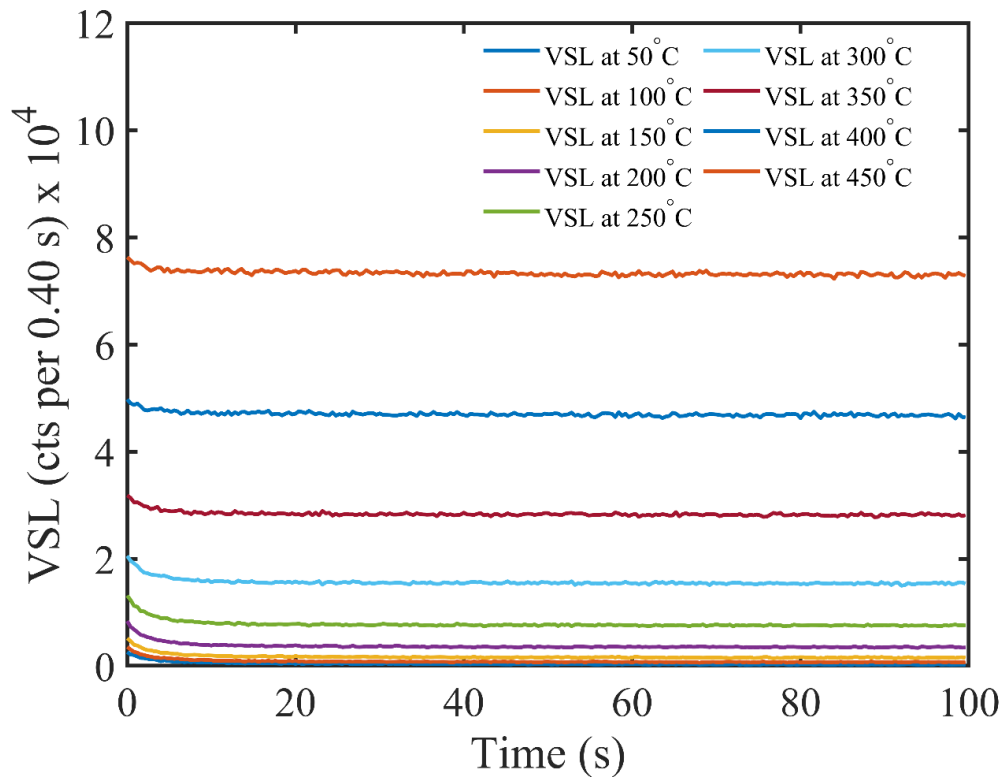


Fig. 4.9: Variation of VSL decay curves with increase in stimulation temperature after 20 Gy dose and preheat of 250 °C for 60 s for KF sample.

4.4.2 Mechanism for pVIRSL

Fig. 4.3c suggests that TL glow peaks < 500 °C are populated through photo-transfer of charges from deep traps (peaks > 500 °C) during a violet stimulation. These photo-transferred charges were detected in the blue window as recombination centres emitting in broad-UV were depleted during violet stimulation (Fig. 4.5c). Since only IR stimulation can be detected in the blue window. Therefore, only post violet IR stimulation, detected in blue window yielded the luminescence from photo-transferred charges. The continuous supply of charges observed in TL and IRSL after repeated violet stimulation suggests that violet stimulation repopulates the IR traps each time. The efficiency of photo-transferred charges progressively diminishes with each cycle, reaching an asymptotic value of approximately 20% of initial pVIRSL signal (Fig. 4.6d). Based on Kalita and Chithambo (2022), Jain and Ankjærgaard (2011), Kumar et al. (2020), and the present observations, a possible mechanism for pVIRSL is that charges in deep reservoir traps are stimulated to the conduction band by violet stimulation, and a fraction of these are trapped at IR traps and give pVIRSL. Fortuitously, dose proportionality is retained in this complex process.

Fig. 4.10 summarizes the mechanism of pVIRSL and a band model modified after Jain et al. (2011). Transition-1 is the excitation of charges during violet stimulation, where charges from all traps get excited to the conduction band, some of the charges are recaptured at the IR trap, and others produce VSL. Subsequently, IR stimulation (Transition-2) probes the recaptured charges and provides pVIRSL. As the fading measurements were made without any delay of IRSL after violet stimulation, therefore, post violet IRSL yields a near zero fading (Devi et al., 2022). Violet stimulation also empties charges from IR traps acquired during geological antiquity and ensures that pVIRSL resulted from photo-bleached charges in the IR traps.

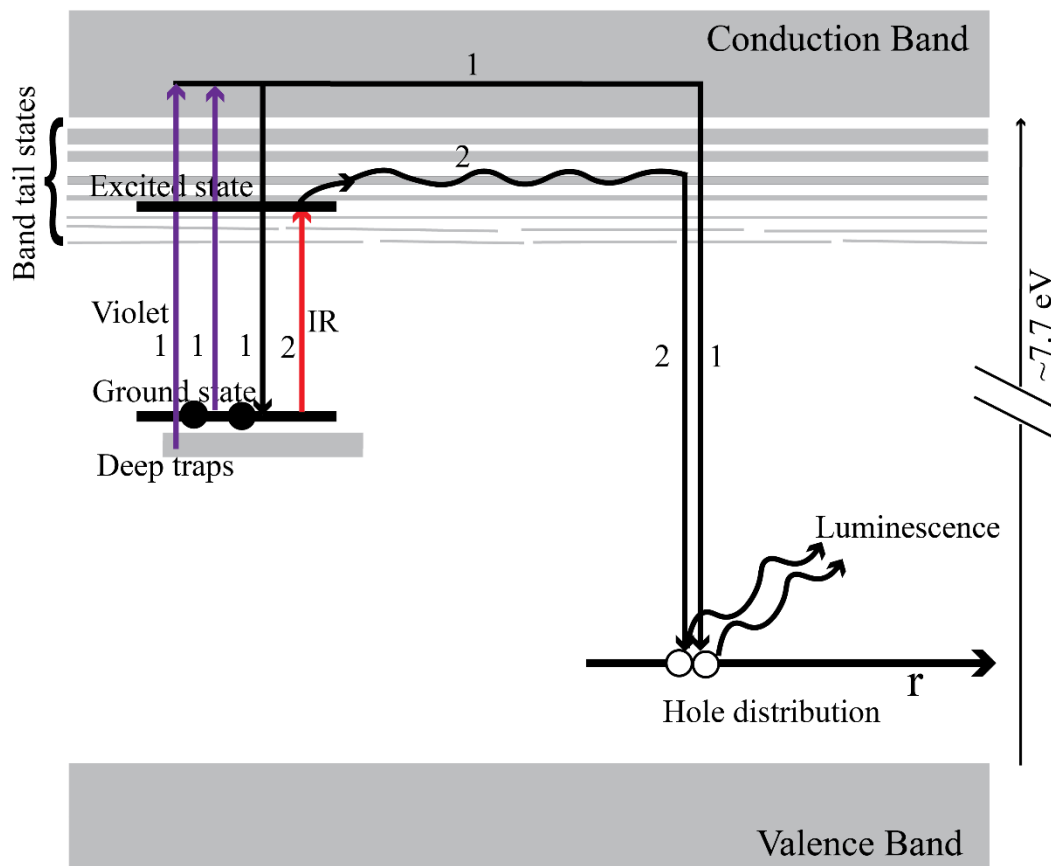


Fig. 4.10: Band model for post violet IRSL signal (modified after Jain et al., 2011). Transition-1 represents the excitation, recombination, and recapture pathway of violet stimulation. Electrons from deep reservoir traps are excited using violet stimulation. The excited electrons go to the conduction band, and some are recaptured to the unoccupied states of the principal trap. These recaptured charges are further probed using IR stimulation (Transition-2) and resulted in pVIRSL in the blue window. (For interpretation of the references to colour in this figure legend, the reader is referred to the Web version of this article.)

4.4.3 Dating using pVIRSL

To assess the suitability of pVIRSL for geochronology, factors such as athermal fading rates, bleachability under daylight, recuperation, recycling, and dose recovery ratio were measured, and the results are discussed below:

4.4.3.1 Bleachability of the deep traps

Luminescence dating relies on a light-bleachable signal, enabling the resetting of its luminescence signal through light exposure facilitating the estimation of age of the event associated with the most recent resetting. Bleachability of pVIRSL by daylight was tested on surface sediment (DH-1) from modern dune sand using the protocol in Table 4.3, Protocol B. The details of the protocol used are discussed later in section 4.5. The average pVIR-SAR dose for a modern desert dune DH1 sample is 0.09 ± 0.14 Gy ($n = 10$), which is near zero. The results suggest that pVIRSL signal has effectively bleached by natural daylight exposure and hence, the signal holds potential for dating the resetting events. Further, to develop a SAR protocol for equivalent dose estimation in the laboratory, a signal should also be bleachable under laboratory conditions to mimic natural daylight bleaching. Given that during SAR measurements, a sample undergoes multiple cycles of irradiation and bleaching, it is important that the carryover of pVIRSL from one SAR cycle to the next is minimal. But as it can be seen from Fig. 4.6d, even after eight repeated cycles of violet

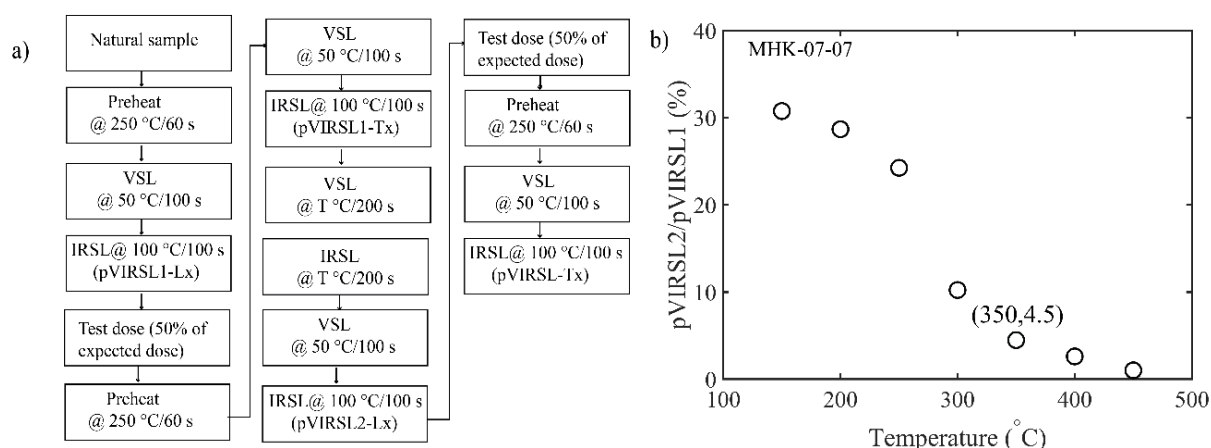


Fig. 4.11: a) Measurement protocol to test the bleachability of pVIRSL signal in the reader at the variable temperature of violet and IR stimulation (bleaching step). b) Percentage of residual pVIRSL signal ($pVIRSL2/pVIRSL1$; test dose normalised) at variable elevated temperature of violet and IR bleaching for MHK-07-07 sample. Each data point represents a single aliquot with natural dose. At illumination temperature 350 °C, the residual pVIRSL signal is 4.5%.

and IR stimulation, still 20% of the charges are left from the deep reservoir traps. Therefore, the bleachability of the pVIRSL signal was explored in the TL/OSL reader. The measurement protocol used is provided Fig. 4.11a. The bleaching steps contains both violet and IR stimulation for 200 s at variable temperatures ranging from 150 to 450 °C. The pVIRSL signal measured prior to bleaching is denoted as pVIRSL1, while pVIRSL measured subsequent to bleaching is represented as pVIRSL2. The ratio of pVIRSL2/pVIRSL1 measures the residual pVIRSL after the reader bleaching at temperatures in the range of 150 to 450 °C, and results are shown in Fig. 4.11b. The ratio of pVIRSL2/pVIRSL1 decreases with violet and IR stimulation at increasing temperatures. Bleaching at 350 °C for 200 s reduces the residual signal to 4.5% of the initial value, and hence, in the SAR protocol, 350 °C was used to bleach pVIRSL at the end of each dose measurement cycle.

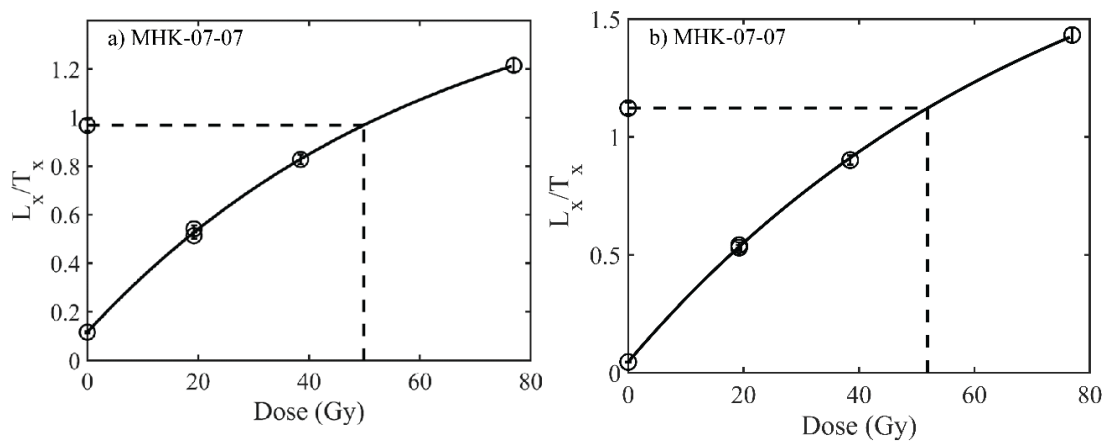


Fig. 4.12: a) DRC constructed using pVIR-SAR protocol (Table 4.3, Protocol A) for MHK-07-07 sample. The D_e , recycling ratio and recuperation are 50 ± 2 Gy, 1.06 ± 0.04 , and $12.0 \pm 0.5\%$, respectively. b) DRC constructed using pVIR-SAR protocol (Table 3, Protocol B) for the MHK-07-07 sample. The D_e , recycling ratio and recuperation are 52 ± 2 Gy, 1.02 ± 0.03 , and $4.1 \pm 0.1\%$, respectively.

Based on the foregoing, a regeneration protocol for the pVIRSL was explored (Table 4.3, Protocol A). This differs from the SAR protocol of Murray and Wintle (2000) in respect of stimulations and bleaching steps (steps 3, 4, 7, 8, 9, and 10). In the present work, two step stimulation (violet (50 °C, 100 s) and IR (100 °C, 100 s)) and bleaching (violet (350 °C, 200 s) and IR (350 °C, 200 s)) were used. A preheat of 250 °C for 60 s was used after each irradiation based on preheat plateau (Fig. 4.13b). The dose response curve (DRC) for an aliquot of MHK-07-07 gave a recycling ratio of 1.06 ± 0.04 and the equivalent dose for this

DRC is 50 ± 2 Gy (Fig. 4.12a) concurred with the expected K-feldspar dose of 56 ± 7 Gy. This, however, gave a recuperation of 12%, ideally, it should be less than 5% (Murray and Wintle, 2000). Bleaching temperature above 350 °C reduced the recuperation, and but it was set at 350 °C temperature to avoid sensitivity changes due to heat. Therefore, further optimization on the stimulation temperature of IR following a violet bleach, preheat temperature, and test dose were made. All optimization measurements were made on MHK-07-07, having an equivalent dose of 56 ± 7 Gy. The dose response of pVIRSL was explored for optimized parameters, and their applicability was further explored on all natural samples mentioned in Table 4.1.

Table 4.3: Parameters for preliminary pVIR-SAR protocol (A). Parameters for optimized pVIR-SAR protocol (B) for the equivalent dose estimation. The text in bold are optimized parameters.

Step	Protocol (A)	Protocol (B)	Remarks
1.	Natural signal	Natural signal	
2.	Preheat (250 °C for 60 s)	Preheat (250 °C, 60 s)	Remove unstable signal
3.	VSL (50 °C, 100 s)	VSL (50 °C, 100 s)	
4.	IRSL (100 °C, 100 s)	IRSL (200 °C, 100 s)	L_n, L_x
5.	Test Dose (10-20% of D_e)	Test Dose (50-80% of D_e)	
6.	Preheat (250 °C, 60 s)	Preheat (250 °C, 60 s)	Remove unstable signal
7.	VSL (50 °C, 100 s)	VSL (50 °C, 100 s)	
8.	IRSL (100 °C, 100 s)	IRSL (200 °C, 100 s)	T_n, T_x
9.	VSL (350 °C, 200 s)	VSL (350 °C, 200 s)	Illumination
10.	IRSL (350 °C, 200 s)	IRSL (350 °C, 200 s)	Illumination
11.	Give dose and return to step 2	Give dose and return to step 2	

4.4.3.2 Stimulation temperature for IRSL

Murray and Wintle (2000) suggested that higher stimulation temperatures reduce recuperation. Therefore, in the present study, the recuperation of the DRC was observed by increasing the stimulation temperature of pVIRSL from 100 to 200 °C (step-4, 8; Table 4.3, Protocol A). The results are shown in Fig. 4.13a. The recuperation reduced from 12% to 4% for IR stimulation temperature from 100 to 200 °C for the MHK-07-07 sample. DRC of the sample for post violet IRSL at 200 °C is shown in Fig. 4.12b. A recycling ratio of 1.02 ± 0.03 and recuperation of $4.1 \pm 0.1\%$ was obtained. Thus, IR stimulation at 200 °C was used for equivalent dose estimations of other samples used in the study.

4.4.3.3 Preheat temperature

Due to the different thermal stability of traps for younger and older samples, the preheat temperature could differ for different samples (Roberts, 2012). The suitable temperature for preheating the sample can be tested using the preheat plateau test (Murray and Roberts, 1998; Murray and Wintle, 2000). For the preheat temperature, preheat plateau test was carried out on a natural dose of PRL2 sample. The natural dose of the sample was measured at variable preheat temperatures ranging from 200 to 340 °C. The D_e values estimated using pVIRSL signal exhibited plateau between 220-260 °C for the PRL2 sample, where D_e values varied within $\pm 5\%$ (Fig. 4.13b). A uniform preheat of 250 °C for 60 s was therefore used for all the samples.

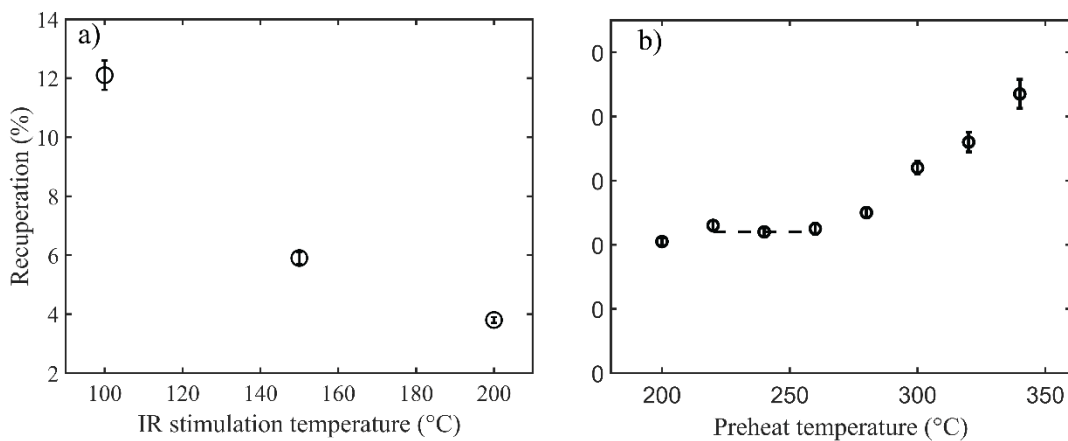


Fig. 4.13: a) Variation of recuperation for pVIR-SAR with IRSL stimulation temperature of the MHK-07-07 sample. Recuperation is $<5\%$ for pVIRSL at 200 °C. b) D_e plateau with preheat temperature for PRL2 sample. Here, D_e at each preheat temperature is the mean of three aliquots. All D_e values fall within $\pm 5\%$ of each other in the preheat temperature range of 220 to 260 °C.

4.4.3.4 Optimization of the test dose

Colarossi et al. (2018) reported that the magnitude of the test dose during pIRIR-SAR influences the growth curve. Lower test doses ($<15\%$ of equivalent dose) led to the carryover of charges from the regeneration doses into test dose luminescence (T_x) and resulted in an early saturation of DRC. Higher test doses suppressed the carryover of charges to the next dose and increased the saturation dose of DRC, making it possible to date the older samples. Therefore, these authors recommended using test doses in the range of 15-80% of D_e . In the present study, the dependence of D_e on the test dose was explored on MHK-07-07 and RTP-18-02 samples.

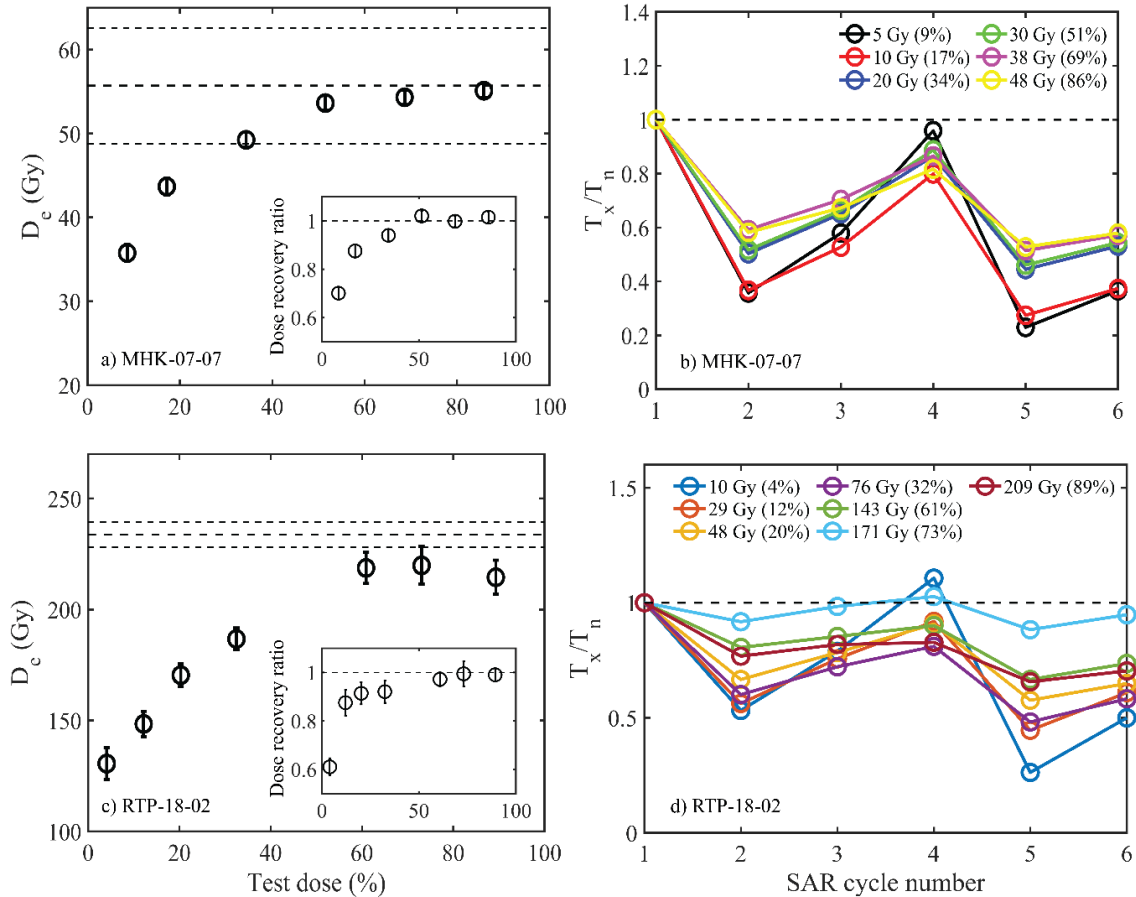


Fig. 4.14: Test dose dependency of dose for MHK-07-07 (a, b) and RTP-18-02 (c, d). At each test dose, D_e is an average of at least three aliquots. Test doses were varied from approximately 5 to 90% of the expected dose. Dose recovery ratios at variable test doses for MHK-07-07 and RTP-18-02 samples are shown in the inset of (a) and (c).

Fig. 4.14a and c suggest that test doses less than 50% of the expected dose underestimate D_e , and test doses exceeding 50% of the anticipated D_e , lead to equivalent doses closer to the expected doses. Fig. 4.14b and d plot the variation T_x/T_n with SAR cycles with test doses for pVIR-SAR and show that T_x follows L_x . This indicates that T_x depends on L_x from the corresponding regeneration dose. Variation in T_x/T_n reduced from 76% to 47% when the test doses changed from 9% to 86% of the expected dose for MHK-07-07. For RTP-18-02, variation reduced from 76 to 25% for a change in test dose from 4 to 89% of the expected dose. The change in T_x/T_n is higher for low test doses, whereas for high test doses, T_x and T_n covaries, suggesting that carryover of charges during high test dose luminescence gets suppressed. Therefore, test doses ranging from 50 to 80% of the expected doses were used. Dose recovery tests also depend on the test dose. A known dose approximately equal to the expected dose was recovered using varied test doses. Inset in

Fig. 4.14a and c shows that dose recovery ratios were less than unity for test doses < 50% of the expected dose and near unity for test doses > 50% for both samples. Therefore, it is desirable to establish the test dose a priori before proceeding with dating analysis. The laboratory saturation doses ($2D_0$) of DRC was also depended on the value of test dose and ranged from 56 Gy to 300 Gy and from 148 Gy to 606 Gy for two independent samples (Table 4.5). These results accord with Colarossi et al. (2018).

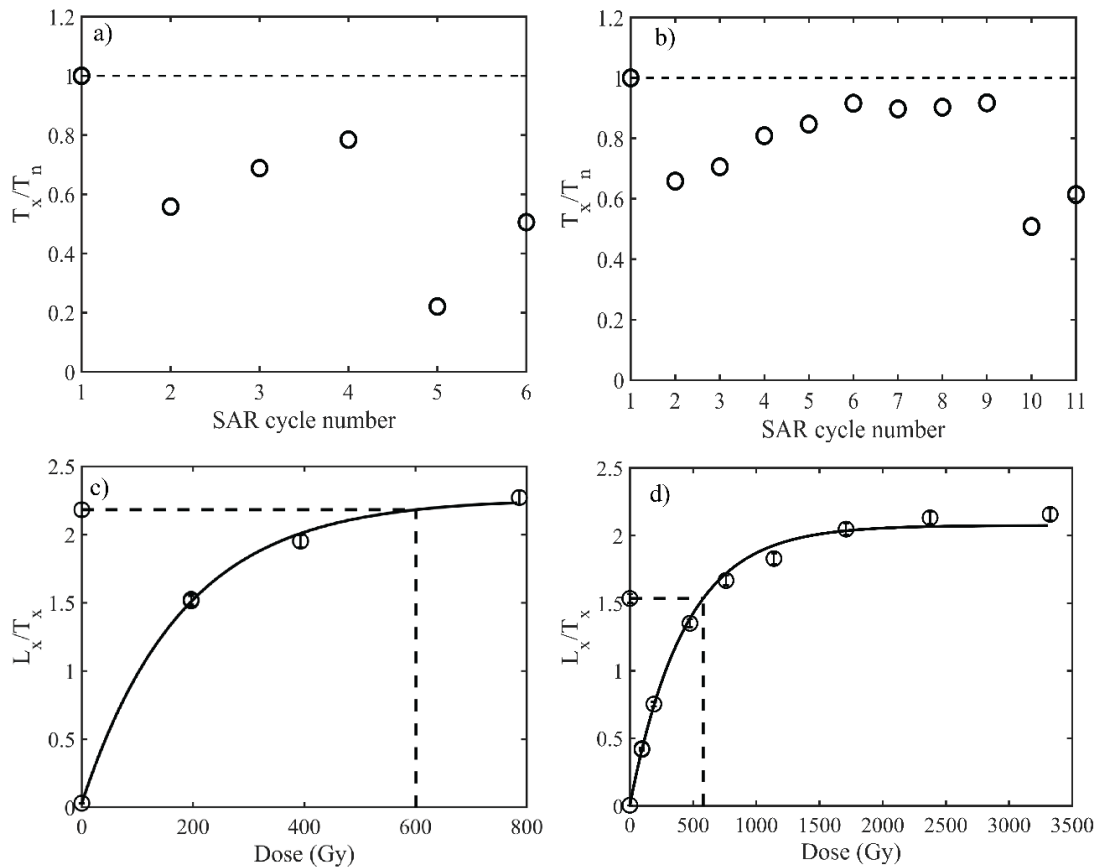


Fig. 4.15: T_x/T_n ratio and DRC for low (~15% of expected dose) and high (~55% of expected dose) test doses of HMP-18-5: a) The ratio of test dose signal from regenerative to natural doses recorded during construction of the DRC for low test doses. b) The ratio of test dose signal from regenerative to natural doses recorded for high test doses. c) DRC constructed at low test doses. The natural normalised intensity lies in the saturation region. d) DRC constructed at high test doses. The natural normalised intensity lies below the saturation region, and the obtained D_e is 580 ± 29 Gy.

For HMP-18-5, the estimated D_e was in saturation for low test doses (i.e., < 20% of the expected dose) (Fig. 4.15c), and at higher test doses (~55% of the expected dose), it was below saturation, and the estimated dose was 580 ± 29 Gy (Fig. 4.15d). Variation of T_x/T_n

reduced from 72 to 45% for test doses ranging from 15 to 55% of the expected dose (Fig. 4.15a, b). These results indicate that variation of D_e with test dose is sample dependent.

Table 4.4: Variation of saturation dose ($2D_0$) with test dose (% of expected doses) for pVIR-SAR protocol for MHK-07-07 and RTP-18-02 sample.

MHK-07-07		RTP-18-02	
Test dose (%)	Saturation dose (Gy)	Test dose (%)	Saturation dose (Gy)
9	56 ± 2	4	148 ± 9
17	85 ± 4	12	256 ± 16
34	142 ± 9	20	336 ± 21
51	162 ± 12	32	357 ± 22
69	227 ± 21	61	431 ± 29
86	300 ± 36	73	552 ± 15
		89	606 ± 23

4.5 pVIRSL Single Aliquot Regenerative Dose (pVIR-SAR) Protocol

Suggested pVIRSL Single Aliquot Regenerative Dose (pVIR-SAR) protocol is shown in Table 4.3, Protocol B. Test dose within 50 to 80% of anticipated D_e was used (step-5). Preheat of 250 °C for 60 s, and optimized pVIRSL at 200 °C (step-4 and -8) was used for D_e estimations. The bleaching step includes both violet and IR stimulation at 350 °C for 200 s (step-9 and -10). Monitoring recuperation and reliability of the sensitivity-corrected signal is ensured through a zero dose and recycling dose during the construction of DRC. These steps are crucial to check the reliability of the obtained D_e values pVIR-SAR protocol. The results are discussed below:

4.5.1 Repeatability and sensitivity changes

The fundamental assumption of the SAR protocol relies on the ability to obtain a signal after each dose and stimulation sequence that serves as a substitute measurement for the sensitivity observed during the preceding measurement cycle. This capability enables the correction of sensitivity variations in both natural and regenerated signals. Change in sensitivity during repeated measurement cycles was investigated through a correlation between regenerative dose (L_x) and test dose luminescence (T_x) after laboratory bleach using sequential stimulation by violet and IR at 350 °C for 200 s. This bleaching was carried out at the end of one cycle of L_x and T_x measurement. A regeneration dose of ~530 Gy and a test dose of ~350 Gy was used on RSN-01-17. The reproducibility of sensitivity corrected pVIRSL signal was tested using this protocol for cycles of

sixteen repeated measurements (Table 4.4). The initial 2 s of pVIRSL decay curves were taken as the signal, and the final 2 s were background.

Table 4.5: Protocol used to explore the L_x and T_x correlation for the RSN-01-17 sample. * represents the doses given to RSN-01-17.

Steps	Protocol
1	Reader bleaching (VSL and IRSL @ 350 °C for 200 s at 70 % power)
2	Dose* (~530 Gy)
3	Preheat @250 °C for 60 s
4	VSL @50 °C for 100 s
5	IRSL @200 °C for 100 s
6	Test dose* (~350 Gy)
7	Preheat @250 °C for 60 s
8	VSL @50 °C for 100 s
9	IRSL @200 °C for 100 s
10	VSL @ 350 °C for 200 s
11	IRSL @ 350 °C for 200 s
12	Return to step 2 (Repeat up to 15 cycles)

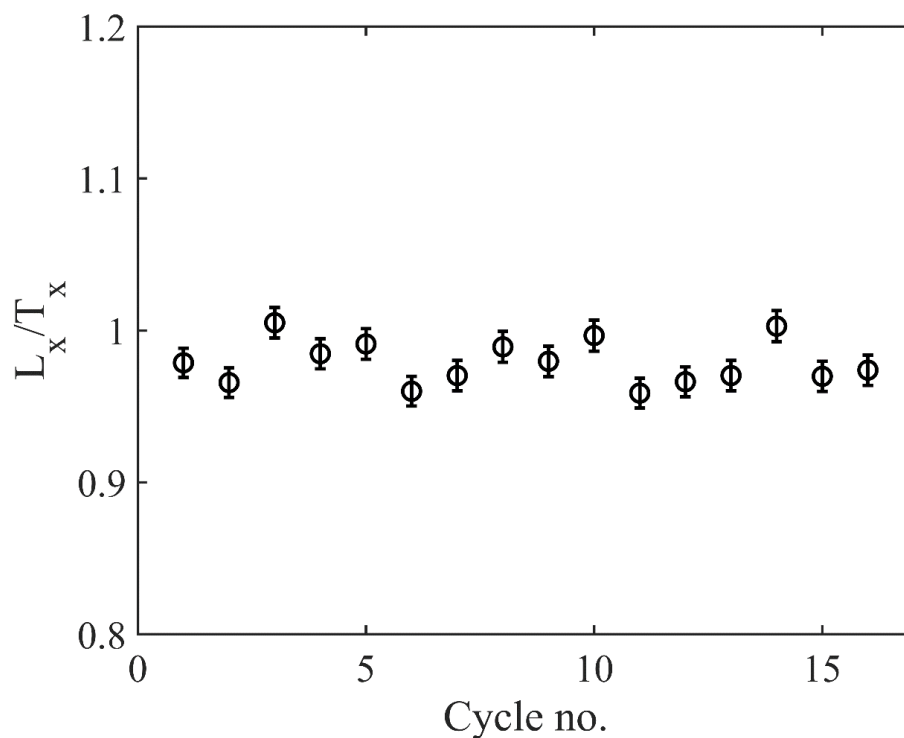


Fig. 4.16: a) Ratio of regeneration dose net pVIRSL signal (L_x : initial signal minus background) to test dose signal (T_x : initial signal minus background) is plotted against measurement cycle number for the RSN-01-17.

Fig. 4.16 plots L_x/T_x values for 16 repeated cycles for RSN-01-17. The L_x/T_x mean is 1.01 ± 0.05 and suggests that pVIRSL is reproducible and that the test dose faithfully corrects for sensitivity changes during the measurements. Fig. 4.16 also suggests that the regenerated pVIRSL (L_x) for a constant dose (~ 530 Gy) corrected by a test dose (T_x) (~ 350 Gy) remains unchanged.

4.5.2 Residual doses of the pVIRSL

The rate of bleaching of pVIRSL was explored under both daylight and filtered sun-lamp for exposures ranging from 0 to 300 min and 0 to 1200 min, respectively. The normalised pVIRSL residual doses estimated for MHK-07-07 sample for different bleaching times are shown in Fig. 4.17. The residual levels are at 11% after ~ 60 min and at 15% after ~ 100 min under natural daylight and filtered sun-lamp, respectively.

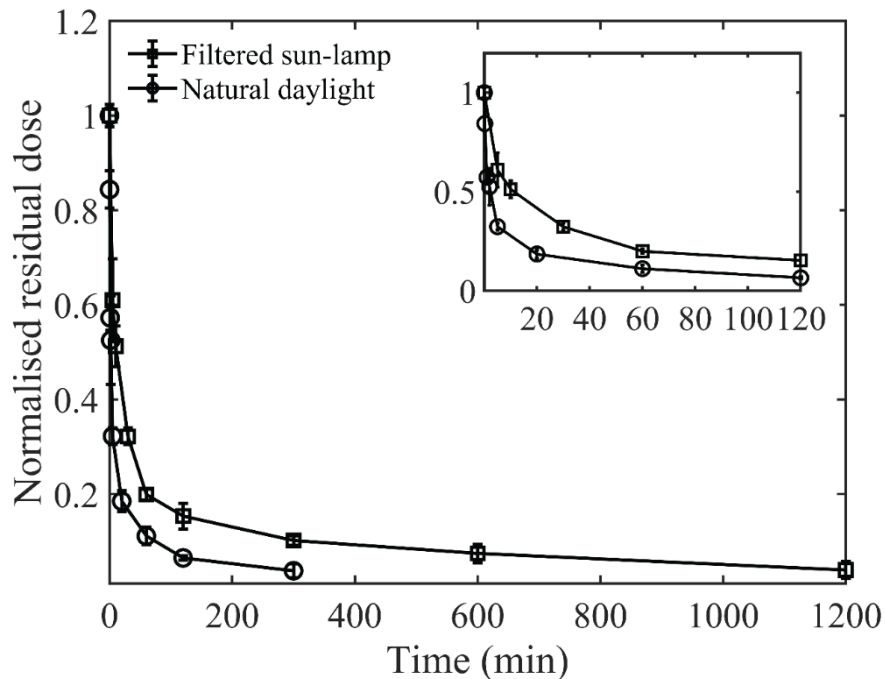


Fig. 4.17: Bleaching curves for a MHK-07-07 sample under UV filtered sun-lamp light and natural daylight exposure. Each point is an average of three aliquots. The pVIRSL signal reaches the residual level in ~ 60 min and ~ 100 min under daylight and solar lamp light exposure, respectively. For clarity data for the initial two hours is shown in the inset.

Further, the residual doses of pVIR-SAR protocol for all samples were measured after five hours of filtered sun-lamp exposure. The residual doses were measured on five aliquots from each sample and are given in Table 4.7. The mean of five residual doses for each

sample ranged from 4.4 ± 0.2 to 21 ± 1 Gy for pVIR-SAR protocol. Whereas the residual doses for pIRIR-SAR ranged from 10 ± 1 to 43 ± 8 Gy (Table 4.8). The pVIR-SAR residual doses were 23 to 67% lower than the pIRIR-SAR, suggesting that pVIR-SAR protocol may provide a better option for young samples. The residual doses were subtracted from D_e values.

4.5.3 Dose recovery

To ensure that pVIRSL signal provides reliable dose estimates, the dose recovery test was conducted (Wallinga et al., 2000). The dose recovery ratio examines the ability to accurately recover the known irradiation dose from the luminescence signal. For dose recovery test, a known dose approximately equal to equivalent dose was given after the five hour filtered sun-lamp bleaching. The given doses were recovered using a pVIR-SAR protocol. Five aliquots per sample were measured for the dose recovery test. The residual doses subtracted recovered doses were used for the dose recovery ratios. The acceptance criterion set for this test was within $\pm 10\%$ (Murray and Wintle, 2000). The dose recovery ratio for pVIR-SAR ranges between 0.96 and 1.08 and lie within the acceptable criterion of SAR protocol (Table 4.7). However, the dose recovery ratios for pIRIR on the same set of samples ranged from 0.95 to 1.42 (Table 4.8). These results indicate that dose ratios of pIRIR-SAR are higher than the accepted criteria, similar results were also reported by previous studies (Li and Li, 2014 and references therein).

4.5.4 Athermal stability of the pVIRSL

As shown in Chapter 3, the pVIRSL at 100 °C results from the stable charges and results in near zero fading in feldspar. Similarly, athermal fading rates of optimized pVIRSL at 200 °C were also explored for the samples used in the present study. All fading measurements were carried out using the protocol mentioned in Fig. 3.3b. The samples were bleached under a filtered sun-lamp for five hours. A known dose approximately equal to the expected equivalent dose was administered. A delay of 1 to 8 days was provided after preheating of 250 °C for 60 s to estimate the fading rates (Auclair et al., 2003; Huntley and Lamothe, 2001). The t_c value used was two days. Most samples returned near zero athermal fading rates ($g \leq 0.5$ % per decade, $n=15$) as shown in Fig. 4.18 and in Table 4.7. However, sample PRL0 and MHD-02-17 returned a g -value of 1.9 ± 0.1 and $2.9 \pm 0.3\%$ per decade, and these would need further investigations.

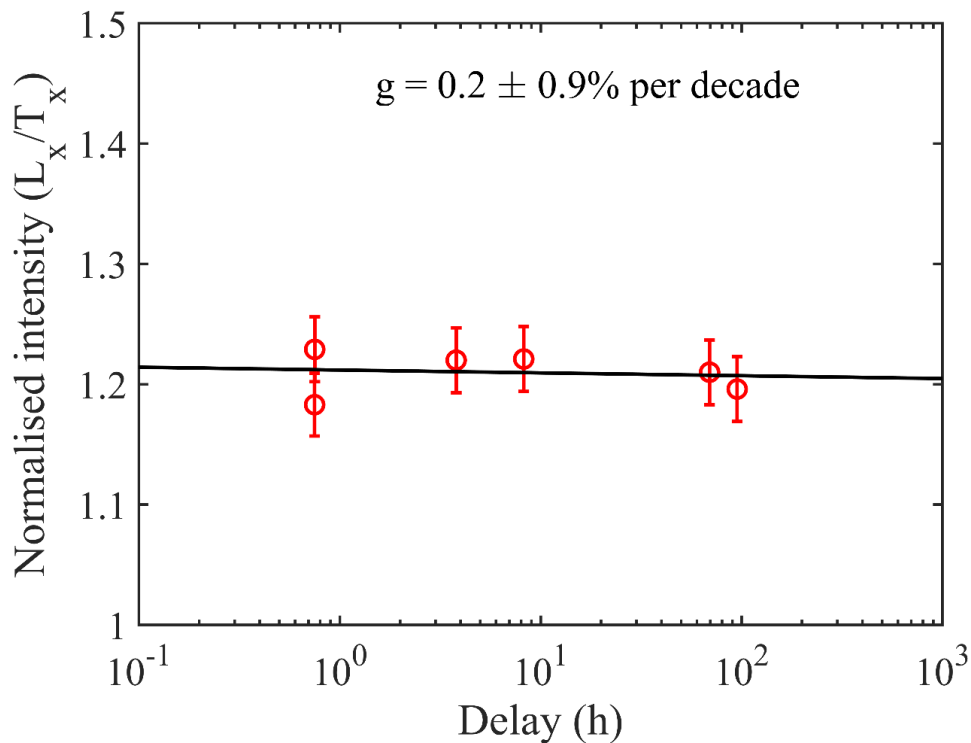


Fig. 4.18: Fading rate [g (% per decade)] results for RSN-01-17 sample for pVIRSL at 200 °C.

4.5.5 Saturation dose

The saturation dose refers to the maximum dateable limit of luminescence dosimetry of particular signal and is the amount of ionizing radiation that a mineral can accumulate in its traps. It is generally considered as dose corresponding to the 86% of maximum normalised intensity in the DRC. For the estimation of laboratory saturation doses ($2D_0$) for pVIR-SAR, DRCs for regeneration dose up to 3500 Gy were constructed. A single saturating exponential function was used for DRC fitting. The pVIR-SAR saturation doses of the samples ranged from 295 to 970 Gy (Table 4.6). The best case example of MHD-01-17 had $2D_0$ of ~1000 Gy, recycling ratio of 1.00 ± 0.05 , and a recuperation of $2.6 \pm 0.1\%$, respectively (Fig. 4.19). A dose rate of 3.35 ± 0.15 Gy/ka implies an age of 300 ka.

4.5.6 Comparison with expected ages

The above results confirmed that the pVIR stimulation probes the non-fading charges, giving zero laboratory fading rate. Although demonstrating that the pVIR-SAR protocol performs reliably, using tests such as the recycling ratio, recuperation, preheat plateau, and dose recovery tests. The most important test of the reliability of any dating technique is

whether it can yield consistent results when compared with doses for the same sample or context obtained using an existing independent dating protocol: BSL-SAR protocol for quartz (Murray and Wintle, 2000) and pIRIR-SAR (pIRIRSL at 290 °C) protocol for feldspar (Buylaert et al., 2011). The pVIR-SAR equivalent doses were compared with expected values based on BSL-SAR of quartz (converted to the K-feldspar doses) and/or

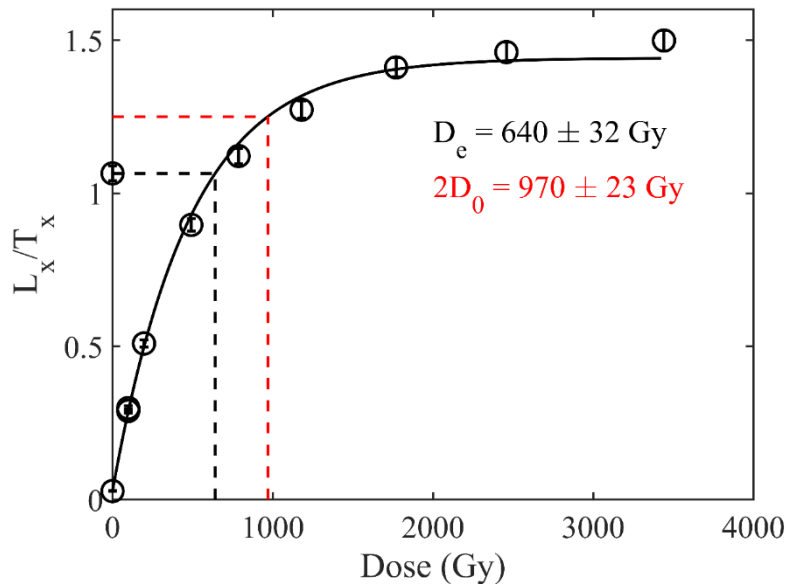


Fig. 4.19: Sensitivity corrected DRC constructed using pVIR-SAR protocol (Table 4.3, Protocol B) for MHD-02-17 sample along with the natural intensity. The single saturating exponential function as in analyst was used for the fitting. The recycling ratio and recuperation are 1.00 ± 0.05 and $2.6 \pm 0.1\%$, respectively. The estimated D_e is 640 ± 32 Gy, and saturation dose ($2D_0$) is 970 ± 23 Gy.

Table 4.6: Saturation doses ($2D_0$) estimated using pVIR-SAR protocol for all samples.

Sample	Test dose used (% of the expected dose)	Saturation dose (Gy)
PRL0	50	295 ± 9
PRL2	50	360 ± 8
MHK-07-07	50	360 ± 7
RTP-18-2	61	552 ± 15
RSN-01-17	74	829 ± 18
HMP-18-5	58	864 ± 18
MHD-02-17	75	972 ± 23

pIRIR-SAR based doses on K-feldspar (Table 4.7). The quartz doses were converted into feldspar doses using the formula: [(feldspar dose rate x quartz dose)/quartz dose rate]. Table 4.7 and Fig. 4.20 compares pVIR-SAR ages with expected ages which are consistent within $\pm 2\sigma$ error. One sample RTP-18-02 has an additional age control from YTT event of around 75 ka. The age of this sample estimated using pVIR-SAR is 69 ± 5 ka, and this accords with expected age of 75 ka (age of YTT).

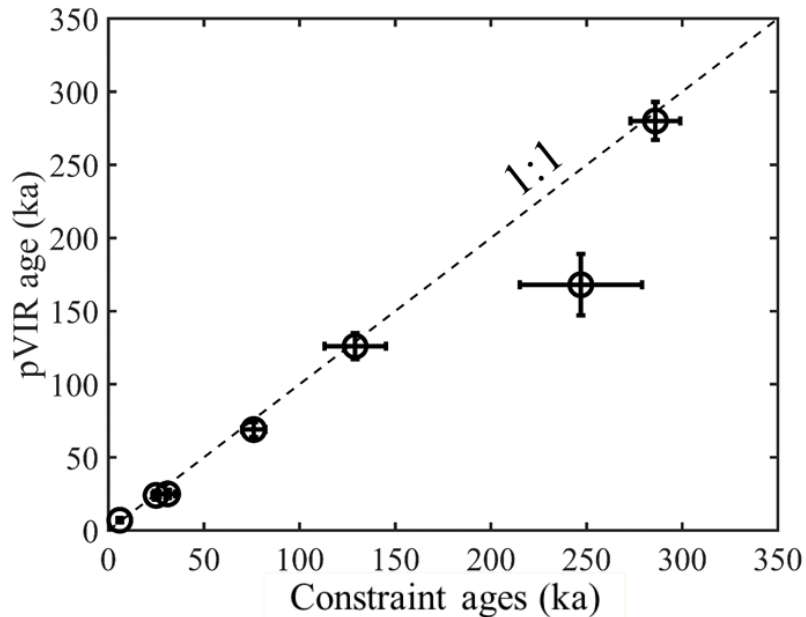


Fig. 4.20: Ages obtained using pVIR-SAR protocol with the ages constraint using BSL-SAR and pIRIR-SAR.

It is interesting to note that for one sample HMP-18-5, the obtained pVIR age was 164 ± 21 ka and the pIRIR age was $>247 \pm 32$ ka. These ages are not consistent and this needs further probing. For MHD-02-17, both the pVIRSL and pIRIRSL gave fading of 2.8 ± 0.3 and $2.7 \pm 0.6\%$ per decade and ages agree with each other, when corrected for fading using Kars and Wallinga (2009). The fading rate of the pIRIRSL signal can be minimized by adjusting the prior-IR stimulation temperature or by employing multiple steps of IR stimulation, as suggested by Li and Li (2011). Nevertheless, for the current study, the pIRIR-SAR protocol outlined in Table 2.3 was utilized. For PRL0, pVIR age was corrected for fading ($g = 1.9 \pm 0.1\%$ per decade) using Huntley and Lamothe (2001) and the ages agree within 2σ error as shown in Table 4.7.

Table 4.7: Estimated D_e , fading value, recuperation, residual dose, and dose recovery ratio for all samples using the optimized pVIR-SAR protocol. Recuperation observed in all the samples is <5% except for PRL0 (young sample) where it is less than 10%. * represents the fading uncorrected feldspar doses and ages, + represents the quartz converted feldspar doses, and \$ represents the quartz D_e values and dose rates.

Sample name	pVIR D_e (Gy)	Expected D_e (Gy)	Dose rate (Gy/ka)	pVIR Age (ka)	Expected age (ka)	pVIR g-value (% per decade)	Maximum delay for fading (h)	pVIR Residual dose (Gy)	Dose recovery ratio	Remarks
PRL0	$18 \pm 1^*$ 21 ± 1	$14 \pm 2^+$ $11.1 \pm 0.3^{\$}$	2.25 ± 0.17 $1.84 \pm 0.13^{\$}$	$8 \pm 1^*$ 9 ± 1	6 ± 1	1.9 ± 0.1	32	4.4 ± 0.2	0.97 ± 0.05	Quartz age (NCF-BSL-SAR)
PRL2	49 ± 3	$46 \pm 5^+$ $35.7 \pm 0.1^{\$}$	1.87 ± 0.14 $1.45 \pm 0.09^{\$}$	24 ± 3	25 ± 2	-0.5 ± 0.3	41	5.4 ± 0.2	1.08 ± 0.04	Q: BSL-SAR
MHK-07-07	48 ± 1	$56 \pm 7^+$ $43.0 \pm 0.1^{\$}$	1.82 ± 0.16 $1.41 \pm 0.12^{\$}$	25 ± 3	31 ± 3	-0.3 ± 0.2	41	5.3 ± 0.2	1.02 ± 0.02	Q: BSL-SAR
RTP-18-2	211 ± 7	234 ± 6	3.07 ± 0.21	69 ± 5	76 ± 6	0.1 ± 0.3	69	8 ± 1	0.97 ± 0.03	F: Youngest Toba Tuff sample
RSN-01-17	500 ± 30	511 ± 62	3.97 ± 0.16	126 ± 9	129 ± 16	-0.2 ± 0.3	95	19 ± 4	1.03 ± 0.03	F: pIRIR-SAR
HMP-18-5	340 ± 30	$325 \pm 12^*$ $>511 \pm 2$	2.07 ± 0.12	164 ± 21	$157 \pm 11^*$ $>247 \pm 32$	0.5 ± 0.3	106	12 ± 2	0.96 ± 0.05	F: pIRIR-SAR
MHD-02-17	$484 \pm 19^*$ $>940 \pm 4$	$505 \pm 37^*$ $>956 \pm 2$	3.35 ± 0.15	$144 \pm 9^*$ $>280 \pm 13$	$151 \pm 13^*$ $>286 \pm 13$	2.8 ± 0.3	132	21 ± 1	1.06 ± 0.05	F: pIRIR-SAR

Table 4.8: D_e values, fading values, residual doses, and dose recovery ratios for all samples using the pIRIR-SAR protocol. Recuperation in all the samples was <5%. The D_e values are the residual subtracted and fading corrected. * represents the fading corrected feldspar doses and ages.

Sr. no	Sample name	D_e (Gy)	Age (ka)	g-value (% per decade)	Maximum delay for fading (h)	Residual dose (Gy)	Dose recovery ratio
1	PRL0	38 ± 2	17 ± 2	-	-	13.4 ± 0.4	1.42 ± 0.04
2	PRL2	70 ± 2	38 ± 3	-	-	12.4 ± 0.3	1.14 ± 0.04
3	MHK-07-07	58 ± 2	32 ± 3	-	-	11.8 ± 0.3	1.13 ± 0.03
4	RTP-18-02	234 ± 6	76 ± 6	0.1 ± 1.1	62	10 ± 1	1.09 ± 0.06
5	RSN-01-17	511 ± 62	129 ± 16	-0.3 ± 1.4	190	43 ± 8	1.07 ± 0.10
6	HMP-18-5	325 ± 12 $>511 \pm 2^*$	157 ± 11 $>247 \pm 32^*$	2.9 ± 0.4	86	22 ± 1	0.95 ± 0.04
7	MHD-02-17	505 ± 37 $>956 \pm 2^*$	151 ± 13 $>286 \pm 13^*$	2.7 ± 0.6	190	37 ± 1	1.09 ± 0.06

4.6 Luminescence Mechanism of the Optimized Parameter pVIRSL at 200 °C

The proposed mechanism of pVIRSL in subsection 4.4.2 was at stimulation temperature of 50 °C for both violet and IR. However, after optimization the pVIRSL signal at 200 °C was used for dosimetric measurements as it followed all the criteria for SAR protocol. Therefore, the luminescence production mechanism for pVIRSL at 200 °C was explored on KF using a protocol mentioned in Table 4.9. For comparison, measurements of pVIRSL at both 50 and 200 °C were carried out. The pVIRSL (both violet and IR at 50 °C for 100 s) signal was measured after the dose of 20 Gy, preheat of 250 °C for 60 s, and IR wash (50 °C for 100 s). This signal is named pVIRSL1. On the same aliquot, similar steps were repeated after the TL wash of 500 °C but without IR wash, and this signal was termed as pVIRSL2. Retrapping from the principal trap during violet stimulation was computed as $(pVIRSL2 - pVIRSL1) / pVIRSL2$ (Table 4.9). The same procedure was repeated for IR at

200 °C. The value of (pVIRSL2-pVIRSL1)/pVIRSL2 is -22% for IRSL at 50 °C and 56% for IRSL 200°C (Table 4.10). The results indicate that IRSL at 50 °C from the principal trap is consumed during violet stimulation; however, IRSL at 200 °C does not get consumed during violet stimulation and contributes to the pVIRSL. Therefore, resulting pVIRSL at 50 °C has a single origin, i.e., photo-transfer from deep traps, however pVIRSL at 200 °C has dual origins a) recapture of charges from the principal trap and b) photo-transfer of charges from deep traps as observed from KF.

Table 4.9: Protocol used to quantify the IRSL from principal trap contributing to the pVIRSL.

Steps	Protocol
1	TL 500 °C @ 2 °C/s
2	Dose (~20 Gy)
3	Preheat @250 °C for 60 s
4	IRSL @50 or 200 °C for 100 s
5	VSL @50 °C for 100 s
6	IRSL @50 or 200 °C for 100 s (pVIRSL1)
7	TL 500 °C @ 2 °C/s
8	Dose (~20 Gy)
10	Preheat @250 °C for 60 s
11	VSL @50 °C for 200 s
12	IRSL @50 or 200 °C for 100 s (pVIRSL2)

Table 4.10: Results of quantification of the IRSL from principal trap contributing to the pVIRSL.

Sample	IRSL contribution to pVIRSL at 50 °C	IRSL contribution to pVIRSL at 200 °C
KF	-22%	56%
PRL0	45%	74%
PRL2	-20%	68%
MHK-07-07	-20%	62%
RTP-18-02	2%	73%
RSN-17-01	-2%	79%
HMP-18-05	-8%	49%
MHD-17-02	30%	66%

Table 4.10 provides percentage retrapping from the principal trap for the natural samples. For PRL2, MHK-07-07, RTP-18-02, RSN-01-17, and HMP-18-05, the retrapping from IR at 50 °C from principal trap to pVIRSL signal was <2%. However, for PRL0 and MHD-

17-02, retrapping of charges from IR at 50 °C was 30% and 45%, respectively, and could be the reason for their athermal fading as IR at 50 °C originates from the recombination of proximal electron-hole pairs and hence is more prone to fading (Poolton, 1994). The results also indicate that retrapping from the principal trap for IR at 50 °C is sample dependent. A more specific spectroscopic study may be needed to understand the mechanism in detail. In the future, it may be of interest to include a step of IR stimulation at 50 °C prior pVIRSL measurement to eliminate the IR 50 °C contribution from the principal trap. This may facilitate the isolation of a more stable signal. A significant contribution (>50%) from IR at 200 °C from principal traps to the pVIRSL was obtained for all samples. Therefore, in natural samples, pVIRSL at 200 °C has a dual origin, indicating the DRCs for the pVIR-SAR protocol are from photo-transfer from deep traps and retrapping from the principal trap.

An alternate explanation for fading obtained in PRL0 and MHD-17-02 could be the instability of some of the recombination centres (Kumar et al., 2022). It may be possible that all the nearest recombination centres are not consumed during violet stimulation, hence participating in the pVIRSL and leading to fading. However, it is not observed for other samples.

4.7 Conclusions

The present work probes the mechanism for non-fading pVIRSL and tests its potential for K-feldspar dating. The take-home inferences are:

1. Violet stimulation at 50 °C probes the TL peaks greater than 500 °C and causes photo-transfer of charges from the deeper traps to the shallower traps, and IR stimulation provides pVIRSL. Deep traps >500 °C serve as reservoir traps. Violet stimulation at 50 °C probes the TL peaks below 800 °C.
2. Photo-transferred charges give luminescence only in the blue window due to availability of recombination centres emitting in blue window after the violet stimulation.
3. The pVIRSL at 50 °C results from the photo-transfer of charges from traps (>500 °C) except for PRL0 and MHD-02-17. In these two samples, IR 50 °C from principal trap contributes to pVIRSL at 50 °C, hence results in fading.

4. The pVIRSL at 200 °C has a dual origin, a) photo-transfer from deep traps and b) recapture from the principal trap, in all samples used in the study.
5. Deep traps are sensitive to violet light and also to daylight. This makes pVIRSL suitable for dating. Typically, 60 min of daylight exposure reduced the pVIRSL to a residual dose of a few Gy.
6. Photo-transferred IRSL in most samples had near zero athermal fading. However, two samples, PRL0 and MHD-02-17, returned a g-value of 1.9 ± 0.1 and $2.8 \pm 0.3\%$ per decade, respectively.
7. An augmented pVIR-SAR protocol is presented. Optimized parameters viz. preheat at 250 °C for 60 s, pVIRSL at 200 °C for 100 s, bleaching using both violet and IR stimulation at 350 °C for 200 s and test dose in range of 50 to 80% of expected dose, followed all the criterion for SAR protocol. The pVIR-SAR provides doses with low recuperation (<5% and for PRL0 <10%), good recycling and dose recovery (within 10%), near zero fading, and residual doses < 21 Gy (lower than pIRIR-SAR) and provided reliable ages ranging from 8 to >280 ka. These accord with BSL-SAR or pIRIR-SAR estimates.
8. The pVIR-SAR dose response curve suggests a high laboratory saturation dose ($2D_0 \sim 1000$ Gy), implying the methodology can be used for higher doses.

The pVIR-SAR protocol has been implemented on a limited number of samples. To assess its applicability and validate its effectiveness, additional samples from diverse geological settings worldwide are required.

Chapter 5

Application of pVIR-SAR Protocol for Polymineral Natural Samples

5.1 Introduction

Chapter 4 discusses the use of pVIRSL for equivalent dose estimation using a single aliquot regenerative dose protocol (pVIR-SAR). This chapter examines the potential of the pVIR-SAR protocol in natural polymineral sediments. In this, experiments on two grain sizes viz., polymineral fine-(4-11 μm) and coarse-grains (90-150 μm) were explored and validated.

The use of luminescence in dating fine grains was developed by Zimmerman (1971), in the context of dating of fired pottery (Zimmerman, 1971). A notable physics was the development of measurements of alpha efficiency and appropriate dose rate calculations. Subsequently, Wintle and Huntley (1979) used fine grains in the dating of sediments. Fine grain dating is applicable in depositional environments, such as lacustrine, pottery and volcanic ash where the sand-sized quartz or feldspar grains are rare or absent. The polymineral fine grain dating is mainly carried out due to the mineral separation difficulty for such small grain size, though later developments made it possible to use silica saturated hydrofluoric silicic acid to extract quartz only fraction. An alternative approach was to use a double SAR (DSAR) approach with post Infrared (IR) blue stimulation, which removed the feldspar, blue stimulation contribution through an IRSL treatment and therefore enhanced the OSL from quartz (Banerjee et al., 2001; Roberts and Wintle, 2001, 2003). Duller and Bøtter-Jensen (1993) reported that even after an extended IR stimulation at 50 $^{\circ}\text{C}$, some of the feldspar signal still left. Due to the higher luminescence sensitivity of feldspar with respect to quartz, the OSL from feldspar contributes to total OSL significantly.

Therefore, different combinations of IR stimulation temperature and time were explored to minimize feldspar signal contamination of the quartz signal (e.g., Roberts, 2007; Dogan et al., 2015). Jain and Singhvi (2000) reported that IR stimulation at high temperatures can deplete the quartz signal. Further attempts were made to date polymineral fine-grain samples using feldspar, primarily because its signal can be selectively extracted using IR stimulation (Hütt et al., 1988). (Buylaert et al., 2012). The use of pIRIR signal at elevated temperatures (225 °C and 290 °C) was found to be relatively less affected by athermal fading and has enabled the extension of the dating range (Buylaert et al., 2009; Morthekai et al., 2015; Thomsen et al., 2008). However, pIRIRSL has poor bleachability, resulting in high residual doses in the range Gy, which need due caution (Li and Li, 2011; Liu et al., 2018; Yi et al., 2016).

The pVIRSL signal was explored for dating of polymineral samples by using its feldspar IRSL. The pVIRSL signal selectively probes IRSL of feldspar grains after near complete bleaching of OSL from quartz. It is worth noting that pVIRSL is more efficiently bleached by daylight than pIRIRSL, resulting in a lesser partially bleached signal component in pVIRSL compared to pIRIRSL.

5.2 Samples

Table 5.1 provides sample details. Total thirteen samples from diverse locations and depositional histories were analysed. These included three samples from volcanic ashes, four pottery artefacts, and six fluvial sediments. The samples had OSL ages in the range of 500 years to around 68000 years (Mishra et al., 2013). The volcanic ash and pottery artefacts are generally fine grained, and mineral separation is difficult, so polymineral fine grain measurements were done for these samples. For fluvial samples, both coarse and fine grain measurements were conducted.

Chemical treatments for both fine and coarse grain sample preparation are discussed in Chapter 2 (subsection 2.3.1). After the chemical treatment, the luminescence from the sediment sample primarily comprises of quartz and feldspars, with occasional contribution from zircons (Sutton and Singhvi, 1983; Singhvi and Zimmerman, 1979). Two types of feldspars viz. K-feldspar and Na-feldspar are present in varying proportions. Therefore, a museum specimen of sodium-rich feldspar (sample code: NaF) was also used during analysed. X-ray diffraction (XRD) analysis confirmed it to be albite (98.8%). Its pVIRSL

characteristics and athermal fading rate along with its usability for a SAR protocol were explored.

Table 5.1: List of samples along with geological location, expected age, and age controls. Here CG and FG stands for coarse and fine grains, respectively. FG and CG represents the fine and coarse grains, respectively. All IR50 and pIRIR measurements were made on feldspar.

Sr no	Sample code	Latitude Longitude	Grain size	Expected age (ka)	Age controls	Reference
Volcanic ash fine grain sample						
1	PRL23-01	(15° 19' 23.2716" N, 78° 8' 2.2488" E)	FG	16 ± 1	pIRIR-SAR	This study
2	PRL23-02	(15° 19' 23.2716" N, 78° 8' 2.2488" E)	FG	20 ± 1	pIRIR-SAR	This study
3	PRL23-03	(15° 08' 15.19" N, 79° 25' 27.16" E)	FG	28 ± 2	pIRIR-SAR	This study
Pottery fine grain sample						
4	PRL23-04	(8° 38' 23.3" N, 78° 03' 27.9" E)	FG	0.5 ± 0.1	IR50-SAR	This study
5	PRL23-05	(8° 38' 23.3" N, 78° 03' 27.9" E)	FG	1.6 ± 0.4	IR50-SAR	This study
6	PRL23-06	(8° 35' 60" N , 77° 54' 0" E)	FG	2.9 ± 0.2	pIRIR-SAR	This study
7	PRL23-07	(8° 35' 60" N , 77° 54' 0" E)	FG	3.0 ± 0.2	pIRIR-SAR	This study
Fluvial coarse grain sample						
8	MHK-09-12	(22° 13' 44" N 76° 01' 36" E)	CG	65 ± 7	Quartz BSL-SAR	(Mishra et al., 2013)
9	MHK-09-13	(22° 13' 44" N 76° 01' 36" E)	CG	68 ± 7	Quartz BSL-SAR	(Mishra et al., 2013)
10	PRL23-08	(9° 2' 52.8" N, 78° 16' 12" E)	CG	31 ± 2	Quartz BSL-SAR	This study
11	PRL23-09	(9° 2' 52.8" N, 78° 16' 12" E)	CG	59 ± 3	Quartz BSL-SAR	This study
Fluvial fine grain sample						
10	PRL23-08	(9° 2' 52.8" N, 78° 16' 12" E)	FG	31 ± 2	Quartz BSL-SAR	This study
11	PRL23-09	(9° 2' 52.8" N, 78° 16' 12" E)	FG	59 ± 3	Quartz BSL-SAR	This study
12	PRL23-10	(29° 6' 25.344" N, 75° 1' 27.6096" E)	FG	1.0 ± 0.1	IR50-SAR	This study
13	PRL23-11	(29° 6' 25.344" N, 75° 1' 27.6096" E)	FG	2.1 ± 0.1	IR50-SAR	This study

5.3 Methodology

The study comprises three key experiments:

1. Measurement of equivalent doses for samples with mixed mineralogy

In this experiment, samples with mixed mineralogy were analysed to assess the suitability of pVIR-SAR protocol. Natural samples contain a mixture of minerals, and in some scenarios, it is not possible to separate minerals. Therefore, the pVIR-SAR protocol was tested for D_e estimation in such complex mineral assemblages. The estimated doses were subsequently compared with constraint doses determined using well-established signals.

2. Variations with grain sizes

This experiment explored the variation of pVIRSL ages with different grain size fractions within the same sample. This investigation is significant because it provides insights into whether certain grain size fractions exhibit more reliable dating results with the pVIR-SAR protocol. It can also help to identify potential advantages and limitations associated with specific grain size fractions. The fluvial samples were investigated to test the bleaching efficiency of quartz and feldspar at different grain sizes in the fluvial settings. Feldspar from fluvial settings is often poorly bleached due to insufficient light exposure. Experiments were conducted to identify suitable grain size for dating using pVIRSL.

3. Measurement of athermal fading rates, residual signal, reproducibility, and comparison of pVIR-SAR ages with controls from other luminescence dating protocols

This experiment focused on quantifying athermal fading rates for the pVIRSL signal, assessing the level of residual signal that may remain after bleaching and evaluating the reproducibility of pVIRSL measurements. For all the polymineral samples, athermal fading rates of pVIRSL and of other signals, such as IRSL and pIRIRSL involving feldspar measurements, were estimated and compared. The fading rate measurements were made using methodology described in Chapter 3 (subsection 3.3). The residual doses of all signals were explored after the five hour bleaching under filtered sun-lamp to explore the bleaching efficiency of each signal. The dose recovery tests were carried out to test the reproducibility of the SAR protocols used. The methodology for residual dose and dose recovery measurements is described in Chapter 4 (subsections 4.5.2 and 4.5.3). For all the fine-grain samples, alpha efficiencies were estimated for all signals. To determine the alpha efficiency (α -value), six aliquots of each sample were irradiated under vacuum using a calibrated six

seater ^{241}Am alpha source (Singhvi and Aitken, 1978). Prior to alpha irradiation, the samples were bleached with the sun-lamp for five hours. The bleached samples were given a known alpha dose, and equivalent beta doses were estimated using SAR protocols for IR, pVIR, and pIRIR signals for their beta doses induced by alpha irradiation.

The pVIR ages were compared with SAR ages on quartz BSL (Murray and Wintle, 2000), feldspar IR (50 °C) (Wallinga et al., 2000), and pIRIR (290 °C) (Buylaert et al., 2009) ages. The BSL-SAR was applied to samples where the age is in the datable range of quartz. For younger polymineral samples, the IR-SAR protocol was utilized, while the pIRIR-SAR protocol was employed for older samples. The ages estimated using quartz BSL, feldspar IR, and pIRIR signals were below the saturation of dose response curve (DRC) and satisfied the criteria of SAR protocol. Therefore, these ages were considered as independent ages.

The concentration of radioactive nuclides in the samples was determined using a high-resolution HPGe detector. In the dose rate computations, volumetric corrections were applied to meet the infinite dose matrix criterion.

5.4 Results and Discussion

5.4.1 Quartz and sodium feldspar contamination

As discussed the key minerals are quartz-, K-feldspar and Na-feldspar. Therefore, pVIRSL from all these minerals was measured after the constant dose of approximately 20 Gy. Signals from all samples were weight normalised for comparison. Fig. 5.1a compares the weight normalised pVIRSL decay curves from quartz (calibration quartz: batch 122), Na-feldspar (NaF), and K-feldspar (KF). pVIRSL from an empty disc is also shown for comparison. Weight normalised pVIRSL from quartz and an empty disc was at the background level, and pVIRSL from both potassium and sodium rich feldspars was approximately 1×10^5 counts per second per unit weight. Previous studies reported that IRSL emission of sodium rich feldspar peaks in the yellow-green emission band, whereas K-feldspar emission peaks in the violet (Baril and Huntley, 2003; Krbetschek et al., 1997). Sohpati et al., 2013 suggested that the blue pIRIR signal of sodium-rich feldspar is due to contamination from potassium-rich feldspar as both sodium and potassium feldspar exist in an exsolution form, rendering complete separation unattainable. Therefore, the pVIR-SAR not only offers the advantage of dating the samples where feldspar cannot be separated from quartz but can even discern between K- and Na-feldspars based in their

emission in blue and yellow region. This possibility also eliminates the tedium of separation of fine grain minerals.

Athermal fading of pVIRSL for polymineral samples was also measured. Fig. 5.1a shows that quartz does not respond to pVIR stimulation, and with the exception of volcanic contexts, it does not show athermal fading (Tsukamoto et al., 2007; Ankjærgaard et al., 2013). Thomsen et al. (2008) reported that sodium rich feldspar typically exhibits more athermal fading than potassium feldspar and this was explored further. Fig. 5.1b shows the variation of test dose normalised intensity with delay time. The weighted mean of athermal fading rates of fifteen aliquots for NaF was $0.1 \pm 0.2\%$ per decade, indicating that pVIRSL probes the stable charges in NaF.

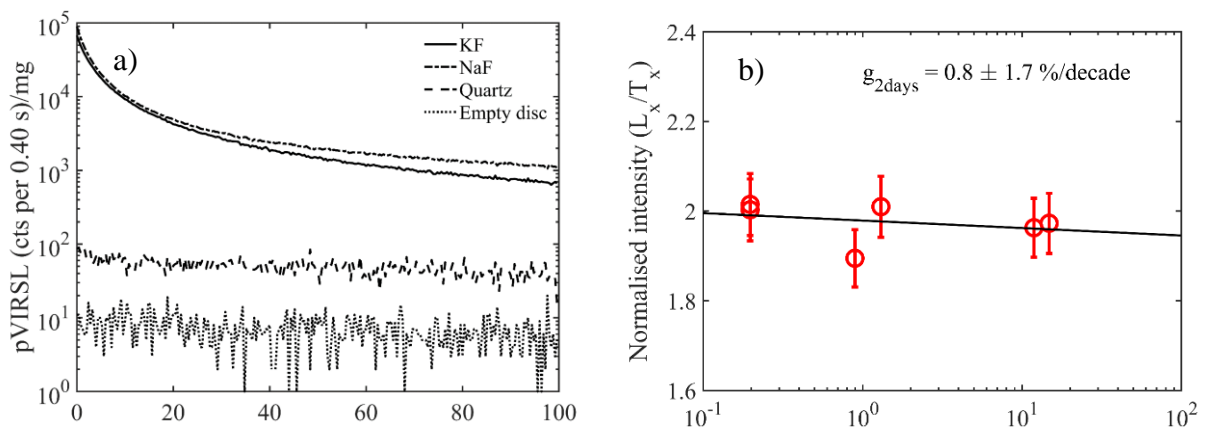


Fig. 5.1: a) Weight normalised shine down curves of pVIRSL from potassium feldspar (KF), sodium feldspar (NaF), quartz and empty disc are shown. b) Normalised luminescence intensity variation with delay time in NaF.

5.4.2 Luminescence characteristics and dose determination

Fig. 5.2 to 5.4 show pVIRSL optical decay curves and dose-response curves (DRCs) for volcanic ash samples (PRL23-01, PRL23-02, and PRL23-03), pottery samples (PRL23-PRL04, PRL23-05, PRL23-06, and PRL23-07) for fluvial samples (PRL23-10 and PRL23-11). Table 5.2 provides the equivalent doses based on 15 aliquots/sample. The acceptance criterion was recycling ratio < 10% of unity and recuperation < 5% of the natural signal. The pVIR-SAR D_e-values were compared with doses from BSL-SAR, IR-SAR, and pIRIR-SAR. The residual doses were subtracted from D_e-values to obtain the true equivalent dose of samples. The estimated, fading corrected D_e-values from all protocols are collated in Table 5.2. The pVIR doses are close to the expected doses except for PRL23-08 and PRL23-09. For these samples, the D_e-values estimated using pIRIRSL greater than pVIRSL

showing the overestimation in the pIRIRSL due to its slow bleaching under natural sunlight.

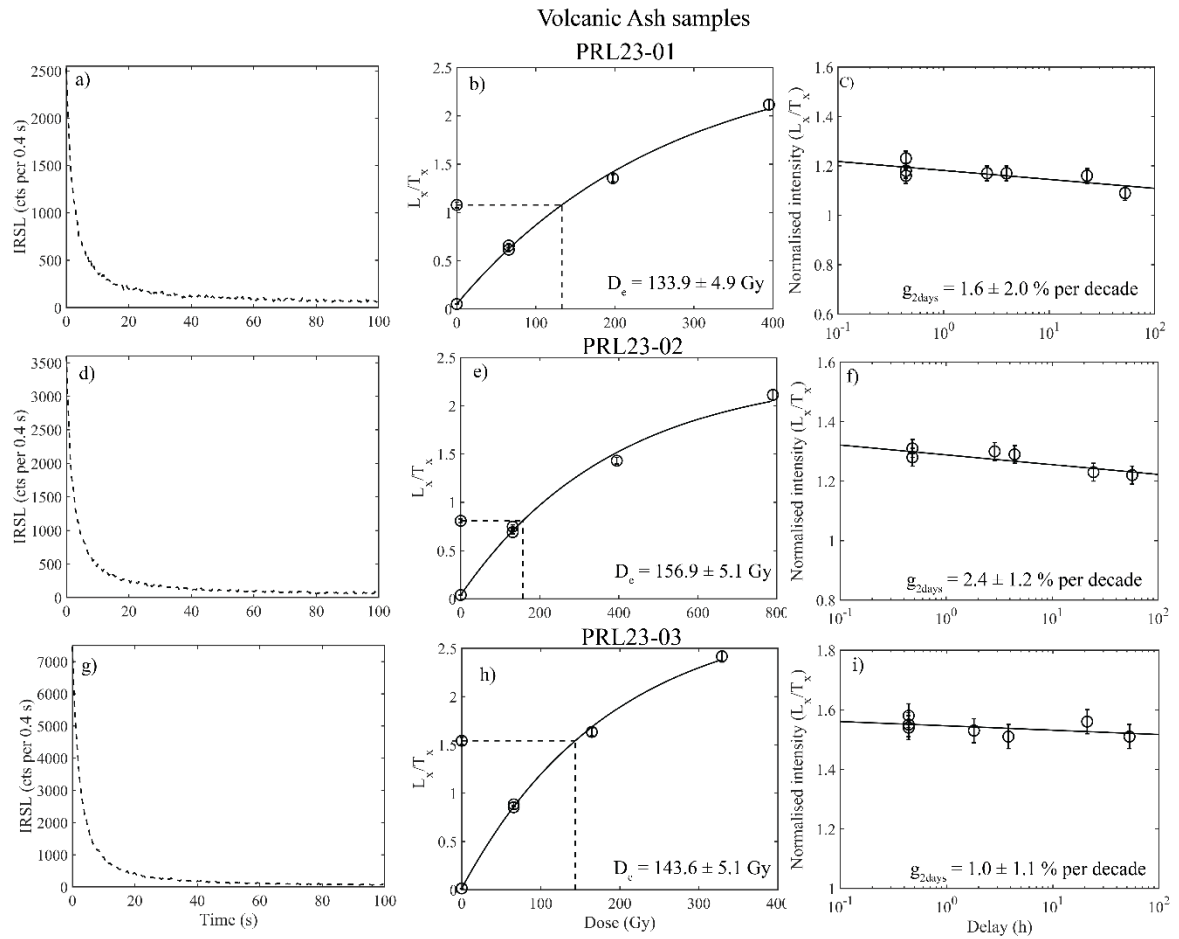


Fig. 5.2: pVIRSL decay curves, dose response curves and variation of normalised intensity with delay time for all volcanic samples named PRL23-01, PRL23-02, and PRL23-03.

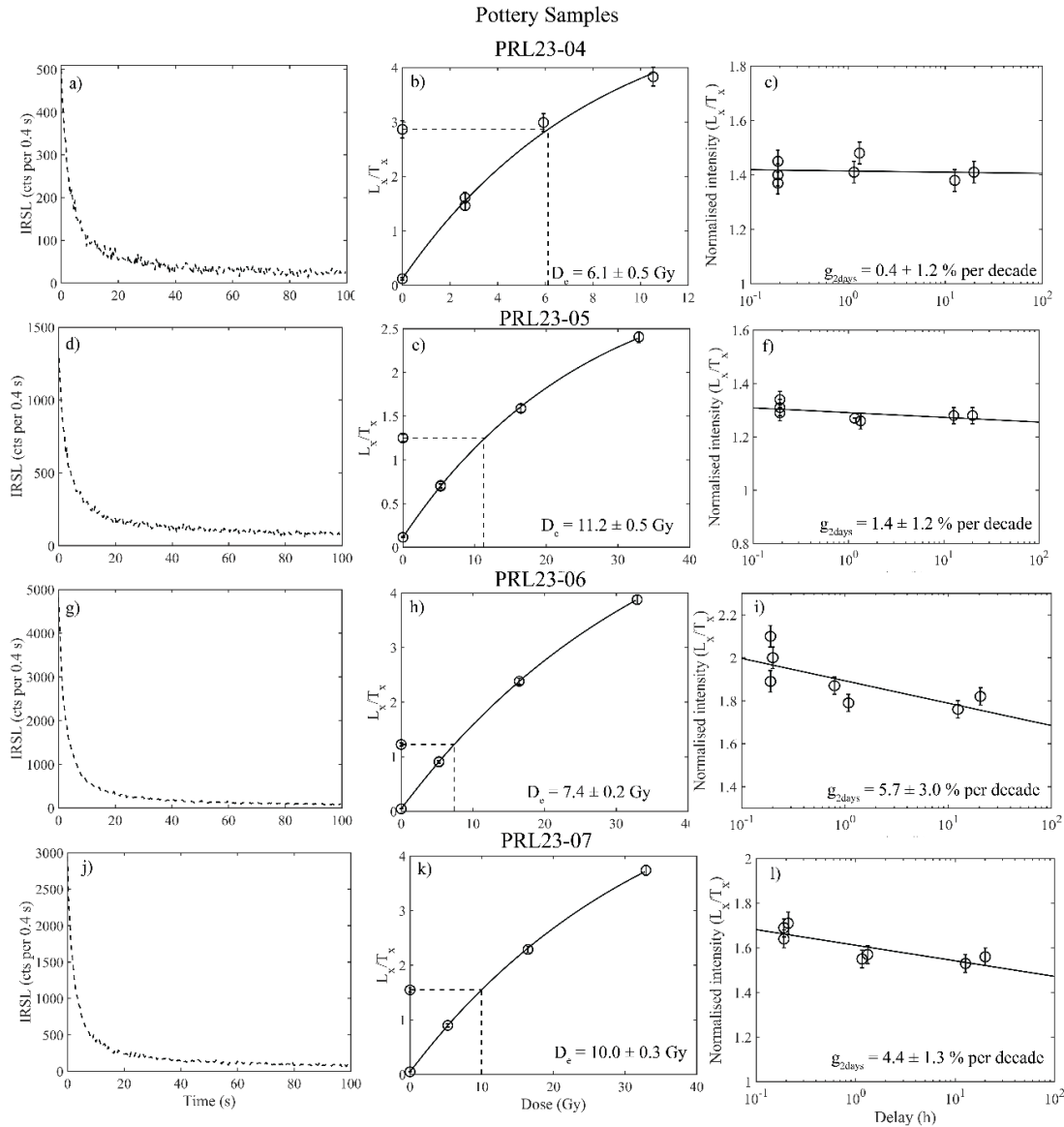


Fig. 5.3: The pVIRSL decay curves, dose response curves, and variation of normalised intensity with delay time for all pottery fine grain samples named PRL23-04, PRL23-05, PRL23-06, and PRL23-07.

5.4.3 Residual dose

The mean residual doses for pVIR-SAR protocol ranged from 3.3 ± 0.2 Gy to 10.0 ± 0.2 Gy for all samples. The residual doses for pIRIR-SAR ranged from 10.3 ± 0.6 Gy to 34.4 ± 0.5 Gy. Table 5.2 collates the data. The residual doses of pVIR-SAR are 30 to 70% lower than the pIRIR-SAR residual doses under the solar lamp bleaching for five hours. Residual doses of fine grains pottery samples assumed zero due to thermal resetting of all signals during the firing of pottery. Lower residual doses for pVIR-SAR compared to pIRIR-SAR

also indicate that pVIR-SAR might provide more accurate equivalent dose estimates due to reduced signal overestimation for all samples.

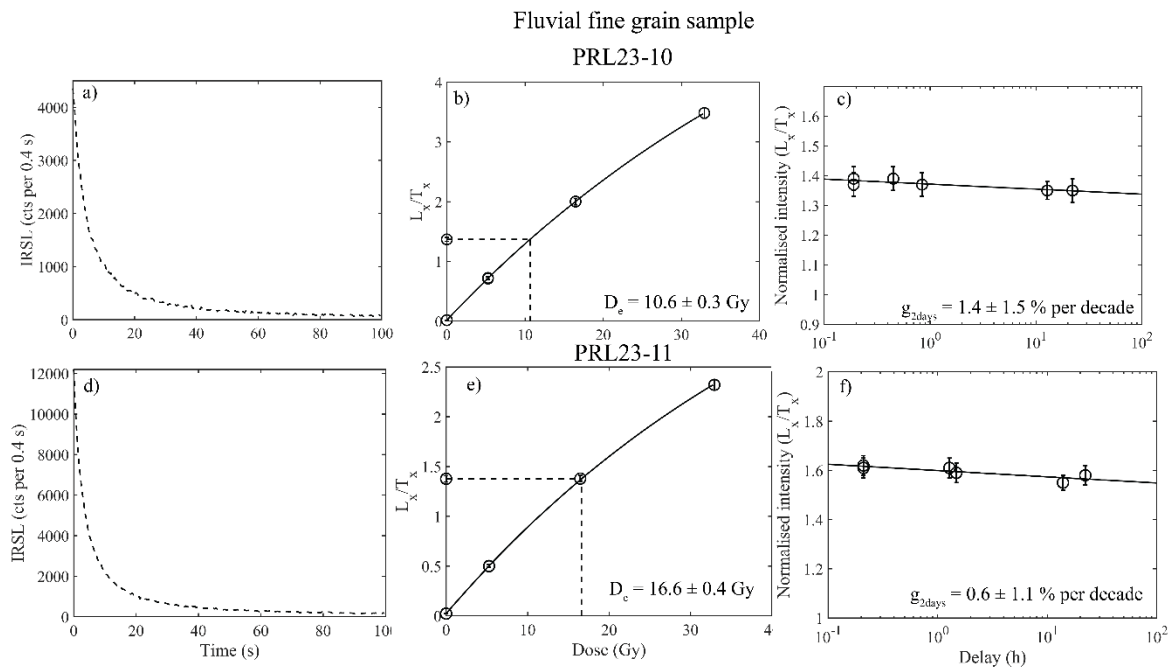


Fig. 5.4: The pVIRSL decay curves, dose response curves and variation of normalised intensity with delay time for fine grain fluvial samples named PRL23-10 and PRL23-11.

5.4.4 Dose recovery

A mean of five aliquots per sample was used to estimate the recovered doses. The residual doses were subtracted from the recovered doses for dose recovery tests. The dose recovery ratios for pVIR-SAR ranged from 0.99 to 1.06, and for pIRIR-SAR, the ratio ranged from 0.93 to 1.12 (Table 5.2).

5.4.5 Athermal Fading

Athermal fading rates were measured for pVIRSL, IRSL, and pIRIRSL signals from polymineral samples. The delay time duration depended on the equivalent dose of the samples. A constant t_c value of 2 days was used. For fine grain samples, eight out of thirteen had pVIRSL athermal fading rates ≤ 1.1 % per decade (Table 5.2). Normalised intensities plotted against delay time are depicted in Fig. 5.2 to 5.5. Given that low fading rates would not change the final age estimations, no age corrections were conducted (Buylaert et al., 2012). Remaining five samples PRL23-02, PRL23-04, PRL23-05, PRL23-06, and PRL23-07, had g -values as 2.3 ± 0.2 , 1.3 ± 0.4 , 1.4 ± 0.1 , 5.9 ± 0.6 , and 4.0 ± 0.4 % per decade, respectively. For IR and pIRIR, PRL23-09 had g -values < 1.1 % per decade (Table 5.2; Fig.

5.6). For all other samples fading rates were higher. The fading values of pVIRSL signal are equal to or lower than the IRSL and pIRIRSL except for PRL23-06 and PRL23-07 pottery samples. For polymineral coarse grains, out of four samples, the fading rates of three samples were $\leq 1.1\%$ per decade for the pVIRSL signal (Table 5.2). The PRL23-09 sample exhibited a fading rate of $1.5 \pm 0.4\%$ per decade. In contrast, the pIRIRSL signal demonstrated a fading rate exceeding 1.1% per decade for three out of four samples. In the case of the volcanic ash samples, the fading rates of pVIRSL are lower than the pIRIRSL, indicating that pVIRSL probes the athermally more stable charges than pIRIRSL. The above discussed results indicate that pVIRSL probes charge more stable traps than pIRIRSL in both fine and coarse grain fractions of fluvial samples.

For PRL23-06 and PRL23-07 pottery samples, pVIRSL fading rates are higher than pIRIRSL. The IRSL fading rates for these two samples were greater than 10% per decade. The XRD analysis showed that these two samples were rich in sanidine (Singh et al., (in preparation)), which could be the possible reason for higher fading in these two samples. Polymeris et al. (2022) reported that sanidines yield more intense fading among three groups of k-feldspar. For all coarse grains, pVIRSL fading rates were $<1\%$ per decade except for PRL23-09, the g-values are $1.5 \pm 0.4\%$ per decade. In contrast, the pIRIRSL g-values were greater than 1% per decade for all four coarse grain fractions.

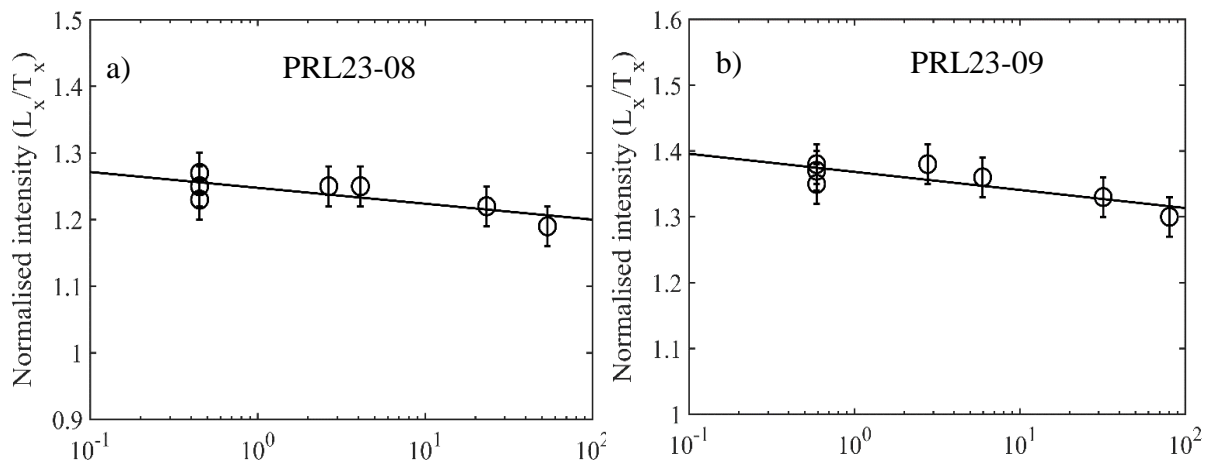


Fig. 5.5: Normalised intensity with delay time for fine grain PRL23-08 and PRL23-09 sample.

Table 5.2: Estimated D_e values, fading value, recuperation, residual dose, and dose recovery ratio for all samples using pVIR-SAR, IR and pIRIR protocol. Recuperation observed in all the samples is <5%. The D_e values are corrected for fading, wherever applicable. The residual doses are subtracted from both estimated doses from natural sample and recovered doses from given dose for dose recovery test. Here \$ represents the ages estimated using IR-SAR protocol.

Sample name	pVIR D_e (Gy)	IR/pIRIR D_e (Gy)	pVIR Age (ka)	IR/pIRIR Age (ka)	pVIR g-value (% per decade)	IR/pIRIR g-value (% per decade)	pVIR Residual dose (Gy)	IR/pIRIR Residual dose (Gy)	pVIR Dose recovery ratio	IR/pIRIR Dose recovery ratio
Volcanic ash fine grains										
PRL23-01	137 ± 4	140 ± 9	17 ± 1	16 ± 1	1.1 ± 0.2	1.5 ± 0.5	5.1 ± 0.4	10.7 ± 0.8	1.00 ± 0.02	0.94 ± 0.03
PRL23-02	176 ± 5	146 ± 8	26 ± 1	20 ± 1	2.3 ± 0.2	2.5 ± 0.4	4.9 ± 0.3	10.3 ± 0.6	0.99 ± 0.02	0.99 ± 0.03
PRL23-03	183 ± 13	222 ± 22	27 ± 3	31 ± 3	1.1 ± 0.4	1.9 ± 0.4	5.7 ± 0.2	10.7 ± 1.2	1.01 ± 0.04	0.93 ± 0.02
Pottery fine grains										
PRL23-04	6.3 ± 0.3	4.0 ± 0.6 ^{\$}	0.9 ± 0.1	0.5 ± 0.1 ^{\$}	0.4 ± 0.3	4.8 ± 1.2 ^{\$}	n.m.	n.m.	n.m.	n.m.
PRL23-05	13.3 ± 0.3	12 ± 3 ^{\$}	1.8 ± 0.1	1.6 ± 0.4 ^{\$}	1.4 ± 0.1	7.1 ± 1.4 ^{\$}	n.m.	n.m.	n.m.	n.m.
PRL23-06	13.1 ± 0.8	16.0 ± 0.5	3.2 ± 0.3	4.5 ± 0.3	5.9 ± 0.6	3.3 ± 0.4	n.m.	n.m.	n.m.	n.m.
PRL23-07	14.5 ± 0.4	20 ± 1	3.4 ± 0.3	5.1 ± 0.5	4.0 ± 0.4	3.2 ± 0.3	n.m.	n.m.	n.m.	n.m.
Fluvial coarse grains										
MHK-09-12	96 ± 5	96 ± 11	58 ± 7	58 ± 9	0.5 ± 0.5	1.1 ± 0.6	3.3 ± 0.2	15.6 ± 0.9	1.01 ± 0.02	0.95 ± 0.02
MHK-09-13	109 ± 7	120 ± 11	60 ± 7	66 ± 9	0.2 ± 0.5	1.2 ± 0.7	3.9 ± 0.1	5.5 ± 0.1	1.05 ± 0.02	1.09 ± 0.03
PRL23-08	226 ± 6	311 ± 23	63 ± 3	86 ± 8	0.9 ± 0.4	1.4 ± 0.6	10.0 ± 0.2	34.4 ± 0.5	1.06 ± 0.03	1.11 ± 0.02
PRL23-09	307 ± 16	390 ± 22	114 ± 9	144 ± 12	1.5 ± 0.4	1.9 ± 0.6	8.0 ± 0.1	32.0 ± 0.5	1.03 ± 0.03	1.12 ± 0.03
Fluvial fine grains										
PRL23-08	144 ± 2	270 ± 10	37 ± 1	68 ± 3	1.0 ± 0.1	3.6 ± 0.2	4.4 ± 0.1	22.8 ± 0.6	1.06 ± 0.02	1.07 ± 0.03
PRL23-09	211 ± 5	327 ± 7	78 ± 4	126 ± 6	0.8 ± 0.5	0.8 ± 0.5	8.1 ± 0.2	24.2 ± 1.4	0.98 ± 0.02	0.96 ± 0.02
PRL23-10	9.6 ± 0.5	5.5 ± 0.3 ^{\$}	1.6 ± 0.1	1.0 ± 0.1 ^{\$}	1.3 ± 0.4	1.3 ± 0.5 ^{\$}	2.11 ± 0.04	n.m.	1.02 ± 0.02	n.m.

PRL23-11	15.0 ± 0.3	12.2 ± 0.5 ^s	2.5 ± 0.1	2.1 ± 0.1 ^s	0.8 ± 0.3	2.0 ± 0.4 ^s	2.20 ± 0.03	n.m.	0.98 ± 0.02	n.m.
----------	------------	-------------------------	-----------	------------------------	-----------	------------------------	-------------	------	-------------	------

Table 5.3: Dose rate details of all samples.

Sample	U (ppm)	Th (ppm)	K (%)	a-value			Dose rate* (Gy/ka)		Water content (%)	Depth (cm)
				IR	pVIR	pIRIR	Q/pVIR	IR/pIRIR		
Volcanic ash fine grains										
PRL23-01	5.7 ± 0.1	29.3 ± 0.6	3.7 ± 0.1	n.m.	0.067 ± 0.004	0.086 ± 0.007	8.5 ± 0.3	9.0 ± 0.3	15 ± 5	130
PRL23-02	4.3 ± 0.1	24.7 ± 0.8	2.9 ± 0.1	n.m.	0.088 ± 0.004	0.119 ± 0.006	6.9 ± 0.2	7.5 ± 0.3	15 ± 5	255
PRL23-03	5.0 ± 0.1	28.8 ± 0.6	3.3 ± 0.1	n.m.	0.060 ± 0.002	0.083 ± 0.004	7.4 ± 0.1 6.7 ± 0.4*	8.0 ± 0.2 7.2 ± 0.3*	20 ± 5	200
Pottery fine grains										
PRL23-04	4.2 ± 0.1	22.9 ± 0.5	3.6 ± 0.1	0.093 ± 0.001	0.071 ± 0.001	n.m.	6.9 ± 0.1	7.3 ± 0.1 ^s	20 ± 2	200
PRL23-05	2.9 ± 0.1	32.0 ± 1.1	3.2 ± 0.05	0.095 ± 0.002	0.087 ± 0.001	n.m.	7.4 ± 0.1	7.5 ± 0.1 ^s	20 ± 2	172
PRL23-06	2.5 ± 0.4	11.5 ± 1.8	1.8 ± 0.1	n.m.	0.099 ± 0.001	0.059 ± 0.001	4.0 ± 0.3	3.5 ± 0.2	8 ± 7	135
PRL23-07	2.5 ± 0.7	12.7 ± 2.6	1.9 ± 0.1	n.m.	0.110 ± 0.002	0.081 ± 0.001	4.3 ± 0.3	3.9 ± 0.3	10 ± 7	26
Fluvial coarse grains										
MHK-09-12	1.36 ± 0.27	3.62 ± 0.95	0.67 ± 0.09	n.m.	n.m.	n.m.	1.07 ± 0.12	1.47 ± 0.12	15 ± 5	440
MHK-09-13	1.38 ± 1.33	4.44 ± 1.16	0.78 ± 0.06	n.m.	n.m.	n.m.	1.21 ± 0.12	1.71 ± 0.12	15 ± 5	490
PRL23-08	0.77 ± 0.03	8.02 ± 0.19	2.3 ± 0.04	n.m.	n.m.	n.m.	3.0 ± 0.1	3.0 ± 0.1	5.0 ± 2.5	90
PRL23-09	0.88 ± 0.03	7.88 ± 0.22	1.34 ± 0.03	n.m.	n.m.	n.m.	2.1 ± 0.1	2.1 ± 0.1	5.0 ± 2.5	140
Fluvial fine grains										
PRL23-08	0.77 ± 0.03	8.02 ± 0.19	2.3 ± 0.04	n.m.	0.095 ± 0.002	0.105 ± 0.002	3.9 ± 0.1	4.0 ± 0.1	5.0 ± 2.5	90
PRL23-09	0.88 ± 0.03	7.88 ± 0.22	1.34 ± 0.03	n.m.	0.080 ± 0.006	0.220 ± 0.013	2.9 ± 0.1	3.8 ± 0.1	5.0 ± 2.5	140
PRL23-10	4.01 ± 0.05	16.81 ± 0.27	2.55 ± 0.04	0.034 ± 0.001	0.059 ± 0.001	n.m.	5.8 ± 0.2	5.4 ± 0.2 ^s	10 ± 5	50
PRL23-11	4.33 ± 0.05	17.34 ± 0.27	2.76 ± 0.04	0.047 ± 0.001	0.057 ± 0.001	n.m.	6.1 ± 0.2	5.9 ± 0.2 ^s	10 ± 5	200

** Represents the dose rate after volumetric correction and [§] represents the dose rates for IRSL at 50 °C. n.m. stands for not measured. Dose rates are calculated using standard infinite matrix assumption using offline Dose Rate calculator (DRc; Tsokolas et al., 2016). The conversion factors used in DRc software are by Guérin et al. (2011). The a-value and beta attenuation factors were estimated using Guérin and Mercier (2012) and Nathan and Mauz (2008), respectively.*

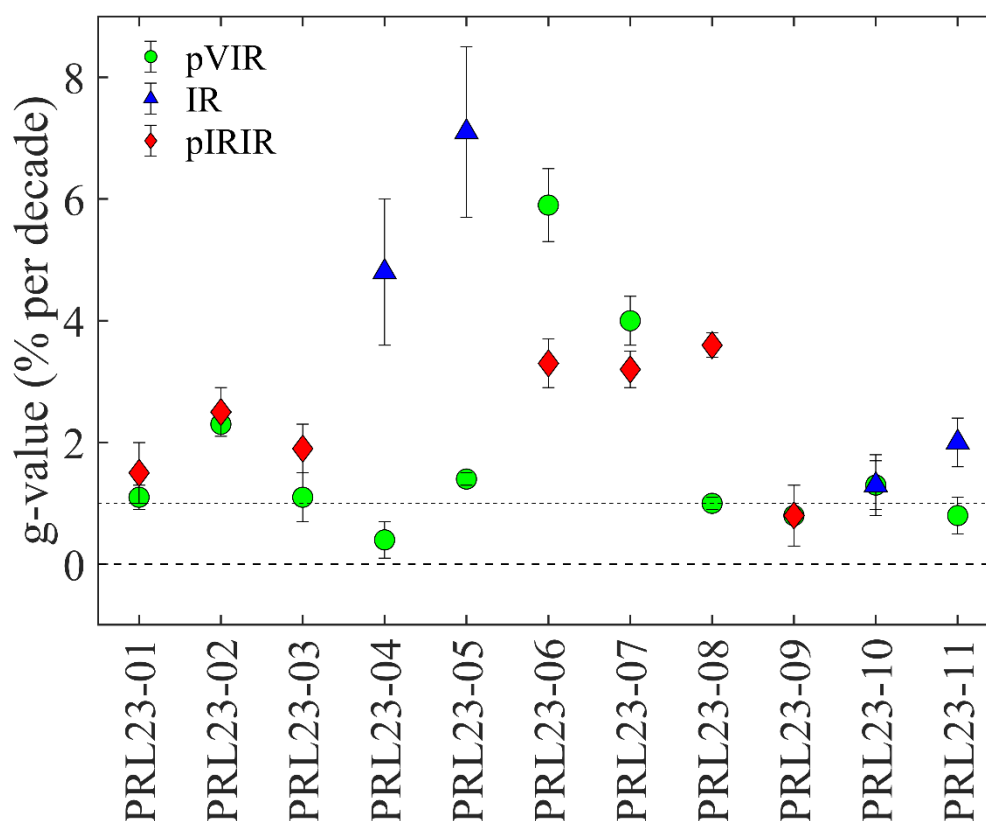


Fig. 5.6: Average fading rate values for all fine grain polymineralic samples. Fading corrections in ages for fading rates less than one were not made (Buylaert et al. 2012).

5.4.6 | Dose rate determination

The dose rate of all samples is listed in Table 5.3. The dose rate of samples ranged from 1.07 to 9.00 Gy/ka. The conversion factor for dose rate estimation used are mentioned in section 2.4.2. The internal radioactivity of K-feldspar due to ^{40}K is considered as $12.5 \pm 0.5\%$ (Huntley and Baril, 1997), whereas sodium feldspar does not possess any radioactive elements. In cases where the ^{40}K concentration is uniformly distributed, the dependence on grain size in the range up to 300 μm is insignificant for potassium concentration below 5% (Sohbati et al., 2013; Fig. 1). This is due to the range of beta particle (3 mm) is greater than the desired grain size for luminescence measurements. Consequently, it is reasonable to assume that all feldspar grains have received uniform doses during their geological antiquity, making them suitable for dosimetry. The dose rate contribution due to internal radioactivity of ^{40}K is $< 1\%$ of the total dose rate for fine grains and $< 5\%$ for coarse grains, thus exerting minimal impact on the dose rate. For all polymineral grain measurements, a

uniform value of $12.5 \pm 0.5\%$ for internal ^{40}K is assumed as only feldspar yields to pVIRSL. Pottery samples PRL23-06 and PRL23-07 were hollow from inside, therefore corrections were made for doses deposited by gamma radiations. After considering these corrections dose rate reduced from 4.0 ± 0.2 Gy/ka to 3.5 ± 0.2 Gy/ka and 4.5 ± 0.3 Gy/ka to 3.9 ± 0.3 Gy/ka for PRL23-06 and PRL23-07 sample for pIRIRSL signal, respectively. Similarly, for pVIRSL signal dose rates reduced from 4.5 ± 0.3 Gy/ka to 4.0 ± 0.3 Gy/ka and 4.9 ± 0.4 Gy/ka to 4.3 ± 0.3 Gy/ka for PRL23-06 and PRL23-07 sample, respectively (Singh et al., (in preparation)). For coarse grains, alpha irradiated skin was etched using HF treatment. However, the size of fine grains is less than the range of alpha particles. Hence, alpha efficiency is considered for dose rate estimation of fine grains as discussed below:

5.4.6.1 Alpha efficiency

For polymineral fine grain samples, the alpha efficiency was estimated for pVIRSL, IRSL, and pIRIRSL signals as detailed in section 5.3. The alpha efficiencies were estimated using Eq. 2.2 discussed in Chapter 2 and are listed in Table 5.3. The alpha efficiencies for volcanic ash samples ranged from 0.060 ± 0.002 to 0.088 ± 0.004 for pVIRSL and 0.083 ± 0.004 to 0.119 ± 0.006 for pIRIR signal. For fluvial samples PRL23-10 and PRL23-11, a-values ranged from 0.034 ± 0.001 and 0.047 ± 0.001 for IR and 0.059 ± 0.001 and 0.057 ± 0.001 for pVIRSL. Similarly, for PRL23-08 and PRL23-09 fluvial samples, a-values are 0.095 ± 0.002 and 0.080 ± 0.006 for pVIRSL and 0.105 ± 0.002 and 0.220 ± 0.013 for pIRIR signal. For PRL23-04 and PRL23-05 pottery samples, a-values ranged from 0.093 ± 0.001 and 0.095 ± 0.002 for IR, 0.071 ± 0.001 and 0.087 ± 0.001 for pVIRSL. For PRL23-05 and PRL23-06 pottery samples, a-values are 0.099 ± 0.001 and 0.110 ± 0.002 for pVIRSL and 0.059 ± 0.001 and 0.081 ± 0.001 for pIRIR signal. The results indicate that a-values for pIRIRSL > pVIRSL > IRSL for volcanic ash and fluvial samples (Fig. 5.7). However, a different trend was obtained for pottery samples; a-values for IR are higher than pVIRSL. In comparison, pVIRSL a-values are higher than pIRIRSL for PRL23-06 and PRL23-07. The a-values varied depending on the sample and signal used.

The distinct values of alpha efficiencies for different samples reflect the different responses of fine-grain samples to alpha radiation. These variations may be attributed to the diverse mineralogical compositions, crystal structures, and sensitivities of individual signals to alpha radiation interactions. Understanding the interplay between alpha efficiencies and

luminescence signals is crucial for optimizing dose reconstruction protocols, and it needs further exploration. This will be explored in the future.

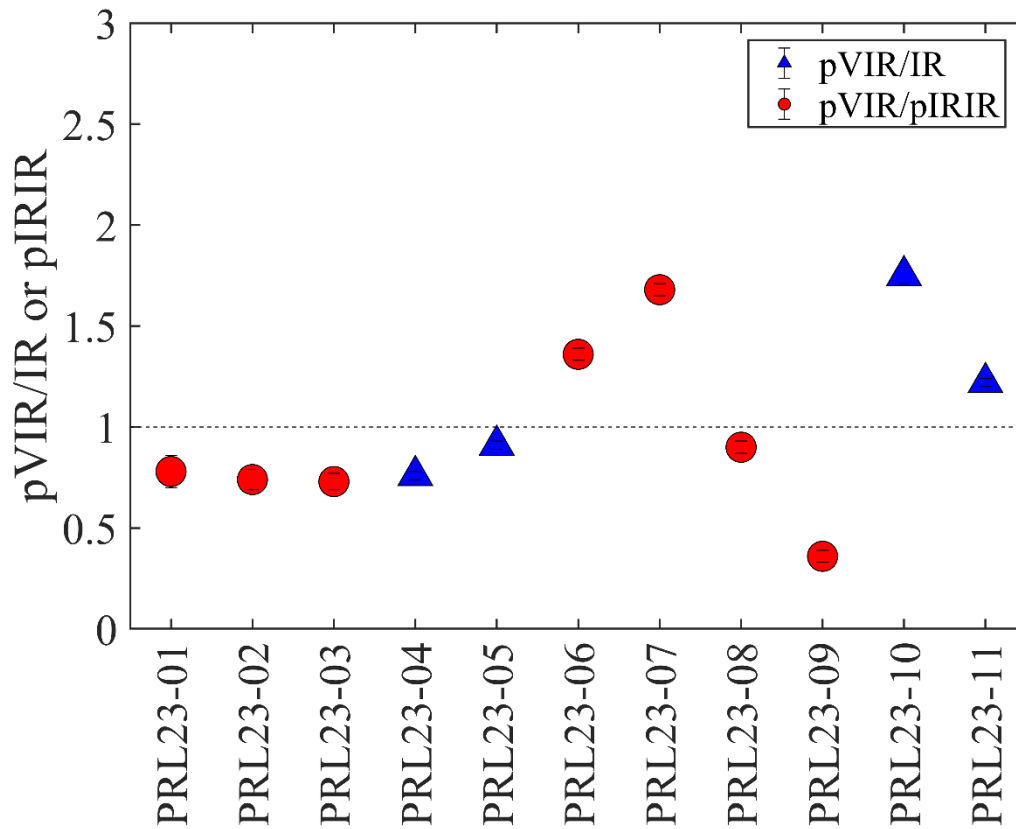


Fig. 5.7: Alpha efficiency of all samples.

5.4.6.2 Volumetric correction for heterogeneous sedimentary layers

The PRL23-03 sample has an average thickness of around 30 cm for the ash layer. The underlying and overlying sediment layers have lower radioactive concentrations compared to the ash layer deposit. In this case, the infinite matrix assumption is valid only for the alpha and beta particles, as their range is 20 μm and 30 mm in the sediments. However, the gamma radiations have a range of ~ 30 cm. Therefore, the infinite matrix assumption is not valid for the ash layer. Therefore, volume corrections for the gamma dose rate were made. The field representation of the volcanic ash layer is shown in Fig. (5.8a, b). A sphere of radius 'r' equal to 30 cm has three layers: two sedimentary (1 and 3) and an ash layer (2) (Fig. 5.8b). The approximate thickness of the ash layer deposit is 30 cm. The volumetric corrections for the dose deposited by gamma rays in the ash sample is given below.

$$Volume_s * \gamma_s = Volume_1 * \gamma_1 + Volume_2 * \gamma_2 + Volume_3 * \gamma_3$$

Considering the volume of the sphere, hemisphere, and cylinder, the above equation can be written as:

$$\gamma_s = \frac{3}{4r} \left(\frac{2r}{3} - \frac{h}{2} \right) (\gamma_1 + \gamma_3) + \frac{3h\gamma_2}{4r}$$

This equation is used for the volumetric correction to compute the dose rate from gamma rays. Considering the volumetric corrections, the total dose rate of the PRL23-03 ash sample reduced from 7.4 ± 0.1 Gy/ka to 6.7 ± 0.4 Gy/ka and from 8.0 ± 0.2 Gy/ka to 7.2 ± 0.3 Gy/ka for pVIRSL and pIRIRSL, respectively.

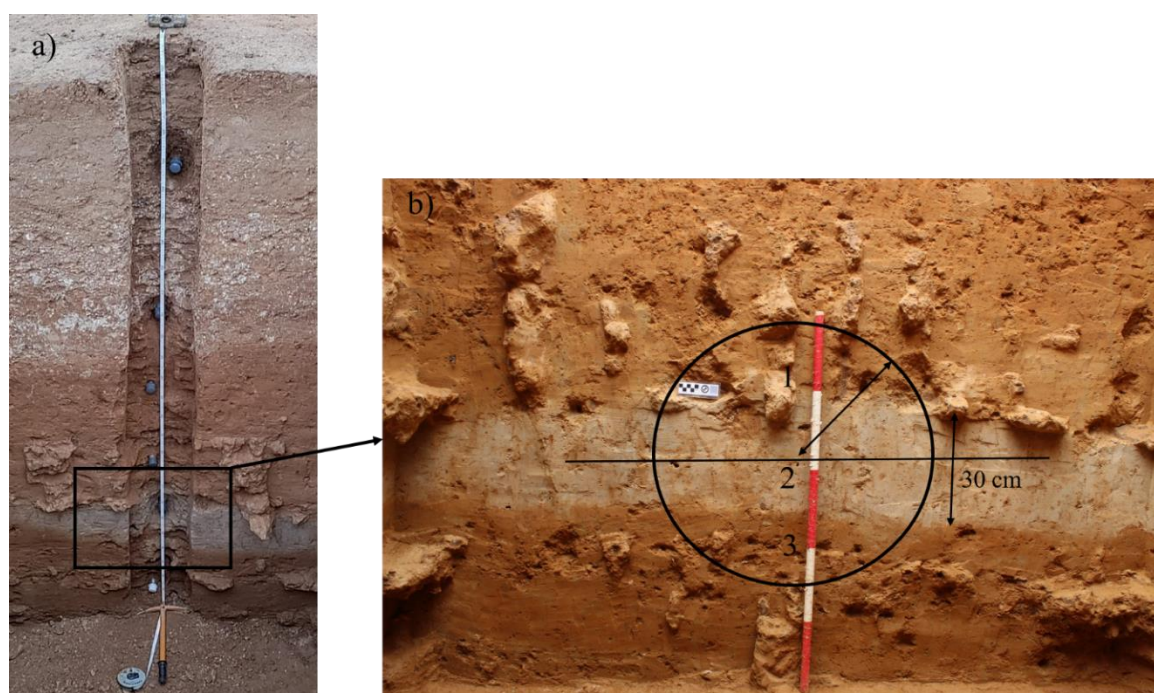


Fig. 5.8: a) OSL sampling of PRL23-03 volcanic ash sampling site. b) Zoomed view of deposited volcanic ash layer. The thickness of ash layer is ~30 cm. A sphere of radius 30 cm is considered for volumetric corrections for dose deposited by gamma radiations.

5.5 Age Determination from Polymineral Fine- and Coarse-grain Fractions

5.5.1 Fine grains

In this section, the age determined from the polymineral fine grain samples are discussed and compared with the constraint ages from other luminescence signals, which are well

established. Ages were estimated considering a-values in the dose rate calculations. The volumetric corrections were applied for gamma dose rate, wherever applicable.

5.5.1.1 Volcanic ash

We have determined the ages of three volcanic ash samples PRL23-01, PRL23-02, and PRL23-03. The pVIR age of PRL23-01 is 17 ± 1 ka, which accords well with the pIRIR age of 16 ± 1 ka (Table 5.2). Similarly, for PRL23-02, the pVIR and pIRIR ages are 26 ± 1 ka and 20 ± 1 ka, respectively and for PRL23-02 are consistent within 20% of uncertainty (Fig. 5.9). The ages of three volcanic ash samples represent the reworked ash events which is also confirmed by field expert (Personal communication with Mr. Anil Devara, MSU, Baroda). The pVIR and pIRIR-SAR ages of all samples are consistent within two sigma errors (Fig. 5.9). Both PRL23-01 and PRL23-02 samples were collected from the same stratigraphy. The PRL23-01 sample was above the PRL23-02. Both pVIR and pIRIR ages of these samples followed the chronological order, further supporting that the ages are correct.

The PRL23-03 sample contains distinct sediment layers, including layers 1, 2, and 3, and an ash sample was collected from layer 2 (layers 1, 2, and 3; Fig. 5.8). The volumetric correction for gamma dose rates was applied for layer 2. The results demonstrate that volumetric correction of the PRL23-03 sample reduced the total dose rate by 7%. After the volumetric corrections, the pVIR and pIRIR ages are 27 ± 3 ka and 31 ± 3 ka, respectively, consistent within the error limit (Fig. 5.9). The PRL23-03 has an additional control from the sediment layer lying above and below the ash deposit. PRL23-03 sample ages agree with bounding feldspar pIRIR. The age of sediment above the ash deposit is 28 ± 1 ka, and sediment beneath the volcanic ash has an age of 32 ± 2 ka (Personal communication; Mr. Anil Devara, MSU, Baroda). Further, the residual doses associated with pIRIR-SAR are approximately twice as high as those of pVIR-SAR, thereby highlighting the better bleaching efficiency exhibited by pVIR-SAR in comparison to pIRIR-SAR for volcanic ash samples.

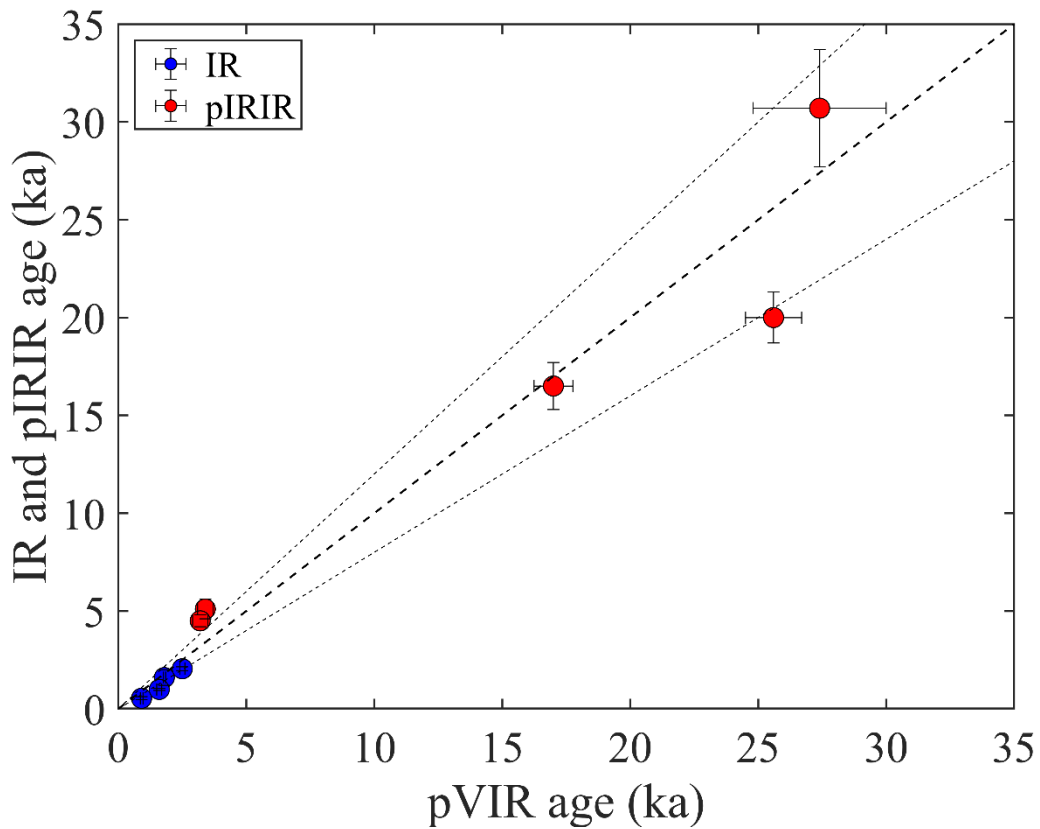


Fig. 5.9: Polymineralic fine grain pVIR ages plotted against the IR and pIRIR ages. The black lines represent the 20% uncertainty.

5.5.1.2 Pottery samples

The ages of four pottery samples PRL23-04, PRL23-05, PRL23-06, and PRL23-07 were determined. For PRL23-04 and PRL23-05, IR-SAR ages are taken as independent ages, as pottery samples were young. For PRL23-04, pVIR age is 1.8 times the age of IR (Table 5.2, Fig. 5.9). The pVIR and IR age of the PRL23-05 are respectively calculated as 1.8 ± 0.1 ka and 1.6 ± 0.4 ka and agree within 20% of uncertainty. The IR- and pVIR-SAR ages for PRL23-05 are consistent with 20%. For pottery samples PRL23-06 and PRL23-07, pIRIR are considered as independent ages as IRSL at 50 °C yielded fading rates >10% per decade, which cannot be corrected using the fading correction age models (Huntley and Lamothe, 2001). The pVIR ages of PRL23-06 and PRL23-07 are 3.2 ± 0.3 ka and 3.4 ± 0.3 ka, respectively, and pIRIR are 4.5 ± 0.3 ka and 5.1 ± 0.5 ka. The pIRIR ages are approximately 1.5 times higher than the pVIR ages. The fading rates of pVIRSL for these samples are higher than pIRIRSL, possibly because of the presence of sanidine, as discussed in

subsection 5.4.4. Residual doses are not estimated for these samples, assuming they were properly bleached due to their firing at temperatures >400 °C.

5.5.2 Coarse grains: Fluvial samples

Four fluvial polymineral coarse grain samples from two different locations were used for age estimations. The pVIR and pIRIR ages of MHK-12-09 are 58 ± 7 ka and 58 ± 9 ka, respectively, and are consistent with the expected quartz age of 65 ± 7 ka. Similarly, for MHK-13-09, pVIR- and pIRIR-SAR ages are 60 ± 7 ka and 66 ± 9 ka, and consistent with expected ages based on quartz BSL age of 68 ± 7 ka (Mishra et al., 2013). For polymineral coarse grain samples named MHK-12-09 and MHK-13-09, both pVIR and pIRIR-SAR ages are in agreement with the expected quartz ages within 2σ uncertainty (Fig. 5.10). Fading rates for pVIRSL for both samples are negligibly small and notably lower than the pIRIRSL. The age agreement of both feldspar polymineral ages and quartz ages suggests effective bleaching of feldspar grains during the deposition. The results also indicate that pVIR-SAR works well for polyminerals; hence, no mineral separation is required. After the removal of carbonates and organic matter from sediments, only 10% HF treatment for 40 minutes is required to remove alpha irradiated skin for coarse grains. This opens up new opportunities for in situ measurement of samples without requiring desired mineral separation. The pVIR-SAR residual doses are also lower than the pIRIR-SAR protocol, again highlighting the better bleachability of pVIRSL than pIRIRSL.

Further, the ages of polymineral fluvial coarse grain samples PRL23-08 and PRL23-09 were determined. These two samples belong to the same location. The pVIR and pIRIR ages of PRL23-08 are 63 ± 3 ka and 86 ± 8 ka, respectively, and for PRL23-09, the ages are 114 ± 9 ka and 144 ± 12 ka, respectively (Table 5.2; Fig. 5.10). The ages overestimated from the expected ages estimated using quartz, which were 31 ± 2 ka and 59 ± 3 ka for PRL23-08 and PRL23-09, respectively. Both pVIR and pIRIR ages showed an overestimation in the ages than the expected age estimated using BSL-SAR quartz. This discrepancy suggests a twofold overestimation in the polymineral coarse grain pVIR ages and a threefold overestimation in the pIRIR ages when compared with the expected ages. This discrepancy indicates that feldspar is not properly bleached during deposition for these samples. Overestimation in the ages of polymineral coarse grain demonstrates that coarse grain feldspars exhibit poor bleachability in this fluvial setting, leading to an overestimation of sample ages. Although both feldspar signals overestimating ages, but lower pVIR ages

than pIRIR ages imply that pVIRSL has better bleaching efficiency for feldspar compared to pIRIRSL.

A previous study by Fuller et al., 1994 reported that fine grains might have better bleachability in comparison to coarse grains in fluvial contexts. In a fluvial setting, finer grains remain in water suspension for longer than coarse sediments because of their small size, and hence, they are exposed to daylight for a long time. For the same samples, the bleaching behaviour of polymineral fine grain is explored using both the pVIR-SAR and pIRIR-SAR protocol. Therefore, polymineral fine grain ages were estimated for PRL23-08 and PRL23-09. The pVIR fine grain age of PRL23-08 is 37 ± 1 ka and consistent with a quartz age of 31 ± 2 ka within 20% uncertainty. For PRL23-09, the pVIR age is 78 ± 4 ka, also consistent within 20% uncertainty with the expected age of 59 ± 3 ka (Fig. 5.10). The obtained pVIR fine grain age of PRL23-08 and PRL23-09 agree with the quartz age within 20% uncertainty. On the contrary, the pIRIR fine grain ages for these two samples were still two times the expected ages i.e., 68 ± 3 ka and 126 ± 6 ka, respectively (Table 5.2). Finer grains display higher bleachability in contrast to coarser grains. The findings indicate that pVIRSL exhibits more rapid bleaching under daylight conditions than pIRIRSL in fine and coarse grain fractions. Hence, pVIRSL from fine grains could be an alternative dating method for fluvial samples. The results accord with Fuller et al. (1994). These indicate that pVIR-SAR will be helpful for the challenges associated with fluvial sample dating and is a reliable alternative dating method for accurate age determination. The comparison of coarse grain feldspar ages with fine grain ages can be helpful in predicting the bleachability of the sample. This approach may also prove valuable in scenarios where quartz grains exhibit low sensitivity, and feldspars show inadequate bleachability, such as in samples collected from the Himalayas and Antarctica regions.

Further, the ages of two additional fluvial fine grain samples, PRL23-10 and PRL23-11, collected from the same stratigraphy were determined. These two samples were young. Therefore, the IR were taken as independent ages. For fine grain fraction from fluvial sample PRL23-10, the pVIR age is 1.6 ± 0.1 ka and IR age is 1.0 ± 0.1 ka. The pVIR age is approximately 1.5 times higher than the IR₅₀ age, although the fading characteristics of both signals are comparable (Table 5.2; Fig. 5.9). For PRL23-11, the pVIR age is 2.5 ± 0.1 ka, and IR age is 2.1 ± 0.1 ka, and these agree within 20% of uncertainty (Table 5.2). The ages of both samples are in chronological order, supporting the accuracy of the ages from both protocols.

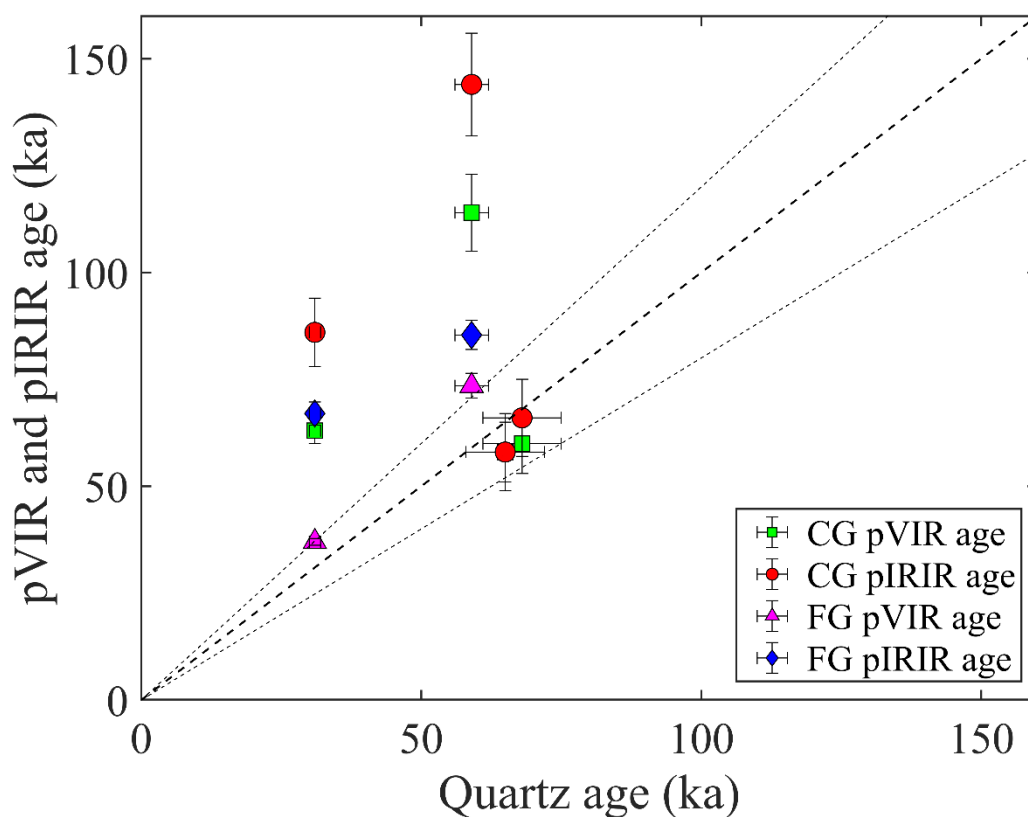


Fig. 5.10: Comparison of coarse and fine grain pVIR and pIRIR ages with the expected ages (quartz ages) of fluvial samples. The black lines represent the 20% uncertainty.

5.6 Conclusions

The study tested the potential of pVIR-SAR protocol for natural polymineral fine- and coarse-grain samples from various depositional environments. The estimated ages were compared with IR (infrared at 50 °C) and pIRIR-SAR (post-infrared infrared at 290 °C) ages. The study provides valuable insights into luminescence dating using pVIR-SAR and pIRIR-SAR protocols on polymineral samples. The findings suggest that pVIR-SAR might offer advantages in terms of signal bleaching efficiency.

The important findings are outlined below:

1. K-feldspar and Na-feldspar yields pVIRSL signal ($\sim 10^5$ counts per second per unit weight). As expected, the pVIRSL signal was not observed from quartz.
2. Athermal fading rates of pVIRSL for both fine- and coarse-grain are equal to or lower than IR and pIRIR signals. Two exceptions were PRL23-06 and PRL23-07,

where pVIRSL fading is greater than pIRIRSL. The results indicate that pVIRSL results from the charges from more stable traps than IRSL and pIRIRSL for most of the samples used in the study. Apart from these samples, in the sodium rich feldspar also pVIRSL resulted from the charges from the non-fading traps.

3. Results suggest that alpha efficiencies of pIRIR are higher than pVIR, which, in turn, are higher than IR for volcanic ash and fluvial sample. However, for pottery samples, the trend of a-values is reversible. This needs further exploration and probing.
4. The pVIR-SAR protocol works well for ash and fine grain polymineral samples. The pVIR-SAR protocol enabled the dating of polymineral fine- and coarse-grain sediments from a few years to ~68 ka. The ages are consistent with geological reasoning and available age controls. The pVIR-SAR protocol for dating polymineral fine- and coarse-grain samples enables the dating of samples where feldspar cannot be fully separated from quartz. Therefore, no mineral separation is required; only HCl and H₂O₂ treatment is required to remove the carbonates and organic material. An additional 10% HF treatment is required for coarse grains to remove the alpha irradiated skin. The estimated ages were in good agreement with the expected ages.
5. The ages estimated using pVIR-SAR for fine grains were in agreement within 20% with quartz ages. Also, the residual doses from the pVIR-SAR protocol are lower than the pIRIR-SAR, indicating better bleachability of pVIR than pIRIR signal for feldspar.

The findings presented herein suggest that pVIR-SAR could be a valuable tool for addressing the dating challenges posed by fluvial samples and may serve as a reliable alternative dating method for precise age determination. Comparing coarse-grain feldspar ages with fine-grain ages can offer insights into predicting the bleachability of the sample. This approach could prove particularly beneficial in scenarios where quartz grains exhibit low sensitivity and feldspars display insufficient bleachability, as often encountered in samples from regions like the Himalayas and Antarctica.

Chapter 6

An Attempt to Date Glacially Polished Samples using Luminescence Surface Exposure Dating

6.1 Introduction

The present Chapter discusses the applicability of pVIRSL signal for rock surface exposure studies using polymineral coarse grains from rock sample. As discussed in Chapter 1, rock surface dating using luminescence is applied to determine the duration of exposure to daylight (exposure ages) of rocks (Habermann et al., 2000; Sohbaty et al., 2011). Sohbaty et al. (2011) and others have successfully dated young samples (age < 1 ka), but for older samples, the application of Luminescence Rock Surface Exposure Dating (LRSED) has been due to challenges to get suitable calibration samples (Freiesleben et al., 2023; Gliganic et al., 2018).

The current Chapter addresses the application of LRSED for samples older than 1 ka and discusses the challenges faced. The glacially polished bedrocks samples from Nubra Valley, Ladakh, located within the Himalayan range were collected. Ladakh has provided an extensive record of multiple glacial and interglacial cycles with advance and retreat of glaciers (Dortch et al., 2013, Ganju et al., 2018; Sharma et al., 2018, 2016; Shukla et al., 2020). The bedrock surfaces were exposed to daylight during marine isotope stage-2 (MIS-2) in glacial stage. The rock samples have an expected age between 18 to 30 ka based on luminescence burial dating of sediments and cosmogenic radionuclides (CRN) (Ganju et al., 2018; Jena et al., 2023). The present study comprised:

1. Measurements of luminescence depth profiles for IRSL and pVIRSL signals for the exposure age estimation.
2. Sensitivity of the luminescence depth model for different parameters was explored. The different environmental factors such as climate, precipitation, and microbial activity influencing the luminescence signals were also explored, and their subsequent interpretation is provided. A petrological analysis using a scanning electron microscope with an energy dispersive X-ray spectrometer (SEM-EDS) of the rock samples was carried out, and the obtained results are discussed.

6.2 Sample and Methodology

The samples were collected from glacially polished bedrocks from four sites in the Nubra Valley, Ladakh ($34^{\circ} 34' 05.2''$ N, $77^{\circ} 37' 09.7''$ E). The samples were collected from locations previously sampled for cosmogenic radionuclide (CRN) dating by Jena et al. (2023).

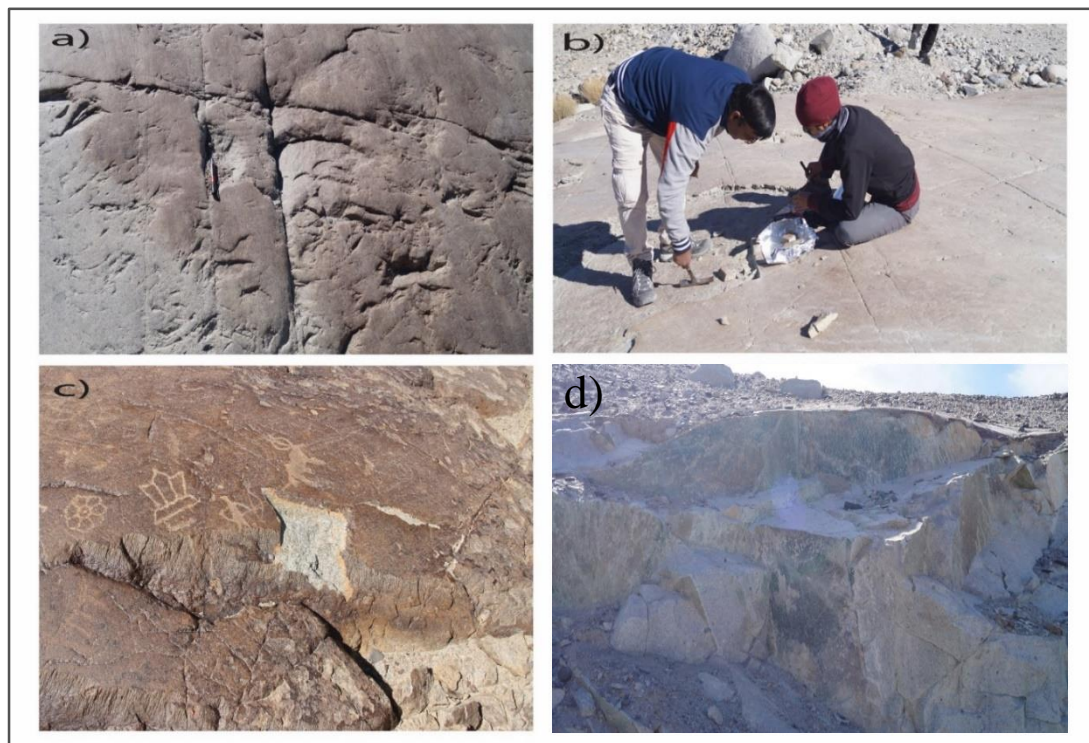


Fig. 6.1: a) Bedrock surface having striations and chatter marks. b) Sample collected from the glacially polished bedrock surface. c) Polished bedrock surface having desert varnish and d) sample collected for calibration with a known age (~15 yrs).

The bedrock samples are feldspar-rich granites. The basic premise was that the samples were exposed to daylight during glacier recession largely by vertical thinning of the ice

(Ganju et al., 2013). Luminescence dating of buried sediments of moraines (Ganju et al., 2018) and ^{10}Be dating of exposed bedrock surface (Jena et al., 2023) suggest that the exposure to daylight should have started from 18 to 30 thousand years. The surfaces of these bedrocks exhibit striations and chatter marks whose preservation suggests that the sub aerial erosion of rock was minimal. The presence of a dark brown desert varnish layer on the samples also suggested that polished rock surfaces did not suffer erosion (Fig. 6.1). A sample from the same rock type, exposed during a road cut created about 15 yrs ago, was collected for calibration to estimate attenuation coefficient (μ) and detrapping rate ($\sigma\phi_0$). Samples were wrapped in aluminium foil in the field to prevent further exposure to light and subsequent processing was under red light ($> 630 \text{ nm}$). The sample preparation procedure is depicted in Fig. 6.2 and the preparation methodology is given in Chapter 2 (subsection 2.4.2.3). The prepared samples were mounted on the stainless-steel discs using silicon oil and measured in a TL/OSL reader.

6.3 Measurement Protocols

Measurements were carried out on the polymineral samples without mineral separation, given that only feldspar responds to IR stimulation (Hutt et al., 1988). Both pIRIR at 225 °C and pVIR at 200 °C signals were measured using the protocol in Table 6.1. Adequate grains were successfully retrieved from all rock slices of ~1 mm thick. Three aliquots for every slice, up to a core depth of 30 mm were measured.

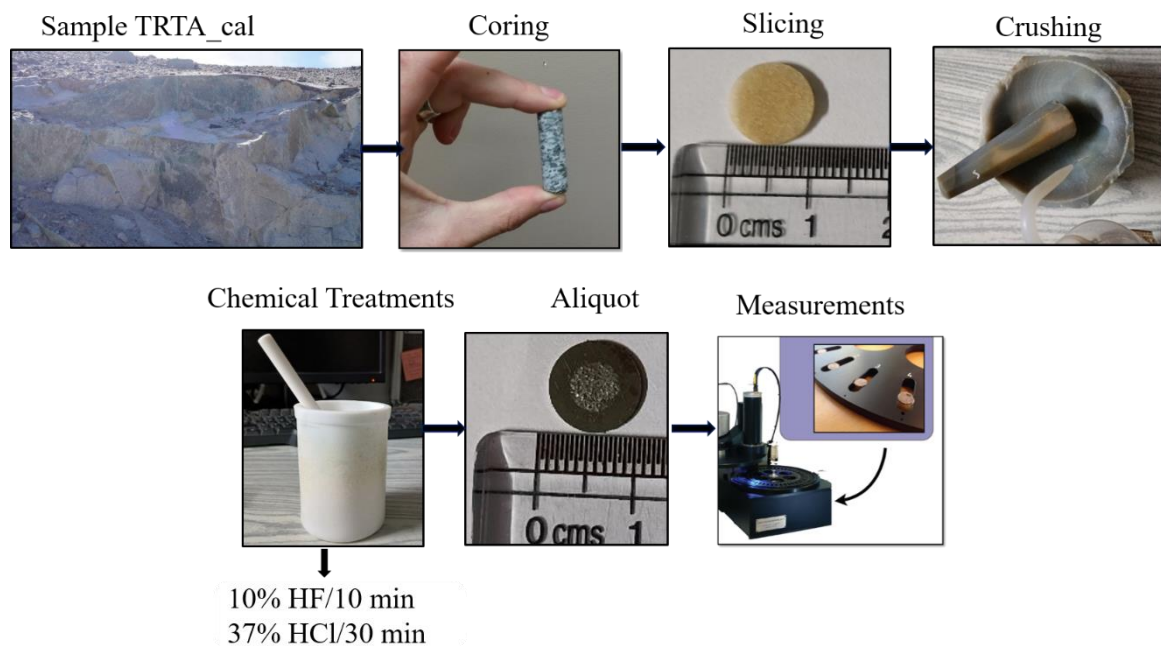


Fig. 6.2: Procedure followed for sample preparation for rock surface exposure dating.

For each aliquot, the natural luminescence signal (L_n) and the subsequent test dose luminescence signal (T_n) were measured as in the first cycle of SAR protocol (Murray and Wintle, 2000). A uniform test dose of ~ 20 Gy was used for all T_n measurements. A preheat temperature of 250 °C for 60 s was used prior to both natural and test dose measurements. The IR at 50 °C for 100 s and pIRIR at 225 °C for 100 s was applied to measure L_n .

Similarly, for pVIRSL measurements, IR at 200 °C (pVIR) was recorded after violet stimulation at 50 °C for L_n . Normalization was done using the average luminescence derived from L_n/T_n values of the five deepest depths that formed a saturation plateau. The normalised luminescence signal was plotted against depth and fitted to the luminescence depth model (Sohbati et al., 2011).

Table 6.1: Protocol for measuring luminescence depth profiles for pIRIRSL and pVIRSL signals.

Step	Treatment (pIRIR225)	Treatment (pVIR200)	Observed measurement
1.	Natural signal	Natural signal	
2.	Preheat at 250 °C for 60 s	Preheat at 250 °C for 60 s	Remove thermally unstable traps
3.	IRSL at 50 °C for 100 s	VSL at 50 °C for 100 s	
4.	IRSL at 225 °C for 100 s	IRSL at 200 °C for 100 s	L_n
5.	Test dose (~ 20 Gy)	Test dose (~ 20 Gy)	
6.	Preheat at 250 °C for 60 s	Preheat at 250 °C for 60 s	Remove thermally unstable traps
7.	IRSL at 50 °C for 100 s	VSL at 50 °C for 100 s	
8.	IRSL at 225 °C for 100 s	IRSL at 200 °C for 100 s	T_n

Athermal fading rates of both IR and pIRIR signals were estimated on grains of the calibration sample as it is bleached under daylight. The calculated weighted mean values of fading rates for IR and pIRIR were 0.8 ± 0.8 % per decade and -1.0 ± 1.1 % per decade, i.e., near zero, respectively (Fig. 6.3). The results indicate that both signals did not suffer from athermal fading. Therefore, IR was employed for exposure ages, as it also exhibits a high degree of bleachability than pIRIR signals (Poolton et al., 2002). Attenuation coefficient (μ) and detrapping rate ($\sigma\phi_0$) in Eq. 1.17 were estimated on the calibration sample from the road cut. These estimated parameters were utilized in model fitting to estimate the exposure ages.

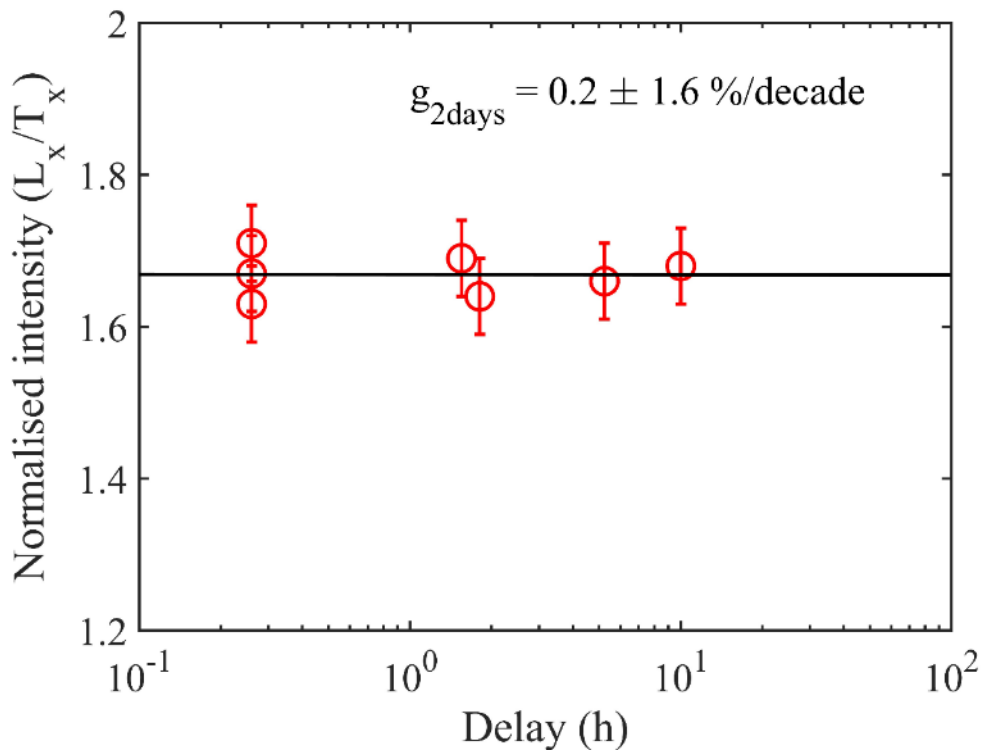


Fig. 6.3: Fading rate measurements for IR signal for TRTX-cal sample. The weighted mean of the fading rate is $0.8 \pm 0.8\%/decade$.

Methodology of Biswas et al. (2023) was used to compute the exposure ages. In brief, the MATLAB code was executed for a total of 10,000 randomly generated paths. The criteria for accepting a path as valid for exposure age calculation was the probability of best fit greater than random numbers generated between 0 and 1. A distribution of exposure ages was obtained from the fitting data of accepted paths. The final exposure age of the bedrock surface was determined as the median value of this normal distribution, with a 1σ uncertainty accounted for in the calculation

6.4 Results and Discussion

6.4.1 Estimation of attenuation coefficient and detrapping rate

Samples used in this study were collected within a radius of less than 1 km, and therefore, it can be assumed that the daylight flux received by all the samples was the same. In the present work, the parameters were obtained empirically by fitting Eq. 1.17 to calibration sample, with known exposure age of 15 yrs (Fig. 6.4). As expected, the data followed a

sigmoidal trend, and parameters were estimated based on the best fit of Eq. 1.17 in the data (Sohbati et al., 2011). The parameters were estimated for both first and second order kinetics for IR and pVIR signals. The estimated values are shown in Fig. 6.4. For IR for μ and $\sigma\phi_0$ are 0.8 mm^{-1} and $1.0 \times 10^{-6} \text{ s}^{-1}$ from first order fitting. Similarly, for second order fitting, the values are 1.1 mm^{-1} and $1.6 \times 10^{-5} \text{ s}^{-1}$, respectively. The μ and $\sigma\phi_0$ for pVIR are 0.6 mm^{-1} and $1.6 \times 10^{-8} \text{ s}^{-1}$ for first order and 0.9 mm^{-1} and $8.0 \times 10^{-8} \text{ s}^{-1}$ for second order.

6.4.2 IRSL depth profiles

IRSL exposure ages for bed rock samples were derived by fitting their normalised luminescence-depth profiles with Eq. 1.17 and using μ and $\sigma\phi_0$ value from the calibration sample. The fitted normalised IRSL signal–depth curves and their exposure ages are summarized in Fig. 6.5 and Table 6.2, respectively. Here also, data points followed a sigmoidal trend (Sohbati et al., 2011).

The scatter in data profiles is possibly due to the heterogeneous distribution of opaque minerals in the granitic rocks (Meyer et al., 2018). Fig. 6.5 shows IR profiles of all samples, and the model was fitted using first order kinetics. The exposure ages of samples are far too young compared to the expected ages of 18 to 30 ka (Table 6.2). The uncertainties on both the positive and negative sides of the ages differ due to the asymmetrical distribution of exposure ages obtained from the accepted paths (Biswas et al., 2023). The potential cause for these substantial uncertainties may be attributed to data scatter.

The model in Eq. 1.17 assumes that the rate of decay of OSL signal due to light follows the first-order decay equation, which results in a single exponential decay of OSL with stimulation light. The assumption is not true for feldspar as IRSL decay of feldspar follows a stretched exponential function (Bailif and Barnett, 1994). Therefore, for feldspar, the general order kinetics (GOK) model is suggested for fitting the luminescence depth model (Biswas et al., 2023; Freiesleben et al., 2022). The decay of IRSL of feldspar in GOK model is described as:

$$\frac{d\bar{n}}{dt} = -\sigma\phi\bar{n}^b \quad (6.1)$$

$$\bar{n} = (1 + (b - 1)\sigma\phi t)^{\frac{1}{1-b}} \quad (6.2)$$

$$\frac{d\bar{n}(x,t)}{dt} = (1 - \bar{n}(x,t))F(x) - \bar{n}^b(x,t)E(x) \quad (6.3)$$

Where \bar{n} is the ratio of the number of trapped electrons (n) to the total number of available traps (N) and b is the order of kinetics.

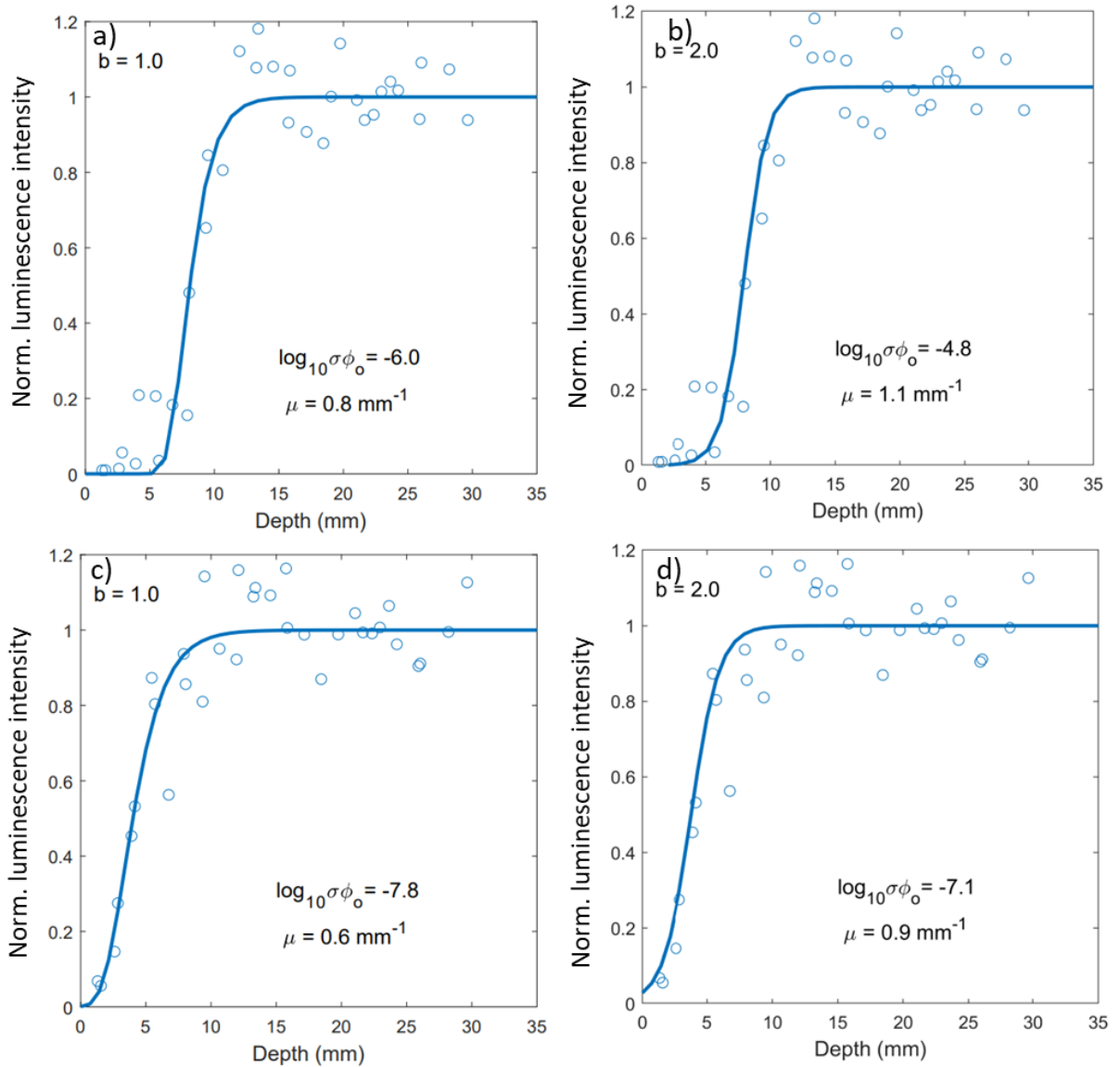


Fig. 6.4: Estimation of parameters such as $\sigma\phi_0$ and μ for the calibration sample TRTX-Cal of known age of 15 yrs for depth profiles for both IR (a and b) and pVIR (c and d) signals for first and second order kinetics. Normalization was done using the average luminescence derived from the five deepest depth L_n/T_n values, which were in saturation.

By putting the values of $E(x)$ and $F(x)$ from Eq. (1.10) and Eq. (1.11), the rate equation of IRSL at depth x (mm) and time t (ka) is:

$$\frac{d\bar{n}}{dt} = (1 - \bar{n}) \frac{D_r}{D_o} - \bar{n}^b \sigma \phi_o e^{-\mu x} \quad (6.4)$$

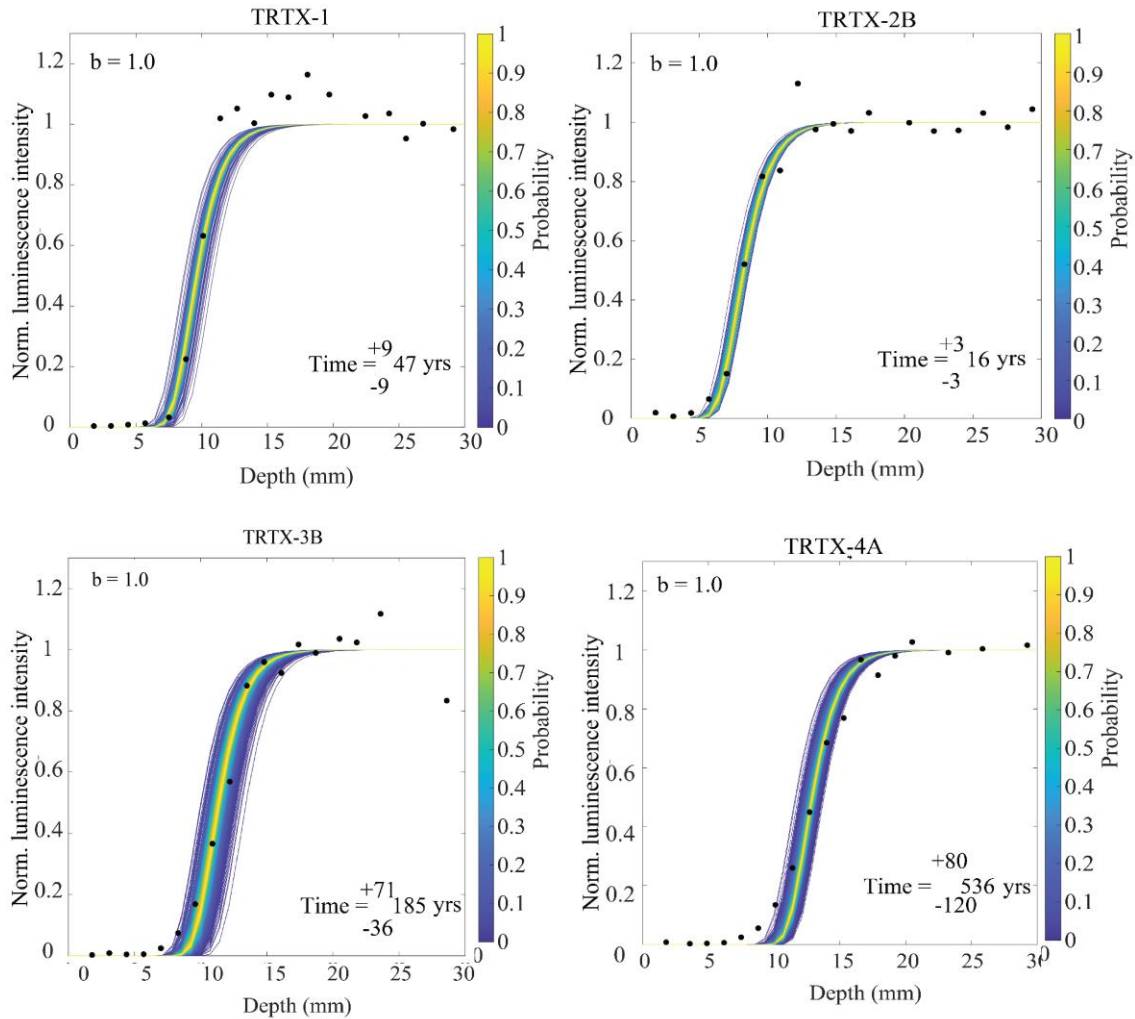


Fig. 6.5: Exposure ages estimated using first order kinetics for IR data for TRTX-1, TRTX-2B, TRTX-3B, and TRTX-4A

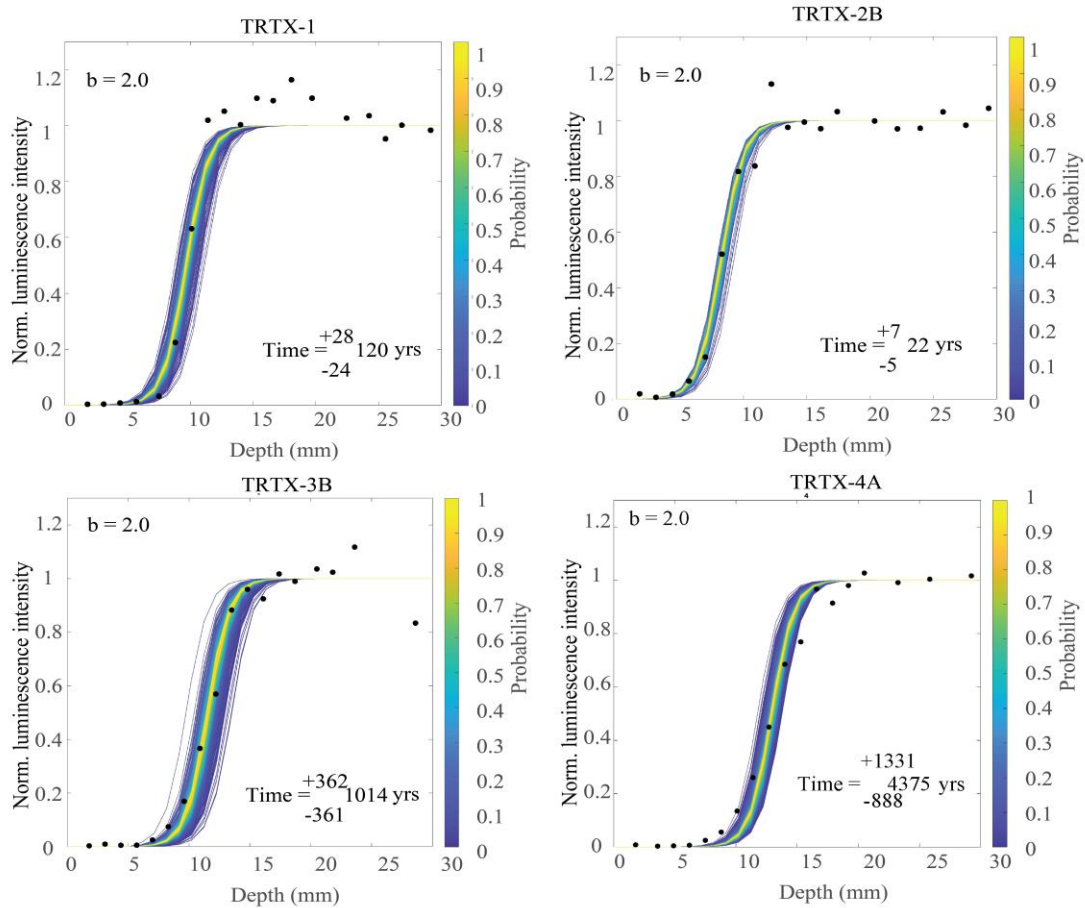


Fig. 6.6: Exposure ages estimated using second order kinetics for IR data for TRTX-1, TRTX-2B, TRTX-3B, and TRTX-4A. The potential cause for these substantial uncertainties may be attributed to data scatter.

Table 6.2: Exposure ages of all samples for IRSL and pVIRSL for both first order and second kinetics.

Sample	First Order		Second Order	
	IR age (yrs)	pVIR age (yrs)	IR age (yrs)	pVIR age (yrs)
TRTX-1	47^{+9}_{-9}	26^{+4}_{-4}	120^{+24}_{-24}	52^{+18}_{-14}
TRTX-2B	16^{+3}_{-3}	19^{+4}_{-4}	22^{+7}_{-5}	31^{+24}_{-5}
TRTX-3B	185^{+71}_{-36}	63^{+12}_{-16}	1014^{+362}_{-362}	218^{+92}_{-92}
TRTX-4	536^{+80}_{-120}	51^{+12}_{-8}	4375^{+1331}_{-888}	154^{+44}_{-44}

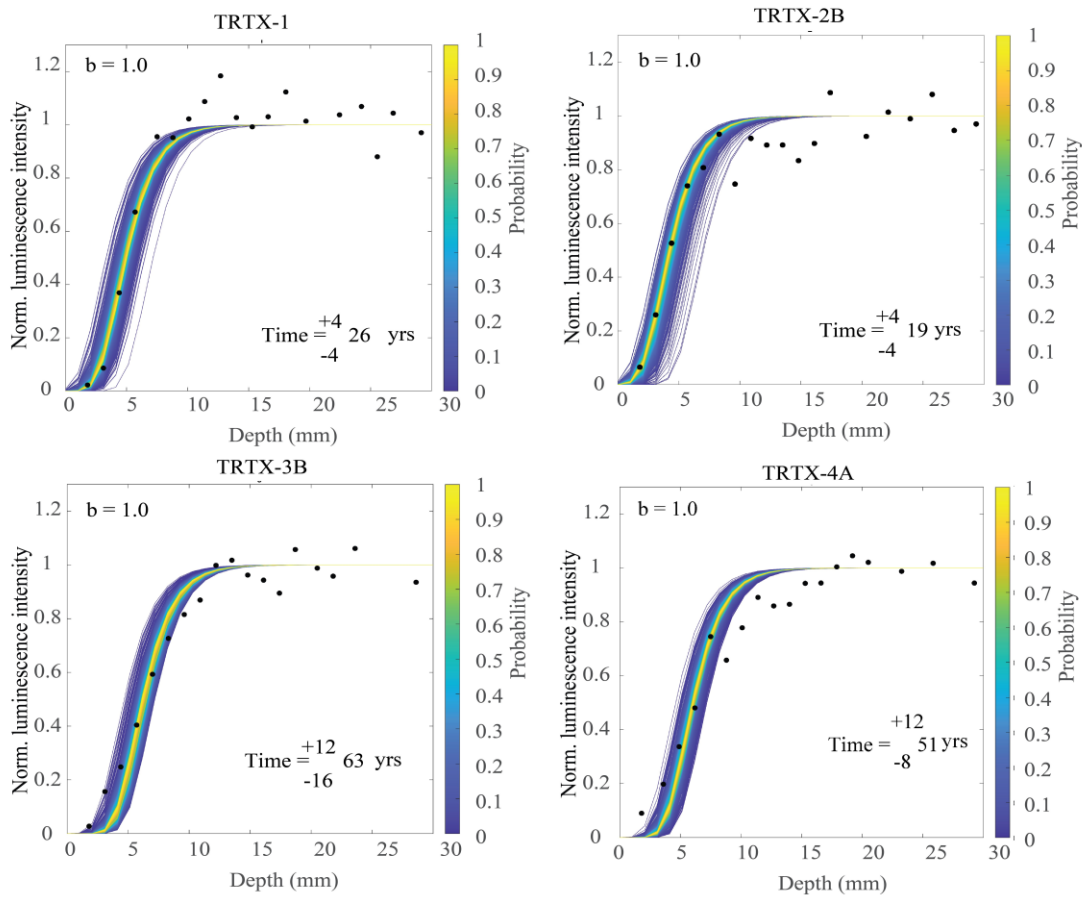


Fig. 6.7: Exposure ages estimated using first order kinetics for pVIR data for TRTX-1, TRTX-2B, TRTX-3B, and TRTX-4A.

For our study, we have used extreme case of second order kinetics i.e., $b = 2$ for fitting the normalised IRSL-depth data following Biswas et al. (2023) which suggest second order kinetics yields exposure ages comparable to the expected ages. The fitted normalised IRSL signal–depth curves using second order kinetics of all dating samples and the associated exposure ages are summarized in Fig. 6.6 and Table 6.2, respectively. The exposure ages estimated using second order increased by one order of magnitude. The underestimation of the expected ages was reduced using second order kinetics but still the expected ages were underestimated. Ages computed using both the first and second order kinetics were 98% and 85% lower than expected ages, respectively. These results suggest that further improvement is needed in the LRSED.

6.4.3 pVIRSL depth profiles

The luminescence depth profile using pVIRSL signal gave a similar underestimation and are given in Table 6.2. Similar results for exposure ages were obtained for pVIRSL. The

pVIR exposure ages for the samples TRTX-1, TRTX-2B, TRTX-3B, and TRTX-4A were found to be 26_{-4}^{+4} a, 19_{-4}^{+4} a, 63_{-16}^{+12} a, and 51_{-8}^{+12} a, respectively, using first order kinetics. The summary of fitted normalised pVIRSL signal depth curves of all dating samples and their exposure ages are given in Fig. 6.7 and Table 6.2, respectively. The expected ages using first order kinetics were underestimated by approximately 99%. The exposure ages for pVIR using second order kinetics fitting of the luminescence depth data for the samples TRTX-1, TRTX-2B, TRTX-3B, and TRTX-4A were 52_{-14}^{+18} a, 31_{-5}^{+24} a, 218_{-92}^{+92} a, and 154_{-44}^{+44} a, respectively. The fitted normalised data for all samples for second order kinetics for pVIR is shown in Fig. 6.8, and a summary of the ages is provided in Table 6.2. The pVIR exposure ages using second order kinetics also showed underestimation in the ages of the bedrock sample. The results indicate that IR data underestimation was lower than pVIR data.

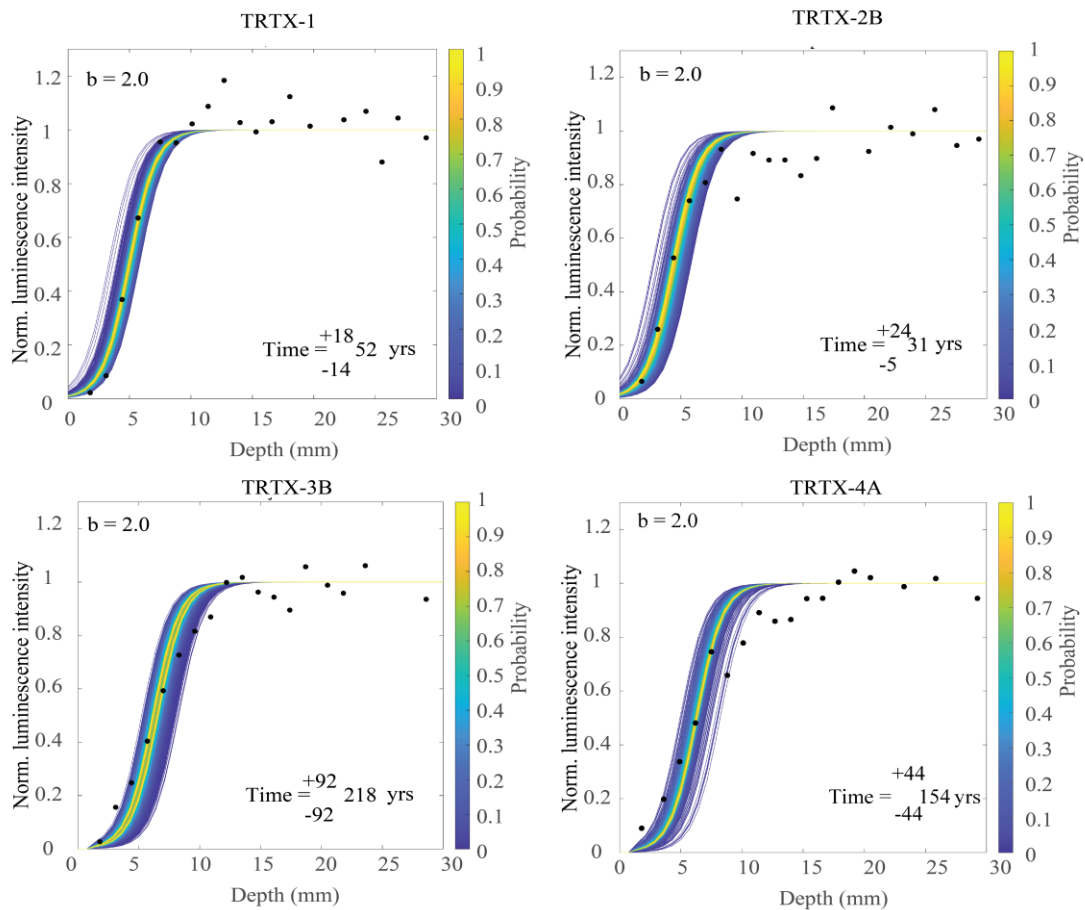


Fig. 6.8: Exposure ages estimated using second order kinetics for pVIR data for TRTX-1, TRTX-2B, TRTX-3B, and TRTX-4A.

There could be several reasons for such a discordance between the obtained ages and the expected ages. A possibility could be that the calibration experiment was inappropriate due to differences in opacities of the rocks due to presence of desert varnish on the rock age samples that would have reduced the light flux to the minerals inside the rocks. Meyer et al. (2018) have suggested that petrological analysis should be carried out to understand the mineralogy of the rock samples. Therefore, mineralogical studies were carried out and discussed in the coming sections.

6.4.4 Scanning electron microscope with energy dispersive X-ray spectroscopy (SEM-EDS)

Scanning electron microscopy with energy dispersive X-ray spectroscopy (SEM-EDS) is used for mineralogical studies of rocks as discussed in Chapter 2 (subsection 2.5.2). The results are discussed below:

6.4.4.1 Role of desert varnish

Desert varnish is a lustrous layer that forms on rocks in dry, arid, and semi-arid environments. Ladakh is a region conducive to desert varnish formation due to its dry climate, low precipitation, high altitude, and limited vegetation. Desert varnish is created through the oxidation of iron and manganese by bacteria, which are abundant in arid environments. Composition of desert varnish depends on local geological conditions, temperature, and environmental factors. Primarily, desert varnish consists of manganese, iron oxides, and clay minerals. The desert varnish forms when wind-blown dust and clay particles settle on the surface of rocks. In Nubra Valley a dark brown layer can be seen in Fig. 6.9, also reported by Dortch et al. (2010). All samples, except the calibration sample had a thick layer of desert varnish. The SEM-EDS measurements showed the presence of MnO and FeO on the surfaces of rock samples (Fig. 6.10). Fig. 6.10 showed that desert varnish was up to 2 mm thick on the rock surfaces, and none was observed on the surface of calibration sample. Desert varnish formation can take thousands of years and therefore it was not seen on a freshly exposed calibration sample (~15 yrs).

As discussed in Chapter 1, luminescence bleaching depth model by Sohbati et al., 2012, suggest two critical factors: the effective detrapping rate ($\sigma\phi_0$) and the attenuation factor (μ) on luminescence-depth profiles. To compare luminescence-depth profiles from different surfaces, the attenuation coefficient and detrapping rate must be the same for all samples. Any variation would result in discordant results. In addition to this, uneven

distribution of non-transparent minerals, common in rocks with diverse mineral varieties like granitic rocks with felsic minerals, can notably affect the ability to reproduce these profiles (Meyer et al., 2018). Because of different mineralogy of calibration sample, parameters estimated from calibration of the model, are not appropriate for age estimations. Furthermore, it can be stated that when rock surfaces are to be dated using the luminescence rock surface exposure dating method, one need to take into account the presence of this thin layer of desert varnish in their studies



Fig. 6.9: Field Photograph of the Study Area: Nubra Valley, Tirith, Ladakh, India ($34^{\circ} 34' 05.2''$ N, $77^{\circ} 37' 09.7''$ E). Desert varnish is prominently observed on all rock formations.

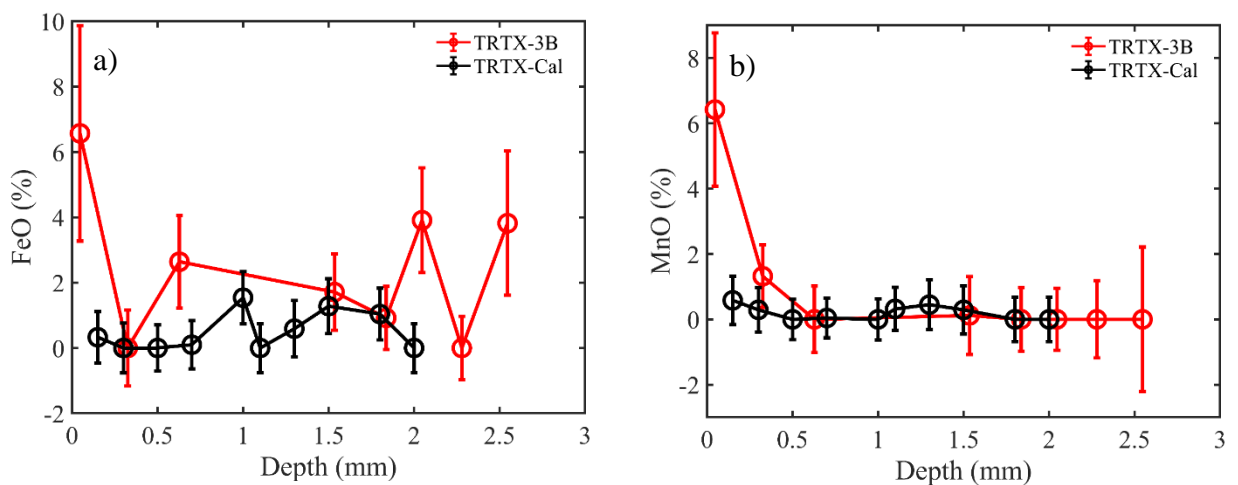


Fig. 6.10: Variation of a) FeO and b) MnO with depth of the rock sample for unknown age (TRTX-3B) and calibration sample (TRTX-cal).

6.4.4.2 Role of Micro fractures

Ladakh region has a geological history marked by numerous cycles of glacial and interglacial activities. Glaciers exert tremendous pressure as they move and flow over the bedrock. The shear stress due to glacial movement can cause the granitic bedrock to form micro-cracks. The weight and movement of the glacier can lead to formation of cracks in both surface and subsurface. In addition, Ladakh experiences temperature fluctuations ranging from approximately $-10\text{ }^{\circ}\text{C}$ to $+20\text{ }^{\circ}\text{C}$, with daytime heating and night time cooling. This leads to a freeze-thaw effect that induce stresses within the granitic rocks leading to development of micro fractures that grow with time. Also, when glaciers retreat the pressure on the bedrock is lowered and this also can lead to the formation or expansion of cracks. The presence of striations on the rocks suggests that the ice mass should have been several meters to a hundred meters.

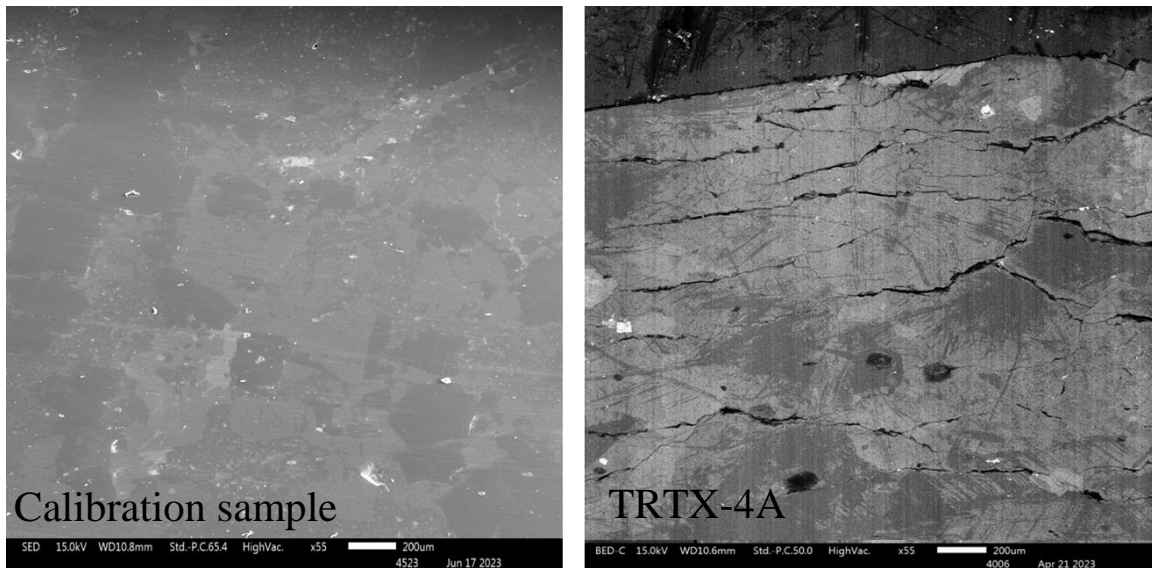


Fig. 6.11: Scanning electron microscope images of the calibration sample and TRTX-4A sample. No microfractures were observed in the calibration samples whereas fractures of thickness of a few micrometers were observed in TRTX-4A samples.

The SEM images of the TRTX-4A and calibration sample are shown in Fig. 6.11. The micro fractures were identified in the TRTX-4A bedrock sample whereas no micro fractures were observed on the calibration sample. It is interesting to see that micro fractures were only observed in the bedrock samples with unknown ages as the surface of these samples has faced glacial and interglacial activities. The calibration sample is a freshly cut sample at 3-4 m below the surface of bedrock. As the density of the micro

fractures decreases with depth, these are absent at the depth from where calibration sample was collected.

Due to fractures in the rock, the light reflections will be different for calibration and unknown age samples. The present study reported the first observation of micro fractures in the natural samples. Another recent study by Andričević et al. (2023) also found that cracks in rocks affect light flux propagation in the rocks. Their study was based on artificial cracks.

Considering these results, it seems that the calibration sample and rock samples behaved differently in terms of optical attenuation of daylight. Freiesleben et al. (2022), based on similar experiences, suggested that the desirable calibration sample should have exposure age of the same order of magnitude as the sample being dated for exposure age.

6.5 Conclusion

This chapter explored the applicability and challenges of luminescence dating on older samples exposed during marine isotope stage-2 (MIS-2) collected from Nubra Valley, Ladakh, Himalaya. The surfaces of the bedrock samples were glacially polished. The samples have expected an age of 18-30 ka (Ganju et al., 2018; Jena et al., 2023). The IR and pVIRSL signals were used to find the exposure ages of the samples. The methods suggested by Sohbaty et al. (2011) and Biswas et al. (2023) were used to find the exposure ages of the samples. A sample of known age (~15 yrs) was used to find the parameters such as attenuation coefficient and de-trapping rate. Both IR and pVIR signals followed the sigmoidal trend with depth in the rocks, as expected by the model (Sohbaty et al., 2011). The parameters estimated from a known age sample were used to calculate the unknown exposure ages of samples. The main conclusions of the study are listed below:

1. The attenuation coefficient and de-trapping rate derived from the calibration method resulted in an underestimation of the ages. The second order kinetics improved the ages, but still, ages were underestimated significantly. These findings suggest that the parameters derived from calibration were inappropriate for the estimation of ages for samples with unknown ages.
2. The underestimation in age estimations could be due to variations in rock opacity induced by the presence of desert varnish on rock surfaces. Presence of a dark brown layer on their uppermost surfaces, extending to a depth of a few millimetres, notably

darker than the fresh rock sample beneath. This observation implies a mineralogical alteration within the rock material. SEM-EDS analyses confirmed the presence of FeO and MnO on the surface of rock samples and its absence in the case of calibration sample. FeO and MnO confirmed desert varnish on rock samples of ~2 mm thick. Consequently, the study reminds the necessity of accounting for the presence of the desert varnish layer in luminescence-based surface exposure dating methodologies.

3. SEM images of the samples showed the presence of micro-fractures in the rocks. No fractures were observed on the calibration sample. Cracks can form in glacially polished granitic bedrock due to a combination of factors, including glacial activity, temperature fluctuations, abrasion, and geological conditions. These factors can lead to the formation and propagation of cracks in the granitic bedrock over geological time scales. As the density of the micro fractures decreases with depth. The calibration sample was taken from a freshly exposed surface resulting from a road excavation conducted during 2006 and 2007, at a depth of a few meters from the bedrock surface. At this depth, cracks may be absent and hence, not observed in the calibration sample. Due to fractures in the rock, the light reflections will be different for calibration and unknown age samples. Hence, the calibration parameters may not be suitable for the estimation of exposure of older samples.

The results presented in this Chapter provided an insight into the need for a more nuanced understanding of field based variables and their modelling.

Chapter 7

Summary and Future Prospect

7.1 Summary

Our study encompasses a comprehensive exploration of the various spectral regions of feldspar, systematically assessing their athermal stability through different stimulation and emission combinations. The luminescence production mechanism of feldspar is complex due to its complex defect structure and has not been fully understood yet. The current understanding of the luminescence mechanism of feldspar is based on the existence of a principal trap, also known as a dosimetric trap. We rigorously investigated aspects associated with the mechanism of luminescence in feldspar and studied the traps and recombination centres responsible for luminescence in feldspar.

The specific objectives of the thesis were to

1. Investigate the luminescence characteristics of different spectral regions of feldspar with varied stimulation wavelengths, aiming to identify signals with minimal fading tendencies.
2. Develop dating protocols for the signals with minimal fading identified in Objective #1 and validate their applicability for dating samples from diverse geological environments.
3. Establish a methodology for dating the surfaces of rocks and compare the ages obtained using new signals with minimum fading with the signals previously used for dating in the context of glacially polished samples.

A summary of the results presented in the thesis is given below:

1. Multispectral luminescence studies using the different combinations of stimulation and detection spectral windows were carried out. The athermal fading rates using both single stimulation and sequential double stimulation combinations were estimated. A single stimulation experiment showed that irrespective of the detection window, stimulation with IR, green, blue, and violet stimulation led to similar fading rates of ~7% per decade. The fading rates were higher for the broad-UV emission (260-400

nm), followed by the narrow-UV (327-353 nm), with the blue window providing the lowest fading rates (320-520 nm).

2. Double stimulation experiments led to a significant reduction in the fading rates in the second stimulation. When energies of both applied stimulations were in the increasing order of energies (IR-green, IR-blue, IR-violet, green-blue, and blue-violet), the fading rates for each second stimulation increased with an increase in the excitation energy of the second stimulation, possibly due to the recapture of electrons from the high energy stimulation (Jain and Ankjærgaard, 2011; Kumar et al., 2020) and the instability of recombination centres emitting in the UV window (Clarke and Rendell, 1997; Thomsen et al., 2008). These observations need further investigation to further elucidate the mechanism of production of luminescence in feldspars.
3. Finite signals with IR stimulation after green, blue, and violet light stimulations were observed. The fading rates of IRSL after green, blue, and violet decreased with an increase in the energy of stimulation-1. This could be due to an increase in the energy of stimulation-1, which results in a larger number of distant donor-acceptor pairs participating in the IRSL signal.
4. Among all possible combinations of stimulation and observation bands post violet IRSL (both violet stimulation at 50 °C and IR at 100 °C for 100 s; pVIRSL) provided a minimal fading rate ($g_{AV} = 0.0 \pm 0.1\%$ per decade). The stability of pVIRSL was tested on several geological samples, and near-zero fading was observed in almost all samples. However, there was a single exception for which a small fading value was observed (PRL5; $g_{AV} = 3.4 \pm 0.6\%$ per decade). The near zero fading rates of pVIRSL make it a candidate for the dating of sediments from geological and archeological contexts.
5. Experiments suggested that violet stimulation at 50 °C causes photo-transfer of charges from TL traps deeper than 500 °C to the shallower IR sensitive traps (<500 °C). The IR stimulation following violet exposure then stimulates the charges from the shallower IR sensitive traps to provide pVIRSL. Repeated measurements of pVIRSL at 50 °C on the same sample without any irradiation suggested that deep traps (TL >500 °C) serve as reservoir traps, which consistently supplies electron to shallower traps. The deep reservoir traps lie below the principal trap of feldspar. Photo-transferred charges provide luminescence only in the blue window due to the availability of recombination centres emitting in the blue window after the violet stimulation. In most of the samples,

the pVIRSL at 50 °C resulted from the photo-transfer of charges from traps (>500 °C). However, pVIRSL at 200 °C had a dual origin: a) photo-transfer from deep traps and b) recapture from the principal trap, in all samples.

6. Reservoir traps sensitive to violet stimulation at 50 °C are bleachable under daylight. This makes pVIRSL suitable for dating. Typically, 60 min of daylight exposure reduced the pVIRSL to a residual dose of a few Gy (10% of the equivalent dose). An augmented SAR protocol for pVIRSL (pVIR-SAR) is developed based on a detailed study with optimized measurement conditions. The optimised parameters are: preheat at 250 °C for 60 s, pVIRSL measurement at 200 °C for 100 s, bleaching using a sequence of violet and IR stimulation at 350 °C for 200 s, and a test dose in the range of 50 to 80% of the expected equivalent dose. These parameters ensured that the pVIR-SAR protocol satisfied all the criteria for the use of a SAR protocol. The pVIR-SAR provided low recuperation doses (< 5%), good recycling and dose recovery (within 10% of unity), near zero athermal fading, and low residual doses on daylight bleaching (< 21 Gy). Its use leads to age estimates consistent with available controls and with geological reasoning. So far, this was tested in the age range of 6 to >286 ka. The pVIR-SAR dose response curve suggests a laboratory saturation dose ($2D_0 \sim 1000$ Gy), implying that under a normal radiation dose environment, ages up to 300 ka (assuming a dose rate of 3 Gy/ka) can be obtained. The residual doses from the pVIR-SAR protocol are lower than the pIRIR-SAR, indicating better bleachability of pVIRSL than pIRIRSL.
7. K-feldspar and Na-feldspar both give pVIRSL signal ($\sim 10^5$ counts per second per unit weight), and quartz does not give the pVIRSL. This provides an opportunity to use pVIR-SAR protocol to polymineral fine- and coarse-grain samples without any mineral separation, as pVIR stimulates feldspars only. Therefore, pVIR-SAR protocol enables the dating of samples where feldspar cannot be fully separated from quartz. The pVIR-SAR protocol worked well for volcanic ash and fine grain polymineral samples for a range of samples dated to a few years to up to 68 ka.
8. Athermal fading rates of pVIRSL for both fine- and coarse-grain were lower than the IRSL and pIRIRL signals. The results indicate that pVIRSL originates from the charges from stable traps than IRSL and pIRIRSL for most of the samples investigated in the study. In addition to these samples, the sodium-rich feldspar sample also exhibited a near-zero fading in the pVIRSL signal. Two exceptions observed were fine

grain PRL23-10 and PRL23-11 sample, where the XRD-data showed that these samples were rich in sanidines. Polymeris et al. (2022) reported that sanidines have more intense fading among three groups of k-feldspar. For these samples, pVIRSL fading was greater than pIRIRSL.

9. The study examined the dating of polymineral fluvial samples and observed the limited bleachability of coarse-grain feldspars in the context of the pIRIRSL signal for two samples. Interestingly, for the same set of samples, the pVIR-SAR dating of fine-grain polymineral feldspar provided ages that were consistent with independent ages, with an uncertainty of within 20%. This suggests that pVIR-SAR for fine-grained sediments can be a valuable dating method in situations where coarse-grain quartz exhibits low sensitivity and feldspar pIRIRSL signals display slower bleaching rates, such as in the case in regions like the Himalayas and Antarctica.
10. Furthermore, the thesis explored the applicability and challenges of using luminescence dating for old exposed rock samples from Nubra Valley, Ladakh, Himalayas. Geological evidence suggests that the surface of the bedrock was glacially polished. Thus, the luminescence of the samples was expected to be saturation/equilibrium when it was exposed to daylight after the retreat of the glacier. The samples have an expected exposure age of 18 to 30 ka (Ganju et al., 2018; Jena et al., (2023)). The IRSL and pVIRSL signals were used to measure the exposure ages of the samples using the methodology suggested by Sohbaty et al. (2011) and Biswas et al. (2023). Both IRSL and pVIRSL signals followed the sigmoidal trend with depth in the rock as predicted by the model (Sohbaty et al., 2011), but an age underestimation was seen. The possible reasons for such a large discordance were explored. The underestimation could be due to improper fitting, the difference in surface characteristics of the calibration sample and actual sample, and structural microfractures. The use of second order kinetics improved the ages, but still, the ages were underestimated by approximately 85%. The role of desert varnish and structural micro-cracks inside the rocks that modify the apparent transparency of the sample and luminescence depth profiles were explored. Scanning electron microscopy with energy dispersive X-ray spectroscopy (SEM-EDS) analysis showed the presence of desert varnish and cracks in the undated rock samples. The calibration sample, however, had no desert varnish and cracks, indicating that the parameters derived from the calibration sample were not suitable for estimating the ages of the unknown age

samples. These suggest that the parameters derived from young calibration samples are inappropriate for age estimation of old samples. These results support the modelling results of Freiesleben et al. (2022) that to find the exposure ages of the samples, a calibration sample of exposure time of the same order of magnitude as the unknown exposure time is required. Consequently, the study led to the need for caution in the choice of calibration samples and their similarity with undated surfaces in relation to secondary effects like desert varnish and microfractures. It also highlights prospects for refining luminescence dating techniques and addressing the complexities associated with surface exposure dating of polished rock samples.

In conclusion, the thesis work contributes to the advancement of luminescence dating by expanding our understanding of feldspar luminescence and offering a viable alternative for dating samples from various geological settings. It also sheds light on the challenges and complexities associated with dating exposed rock surfaces, highlighting the need for continued refinement of luminescence dating techniques in these contexts.

7.2 Future Outlook

Projecting into the future, the properties of pVIRSL open new possibilities for areas when quartz has low sensitivity and feldspar has poor bleachability and athermal fading. In the Indian context, it will be interesting to test this signal for the dating of glacial moraines—both for their academic and societal importance. Other areas of applications are discussed below.

1. The luminescence production mechanism of feldspar is complex due to its complex defect structure. The present study used deep traps beneath the principal trap of feldspar. It is desirable to attempt a better understanding of the feldspar mechanism to extend the dating limit of luminescence. Several techniques are used to understand the mechanism of feldspar and their application in dating. These include a) Infrared-photoluminescence (IR-PL), b) infrared-radioluminescence (IR-RL), c) post-IR IRSL (pIRIRSL), d) multiple elevated temperatures pIRIRSL (MET-pIRIRSL), and e) photo-transferred thermoluminescence (PTTL). Both IR-PL and IR-RL result from the trapping of electrons to their centres and provide information about electron traps. The remaining luminescence signals result from the recombination centres, providing information about holes at recombination centres. The combined studies from these

methods can provide further insight into the luminescence production mechanism and hence provide more robust methods for feldspar dating and its new applications in various fields.

2. As violet stimulation bleaches the signal from other minerals present along with feldspar in the pVIR-SAR protocol, the signal can be used for the dating of the samples where feldspar is present in the inclusions and cannot be separated from quartz using chemical treatments on the lines similar to Huntley et al. (1993). Hence, a new application of luminescence to date inclusion can be developed.
3. Emission of pVIRSL in sodium rich feldspar is also attractive as it is devoid of internal radioactivity and is widely available in nature (Sohbati et al., 2013). The pVIRSL signal yielded the near zero fading results in sodium rich feldspars. Therefore, the pVIR-SAR protocol for Na-Feldspar dating can be a new area of application.
4. One of the advantages of the pVIR-SAR protocol is that it can be used without the need to separate individual minerals from the sample. This is significant because mineral separation can be a time-consuming and technically challenging process. The pVIR stimulation probes the stable signal from feldspar, and it can pick selectively feldspar signal from the polymineral. Therefore, it could be a potential candidate for in situ dating of surfaces in future missions to planets like Mars. This is important because it provides insights into the timeline of geological processes and the history of the celestial bodies. This information is crucial for understanding how these bodies have changed over time and what geological processes have shaped them.
5. As discussed in Section 7.1, in the rock surface exposure studies, both the IR and pVIR signals underestimated ages. Petrological analysis suggested the presence of desert varnish and microfractures on the bedrock surfaces. The effect of desert varnish and microfractures needs to be quantified and incorporated into the surface exposure studies. The time taken for the development of desert varnish varies from a few decades to thousands of years, depending on climate, rock type, and microbial activity. Similarly, the formation of microfractures depends on glacial retreatment and climatic conditions. These two factors affect the light transmission and propagation through the rock by modulating the attenuation coefficient, ultimately reducing the detrapping rate. Because of the build-up/thickening of desert varnish, assumptions including the negligible trapping rate due to the radioactivity of the rock,

constant attenuation coefficient, and detrapping rate will not be applicable. As the detrapping rate decreases with time, the trapping rate begins to assume significance. Therefore, the trapping rate needs to be considered in the model, and a new theoretical framework needs to be developed. Furthermore, we need a quantitative estimation of the attenuation coefficient as a function of time in order to refine the model calculations. A systematic experimental study for the correlation of variable environmental conditions and desert varnish build-up needs to be carried out to develop time dependent mathematical model that incorporates the changing attenuation coefficients and detrapping rates. Further, the time-dependent model needs to be tested on samples of known age to assess its accuracy. Beyond a particular thickness, desert varnish blocks further penetration of daylight into the rock. As a result, the luminescence of the burial following exposure will start. From this burial, the formation time of desert varnish to a particular thickness can be estimated. This will be a new application of surface exposure dating for such studies.

Bibliography

- Aitken, M. J., Tite, M. S., Reid, J., 1964. Thermoluminescent dating of ancient ceramics. *Nature* 202, 1032-1033.
- Aitken, M. J., Zimmerman, D. W., Fleming, S. J., 1968. Thermoluminescent dating of ancient pottery. *Nature* 219, 442-445.
- Aitken, M.J. 1998. *An introduction to Optical Dating*. Oxford University Press. Oxford.
- Aitken, M.J., 1985. *Thermoluminescence Dating*, vol. 359. Academic Press, London, ISBN 0-12-046380-6.
- Akhilesh, K., Pappu, S., Rajapara, H.M., Gunnell, Y., Shukla, A.D., Singhvi, A.K., 2018. Early Middle Palaeolithic culture in India around 385–172 ka reframes Out of Africa models. *Nature* 554, 97.
- Andričević, P., Sellwood, E. L., Eppes, M. C., Kook, M., & Jain, M., 2023. Passive atomic-scale optical sensors for mapping light flux in ultra-small cavities. *Scientific Reports*, 13(1), 5309.
- Anil, D., Chauhan, N., Ajithprasad, P., Devi, M., Mahesh, V., Khan, Z., 2022. An Early Presence of Modern Human or Convergent Evolution? A 247 ka Middle Palaeolithic Assemblage from Andhra Pradesh, India. *J. Archaeol. Sci. Reports* 45, 103565. <https://doi.org/10.1016/j.jasrep.2022.103565>.
- Anil, D., Devi, M., Blinkhorn, J., Smith, V., Sanghode, S., Mahesh, V., Khan, Z., Ajithprasad, P., Chauhan, N., 2023. Youngest Toba Tuff deposits in the Gundlakamma river basin, Andhra Pradesh, India and their Role in Evaluating Late Pleistocene Behavioural Change in South Asia. *Quaternary Research*, 1-12. <https://doi.org/10.1017/qua.2023.13>.
- Ankjærgaard, C., Jain, M., Wallinga, J., 2013. Towards dating Quaternary sediments using the quartz Violet Stimulated Luminescence (VSL) signal. *Quat. Geochronol.* 18, 99–109. <https://doi.org/10.1016/j.quageo.2013.06.001>
- Auclair, M., Lamothe, M., Huot, S., 2003. Measurement of anomalous fading for feldspar IRSL using SAR. *Radiat. Meas.* 37, 487–492.

- Bailif, I.K., Barnett, S.M., 1994. Characteristics of infrared-stimulated luminescence from a feldspar at low temperatures. *Radiat. Meas.* 23, 541–545 (1994). [https://doi.org/10.1016/1350-4487\(94\)90096-5](https://doi.org/10.1016/1350-4487(94)90096-5)
- Bailiff, I. K., 2022. Luminescence dating of pottery and bricks. In *Encyclopedia of Geoarchaeology* (pp. 1-6). Cham: Springer International Publishing. https://doi.org/10.1007/978-3-030-44600-0_49-1
- Baril, M.R., Huntley, D.J., 2003. Infrared stimulated luminescence and phosphorescence spectra of irradiated feldspars. *J. Phys. Condens. Matter* 15, 8029–8048. <https://doi.org/10.1088/0953-8984/15/46/018>
- Baril, M.R., Huntley, D.J., 2003. Optical excitation spectra of trapped electrons in irradiated feldspars. *J. Phys. Condens. Matter* 15, 8011–8027. <https://doi.org/10.1088/0953-8984/15/46/017>
- Biswas, R.H., Herman, F., King, G.E., Braun, J., 2018. Thermoluminescence of feldspar as a multi-thermochronometer to constrain the temporal variation of rock exhumation in the recent past. *Earth Planet. Sci. Lett.* 495, 56–68. <https://doi.org/10.1016/j.epsl.2018.04.030>
- Biswas, R.H., Pathan, A.N., Malik, J.N., 2023. General order kinetics model for OSL rock surface exposure dating. *Proc. Indian Natl. Sci. Acad.* <https://doi.org/10.1007/s43538-023-00172-y>
- Bailiff, I.K., Poolton, N.R.J., 1991. Studies of charge transfer mechanisms in feldspars. *Int. J. Radiat. Appl. Instrumentation. Part 18*, 111–118. [https://doi.org/10.1016/1359-0189\(91\)90101-M](https://doi.org/10.1016/1359-0189(91)90101-M)
- Biswas, R.H., Williams, M.A.J., Raj, R., Juyal, N., Singhvi, A.K., 2013. Methodological studies on luminescence dating of volcanic ashes. *Quat. Geochronol.* 17, 14–25. <https://doi.org/10.1016/j.quageo.2013.03.004>
- Bøtter-Jensen, L., Thomsen, K.J., Jain, M., 2010. Review of optically stimulated luminescence (OSL) instrumental developments for retrospective dosimetry. *Radiat. Meas.* 45, 253–257. <https://doi.org/10.1016/j.radmeas.2009.11.030>
- Buckland, C.E., Bailey, R.M., Thomas, D.S.G., 2019. Using post-IR IRSL and OSL to date young (< 200 yrs) dryland aeolian dune deposits. *Radiat. Meas.* 126, 106131. <https://doi.org/10.1016/j.radmeas.2019.106131>

- Buylaert, J., Jain, M., Murray, A.S., Thomsen, K.J., Thiel, C., Sohbati, R., 2012. A robust feldspar luminescence dating method for Middle and Late Pleistocene sediments. *Boreas* 41, 435–451.
- Buylaert, J.P., Murray, A.S., Thomsen, K.J., Jain, M., 2009. Testing the potential of an elevated temperature IRSL signal from K-feldspar. *Radiat. Meas.* 44, 560–565.
- Buylaert, J.P., Murray, A.S., Thomsen, K.J., Jain, M., 2009. Testing the potential of an elevated temperature IRSL signal from K-feldspar. *Radiat. Meas.* 44, 560–565. <https://doi.org/10.1016/j.radmeas.2009.02.007>.
- Buylaert, J.P., Thiel, C., Murray, A.S., Vandenberghe, D.A.G., Yi, S., Lu, H., 2011. IrsL and post-ir irsl residual doses recorded in modern dust samples from the chinese loess plateau. *Geochronometria* 38, 432–440. <https://doi.org/10.2478/s13386-011-0047-0>
- Buylaert, J.P., Vandenberghe, D., Murray, A.S., Huot, S., De Corte, F., Van den Haute, P., 2007. Luminescence dating of old (>70 ka) Chinese loess: A comparison of single-aliquot OSL and IRSL techniques. *Quat. Geochronol.* 2, 9–14. <https://doi.org/10.1016/j.quageo.2006.05.028>
- Chauhan, N., Choi, J. H., Kim, J. Y., & Lee, G., 2015. Application of newly developed NCF-SAR protocol to Quaternary sediments from Suncheon and Jeongok, South Korea. *Geosciences Journal*, 19, 407-413.
- Chandel, H. N., Patel, A. D., Vaghela, H. R., & Ubale, G. P., 2006. An effective and reusable sampling pipe for luminescence dating. *Ancient TL*, 24(1), 21-22.
- Chauhan, N., Selvam, T. P., Anand, S., Shinde, D. P., Mayya, Y. S., Feathers, J. K., & Singhvi, A. K., 2021. Distribution of natural beta dose to individual grains in sediments. *Proceedings of the Indian National Science Academy*, 87, 613-627. <https://doi.org/10.1007/s43538-021-00057-y>.
- Chauhan, N., Singhvi, A. K., 2011. Distribution of SAR paleodoses due to spatial heterogeneity of natural beta dose. *Geochronometria* 38, 190-198.
- Chawla S, Gundurao, T.K., Singhvi, A.K., 1998. Quartz thermoluminescence: dose and dose rate effects and their implications. *Radiat. Meas.* 29 (1), 53–63.
- Clark, R. J., & Sanderson, D. C. W., 1994. Photostimulated luminescence excitation spectroscopy of feldspars and micas. *Radiat. Meas*, 23, 641-646.

Clarke, M.L., Rendell, H.M., 1997. Infra-red stimulated luminescence spectra of alkali feldspars. *Radiat. Meas.* 27, 221–236.

Colarossi, D., Duller, G.A.T., Roberts, H.M., 2018. Exploring the behaviour of luminescence signals from feldspars: Implications for the single aliquot regenerative dose protocol. *Radiat. Meas.* 109, 35–44. <https://doi.org/10.1016/j.radmeas.2017.07.005>.

Colls, A.E., Stokes, S., Blum, M.D., Straffin, E., 2001. Age limits on the Late Quaternary evolution of the upper Loire River. *Quat. Sci. Rev.* 20, 743–750. [https://doi.org/10.1016/S0277-3791\(00\)00048-2](https://doi.org/10.1016/S0277-3791(00)00048-2)

Daniels, F., Boyd, C. A., Saunders, D. F., 1953. Thermoluminescence as a research tool. *Science* 117, 343-349.

Devi, M., Chauhan, N., Rajapara, H., Joshi, S., Singhvi, A.K., 2022. Multispectral athermal fading rate measurements of K-feldspar. *Radiat. Meas.* 156, 106804. <https://doi.org/10.1016/j.radmeas.2022.106804>.

Devi, M., Chauhan, N., & Singhvi, A. K., 2024. Post-violet infrared stimulated luminescence (pVIRSL) dating protocol for potassium feldspar. *Quaternary Geochronology*, 79, 101487. <https://doi.org/10.1016/j.quageo.2023.101487>

Deer, W. A., Howie, R. A., & Zussman, J. 2013. An introduction to the rock-forming minerals. Mineralogical Society of Great Britain and Ireland. <https://doi.org/10.1180/DHZ>

Ditlefsen, C., Huntley, D.J., 1994. Optical excitation of trapped charges in quartz, potassium feldspars and mixed silicates: The dependence on photon energy. *Radiat. Meas.* 23, 675–682. [https://doi.org/10.1016/1350-4487\(94\)90003-5](https://doi.org/10.1016/1350-4487(94)90003-5)

Dogan, T., Çetin, H., Yegingil, Z., Topaksu, M., Yüksel, M., Duygun, F., ... & Yegingil, İ. (2015). Optically stimulated luminescence dating of Holocene alluvial fans, East Anatolian Fault System, Turkey. *Radiation Effects and Defects in Solids*, 170(7-8), 630-644.

Dortch, J. M., Owen, L. A., & Caffee, M. W., 2010. Quaternary glaciation in the Nubra and Shyok valley confluence, northernmost Ladakh, India. *Quaternary Research*, 74(1), 132-144.

Dortch, J. M., Owen, L. A., & Caffee, M. W., 2013. Timing and climatic drivers for glaciation across semi-arid western Himalayan–Tibetan orogen. *Quaternary Science Reviews*, 78, 188-208.

- Duller, G.A.T., 1997. Behavioural studies of stimulated luminescence from feldspars. *Radiat. Meas.* 27, 663–694. [https://doi.org/10.1016/S1350-4487\(97\)00216-3](https://doi.org/10.1016/S1350-4487(97)00216-3)
- Duller, G.A.T., 2003. Distinguishing quartz and feldspar in single grain luminescence measurements. *Radiat. Meas.* 37, 161–165.
- Duller, G.A.T., Bøtter-Jensen, L., 1993. Luminescence from potassium feldspar stimulated by infrared and green light. *Radiat. Prot. Dosimetry* 47, 683–688. <https://doi.org/https://doi.org/10.1093/oxfordjournals.rpd.a081832>
- Duller, G.A.T., Wintle, A.G., 1991. On infrared stimulated luminescence at elevated temperatures. *Int. J. Radiat. Appl. Instrumentation. Part 18*, 379–384. [https://doi.org/10.1016/1359-0189\(91\)90003-Z](https://doi.org/10.1016/1359-0189(91)90003-Z).
- Duval, M., Guilarte, V., Campaña, I., Arnold, L., Miguens, L., Iglesias, J., González-Sierra, S., 2018. Quantifying hydrofluoric acid etching of quartz and feldspar coarse grains based on weight loss estimates: implication for ESR and luminescence dating studies. *Ancient TL*, Vol. 36(1), 1-14.
- Fattahi, M., Stokes, S., 2003. Red luminescence from potassium feldspar for dating applications: a study of some properties relevant for dating. *Radiat. Meas.* 37, 647–660. [https://doi.org/10.1016/S1350-4487\(03\)00246-4](https://doi.org/10.1016/S1350-4487(03)00246-4)
- Fattahi, M., Stokes, S., 2000. Extending the time range of luminescence dating using red TL (RTL) from volcanic quartz. *Radiat. Meas.* 32, 479–485. [https://doi.org/10.1016/S1350-4487\(00\)00105-0](https://doi.org/10.1016/S1350-4487(00)00105-0)
- Freiesleben, T., Sohbaty, R., Murray, A., Jain, M., Al Khasawneh, S., Hvidt, S., Jakobsen, B., 2015. Mathematical model quantifies multiple daylight exposure and burial events for rock surfaces using luminescence dating. *Radiat. Meas.* 81, 16–22. <https://doi.org/10.1016/j.radmeas.2015.02.004>
- Freiesleben, T.H., Thomsen, K.J., Jain, M., 2023. Novel luminescence kinetic models for rock surface exposure dating. *Radiat. Meas.* 160, 1–38. <https://doi.org/10.1016/j.radmeas.2022.106877>
- Frouin, M., Huot, S., Kreutzer, S., Lahaye, C., Lamothe, M., Philippe, A., Mercier, N., 2017. An improved radiofluorescence single-aliquot regenerative dose protocol for K-feldspars. *Quat. Geochronol.* 38, 13–24. <https://doi.org/10.1016/j.quageo.2016.11.004>

- Fuller, I.C., 1994. Stimulated Luminescence of an Alluvial Sediment from the Danube 13.
- Galbraith, R. F., Green, P. F., 1990. Estimating the component ages in a finite mixture. *International Journal of Radiation Applications and Instrumentation. Part D. Nuclear Tracks and Radiation Measurements* 17, 197-206.
- Galbraith, R. F., Roberts, R. G., Laslett, G. M., Yoshida, H., Olley, J. M., 1999. Optical dating of single and multiple grains of quartz from Jinmium rock shelter, northern Australia: Part I, experimental design and statistical models. *Archaeometry* 41, 339-364.
- Ganju, A., Nagar, Y. C., Sharma, L. N., Sharma, S., & Juyal, N. (2018). Luminescence chronology and climatic implication of the late quaternary glaciation in the Nubra valley, Karakoram Himalaya, India Sample type. *Palaeogeography, Palaeoclimatology, Palaeoecology*, 502(October 2017), 52–62. <https://doi.org/10.1016/j.palaeo.2018.04.022>
- Garlick, G. F. J., and Gibson, A. F. (1948). The electron trap mechanism of luminescence in sulphide and silicate phosphors. *Proceedings of Physics society* 60, 574.
- Gliganic, L.A., Meyer, M.C., Sohbat, R., Jain, M., Barrett, S., 2018. Quaternary Geochronology OSL surface exposure dating of a lithic quarry in Tibet: Laboratory validation and application. *Quat. Geochronol.* 0–1. <https://doi.org/10.1016/j.quageo.2018.04.012>
- Godfrey-Smith, D.I., Cada, M., 1996. IR stimulation spectroscopy of plagioclase and potassium feldspars, and quartz. *Radiat. Protect. Dosim.* 66, 379–385.
- Goedicke, C., 1984. Microscopic investigations of the quartz etching technique for TL dating. *Nucl. Tracks Radiat. Meas.* 9, 87–93. [https://doi.org/10.1016/0735-245X\(84\)90026-7](https://doi.org/10.1016/0735-245X(84)90026-7).
- Greilich, S., & Wagner, G. A., 2005. OPTICAL DATING OF GRANITIC STONE SURFACES *. *3*(September 2004), 645–665.
- Griffiths, D. J. (1995). *Introduction to Quantum Mechanics*. Pearson Prentice Hall.
- Grün, R., Packman, S.C., 1994. Observations on the kinetics involved in the TL glow curves in quartz, K-feldspar and Na-feldspar mineral separates of sediments and their significance for dating studies. *Radiat. Meas.* 23, 317–322. [https://doi.org/10.1016/1350-4487\(94\)90058-2](https://doi.org/10.1016/1350-4487(94)90058-2)

- Guérin, G., Mercier, N., 2012. Preliminary insight into dose deposition processes in sedimentary media on a scale of single grains: Monte Carlo modelling of the effect of water on the gamma dose rate. *Radiat. Meas.* 47, 541–547. <https://doi.org/10.1016/j.radmeas.2012.05.004>
- Guérin, G., Mercier, N., & Adamiec, G., 2011. Dose-rate conversion factors: update. *Ancient TL*, 29(1), 5-8.
- Habermann, J., Schilles, T., Kalchgruber, R., & Wagner, È. A., 2000. Steps towards surface dating using luminescence. 32, 847–851. https://www.fysik.dtu.dk/english/research/radphys/research/radiation-instruments/tl_osl_reader/manuals
- Huntley, D. J., Godfrey-Smith, D. I., Thewalt, M. L. W., 1985. Optical dating of sediments. *Nature* 313, 105-107.
- Huntley, D.J., 2006. An explanation of the power-law decay of luminescence. *J. Phys. Condens. Matter* 18, 1359–1365. <https://doi.org/10.1088/0953-8984/18/4/020>
- Huntley, D.J., Baril, M.R., 1997. The K content of the K-feldspars being measured in optical dating or in thermoluminescence dating. *Anc. TL* 15, 11-13.
- Huntley, D.J., Hancock, R.G.V., 2001. The Rb contents of the K-feldspar grains being measured in optical dating. *Anc. TL* 19, 43-46.
- Huntley, D. J., Hutton, J. T., & Prescott, J. R., 1993. Optical dating using inclusions within quartz grains. *Geology*, 21(12), 1087-1090.
- Huntley, D.J., Lamothe, M., 2001. Ubiquity of anomalous fading in K-feldspars and the measurement and correction for it in optical dating. *Can. J. Earth Sci.* 38, 1093–1106. <https://doi.org/10.1139/cjes-38-7-1093>.
- Hütt, G., Jaek, I., Tchonka, J., 1988. Optical dating: K-feldspars optical response stimulation spectra. *Quat. Sci. Rev.* 7, 381–385. [https://doi.org/10.1016/0277-3791\(88\)90033-9](https://doi.org/10.1016/0277-3791(88)90033-9)
- Jain, M, Sohpati, R., Guralnik, B., Murray, A.S., Kook, M., Lapp, T., Prasad, A.K., Thomsen, K.J., Buylaert, J.P., 2015. Kinetics of infrared stimulated luminescence from feldspars. *Radiat. Meas.* 81, 242–250. <https://doi.org/10.1016/j.radmeas.2015.02.006>

- Jain, M., Ankjærgaard, C., 2011. Towards a non-fading signal in feldspar: insight into charge transport and tunnelling from time-resolved optically stimulated luminescence. *Radiat. Meas.* 46, 292–309.
- Jain, M., Singhvi, A.K., 2001. Limits to depletion of blue-green light stimulated luminescence in feldspars: Implications for quartz dating. *Radiat. Meas.* 33, 883–892. [https://doi.org/10.1016/S1350-4487\(01\)00104-4](https://doi.org/10.1016/S1350-4487(01)00104-4).
- Jain, M., Sohbati, R., Guralnik, B., Murray, A.S., Kook, M., Lapp, T., Prasad, A.K., Thomsen, K.J., Buylaert, J.P., 2015. Kinetics of infrared stimulated luminescence from feldspars. *Radiat. Meas.* 81, 242–250. <https://doi.org/10.1016/j.radmeas.2015.02.006>.
- Jena, P. S., Bhushan, R., Sharma, S., Dabhi, A. J., Ajay, S., Raj, H., & Juyal, N., 2023. ¹⁰Be exposure age dating of moraine boulders and glacially polished bedrock surfaces in Karakoram and Ladakh Ranges, NW Himalaya: Implications in Quaternary glaciation studies. *Journal of Geophysical Research: Earth Surface*, 128(11), e2023JF007216. <https://doi.org/10.1029/2023JF007216>
- Jenkins, G.T.H., Duller, G.A.T., Roberts, H.M., Chiverrell, R.C., Glasser, N.F., 2018. A new approach for luminescence dating glacio fluvial deposits - High precision optical dating of cobbles. *Quat. Sci. Rev.* 192, 263–273. <https://doi.org/10.1016/j.quascirev.2018.05.036>
- Kalita, J.M., Chithambo, M.L., 2021. Blue- and infrared-light stimulated luminescence of microcline and the effect of optical bleaching on its thermoluminescence. *J. Lumin.* 229, 117712. <https://doi.org/10.1016/j.jlumin.2020.117712>
- Kalita, J.M., Chithambo, M.L., 2022. Phototransferred thermoluminescence characteristics of microcline (KAlSi₃O₈) under 470 nm blue- and 870 nm infrared-light illumination. *Appl. Radiat. Isot.* 181, 110070. <https://doi.org/10.1016/j.apradiso.2021.110070>
- Kars, R.H., Poolton, N.R.J., Jain, M., Ankjærgaard, C., Dorenbos, P., Wallinga, J., 2013. On the trap depth of the IR-sensitive trap in Na- and K-feldspar. *Radiat. Meas.* 59, 103–113. <https://doi.org/10.1016/j.radmeas.2013.05.002>.
- Kars, R.H., Wallinga, J., 2009. IRSL dating of K-feldspars: modelling natural dose response curves to deal with anomalous fading and trap competition. *Radiat. Meas.* 44, 594–599. <https://doi.org/10.1016/j.radmeas.2009.03.032>.

- Kars, R.H., Wallinga, J., Cohen, K.M., 2008. A new approach towards anomalous fading correction for feldspar IRSL dating- tests on samples in field saturation. *Radiat. Meas.* 43, 786–790.
- Kennedy, G. C., 1959. Date rock and pottery. *Science News Letter* 79, 149.
- Knoll G.F., 2010. *Radiation detection and measurements*. 4th Edition, Wiley, Hoboken, 217.
- Krbetschek, M.R., Trautmann, T., 2000. A spectral radioluminescence study for dating and dosimetry. *Radiat. Meas.* 32, 853–857.
- Krbetschek, M. R., Götze, J., Dietrich, A., & Trautmann, T., 1997. Spectral information from minerals relevant for luminescence dating. *Radiation Measurements*, 27(5-6), 695-748. [https://doi.org/10.1016/S1350-4487\(97\)00223-0](https://doi.org/10.1016/S1350-4487(97)00223-0)
- Krishna, M., Kreutzer, S., King, G., Frouin, M., Tsukamoto, S., Schmidt, C., Lauer, T., Klasen, N., Richter, D., Friedrich, J., Mercier, N., Fuchs, M., 2021. Quaternary Geochronology Infrared radiofluorescence (IR-RF) dating: A review. *Quat. Geochronol.* 64, 101155. <https://doi.org/10.1016/j.quageo.2021.101155>
- Kumar, R., Kook, M., Jain, M., 2020. Understanding the metastable states in K-Na aluminosilicates using novel site-selective excitation-emission spectroscopy. *J. Phys. D: Appl. Phys.* 53. <https://doi.org/10.1088/1361-6463/aba788>.
- Kumar, R., Kook, M., Jain, M., 2021. Sediment dating using Infrared Photoluminescence. *Quat. Geochronol.* 62, 101147. <https://doi.org/10.1016/j.quageo.2020.101147>.
- Kumar, R., Kook, M., Jain, M., 2022. Does hole instability cause anomalous fading of luminescence in feldspar? *J. Lumin.* 252, 119403. <https://doi.org/10.1016/j.jlumin.2022.119403>
- Kumar, R., Kook, M., Murray, A.S., Jain, M., 2018. Towards direct measurement of electrons in metastable states in K-feldspar: Do infrared-photoluminescence and radioluminescence probe the same trap? *Radiat. Meas.* 120, 7–13. <https://doi.org/10.1016/j.radmeas.2018.06.018>.
- Lal, D. (1991). Cosmic ray labeling of erosion surfaces: in situ nuclide production rates and erosion models. *Earth and Planetary Science Letters*, 104(2-4), 424-439.

- Lamothe, M., Auclair, M., Hamzaoui, C., Huot, S., 2003. Towards a prediction of long-term anomalous fading of feldspar IRSL. *Radiat. Meas.* 37, 493–498.
- Lapp, T., Kook, M., Murray, A.S., Thomsen, K.J., Buylaert, J.P., Jain, M., 2015. A new luminescence Detection and Stimulation Head for the Risø TL/OSL reader. *Radiat. Meas.* 81, 178–184. <https://doi.org/10.1016/j.radmeas.2015.02.001>.
- Li, B., Jacobs, Z., Roberts, R.G., Li, S.H., 2014. Review and assessment of the potential of post-ir irsl dating methods to circumvent the problem of anomalous fading in feldspar luminescence. *Geochronometria* 41, 178–201. <https://doi.org/10.2478/s13386-013-0160-3>
- Li, B., Li, S.H., 2011. Luminescence dating of K-feldspar from sediments: A protocol without anomalous fading correction. *Quat. Geochronol.* 6, 468–479. <https://doi.org/10.1016/j.quageo.2011.05.001>.
- Li, B., & Li, S. H., 2011. Thermal stability of infrared stimulated luminescence of sedimentary K-feldspar. *Radia. Meas.* 46(1), 29-36. [10.1016/j.radmeas.2010.10.002](https://doi.org/10.1016/j.radmeas.2010.10.002)
- Li, B., Roberts, R.G., Jacobs, Z., 2013. On the dose dependency of the bleachable and non-bleachable components of IRSL from K-feldspar: Improved procedures for luminescence dating of Quaternary sediments. *Quat. Geochronol.* 17, 1–13. <https://doi.org/10.1016/j.quageo.2013.03.006>
- Liritzis, I., & Galloway, R. B., 1999. Dating implications from solar bleaching of thermoluminescence of ancient marble. *Quat. Geochronol.* 241(2), 361–368.
- Liu, J., Cui, F., Murray, A.S., Sohbaty, R., Jain, M., Gao, H., Li, W., Li, C., Li, P., Zhou, T., Chen, J., 2018. Resetting of the luminescence signal in modern riverbed cobbles along the course of the Shiyang River, China. *Quat. Geochronol.* 49, 184-190. <https://doi.org/10.1016/j.quageo.2018.04.004>.
- Mayya, Y. S., Mortheikai, P., Murari, M. K., Singhvi, A. K., 2006. Towards quantifying beta microdosimetric effects in single-grain quartz dose distribution. *Radiation Measurements* 41, 1032-1039.
- McKinlay, A. F., 1981. Thermoluminescence dosimetry, Adam Hilger Ltd., Bristol.
- Mejdahl, V., 1987. Internal radioactivity in quartz and feldspar grains. *Ancient TL*, 5(2), 10-17.

- Meyer, M.C., Gliganic, L.A., Jain, M., Sohbaty, R., Schmidmair, D., 2018. Lithological controls on light penetration into rock surfaces – Implications for OSL and IRSL surface exposure dating. *Radiat. Meas.* 0–1. <https://doi.org/10.1016/j.radmeas.2018.03.004>
- Mishra, S., Chauhan, N., Singhvi, A.K., 2013. Continuity of Microblade Technology in the Indian Subcontinent Since 45 ka: Implications for the Dispersal of Modern Humans. *PLoS One* 8, 1–14. <https://doi.org/10.1371/journal.pone.0069280>.
- Morthekai, P., Chauhan, P.R., Jain, M., Shukla, A.D., Rajapara, H.M., Krishnan, K., Sant, D.A., Patnaik, R., Reddy, D. V., Singhvi, A.K., 2015. Thermally redistributed IRSL (RD-IRSL): A new possibility of dating sediments near B/M boundary. *Quat. Geochronol.* 30, 154–160. <https://doi.org/10.1016/j.quageo.2015.05.018>.
- Murray, A., Arnold, L.J., Buylaert, J.P., Guérin, G., Qin, J., Singhvi, A.K., Smedley, R. and Thomsen, K.J. 2021. Optically stimulated luminescence dating using quartz. *Nature Reviews Methods Primers*, 1(1): 1–31
- Murray, A.S., Roberts, R.G., 1997. Determining the burial time of single grains of quartz using optically stimulated luminescence. *Earth Planet. Sci. Lett.* 152, 163–180. [https://doi.org/10.1016/S0012-821X\(97\)00150-7](https://doi.org/10.1016/S0012-821X(97)00150-7)
- Murray, A.S., Wintle, A.G., 1999. Isothermal decay of optically stimulated luminescence in quartz. *Radiat. Meas.* 30, 119–125. [https://doi.org/10.1016/S1350-4487\(98\)00097-3](https://doi.org/10.1016/S1350-4487(98)00097-3)
- Murray, A.S., Wintle, A.G., 2000. Luminescence dating of quartz using an improved single-aliquot regenerative-dose protocol. *Radiat. Meas.* 32, 57–73. [https://doi.org/10.1016/S1350-4487\(99\)00253-X](https://doi.org/10.1016/S1350-4487(99)00253-X).
- Ninkovich, D., Shackleton, N.J., Abdel-Monem, A.A., Obradovich, J.D., Izett, G., 1978. K-Ar age of the late Pleistocene eruption of Toba, north Sumatra. *Nature* 276, 574–577. <https://doi.org/10.1038/276574a0>.
- Olley, J., Caitcheon, G., Murray, A., 1998. The distribution of apparent dose as determined by optically stimulated luminescence in small aliquots of fluvial quartz: Implications for dating young sediments. *Quat. Sci. Rev.* 17, 1033–1040. [https://doi.org/10.1016/S0277-3791\(97\)00090-5](https://doi.org/10.1016/S0277-3791(97)00090-5)
- Polikreti, K., Michael, C. T., & Maniatis, Y., 2003. Thermoluminescence characteristics of marble and dating of freshly excavated marble objects. 37, 87–94.

Poolton, N. R. J., Bøtter-Jensen, L., & Johnsen, O., 1995. Thermo-optical properties of optically stimulated luminescence in feldspars. *Radiat. Meas.*, 24, 531-534.

Poolton, N.R.J., Bøtter-Jensen, L., Ypma, P.J.M., Johnsen, O., 1994. Influence of crystal structure on the optically stimulated luminescence properties of feldspars. *Radiat. Meas.* 23 (2–3), 551–554.

Poolton, N.R.J., Kars, R.H., Wallinga, J., Bos, A.J.J., 2009. Direct evidence for the participation of band-tails and excited-state tunnelling in the luminescence of irradiated feldspars. *J. Phys. Condens. Matter* 21. <https://doi.org/10.1088/0953-8984/21/48/485505>.

Poolton, N.R.J., Ozanyan, K.B., Wallinga, J., Murray, A.S., Bøtter-Jensen, L., 2002a. Electrons in feldspar II: A consideration of the influence of conduction band-tail states on luminescence processes. *Phys. Chem. Miner.* 29, 217–225. <https://doi.org/10.1007/s00269-001-0218-2>.

Poolton, N.R.J., Wallinga, J., Murray, A.S., Bulur, E., Bøtter-Jensen, L., 2002b. Electrons in feldspar I: On the wavefunction of electrons trapped at simple lattice defects. *Phys. Chem. Miner.* 29, 210–216. <https://doi.org/10.1007/s00269-001-0217-3>

Porat, N., Faerstein, G., Medialdea, A., Murray, A.S., 2015. Re-examination of common extraction and purification methods of quartz and feldspar for luminescence dating. *Anc. TL* 33, 255–258.

Prasad, A.K., Jain, M., 2018. Breakdown of Kasha's rule in a ubiquitous, naturally occurring, wide bandgap aluminosilicate (feldspar). *Sci. Rep.* 8, 1–12.

Prasad, A.K., Lapp, T., Kook, M., Jain, M., 2016. Probing luminescence centres in Na rich feldspar. *Radiat. Meas.* 90, 292–297.

Prasad, A.K., Poolton, N.R.J., Kook, M., Jain, M., 2017. Optical dating in a new light: A direct, non-destructive probe of trapped electrons. *Sci. Rep.* 1–15. <https://doi.org/10.1038/s41598-017-10174-8>.

Prescott, J.R., Hutton, J.T., 1994. Cosmic ray contributions to dose rates for luminescence and ESR dating: large depths and long-term time variations. *Radiat. Meas.* 23, 497–500. [https://doi.org/10.1016/1350-4487\(94\)90086-8](https://doi.org/10.1016/1350-4487(94)90086-8).

Randall, J. T., and Wilkins, M. H. F., 1945a. *Proceedings of Royal Society of London* 184, 390.

- Randall, J. T., and Wilkins, M. H. F., 1945b. Phosphorescence and electron traps. I. The study of trap distributions. *Proceedings of Royal Society of London* 184, 366.
- Reimann, T., & Tsukamoto, S., 2012. Dating the recent past (< 500 years) by post-IR IRSL feldspar—Examples from the North Sea and Baltic Sea coast. *Quat. Geochronol.* 10, 180-187.
- Reimann, T., Tsukamoto, S., Naumann, M., Frechen, M., 2011. Quaternary Geochronology The potential of using K-rich feldspars for optical dating of young coastal sediments e A test case from Darss-Zingst peninsula (southern Baltic Sea coast). *Quat. Geochronol.* 6, 207–222. <https://doi.org/10.1016/j.quageo.2010.10.001>
- Rhodes, E.J. 2011. Optically Stimulated Luminescence dating of sediments over the past 200,000 years. *Annual Reviews of Earth and Planetary Sciences*, 39: 461-488.
- Riedesel, S., King, G.E., Prasad, A.K., Kumar, R., Finch, A.A., Jain, M., 2019. Optical determination of the width of the band-tail states, and the excited and ground state energies of the principal dosimetric trap in feldspar. *Radiat. Meas.* 125, 40–51. <https://doi.org/10.1016/j.radmeas.2018.08.019>.
- Riedesel, S., Kumar, R., Duller, G.A.T., Roberts, H.M., Bell, A.M.T., Jain, M., 2021. Site-selective characterisation of electron trapping centres in relation to chemistry, structural state and mineral phases present in single crystal alkali feldspars. *J. Phys. D. Appl. Phys.* 54, 385107. <https://doi.org/10.1088/1361-6463/ac10d7>.
- Roberts, R.G., Jones, R., Spooner, N.A., Head, M.J., Murray, A.S., Smith, M.A., 1994. The human colonisation of Australia: optical dates of 53,000 and 60,000 years bracket human arrival at Deaf Adder Gorge, Northern Territory. *Quat. Sci. Rev.* 13, 575–583. [https://doi.org/10.1016/0277-3791\(94\)90080-9](https://doi.org/10.1016/0277-3791(94)90080-9)
- Singh, P., Shukla, I., Singhal, M., Devi, M., Chauhan, N., Kumar, K., Prabakaran, M., Rajan, K., Sivanantham, R., Morthekai, P., (in preparation). Do anomalous fading limit the applicability of luminescence dating of Iron Age urns of Sivagalai, South India?
- Singhvi, A. K., & Aitken, M. J., 1978. Americium-241 for alpha-irradiations. *Ancient TL*, 3, 2-2.
- Singhvi, A. K., Chauhan, N., Biswas, R. H., 2010. A survey of some new approaches in extending the maximum age limit and accuracy of luminescence application to archeological chronometry. *Mediterranean Archaeology and Archaeometry* 4, 9- 15.

- Singhvi, A., Stokes, S., Chauhan, N., Nagar, Y., and Jaiswal, M., 2011, Changes in natural OSL sensitivity during single aliquot regeneration procedure and their implications for equivalent dose determination. *Geochronometria*, 38, 231–241.
- Singhvi, A.K., Wagner, G.A., 1986. Thermoluminescence Dating and its applications to Young Sedimentary Deposits. *Dating young sediments*.
- Sohbati, R., Jain, M., Murray, A., 2012a. Surface exposure dating of non-terrestrial bodies using optically stimulated luminescence: A new method. *Icarus* 221, 160–166. <https://doi.org/10.1016/j.icarus.2012.07.017>.
- Sohbati, R., Liu, J., Jain, M., Murray, A., Egholm, D., Paris, R., Guralnik, B., 2018. Centennial- to millennial-scale hard rock erosion rates deduced from luminescence-depth profiles. *Earth Planet. Sci. Lett.* 493, 218–230. <https://doi.org/10.1016/j.epsl.2018.04.017>.
- Sohbati, R., Murray, A. S., Porat, N., Jain, M., & Avner, U., 2015. Quaternary Geochronology Age of a prehistoric “Rodedian” cult site constrained by sediment and rock surface luminescence dating techniques. *Quaternary Geochronology*, 30, 90–99. <https://doi.org/10.1016/j.quageo.2015.09.002>
- Sohbati, R., Murray, A., Jain, M., Thomsen, K., Hong, S., Yi, K., Choi, J., 2013. Na-rich feldspar as a luminescence dosimeter in infrared stimulated luminescence (IRSL) dating. *Radiat. Meas.* 51–52, 67–82. <https://doi.org/10.1016/j.radmeas.2012.12.011>
- Sohbati, R., Murray, A.S., Chapot, M.S., Jain, M., Pederson, J., 2012b. Optically stimulated luminescence (OSL) as a chronometer for surface exposure dating 117, 1–7. <https://doi.org/10.1029/2012JB009383>
- Spooner, N.A., 1992. Optical dating: preliminary results on the anomalous fading of luminescence from feldspars. *Quat. Sci. Rev.* 11, 139–145.
- Spooner, N.A., 1994. The anomalous fading of infrared-stimulated luminescence from feldspars. *Radiat. Meas.* 23, 625–632.
- Strickertsson, K., 1985. The thermoluminescence of potassium feldspars-Glow curve characteristics and initial rise measurements. *Nucl. Tracks Radiat. Meas.* 10, 613–617. [https://doi.org/10.1016/0735-245X\(85\)90066-3](https://doi.org/10.1016/0735-245X(85)90066-3)

- Thalbitzer Andersen, M., Jain, M., Tidemand-Lichtenberg, P., 2012. Red-IR stimulated luminescence in K-feldspar: Single or multiple trap origin? *J. Appl. Phys.* 112. <https://doi.org/10.1063/1.4745018>.
- Thiel, C., Buylaert, J.P., Murray, A., Terhorst, B., Hofer, I., Tsukamoto, S., Frechen, M., 2011. Luminescence dating of the Stratzing loess profile (Austria) - Testing the potential of an elevated temperature post-IR IRSL protocol. *Quat. Int.* 234, 23–31. <https://doi.org/10.1016/j.quaint.2010.05.018>.
- Thomsen, K.J., Murray, A.S., Jain, M., Bøtter-Jensen, L., 2008. Laboratory fading rates of various luminescence signals from feldspar-rich sediment extracts. *Radiat. Meas.* 43, 1474–1486.
- Tsakalos, E., Christodoulakis, J., Charalambous, L., 2016. The Dose Rate Calculator (DRc) for Luminescence and ESR Dating—a Java Application for Dose Rate and Age Determination. *Archaeometry* 58, 347–352. <https://doi.org/10.1111/arc.12162>
- Tsukamoto, S., Murray, A.S., Huot, S., Watanuki, T., Denby, P.M., Bøtter-Jensen, L., 2007. Luminescence property of volcanic quartz and the use of red isothermal TL for dating tephra. *Radiation Measurements* 42, 190e197
- Urbach, Franz. "Zur lumineszenz der alkalihalogenide." *Sitzungsberichte Akad. der Wiss. Wien* 139 (1930): 363-372.
- Vafiadou, A., Murray, A. S., & Liritzis, I., 2007. Optically stimulated luminescence (OSL) dating investigations of rock and underlying soil from three case studies. 34. <https://doi.org/10.1016/j.jas.2006.12.004>
- Varma, V., Biswas, R.H., Singhvi, A.K., 2013. Aspects of infrared radioluminescence dosimetry in K-feldspar. *Geochronometria* 40, 266–273. <https://doi.org/10.2478/s13386-013-0125-6>
- Visocekas, R., 1979. La luminescence de la calcite après irradiation cathodique: thermoluminescence et luminescence par effet tunnel. (Doctoral dissertation: Université P. et M. Curie, Paris).
- Visocekas, R., 1985. Tunnelling radiative recombination in labradorite: its association with anomalous fading of thermoluminescence. *Nucl. Tracks Radiat. Meas.* 10, 521-529.

Ward, S., Stokes, S., Bailey, R., Singarayer, J., Goudie, A., & Bray, H., 2003. Optical dating of quartz from young samples and the effects of pre-heat temperature. *Radiation Measurements*, 37(4-5), 401-407.

Wintle, A.G., 1973. Anomalous fading of thermo-luminescence in mineral samples. *Nature* 245, 143–144.

Wintle, A.G., Murray, A.S., 2006. A review of quartz optically stimulated luminescence characteristics and their relevance in single-aliquot regeneration dating protocols. *Radiat. Meas.* 41, 369–391. <https://doi.org/10.1016/j.radmeas.2005.11.001>

Wintle, A.G., Murray, A.S., 2006. A review of quartz optically stimulated luminescence characteristics and their relevance in single-aliquot regeneration dating protocols. *Radiat. Meas.* 41, 369–391. <https://doi.org/10.1016/j.radmeas.2005.11.001>

Yi, S., Buylaert, J., Murray, A.S., Lu, H., Thiel, C., Zeng, L.I.N., 2016. A detailed post-IR IRSL dating study of the Niuyangzigou loess site in northeastern China. <https://doi.org/10.1111/bor.12185>.

Zink, A.J.C., Visocekas, R., 1997. Datability of sanidine feldspars using the near-infrared TL emission. *Radiat. Meas.* 27, 251–261.

List of Publications

Published in peer-reviewed journals

1. **Devi, M.**, Chauhan, N., Rajapara, H., Joshi, S., Singhvi, A.K., 2022. Multispectral athermal fading rate measurements of K-feldspar. *Radiat. Meas.* 156, 106804. <https://doi.org/10.1016/j.radmeas.2022.106804>.
2. **Devi, M.**, Chauhan, N., Singhvi, A.K., 2024. Quaternary Geochronology Post-violet infrared stimulated luminescence (pVIRSL) dating protocol for potassium feldspar. *Quat. Geochronol.* 79, 101487. <https://doi.org/10.1016/j.quageo.2023.101487>
3. Anil, D., Chauhan, N., Ajithprasad, P., **Devi, M.**, Mahesh, V., Khan, Z., 2022. An Early Presence of Modern Human or Convergent Evolution? A 247 ka Middle Palaeolithic Assemblage from Andhra Pradesh, India. *J. Archaeol. Sci. Reports* 45, 103565. <https://doi.org/10.1016/j.jasrep.2022.103565>.
4. Anil, D., **Devi, M.**, Blinkhorn, J., Smith, V., Sanghode, S., Mahesh, V., Khan, Z., Ajithprasad, P., Chauhan, N., 2022. Youngest Toba Tuff deposits in the Gundlakamma river basin, Andhra Pradesh, India and their Role in Evaluating Late Pleistocene Behavioural Change in South Asia. *Quaternary Research*, 1-12. <https://doi.org/10.1017/qua.2023.13>.
5. Anil, D., **Devi, M.**, Ati, N., C P, M., Khan, Z., Mahesh, V., Ajithprasad, P., Chauhan, N., Pandey, A., Jha, G., 2023. Diversity of MIS 3 Levallois technology from Motravulapadu, Andhra Pradesh, India-implications of MIS 3 cultural diversity in South Asia. *Frontiers in Earth Science*, 11. <https://doi.org/10.3389/feart.2023.1302419>

Under Preparation

1. **Devi M.**, Singhal M., Chauhan N., Applicability of Post Violet-Infrared Single Aliquot Regenerative (pVIR-SAR) Dose Protocol for Different Types of Samples using Potassium Feldspars
2. **Devi, M.**, Khanduri P., Srivastava Y., Chauhan, N., Singhvi, A.K., An Attempt to Date Glacially Polished Samples from Nubra valley, Karakoram Himalaya, India Using Luminescence Surface Exposure

3. Mehra, S. B. , Nishant, **Devi, M.**, Sarkar, A, Behera. D, Singh, V, Chauhan, N, Agarwal, S, Ambili. A, Chauhan, P. R., Palaeolithic assemblages, raw materials, palaeoenvironments and landscape adaptations in the Lower Son Valley, Uttar Pradesh, India.
4. Anil, D., **Devi, M.**, Khan, Z., Ati, N., Pandey, A., Sinha, D. K., Mahesh, V., Ajithprasad, P., Chauhan, N., Terminal Middle Pleistocene Hominin presence in the Nallamalai hills, Andhra Pradesh: Implications on Origin and Evolution of Middle Palaeolithic technology in South Asia.
5. Anil, D., **Devi, M.**, Aubert, M., Sathe, V., Dolienta, J. E., Ajithprasad, P., Mahesh, V., Khan, Z., Kumari, P., Chauhan, N., Late Pleistocene Fossil remains from Motravulapadu, Southeast Andhra Pradesh, India Taxonomy, Chronology and Associated Archaeological Materials.
6. Anil, D., **Devi, M.**, Ambrose, H., Ajithprasad, P., Mahesh, V., Khan, Z., Chauhan, N., MIS 3 Palaeolithic assemblages from Southeast Andhra Pradesh, India: Implications for Late Pleistocene Hominin behaviour, Dispersals and adaptations in South Asia.
7. Alappat L., **Devi, M.**, Chauhan, N., Sea Level Fluctuation in Tuticorin, Kerala using Optical Stimulated Luminescence Dating.

Presentations in Conferences / Workshops / Symposiums

1. Basics of Luminescence and its Applications in Geology, National Seminar on Geoarchaeology, Department of Geology and Environmental Science, Christ College, Irinjalakuda, Thrissur, Kerala, January 29, 2020. (*Conference invited talk*)

International Meetings

2. **Devi M.**, Chauhan N., Singhvi A.K., TL and OSL trap correlation studies to understand the luminescence mechanism in feldspar, 16th International Luminescence and Electron Spin Resonance Dating Conference (LED-2021), September 13-17, 2021.

3. **Devi M.**, Chauhan N., Singhvi A.K., Post Violet-Infrared Stimulated Luminescence (pVIRSL) Dating using Potassium Feldspar, 6th Asia Pacific Luminescence and ESR dating (APLED-2022), September 26-28, 2022.

National Meetings

4. **Devi M.**, Chauhan N., Singhvi A.K., New Developments in Probing Non-fading traps in K-Feldspar using Multispectral Studies: Implications to Luminescence Dating, National Conference on Luminescence and its Applications (NCLA-2021), December 9-11, 2021.
5. **Devi M.**, Chauhan N., Singhvi A.K., Applicability of Post Violet-Infrared Single Aliquot Regenerative (pVIR-SAR) Dose Protocol for Different Types of Samples using Potassium Feldspars, Workshop on Luminescence Dating and Applications-2023, Indian Institute of Science Education and Research, Kolkata, February 1-3, 2023.
6. **Devi M.**, Khanduri P., Chauhan N., Luminescence Rock Surface Exposure Studies in Ladakh, International Conference on Recent Trends in Science and Engineering-2024, Department of Physics, GOVT. V.Y.T. PG. Autonomous college, Durg, Chhattisgarh in association with Physics Department, IIT Bhilai, February 8-10, 2024.
7. **Devi M.**, Singhal M., Khanduri P., Chauhan N., Singhvi A.K., Application of Post-violet IR Single Aliquot Regenerative (pVIR-SAR) Dose Protocol for Polymineral Fine- and Coarse- grain Samples, Workshop on Luminescence Dating and Applications-2024, Physical Research Laboratory, Ahmedabad, February 21-23, 2024.

Publications Attached with Thesis

Devi, M., Chauhan, N., Rajapara, H., Joshi, S., Singhvi, A.K., 2022. Multispectral athermal fading rate measurements of K-feldspar. *Radiat. Meas.* 156, 106804. <https://doi.org/10.1016/j.radmeas.2022.106804>.

Devi, M., Chauhan, N., Singhvi, A.K., 2024. Quaternary Geochronology Post-violet infrared stimulated luminescence (pVIRSL) dating protocol for potassium feldspar. *Quat. Geochronol.* 79, 101487. <https://doi.org/10.1016/j.quageo.2023.101487>



Multispectral athermal fading rate measurements of K-feldspar

Monika Devi ^{a,b}, Naveen Chauhan ^{a,*}, Haresh Rajapara ^{a,c}, Sachin Joshi ^d, A.K. Singhvi ^a

^a AMOPH Division, Physical Research Laboratory, Navrangpura, Ahmedabad, 380009, India

^b Indian Institute of Technology, Gandhinagar, 382355, India

^c Physics Department, Gujarat University, Ahmedabad, 380009, India

^d The Maharaja Sayajirao University of Baroda, Vadodara, 390002, India

ARTICLE INFO

Keywords:

Luminescence
K-feldspar
Anomalous fading
Multispectral luminescence

ABSTRACT

This study reports athermal fading rates in K-feldspar grains extracted from sediments of varied ages and provenances. Multiple combinations of stimulation and emission spectral regions were examined to identify an optimum combination that provides a luminescence signal with minimal athermal fading. Stimulation wavelengths used were IR (855 ± 33 nm), green (525 ± 30 nm), blue (470 ± 20 nm), and violet (405 ± 15 nm), and detection windows were broad-UV (260–400 nm), narrow-UV (327–353 nm), and blue (320–520 nm).

Athermal fading rates using a single stimulation and sequential double stimulation combinations were estimated. For single stimulation, the average fading rates (g_{AV}) ranged from 6.6 to 7.9% per decade. Sequential double stimulation comprising post green-blue (pGB), post blue-violet (pBV), post blue-IR (pBIR), and post violet-IR (pVIR) gave fading rates ranging from 2.0 to 0.0% per decade. The minimum fading rate value $g_{AV} = 0.0 \pm 0.1\%$ per decade was obtained for pVIR stimulation, and this highlights it as a potential candidate for dating sediments such that the tedium and time of fading measurements can be minimized.

1. Introduction

Quartz has a stable optically stimulated luminescence (OSL) signal, which is easy to bleach under daylight but saturates at low doses of 150–200 Gy (Chawla et al., 1998). This limits its routine applicability to samples of age <200 ka (Aitken, 1985; Wintle and Murray, 2006). In comparison, feldspar has higher OSL [or Infrared stimulated luminescence (IRSL)] sensitivity and a higher saturation dose, and thereby offers the prospects of dating samples from a few decades to a few millions of years. However, it suffers from athermal fading that leads to an underestimation of the age (Spooner, 1994; Visocekas, 1985; Wintle, 1973). Athermal fading is attributed to quantum mechanical tunnelling of the charges leading to loss of luminescence signal (Aitken, 1985; Jain and Ankjærsgaard, 2011; Poolton et al., 2002a, 2002b; Visocekas, 1979).

Production of the IRSL signal in feldspar was explained using donor-acceptor model (Poolton et al., 1994), which states that electron tunnelling occurs from the excited state of the IRSL trap at 1.4 eV. This implies that IRSL decay curve is a function of tunnelling probability which decreases exponentially with the donor-acceptor distance. Thus, as the IRSL decay progresses, the tunnelling life-time also increases with the consumption of proximal pairs. Later signal arising from the distant

pairs are expected to have lower fading (Jain et al., 2015; Poolton et al., 1994; Thomsen et al., 2008). Further, analysis of TL glow curves of feldspars show a continuous distribution of activation energies (Biswas et al., 2018; Duller, 1997; Grün and Packman, 1994; Strickertsson, 1985). Since the charges in distant donor-acceptor recombination pairs (single trap model) or deep traps (multiple trap model) are expected to be more athermally stable, sequential stimulation by increasing energies can probe the luminescence with lower fading rates. Additionally, the use of different detection wavelengths also offers another opportunity to access the more stable emissions (i.e. recombination centres).

Generally, two approaches are used to circumvent the effect of athermal fading. These include (a) laboratory estimation of the fading rate (g-value) and correction of the measured ages for fading (Auclair et al., 2003; Huntley and Lamothe, 2001; Kars et al., 2008), and (b) probing of traps and recombination centres that are less prone to fading (Buylaert et al., 2011, 2012; Krbeschek and Trautmann, 2000; Prasad et al., 2017; Zink and Visocekas, 1997). Applicability of fading correction by Huntley and Lamothe (2001) is restricted to the linear portion of the dose-response curve (DRC), and therefore, depending upon dose rate, its applicability is limited to ages <50 ka. For older samples, prescriptions by Huntley (2006), Kars et al. (2008) and Kars and Wallinga

* Corresponding author.

E-mail address: chauhan@prl.res.in (N. Chauhan).

<https://doi.org/10.1016/j.radmeas.2022.106804>

Received 29 October 2021; Received in revised form 23 May 2022; Accepted 24 May 2022

Available online 31 May 2022

1350-4487/© 2022 Published by Elsevier Ltd.

Table 1

List of samples used and their location, depositional environment, paleodoses.

Sample code	Location	Depositional environment	Known D _e (Gy)	Age control
KF	–	Museum sample	–	–
PRL0	Tamil Nadu	Fluvial	11.1 ± 0.3	Quartz NCF-SAR
PRL1	Rajasthan (Thar desert)	Aeolian	15 ± 1	Feldspar pIRIR
PRL2	Narmada valley	Fluvial	36.0 ± 0.1	Quartz SAR OSL
PRL3	Odisha	Fluvial	77 ± 3	Quartz SAR OSL
PRL4	Andhra Pradesh	Fluvial	217 ± 3	Feldspar pIRIR
PRL5	Chennai (Attirampakkam)	Fluvial	237 ± 23	Feldspar pIRIR

(2009) are used, which use a power-law dependence of athermal fading with time. These models for fading correction assume that the fading rates estimated over laboratory time scales can be extrapolated to geological time scales. However, this assumption is difficult to test in the laboratory.

The second approach attempts to isolate luminescence signals with low or minimal athermal loss of charges. These include methods such as, post infrared-infrared stimulated luminescence (pIRIR) (Thomsen et al., 2008; Buylaert et al., 2009, 2012, 2011), multiple elevated temperature pIRIR (MET-pIRIR) (Li and Li, 2011), thermal redistribution of charges (Morthekai et al., 2015), red luminescence (Zink and Visocekas, 1997), infrared radio-luminescence (IR-RL) (Krbetschek and Trautmann, 2000), photo-transferred thermoluminescence (PTTL) (Kalita and Chithambo, 2021, 2022), and infrared photoluminescence (IR-PL) (Kumar et al., 2018; Prasad et al., 2017). In the pIRIR technique, luminescence signals with IR stimulation at higher temperatures (150–290 °C) are measured after a IR (50 °C) stimulation (Buckland et al., 2019; Buylaert et al., 2009; Jain and Ankjærgaard, 2011; Reimann et al., 2011, Reimann and Tsukamoto, 2012; Thomsen et al., 2008). The MET-pIRIR protocol uses the premise that fading rate of feldspar can be progressively reduced using multiple IR stimulations with increasing stimulation temperature from 50 to 250 °C (Li and Li, 2011). In both the protocols, the IRSL at elevated temperatures show low athermal fading (Buylaert et al., 2012; Li and Li, 2011; Thiel et al., 2011). Previous studies (Buylaert et al., 2012; Li et al., 2014; Poolton et al., 2002a) reported that the elevated temperature pIRIR and MET-pIRIR signals are harder to bleach than the IRSL (50 °C) signal, which can result in the overestimation of ages. Morthekai et al. (2015) proposed that distant pairs can be re-distributed by a thermal treatment, and such re-distributed trapped electrons can be accessed through IRSL measurements at 320 °C. Other efforts included optimization of the detection window to identify more stable signals, such as red (Biswas et al., 2013; Fattahi and Stokes, 2003; Zink and Visocekas, 1997). The red thermoluminescence (TL) emission (590–750 nm) was suggested to have low fading and higher saturation dose as compared to that for conventional blue (360–590 nm) TL emission (Fattahi and Stokes, 2000, 2003; Zink and Visocekas, 1997). Similarly, Thomsen et al. (2008) have reported the lower fading rates for blue detection window ($g = 3.0 \pm 0.1\%$ per decade) than UV ($g = 4.7 \pm 0.3\%$ per decade) in IRSL.

IR-RL provides a stable signal (Frouin et al., 2017; Krbetschek and Trautmann, 2000; Krishna et al., 2021); however, it still has unresolved methodological issues such as differences in the sensitivities of natural IR-RL and regenerated IR-RL (Frouin et al., 2017; Krbetschek and Trautmann, 2000; Varma et al., 2013), signal saturation, and fading, which have so far prevented its routine application (Krishna et al., 2021). Photo-transferred TL induced by blue and infrared light has also shown minimal anomalous fading (Kalita and Chithambo, 2021, 2022). IR-PL offers a good prospect to probe non-fading emission from the IR traps in feldspar (Kumar et al., 2018; Prasad et al., 2017). The IR-PL and

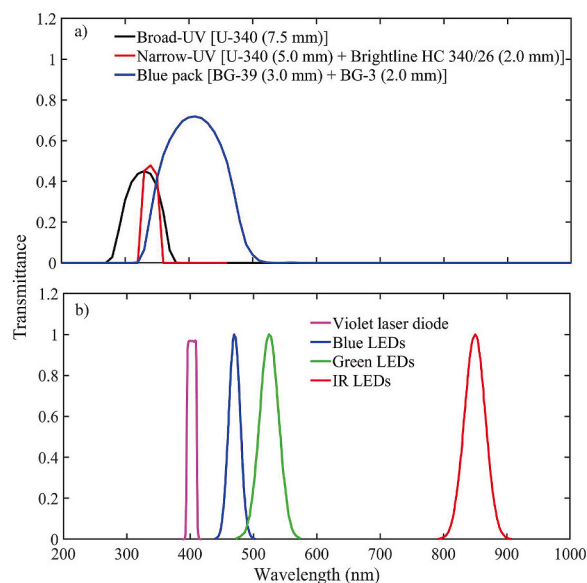


Fig. 1. Different excitation and detection windows a) Transmission characteristics of three different filter combinations b) Emission characteristics of the stimulation LEDs and laser. Stimulations were carried out using 850 nm IR, 525 nm green, and 405 nm violet laser diode. Detections were appropriately made through 260–400 nm [U-340 (Broad-UV)], 327–353 nm [U-340 + Brightline 340/26 (Narrow-UV)], and 320–520 nm [BG-39 + BG-3 (blue)] transmission windows. (Emission data of LEDs were taken from the Risø product catalogue 1811a. The data on transmission spectra of different filters were taken from <https://hoyaoptics.com/wp-content/uploads/2019/10/U340.pdf>).

PTTL are being developed as these show the promise for a non-fading luminescence signal.

The present study explored the multiple combinations of stimulation wavelengths and detection windows to identify the optimum configurations that could provide a signal with minimal athermal fading.

2. Materials and methods

2.1. Samples

Six potassium-rich feldspar samples from sediments with diverse depositional histories and provenances were investigated (Table 1). In addition, a museum specimen of potassium feldspar (KF-microcline), whose mineralogy was confirmed using x-ray diffraction (XRD) (Fig. S1) was also investigated. Table 1 provides the list of samples used, their depositional environments and respective paleodoses (10 Gy–240 Gy). These paleodoses were estimated using the existing protocols, such as blue light stimulated luminescence (BLSL) of quartz and pIRIR for feldspar. Detailed investigations of fading rates for all the combinations were made on one sample (PRL0) due to its higher luminescence sensitivity. Thereafter the optimized combination of spectral windows was used to measure the fading rates for other geological samples.

Feldspar grains were separated through a sequential treatment of sediments with 1N HCl and 30% H₂O₂ to remove the carbonates and organic matter, respectively. Grains of 90–150 μm in diameter were dry sieved, followed by density separation using sodium polytungstate ($\rho = 2.58 \text{ g/cm}^3$) or separation by using the Frantz® magnetic separator at magnetic field strength generated by 1.5 A current (Porat et al., 2015). The separated K-feldspar fraction obtained by the above treatment was etched with 10% hydrofluoric acid for 40 min (Duval et al., 2018; Goedicke, 1984; Porat et al., 2015) to remove the alpha skin, followed by a 30 min treatment with concentrated HCl (38%) to convert insoluble fluorides into soluble chlorides. The museum sample was crushed, dry sieved to get grain size of 90–150 μm in diameter, and then treated with

Table 2

Stimulation and detection spectral region combinations used for fading rate measurements along with their estimated average fading rates [g_{AV} (% per decade)] for single stimulation experiments.

Sr. no.	Stimulation	Stimulation wavelength (nm)	Detection (Filter name)	Transmission range (nm)	g_{AV} (% per decade)
1	Infrared	855 ± 33	Hoya U-340 (Broad-UV)	260–400	7.5 ± 0.3
			BG-39 + BG-3 (Blue)	320–520	6.9 ± 0.3
2	Green	525 ± 30	Hoya U-340 (Broad-UV)	260–400	7.9 ± 0.3
			Brightline (FF-340/26) + U-340 filter (Narrow-UV)	327–353	7.4 ± 0.5
3	Blue	470 ± 20	Hoya U-340 (Broad-UV)	260–400	7.0 ± 0.3
			Brightline (FF-340/26) + Hoya U-340 (Narrow-UV)	327–353	6.7 ± 0.5
4	Violet	405 ± 15	Brightline (FF-340/26) + Hoya U-340 (Narrow-UV)	327–353	6.6 ± 0.5

1N HCl for 10 min to remove surface defects created during crushing. Monolayers of the extracted grains from each sample were mounted on stainless steel discs over an area of 5 mm diameter using Silkospray™, and their TL glow curves were used to confirm that luminescence was typical of feldspars.

2.2. Instrumentation

The measurements were carried out in a Risø-TL/OSL DA-20 reader with a detection and stimulation head (DASH) comprising different stimulation LEDs and detection filters (Bøtter-Jensen et al., 2010; Lapp et al., 2015). Stimulations were carried out using IR (855 ± 33 nm), green (525 ± 30 nm), blue (470 ± 20 nm) LEDs, and violet (405 ± 15 nm) laser. Detection windows used were either of 260–400 nm [U-340 (Broad-UV)], 327–353 nm [U-340 + Brightline 340/26 (Narrow-UV)], or 320–520 nm [Schott BG-39 + BG-3 (blue)] considering compatibility with stimulations (Fig. 1).

2.3. Measurements

Table 2 summarizes the different combinations of stimulation and detection windows used for present studies. Measurements of fading rates [g (% per decade)] used the slope of a plot between measured delayed luminescence intensities and delay times on a logarithmic scale (Auclair et al., 2003). The average fading rate [g_{AV} (% per decade)] is an average of data from 15 aliquots. Fig. 2(a, b) provides a generalized measurement sequence. The samples were bleached in the Risø reader with the wavelength for which the fading rates were to be estimated. The bleaching temperature was 50 °C higher than the stimulation temperature used for fading rate estimations to ensure that the traps corresponding to each stimulation were emptied out. Photon counts from initial 2.40 s were used as the signal, and the normalised averaged photon counts during the final 20 s of the stimulation were taken as the background.

The fading rate measurements were carried out using a single stimulation (Fig. 2a) and double stimulation i.e., successive stimulation of sample aliquots by two different sources (stimulations-1 and 2; Fig. 2b). All stimulation and detection combinations listed in Table 2 were used in

the fading rate measurements of the single stimulation experiments. In the double stimulation experiments, the first five fading measurements were carried out by applying stimulations in the increasing order of their excitation energies (IR-green, IR-blue, IR-violet, green-blue, and blue-violet) (Table 3). The subsequent three experiments were performed using stimulation in decreasing order of their excitation energies (green-IR, blue-IR, and violet-IR) (Table 3).

3. Results

3.1. Fading measurements: single stimulations

The average fading rates (g_{AV}) for each stimulation and detection combination in the single stimulation measurements are presented in Table 2 and Fig. 3. Key observations from this experiment are:

1. Fading rates for all the stimulation and detection combinations lied between 6.6 and 7.9% per decade (Fig. 3).
2. Fading rates were progressively lower from broad-UV, followed narrow-UV and blue (Fig. 3) and accord with Thomsen et al. (2008) and Clarke and Rendell (1997). Lower fading rates for narrow-UV compared to broad-UV indicate that the charges stored in recombination centres, which emit in the lower UV wavelengths of broad-UV transmission, fade more.

3.2. Double stimulations

Table 3 and Fig. 4 provide the g_{AV} -values for each stimulation and detection combination in double stimulations fading measurements. Following the single stimulation experiment results only blue and narrow-UV detection windows were considered for estimating fading rates in double stimulation experiments. Key findings are as follows:

1. Fading rates for stimulation-2 were significantly lower as compared to stimulation-1 (Fig. 4).
2. When stimulations were applied in the increasing order of energies (IR-green, IR-blue, IR-violet, green-blue, and blue-violet), the fading rates for stimulation-2 were higher for higher excitation energy of the stimulation-2 ($g_{AV-violet} > g_{AV-blue} > g_{AV-green}$) (Fig. 4).
3. IRSL after high energy stimulations (green-IR, blue-IR, and violet-IR) gave lower fading rates (Fig. 4).
4. The post violet IRSL (pVIRSL) signal gave near zero fading rates (Fig. 4).

4. Discussion

Results from single stimulation experiments demonstrate that the fading rates for all the stimulation and detection combinations were similar (~7% per decade). The green (~2.3 eV), blue (~2.6 eV), and violet (~3.1 eV) excitation energies are higher than optical trap depth (2.0–2.5 eV) of the principal trap unlike IR (~1.4 eV) (Jain and Ankjærgaard, 2011). This leads to a direct transfer of charges from the ground state of principal trap to the conduction band in case of green, blue and violet stimulation. However, the IR stimulation transfers the electrons to the first excited state of the principal trap due to resonance excitation (Hütt et al., 1988), and thereafter the electrons further move to the band tail states of feldspar. Low mobility of electrons in the band tail states facilitates the proximal donor-acceptor recombination (Jain and Ankjærgaard, 2011). Thus, it is expected that due to high mobility of electrons in conduction band, the green, blue, and violet stimulated luminescence will show lower fading rates than IR stimulation.

Similarity of fading rates observed for the single stimulation and detection combinations indicate that either similar traps and recombination centres are probed by these stimulations or that the population of the proximal donor-acceptor recombination pairs (unstable) is significantly higher than distant donor-acceptor recombination pairs (stable).

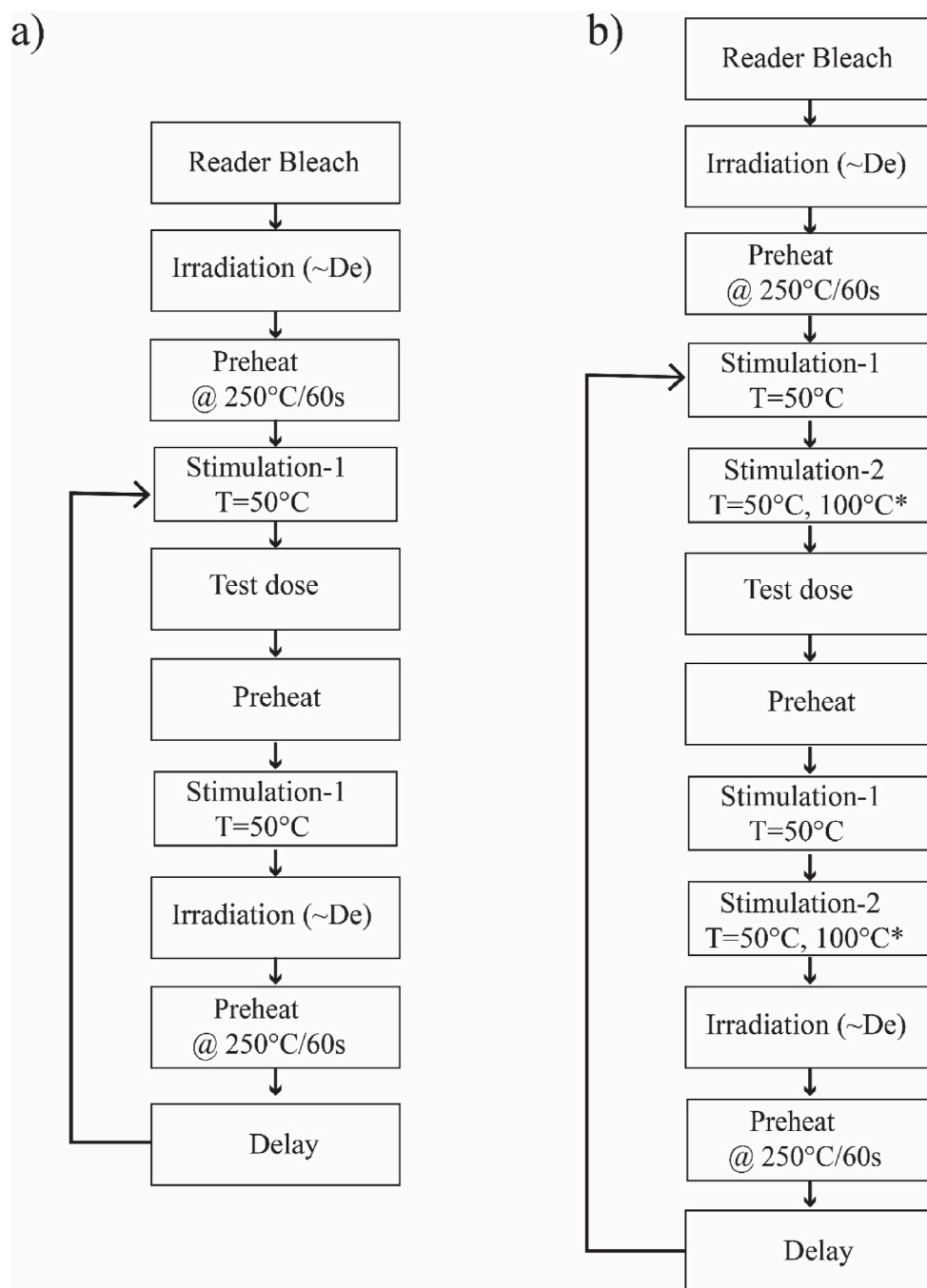


Fig. 2. Methodology for the measurement of fading rates [g_{2days} (% per decade)] using different stimulations, viz., IR (855 ± 33 nm), green (525 ± 30 nm), blue (470 ± 20 nm), and violet (405 ± 15 nm) lights. The detection windows were either broad-UV (260–400 nm), narrow-UV (327–353 nm), or blue (320–520 nm). Fading rate measurements were carried out using both single and double stimulations. For ease of understanding, a given stimulation and detection combination is written as [stimulation, detection] in the text. * IRSL measurements post green, post blue, and post violet stimulation were carried out with sample at 100°C to get good signal to noise ratio.

Table 3
Combinations of stimulations and detection windows used for double stimulation experiments along with the measured g_{AV} -values. The double stimulation experiment comprised sequential stimulation by two wavelengths: stimulation-1 and stimulation-2.

Sr. no.	Stimulation-1			Stimulation-2		
	Stimulation	Detection	g_{AV} (% per decade)	Stimulation	Detection	g_{AV} (% per decade)
1	IR	Blue	7.0 ± 0.2	Green	Narrow-UV	2.3 ± 0.2
2	IR	Blue	7.1 ± 0.1	Blue	Narrow-UV	3.2 ± 0.2
3	IR	Blue	5.7 ± 0.1	Violet	Narrow-UV	4.0 ± 0.4
4	Green	Narrow UV	7.8 ± 0.2	Blue	Narrow-UV	1.1 ± 0.1
5	Blue	Narrow UV	7.3 ± 0.3	Violet	Narrow-UV	1.3 ± 0.2
6	Green	Narrow UV	8.2 ± 0.3	IR	Blue	2.9 ± 0.2
7	Blue	Narrow UV	7.9 ± 0.2	IR	Blue	2.0 ± 0.2
8	Violet	Narrow UV	6.1 ± 0.2	IR	Blue	0.0 ± 0.1

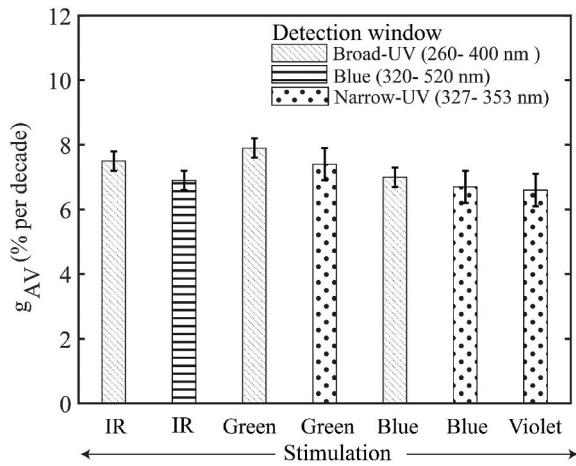


Fig. 3. Average fading rates [g_{AV} (% per decade)] for single stimulation and detection combinations for the PRL0 sample. The x-axis represents the stimulations, and the pattern of the bar represents the detection window. The height of the bar (y-axis) is the g_{AV}-values.

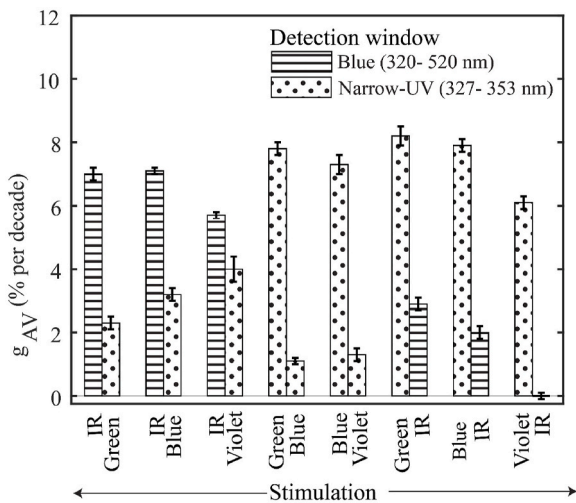


Fig. 4. Average fading rates [g_{AV} (% per decade)] for double stimulation and detection combinations for PRL0 sample. The x-axis represents the stimulations, and the pattern of the bar represents the detection window. The height of the bar (y-axis) is the g_{AV}-values. Double stimulation yielded lower fading rates for each second stimulation. The minimum fading (g_{min} = 0.0 ± 0.1% per decade) was obtained in the post violet IRSL (pVIRSL) signal.

Further attempts to separate the stable component of the luminescence signal from the unstable component using double stimulation experiments showed a significant reduction in the fading rates for stimulation-2 as compared to stimulation-1 (Fig. 4). The results indicate that the nearest donor-acceptor pairs are consumed during the low energy stimulation-1. Hence, the distant donor-acceptor pair participates in the luminescence signal of stimulation-2 and yields low fading rates. These results accord with the donor-acceptor model, which states that initial IRSL signal arise from the proximal donor-acceptor recombination pairs and the latter IRSL signal originates from distant pairs (Jain et al., 2015; Poolton et al., 1994). Hence, the luminescence signal following the IR stimulation originates from the distant pairs. It is also noteworthy that with the increase in excitation energy of stimulation-2, the fading rates also increase (g_{AV-violet} > g_{AV-blue} > g_{AV-green}) (Fig. 4). The possible reason for the increase in fading rates could be the recapture of electrons from the high energy stimulation-2 to the ground state of the principle trap (Jain and Ankjærgaard, 2011; Kumar et al., 2020)

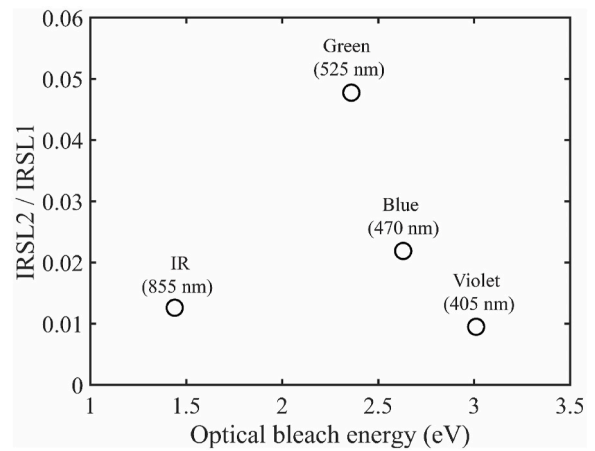


Fig. 5. Ratio of IRSL2 to IRSL1 signals as a function of optical bleach energy. The IRSL1 was measured without any optical bleach and IRSL2 was measured after the optical bleach with IR, green, blue, and violet stimulations. All the stimulations were carried out at 50 °C temperature. A maximum signal is obtained in the IRSL after the green stimulation. The IRSL signal starts to decrease with an increase in the energy of optical bleach. All the applied stimulations were power normalised.

and the instability of charges in recombination centres emitting in the UV window (Clarke and Rendell, 1997; Thomsen et al., 2008). Recaptured electrons from the green, blue, and violet stimulation participate

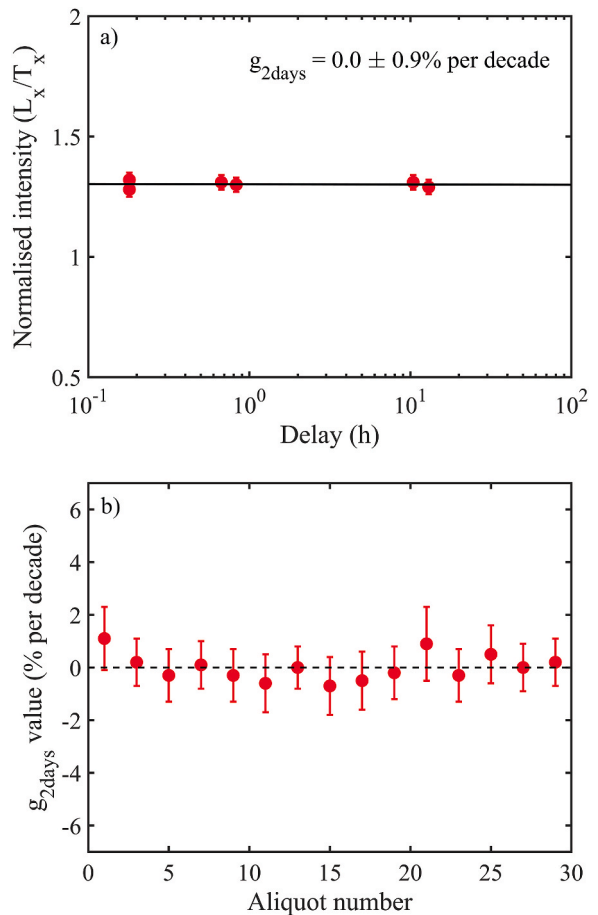


Fig. 6. Fading rate [g_{2days} (% per decade)] results for PRL0 for pVIRSL signal. a) Normalised intensity is constant with delay and hence gives near zero fading rate, b) g_{2days} values for all aliquots are near to the zero line and result in average fading value near to zero.

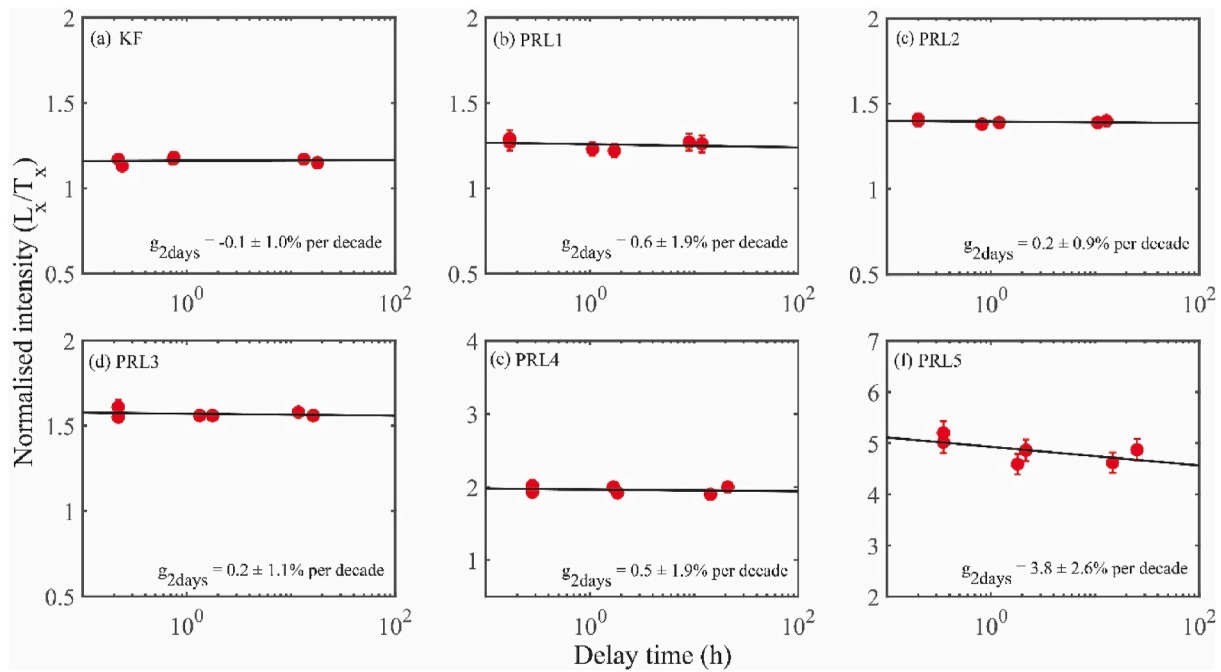


Fig. 7. Fading rate (g_{2days}) measurements for a single aliquot of each sample. The normalised intensities are constant with delay time for the KF, PRL1, PRL2, PRL3, and PRL4 samples. However, for one sample (PRL5, $D_e = 237 \pm 23$ Gy) normalised intensity decrease with delay time and resulted in the $g_{2days} = 3.8 \pm 2.6\%$ per decade.

in the next fading measurement along with charges generated from the fresh irradiation. Increased population of charges participates in the fading measurements, and the probability of quantum mechanical tunnelling from the ground state also increases.

Another possible reason for an increase in fading rate is the instability of UV centres as stimulation-2 is detected in the narrow-UV window in all the cases. Higher excitation energies transport a significantly greater proportion of electrons (20% at room temperature) to the conduction band (Jain and Ankjærgaard, 2011). Hence more UV emitting centres participate in the luminescence and lead to an increase in the fading rates. These observations need verification.

A significant signal in post green-, blue-, and violet-IRSL was observed. Optical decay curves for all stimulations are shown in Fig. S2. Fig. 5 provides the ratio of IRSL signal for the sample as received (IRSL1) and IRSL post green, blue, violet, and IR stimulation (IRSL2). It is noteworthy that IRSL2 was an order of magnitude lower after the green bleach and two orders of magnitudes lower after the blue and violet bleach. On the contrary, only slow decaying portion of the IRSL signal was obtained after IR bleach. This is an interesting outcome as it is unexpected that after optical bleaching of the sample with higher energies any IRSL should arise. This is suggestive of retrapping of charges from the conduction band to the ground state of the principal trap (Jain and Ankjærgaard, 2011; Kumar et al., 2020). These retrapped charges then provide luminescence in stimulation-2 (IRSL detected in the blue window). Other possible reason for the IRSL-2 signal could be the existence of at least two types of traps (Ditlefsen and Huntley, 1994; G.A.T. Duller and Bøtter-Jensen, 1993; Jain and Singhvi, 2001) or multiple traps (Biswas et al., 2018; Ditlefsen and Huntley, 1994; Jain and Singhvi, 2001; Morthekai et al., 2015). The fading rates of above mentioned IRSL signals were measured further. The fading rate of [IR, Blue] was 2.9 ± 0.2 and 2.0 ± 0.2 after [Green, Narrow-UV] and [Blue, Narrow-UV], respectively (Table 3). A noteworthy observation is that the pVIRSL signal gave a near zero g_{AV} -value (Fig. 4). The sensitivity corrected intensity remained constant with delay time for the pVIRSL signal (Fig. 6a). Fading rates [g_{2days} ($t_c = 2$ days)] for 15 aliquots were found to be in the -0.7 to 1.1% per decade ($g_{AV} = 0.0 \pm 0.1\%$ per decade) (Fig. 6b). This suggests that the pVIRSL signal probes the stable centres.

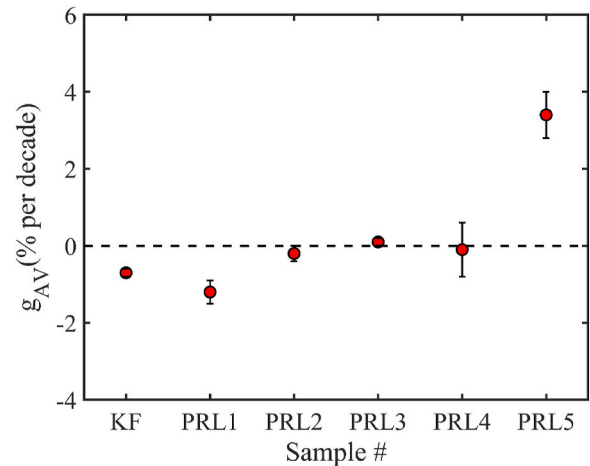


Fig. 8. Average fading rates [g_{AV} (% per decade)] of pVIRSL signal for all samples. The x-axis represents the sample code. The g_{AV} -values are near zero for KF, PRL1, PRL2, PRL3, and PRL4, and for one sample (PRL5, $D_e = 237 \pm 23$ Gy) g_{AV} -value is $3.4 \pm 0.6\%$ per decade.

Table 4

Observed g_{AV} -values for all samples. The paleodoses were estimated using the independently existing protocols.

No.	Sample code	Known D_e (Gy)	g_{AV} (% per decade)
1	KF	0 (F)	-0.7 ± 0.1
2	PRL0	11.1 ± 0.3 (Q)	0.0 ± 0.1
3	PRL1	15 ± 1 (F)	-1.2 ± 0.3
4	PRL2	36.0 ± 0.1 (Q)	-0.2 ± 0.2
5	PRL3	77 ± 3 (Q)	0.1 ± 0.1
6	PRL4	217 ± 3 (F)	-0.1 ± 0.7
7	PRL5	237 ± 23 (F)	3.4 ± 0.6

A decrease in the fading rate for stimulation-2 (IRSL) with an increase in the excitation energy of stimulation-1 (green-IR, blue-IR, and violet-IR) could be due to the fact that higher energy of stimulation-1 leads to the participation of larger number of distant donor-acceptor pairs in the IRSL signal of stimulation-2. As the energy of violet light is highest among all the excitations used, the resulting pVIRSL signal emitted from the recombination of distant donor-acceptor pairs and yields zero fading (Fig. 6a,b).

5. Fading rate of pVIRSL signal

The pVIRSL signal was further tested for other geological samples listed in Table 1 (Fig. 7). Typical g_{AV} -values for these samples were near zero (Fig. 8, Table 4). However, in one sample (PRL5) having paleodose 237 ± 23 Gy, the average fading rate was found to be $\sim 3.4 \pm 0.6\%$ per decade (Fig. 8, Table 4). At the present moment, it will be difficult to specify the reason for this high value, and it needs to be explored more. However, it is interesting to see the promising results for most of the geological as well as controlled museum samples. It indicates the prospects of developing pVIRSL protocol for routine measurements for obtaining ages with minimal fading.

6. Summary and conclusions

In this paper, an attempt to probe the non-fading traps using multi-spectral luminescence studies is made. Key findings are:

1. Single stimulation with any of IR, green, blue, and violet stimulation leads to similar fading rates ($\sim 7\%$ per decade).
2. The fading rates were higher for the broad-UV emission, followed the narrow-UV, with the blue window providing the least fading rates.
3. Significant reduction in the fading rates for the second stimulation was seen (Fig. 4), suggesting that the nearest donor-acceptor recombination population was consumed during the first stimulation hence, the second stimulation probed more distant pairs.
4. In the double stimulations, when both stimulations were applied in the increasing order of energies (IR-green, IR-blue, IR-violet, green-blue, and blue-violet), the fading rates for each second stimulation increased with an increase in the excitation energy of the second stimulation (Fig. 4). The possible reason could be the recapture of electrons from the high energy stimulation (Jain and Ankjærgaard, 2011; Kumar et al., 2020) and the instability of recombination centres emitting in the UV window (Clarke and Rendell, 1997; Thomsen et al., 2008). These observations need further investigation and can hint towards a new understanding of the feldspar luminescence production mechanism.
5. A significant signal in IRSL post green, blue, and violet light stimulations was observed. The obtained IRSL signal yields low fading rates. The possible reason might be that with an increase in the energy of stimulation-1, more distant donor-acceptor pairs participate in the IRSL signal of stimulation-2 Fig. 4.
6. The pVIRSL signal gave zero fading rates for several geological samples used in the study. However, a small fading value was observed in one sample (PRL5; $g_{AV} = 3.4 \pm 0.6\%$ per decade). The reason for high fading is yet to be understood.

Experiments on the suitability for dating and dose response of pVIRSL signal will be reported elsewhere.

Declaration of competing interest

The authors declare that they have no known competing financial interests or personal relationships that could have appeared to influence the work reported in this paper.

Acknowledgments

The authors thank Dr. Linto Allapat (Christ College, Kerala), Mr. Anil Kumar (MSU, Baroda), and Prof. George Mathew (IIT, Bombay) for providing the feldspar samples for analysis. We also thank Dr. Kartika Goswami and Dr. Rahul Kaushal for carefully reading the manuscript and providing constructive comments. Monika thanks Dr. Sebastian Huot for excel macros for fading rate estimations. AKS thanks DST-SERB for DST Year of Science Chair Professorship nucleated at the Physical Research Laboratory. The authors thank two anonymous reviewers and the Editor Dr. Mayank Jain for their constructive comments and valuable suggestions that improved the manuscript.

Appendix A. Supplementary data

Supplementary data to this article can be found online at <https://doi.org/10.1016/j.radmeas.2022.106804>.

References

- Aitken, M.J., 1985. *Thermoluminescence Dating*. Academic Press, London.
- Auclair, M., Lamothe, M., Huot, S., 2003. Measurement of anomalous fading for feldspar IRSL using SAR. *Radiat. Meas.* 37, 487–492.
- Biswas, R.H., Williams, M.A.J., Raj, R., Juyal, N., Singhvi, A.K., 2013. Methodological studies on luminescence dating of volcanic ashes. *Quat. Geochronol.* 17, 14–25. <https://doi.org/10.1016/j.quageo.2013.03.004>.
- Biswas, R.H., Herman, F., King, G.E., Braun, J., 2018. Thermoluminescence of feldspar as a multi-thermochronometer to constrain the temporal variation of rock exhumation in the recent past. *Earth Planet. Sci. Lett.* 495, 56–68. <https://doi.org/10.1016/j.epsl.2018.04.030>.
- Bøtter-Jensen, L., Thomsen, K.J., Jain, M., 2010. Review of optically stimulated luminescence (OSL) instrumental developments for retrospective dosimetry. *Radiat. Meas.* 45, 253–257. <https://doi.org/10.1016/j.radmeas.2009.11.030>.
- Buckland, C.E., Bailey, R.M., Thomas, D.S.G., 2019. Using post-IR IRSL and OSL to date young (< 200 yrs) dryland aeolian dune deposits. *Radiat. Meas.* 126, 106131. <https://doi.org/10.1016/j.radmeas.2019.106131>.
- Buylaert, J.P., Murray, A.S., Thomsen, K.J., Jain, M., 2009. Testing the potential of an elevated temperature IRSL signal from K-feldspar. *Radiat. Meas.* 44, 560–565.
- Buylaert, J.P., Thiel, C., Murray, A.S., Vandenberghe, D.A.G., Yi, S., Lu, H., 2011. Irsi and post-irsl residual doses recorded in modern dust samples from the Chinese loess plateau. *Geochronometria* 38, 432–440. <https://doi.org/10.2478/s13386-011-0047-0>.
- Buylaert, J.P., Jain, M., Murray, A.S., Thomsen, K.J., Thiel, C., Sohbaty, R., 2012. A robust feldspar luminescence dating method for Middle and Late Pleistocene sediments. *Boreas* 41, 435–451.
- Chawla, S., Gundurao, T.K., Singhvi, A.K., 1998. Quartz thermoluminescence: dose and dose rate effects and their implications. *Radiat. Meas.* 29 (1), 53–63.
- Clarke, M.L., Rendell, H.M., 1997. Infra-red stimulated luminescence spectra of alkali feldspars. *Radiat. Meas.* 27, 221–236.
- Ditlefsen, C., Huntley, D.J., 1994. Optical excitation of trapped charges in quartz, potassium feldspars and mixed silicates: the dependence on photon energy. *Radiat. Meas.* 23, 675–682. [https://doi.org/10.1016/1350-4487\(94\)90003-5](https://doi.org/10.1016/1350-4487(94)90003-5).
- Duller, G.A.T., 1997. Behavioural studies of stimulated luminescence from feldspars. *Radiat. Meas.* 27, 663–694. [https://doi.org/10.1016/S1350-4487\(97\)00216-3](https://doi.org/10.1016/S1350-4487(97)00216-3).
- Duller, G.A.T., Bøtter-Jensen, L., 1993. Luminescence from potassium feldspar stimulated by infrared and green light. *Radiat. Protect. Dosim.* 47, 683–688. <https://doi.org/10.1093/oxfordjournals.rpd.a081832>.
- Duval, M., Guilarte, V., Campaña, I., Arnold, L., Miguens, L., Iglesias, J., González-Sierra, S., 2018. Quantifying hydrofluoric acid etching of quartz and feldspar coarse grains based on weight loss estimates: implication for ESR and luminescence dating studies. *Ancient TL* 36 (1), 1–14.
- Fattahi, M., Stokes, S., 2000. Extending the time range of luminescence dating using red TL (RTL) from volcanic quartz. *Radiat. Meas.* 32, 479–485. [https://doi.org/10.1016/S1350-4487\(00\)00105-0](https://doi.org/10.1016/S1350-4487(00)00105-0).
- Fattahi, M., Stokes, S., 2003. Red luminescence from potassium feldspar for dating applications: a study of some properties relevant for dating. *Radiat. Meas.* 37, 647–660. [https://doi.org/10.1016/S1350-4487\(03\)00246-4](https://doi.org/10.1016/S1350-4487(03)00246-4).
- Frouin, M., Huot, S., Kreutzer, S., Lahaye, C., Lamothe, M., Philippe, A., Mercier, N., 2017. An improved radiofluorescence single-aliquot regenerative dose protocol for K-feldspars. *Quat. Geochronol.* 38, 13–24. <https://doi.org/10.1016/j.quageo.2016.11.004>.
- Goedicke, C., 1984. Microscopic investigations of the quartz etching technique for TL dating. *Nucl. Tracks Radiat. Meas.* 9, 87–93. [https://doi.org/10.1016/0735-245X\(84\)90026-7](https://doi.org/10.1016/0735-245X(84)90026-7).
- Grün, R., Packman, S.C., 1994. Observations on the kinetics involved in the TL glow curves in quartz, K-feldspar and Na-feldspar mineral separates of sediments and their significance for dating studies. *Radiat. Meas.* 23, 317–322. [https://doi.org/10.1016/1350-4487\(94\)90058-2](https://doi.org/10.1016/1350-4487(94)90058-2).
- Huntley, D.J., 2006. An explanation of the power-law decay of luminescence. *J. Phys. Condens. Matter* 18, 1359–1365. <https://doi.org/10.1088/0953-8984/18/4/020>.

- Huntley, D.J., Lamothe, M., 2001. Ubiquity of anomalous fading in K-feldspars and the measurement and correction for it in optical dating. *Can. J. Earth Sci.* 38, 1093–1106. <https://doi.org/10.1139/cjes-38-7-1093>.
- Hütt, G., Jaek, I., Tchonka, J., 1988. Optical dating: K-feldspars optical response stimulation spectra. *Quat. Sci. Rev.* 7, 381–385. [https://doi.org/10.1016/0277-3791\(88\)90033-9](https://doi.org/10.1016/0277-3791(88)90033-9).
- Jain, M., Ankjærgaard, C., 2011. Towards a non-fading signal in feldspar: insight into charge transport and tunnelling from time-resolved optically stimulated luminescence. *Radiat. Meas.* 46, 292–309.
- Jain, M., Singhvi, A.K., 2001. Limits to depletion of blue-green light stimulated luminescence in feldspars: implications for quartz dating. *Radiat. Meas.* 33, 883–892. [https://doi.org/10.1016/S1350-4487\(01\)00104-4](https://doi.org/10.1016/S1350-4487(01)00104-4).
- Jain, M., Sohbaty, R., Guralnik, B., Murray, A.S., Kook, M., Lapp, T., Prasad, A.K., Thomsen, K.J., Buylaert, J.P., 2015. Kinetics of infrared stimulated luminescence from feldspars. *Radiat. Meas.* 81, 242–250. <https://doi.org/10.1016/j.radmeas.2015.02.006>.
- Kalita, J.M., Chithambo, M.L., 2021. Blue- and infrared-light stimulated luminescence of microcline and the effect of optical bleaching on its thermoluminescence. *J. Lumin.* 229, 117712 <https://doi.org/10.1016/j.jlumin.2020.117712>.
- Kalita, J.M., Chithambo, M.L., 2022. Phototransferred thermoluminescence characteristics of microcline (KAlSi₃O₈) under 470 nm blue- and 870 nm infrared-light illumination. *Appl. Radiat. Isot.* 181, 110070 <https://doi.org/10.1016/j.apradiso.2021.110070>.
- Kars, R.H., Wallinga, J., 2009. IRSL dating of K-feldspars: modelling natural dose response curves to deal with anomalous fading and trap competition. *Radiat. Meas.* 44, 594–599.
- Kars, R.H., Wallinga, J., Cohen, K.M., 2008. A new approach towards anomalous fading correction for feldspar IRSL dating- tests on samples in field saturation. *Radiat. Meas.* 43, 786–790.
- Krbetschek, M.R., Trautmann, T., 2000. A spectral radioluminescence study for dating and dosimetry. *Radiat. Meas.* 32, 853–857.
- Krishna, M., Kreutzer, S., King, G., Frouin, M., Tsukamoto, S., Schmidt, C., Lauer, T., Klases, N., Richter, D., Friedrich, J., Mercier, N., Fuchs, M., 2021. Quaternary Geochronology Infrared radiofluorescence (IR-RF) dating : a review. *Quat. Geochronol.* 64, 101155 <https://doi.org/10.1016/j.quageo.2021.101155>.
- Kumar, R., Kook, M., Murray, A.S., Jain, M., 2018. Towards direct measurement of electrons in metastable states in K-feldspar: do infrared-photoluminescence and radioluminescence probe the same trap? *Radiat. Meas.* 120, 7–13.
- Kumar, R., Kook, M., Jain, M., 2020. Understanding the metastable states in K-Na aluminosilicates using novel site-selective excitation-emission spectroscopy. *J. Phys. D Appl. Phys.* 53 <https://doi.org/10.1088/1361-6463/aba788>.
- Lapp, T., Kook, M., Murray, A.S., Thomsen, K.J., Buylaert, J.P., Jain, M., 2015. A new luminescence detection and stimulation head for the Risø TL/OSL reader. *Radiat. Meas.* 81, 178–184. <https://doi.org/10.1016/j.radmeas.2015.02.001>.
- Li, B., Li, S.H., 2011. Luminescence dating of K-feldspar from sediments: a protocol without anomalous fading correction. *Quat. Geochronol.* 6, 468–479. <https://doi.org/10.1016/j.quageo.2011.05.001>.
- Li, B., Jacobs, Z., Roberts, R., Li, S.-H., 2014. Review and assessment of the potential of post-IR IRSL dating methods to circumvent the problem of anomalous fading in feldspar luminescence. *Geochronometria* 41, 178–201.
- Morthekai, P., Chauhan, P.R., Jain, M., Shukla, A.D., Rajapara, H.M., Krishnan, K., Sant, D.A., Patnaik, R., Reddy, D.V., Singhvi, A.K., 2015. Thermally re-distributed IRSL (RD-IRSL): a new possibility of dating sediments near B/M boundary. *Quat. Geochronol.* 30, 154–160. <https://doi.org/10.1016/j.quageo.2015.05.018>.
- Poolton, N.R.J., Bøtter-Jensen, L., Ypma, P.J.M., Johnsen, O., 1994. Influence of crystal structure on the optically stimulated luminescence properties of feldspars. *Radiat. Meas.* 23 (2–3), 551–554.
- Poolton, N.R.J., Ozanyan, K.B., Wallinga, J., Murray, A.S., Bøtter-Jensen, L., 2002a. Electrons in feldspar II: a consideration of the influence of conduction band-tail states on luminescence processes. *Phys. Chem. Miner.* 29, 217–225. <https://doi.org/10.1007/s00269-001-0218-2>.
- Poolton, N.R.J., Wallinga, J., Murray, A.S., Bulur, E., Bøtter-Jensen, L., 2002b. Electrons in feldspar I: on the wavefunction of electrons trapped at simple lattice defects. *Phys. Chem. Miner.* 29, 210–216. <https://doi.org/10.1007/s00269-001-0217-3>.
- Porat, N., Faerstein, G., Medialdea, A., Murray, A.S., 2015. Re-examination of common extraction and purification methods of quartz and feldspar for luminescence dating. *Anc. TL* 33, 255–258.
- Prasad, A.K., Poolton, N.R.J., Kook, M., Jain, M., 2017. Optical dating in a new light: a direct, non-destructive probe of trapped electrons. *Sci. Rep.* 7, 1–15. <https://doi.org/10.1038/s41598-017-10174-8>.
- Reimann, T., Tsukamoto, S., 2012. Dating the recent past (< 500 years) by post-IR IRSL feldspar—examples from the north sea and Baltic sea coast. *Quat. Geochronol.* 10, 180–187.
- Reimann, T., Tsukamoto, S., Naumann, M., Frechen, M., 2011. Quaternary Geochronology the potential of using K-rich feldspars for optical dating of young coastal sediments e A test case from Darss-Zingst peninsula (southern Baltic Sea coast). *Quat. Geochronol.* 6, 207–222. <https://doi.org/10.1016/j.quageo.2010.10.001>.
- Spooner, N.A., 1994. The anomalous fading of infrared-stimulated luminescence from feldspars. *Radiat. Meas.* 23, 625–632.
- Strickertsson, K., 1985. The thermoluminescence of potassium feldspars-Glow curve characteristics and initial rise measurements. *Nucl. Tracks Radiat. Meas.* 10, 613–617. [https://doi.org/10.1016/0735-245X\(85\)90066-3](https://doi.org/10.1016/0735-245X(85)90066-3).
- Thiel, C., Buylaert, J.P., Murray, A., Terhorst, B., Hofer, I., Tsukamoto, S., Frechen, M., 2011. Luminescence dating of the Stratzing loess profile (Austria) - testing the potential of an elevated temperature post-IR IRSL protocol. *Quat. Int.* 234, 23–31. <https://doi.org/10.1016/j.quaint.2010.05.018>.
- Thomsen, K.J., Murray, A.S., Jain, M., Bøtter-Jensen, L., 2008. Laboratory fading rates of various luminescence signals from feldspar-rich sediment extracts. *Radiat. Meas.* 43, 1474–1486.
- Varma, V., Biswas, R.H., Singhvi, A.K., 2013. Aspects of infrared radioluminescence dosimetry in K-feldspar. *Geochronometria* 40, 266–273. <https://doi.org/10.2478/s13386-013-0125-6>.
- Visocekas, R., 1979. La luminescence de la calcite après irradiation cathodique: thermoluminescence et luminescence par effet tunnel. Doctoral dissertation. Université P. et M. Curie, Paris.
- Visocekas, R., 1985. Tunnelling radiative recombination in labradorite: its association with anomalous fading of thermoluminescence. *Nucl. Tracks Radiat. Meas.* 10, 521–529.
- Wintle, A.G., 1973. Anomalous fading of thermo-luminescence in mineral samples. *Nature* 245, 143–144.
- Wintle, A.G., Murray, A.S., 2006. A review of quartz optically stimulated luminescence characteristics and their relevance in single-aliquot regeneration dating protocols. *Radiat. Meas.* 41, 369–391. <https://doi.org/10.1016/j.radmeas.2005.11.001>.
- Zink, A.J.C., Visocekas, R., 1997. Datability of sanidine feldspars using the near-infrared TL emission. *Radiat. Meas.* 27, 251–261.



Post-violet infrared stimulated luminescence (pVIRSL) dating protocol for potassium feldspar

Monika Devi^{a,b}, Naveen Chauhan^{a,*}, Ashok K. Singhvi^a

^a AMOPH Division, Physical Research Laboratory, Navrangpura, Ahmedabad, 380009, India

^b Indian Institute of Technology, Gandhinagar, 382355, India

ARTICLE INFO

Keywords:

Thermoluminescence
Optically stimulated luminescence
Post-violet IRSL (pVIRSL)
K-feldspar
Anomalous fading
Photo-transferred luminescence
Recuperation

ABSTRACT

Devi et al. (2022) suggested that post-violet infrared stimulated luminescence (pVIRSL; IRSL at 100 °C after a violet bleach at 50 °C) of K-feldspars, generally has a near zero athermal fading rate. This study explores the mechanism and suitability of the pVIRSL signal for dating applications. The results suggest that pVIRSL is a recuperated signal, arising from the eviction of charges in deep traps by violet stimulation followed by their recapture to the IR traps. A post-violet IR single aliquot regenerative dose (pVIR-SAR) protocol worked well for seven K-feldspar samples from varied depositional environments with ages ranging from 6 to 286 ka. The pVIRSL paleodoses of most samples, accorded with paleodoses computed using the published ages and their environmental dose rates.

1. Introduction

Infrared stimulated luminescence (IRSL) from K-feldspar (Hütt et al., 1988) enabled its use for dating samples where the use of quartz is not possible or when K-feldspar and quartz cannot be separated (Huntley and Lamothe, 2001). IRSL from K-feldspar has a high luminescence sensitivity and a high saturation dose (~1200 Gy), and thus, it offers an opportunity for extending the dating range using luminescence (Buylaert et al., 2011). However, the presence of anomalous fading (athermal loss of trapped charges due to quantum mechanical tunnelling) leads to underestimation of ages, a fact that has limited its use in dating (Aitken, 1985; Spooner, 1992, 1994; Wintle, 1973; Visocekas, 1979).

The trap depth for the principal IRSL trap of K-feldspars is between 2.0 and 2.5 eV (Hütt et al., 1988; Kumar et al., 2020; Riedesel et al., 2019, 2021). Energies of the excited state, sub-conduction band-tail widths (Urbach width, E_u), and the width of the band tail states accessible from the ground state (ΔE) range from 1.44 to 1.48 eV (Hütt et al., 1988; Riedesel et al., 2019, 2021), 0.26 to 0.81 eV (Poolton et al., 2009; Riedesel et al., 2019) and 0.16 to 0.46 eV (Poolton et al., 2009; Riedesel et al., 2019), respectively (Table S1). Mechanism of K-feldspar luminescence by Visocekas (1985) and Jain and Ankjergaard (2011) involves a trap and spatially distributed recombination centres. It is considered that the excited state of the trap overlaps with the band tail states below the conduction band. Stimulation with IR (1.44 eV) moves

charges from the ground state of the trap through a resonant excitation to an excited state; thereafter, they are thermally assisted in the band tail states to radiatively recombine with charges to provide IRSL emission.

According to the donor-acceptor model, IRSL in K-feldspar depends on tunnelling probability that decreases exponentially with increasing donor-acceptor distance (Hütt et al., 1988; Jain et al., 2015; Poolton et al., 1994). Therefore, during an IRSL measurement, proximal charge pairs are consumed first, and distal ones are accessed later. Low tunnelling probability for distal pairs makes the recombination lifetime higher, and resulting in lower fading rates (Jain et al., 2015; Poolton et al., 1994). Such signals have been variously probed, e.g., a) post-IR IRSL (pIRIRSL; Buylaert et al., 2009, 2011, 2012; Biswas et al., 2013; Thomsen et al., 2008), b) multiple elevated temperatures pIRIRSL (MET-pIRIRSL; Li and Li, 2011), c) thermally redistributed IRSL (RD-IRSL; Morthekai et al., 2015), d) infrared photoluminescence (IRPL; Kumar et al., 2018; Prasad et al., 2017), and e) infrared and blue light stimulated photo-transferred thermoluminescence (PTTL; Kalita and Chithambo, 2022).

Using spectroscopic measurements, Thalbitzer Andersen et al. (2012) suggested that both IRSL and pIRIRSL arise from the same trap and the pIRIRSL results from the recombination of more distant charge pairs. Currently, pIRIRSL is widely used for dating. However, issues of poor bleachability, thermal transfer, and sensitivity changes are reported (Colarossi et al., 2018; Duller and Wintle, 1991; Li and Li, 2011;

* Corresponding author.

E-mail address: chauhan@prl.res.in (N. Chauhan).

<https://doi.org/10.1016/j.quageo.2023.101487>

Received 9 October 2022; Received in revised form 21 October 2023; Accepted 24 October 2023

Available online 10 November 2023

1871-1014/© 2023 Elsevier B.V. All rights reserved.

Liu et al., 2018; Yi et al., 2016). Morthekai et al. (2015) proposed that distant pairs can be redistributed by thermal treatment and then accessed through IRSL at 320 °C. This methodology provided ages up to ~800 ka (Morthekai et al., 2015). Currently, IRPL and PTTL signals are being explored because of their potential to provide a stable luminescence signal from K-feldspar (Kalita and Chithambo, 2022; Kumar et al., 2021; Prasad et al., 2017). Reimann et al. (2015) also suggested the use of transferred IRSL at 125 °C (T-IRSL₁₂₅) for feldspar luminescence dating. The T-IRSL₁₂₅ signal was as stable as pIRIRSL at 290 °C and bleaches faster than pIRIRSL. However, an unresolved age underestimation of up to 8% was seen.

Most studies used a blue detection window (320–520 nm) to measure the IRSL. Other emission bands of K-feldspar have also been explored (e.g., Biswas et al., 2013; Duller, 1997; Jain and Singhvi, 2001; Kalita and Chithambo, 2022; Kumar et al., 2020; Thomsen et al., 2008), but their use in routine dating has been limited. Devi et al. (2022) compared different luminescence signals of K-feldspars and their athermal fading rates using varied combinations of stimulation and detection wavelengths and reported that the post-violet IRSL (pVIRSL) has a fading rate (g-value) of ~0% per decade for most samples. This study investigates the production mechanism of pVIRSL and optimized measurement parameters to develop a pVIR-SAR protocol for dating.

2. Samples and experimental setup

Seven samples of known ages from diverse depositional environments were investigated. The expected ages of samples ranged from 6 ka to >286 ka, and their anticipated paleodoses ranged from 11 Gy to >956 Gy (Table 1). The age controls were based on quartz blue stimulated luminescence (BSL) and K-feldspar pIRIRSL. Sample RTP-18-02 had an additional age control as it was from the bottom layer of Youngest Toba Tuff (YTT) deposit securely dated using K–Ar and pIRIRSL dating to ~75 ka (Ninkovich et al., 1978; Anil et al., 2023). A museum specimen of potassium feldspar (KF) was used for experiments to elucidate the mechanism of pVIRSL. X-ray diffraction confirmed it to be a microcline (Devi et al., 2022).

K-feldspar grains were extracted from sediments using a sequential pre-treatment with 1N HCl and 30% H₂O₂ to remove the carbonates and organic matter, respectively, followed by dry sieving to get 90–150 µm grains. K-feldspar grains were separated using sodium polytungstate ($\rho = 2.58 \text{ g/cm}^3$) and Frantz® magnetic separator at magnetic fields of ~7 and ~18 kGauss (Porat et al., 2015). The grains were then etched with 10% hydrofluoric (HF) acid for 40 min (Goedicke, 1984) to remove alpha irradiated skin, followed by 30 min treatment with 12N HCl to convert insoluble fluorides into soluble chlorides and then washed with distilled water. The pVIRSL and pIRIRSL ages of PRL0, RSN-01-17, and

MHD-02-17 are reported for the first time. Dose rate measurement details are provided in Table S2.

A Risø-TL/OSL DA-20 reader with a detection and stimulation head (DASH) comprising multiple stimulation LEDs and automated detection filter changer assembly was used (Bøtter-Jensen et al., 2010; Lapp et al., 2015). The stimulation sources comprised IR emitting LEDs (850 ± 33 nm) and a violet light emitting laser diode (405 ± 15 nm). Detection was made through band pass filters transmitting in 327–353 nm (Hoya U-340 + Semrock Brightline HC 340/26 (Narrow-UV)) for violet stimulation and 320–520 nm (SCHOTT BG-39 + BG-3) for IR stimulation coupled to ET 9107B photomultiplier tube. Daylight bleaching was carried out using Osram ultravitalux 300 W sun-lamp filtered through a glass window.

3. Measurements

Devi et al. (2022) reported a non-fading IRSL signal following a violet stimulation. This study attempted to elucidate the mechanism that leads to a near zero fading signal in pVIRSL and explored its dosimetric properties using the following experiments:

1. Identification of source traps
2. Mechanism of charge transfer
3. Bleachability, recuperation, and reproducibility of pVIRSL

For these experiments, inter aliquot variability was minimized by stabilizing the luminescence sensitivity of aliquots by taking them through five cycles of dose (~20 Gy) followed by TL glows to 500 °C. The TL reproducibility was within 2%. Two such sensitized aliquots of KF sample were used for subsequent experiments described in sub-sections 3.1 and 3.2. The measurement conditions were VSL and IRSL at 50 °C, a dose of 20 Gy, TL glows to 500 °C recorded with a heating rate of 2 °C/s, preheat of 250 °C for 60 s, and detection in the blue window. The choice of luminescence measurements at 50 °C was to ensure that all the measurements were at the same temperature and to minimize any temperature dependent changes in VSL and IRSL yields.

3.1. Source trap and photo-transfer

Protocol in Fig. 1a was used to measure the intensity of pVIRSL and IRSL, and a comparison is given in Fig. 1b. Up to 10% of initial IRSL (IRSL1) was obtained in post-violet IRSL2 even after 100 s of a prior IR stimulation (IRSL1).

Protocol in Fig. 2a was used to identify the TL source traps responsible for pVIRSL, and Fig. 2b plots residual TL after each cycle. The possibility of photo-transfer of charges by violet stimulation to IR light

Table 1

List of samples along with geological location and depositional history, age controls and details. In the table NCF-refers to natural correction factor.

Serial no	Sample code	Location Latitude Longitude	Depositional environment	Expected age (ka)	Age controls	Reference
1	KF	–	Museum	–	–	Devi et al. (2022)
2	DH1	Rajasathan (26 47'59.20" N, 72 18' 42.00" E)	Aeolian	Zero age (Modern)	–	This study
3	PRL0	Tamil Nadu (10° 38' 5.388" N, 79° 49' 45.012" E)	Fluvial	6 ± 1	Quartz NCF-BSL-SAR	This study
4	PRL2	Narmada valley (22° 13' 44" N 76° 01' 36" E)	Fluvial	25 ± 2	Quartz BSL-SAR	Mishra et al. (2013)
5	MHK-07-07	Narmada valley (22° 13' 44" N 76° 01' 36" E)	Fluvial	31 ± 3	Quartz BSL-SAR	Mishra et al. (2013)
6	RTP-18-2	Andhra Pradesh (15.590630°N, 79.194290° E)	Fluvial	76 ± 6 ^a	pIRIR-SAR Feldspar	Anil et al. (2023); Ninkovich et al. (1978)
7	RSN-01-17	Raisan (23° 9' 59.4" N, 72° 39' 38.16" E)	Fluvial	129 ± 16 ^a	pIRIR-SAR Feldspar	This study
8	HMP-18-5	Andhra Pradesh (15° 27' 56.9016" N, 79° 23' 59.0388" E)	Fluvial (archaeological)	>247 ± 32 ^a	pIRIR-SAR Feldspar	Anil et al. (2022)
9	MHD-02-17	Mahudi (23° 30' 0" N, 72° 47' 60" E)	Fluvial	>286 ± 13 ^a	pIRIR-SAR Feldspar	This study

^a The ages are fading corrected.

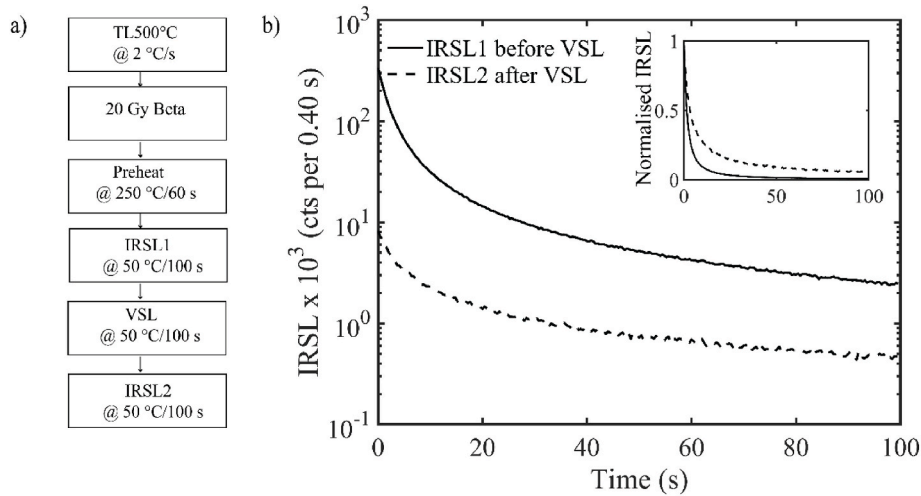


Fig. 1. a) Measurement protocol to explore the relative intensity of pVIRSL compared to IRSL for KF sample. b) IRSL decay curves recorded before (IRSL1) and after (IRSL2) violet stimulation. The signal of IRSL2 is about an order of magnitude smaller than IRSL1. Inset shows the normalised IRSL intensities for IRSL1 and IRSL2.

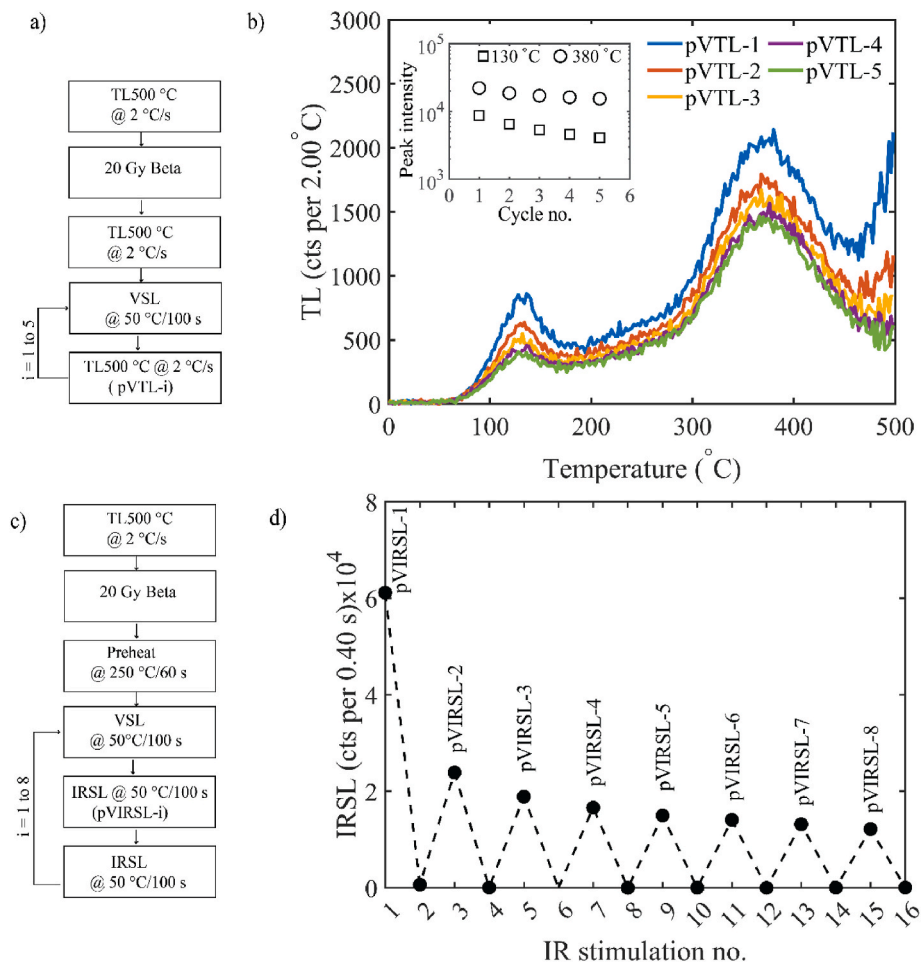


Fig. 2. a) Measurements carried out to explore the TL emissions after the repeated violet stimulation without any additional dose to the KF sample. b) The background subtracted TL glow curves are recorded in the blue window. Inset in the figure shows the variation of the integrated intensity of TL peak at 130 °C (integrated from 120 to 140 °C) and 380 °C (integrated from 370 to 390 °C) with cycle number. c) Measurements carried out to explore the IRSL emissions after the repeated violet stimulation without any additional dose. d) IRSL signal obtained after repetitive violet light stimulation. The IRSL signal intensity is obtained by subtracting the last 2 s signal from the initial 2 s.

sensitive traps was examined using the protocol in Fig. 2c, and results are shown in Fig. 2d.

3.2. Source of pVIRSL

Traps providing charges for IRSL and pVIRSL at 50 °C were determined through the dependence of IRSL on the stimulation temperature of VSL and cut-heat. Fig. 3a and b provide the measurement protocol, and Fig. 3c provides the results.

3.3. Dating using pVIRSL

To assess the suitability of pVIRSL for geochronology, factors such as athermal fading rate, bleachability under daylight, recuperation, recycling, and dose recovery ratio were measured and are discussed below:

a) Bleachability of the deep traps

Bleachability of pVIRSL by daylight was tested for a sample from surface sediment (DH-1) from modern dune sand using the protocol in Table 2 (the protocol steps are discussed in detail in subsection 4.3).

The bleachability of the signal under violet and IR stimulation in the TL/OSL reader was measured to find equivalent exposures that mimic natural daylight bleaching. Given that during SAR measurements, a sample undergoes multiple cycles of irradiation and bleaching, it is important that the carryover of pVIRSL from one cycle to the next is minimal. This was examined using the protocol in Fig. 5a, and Fig. 5b provides the results. The ratio of pVIRSL2/pVIRSL1 measures the residual pVIRSL after a sequence of violet and IR stimulation for 200 s at temperatures in the range of 150–450 °C.

b) Athermal Fading

Fading measurements were made using the protocol given in Table S3. The samples were bleached under a filtered sun-lamp for 5 h. A known dose approximately equal to the expected paleodose was then administered. A delay of 1–8 days was provided after preheating to estimate the fading rates (Auclair et al., 2003; Huntley and Lamothe, 2001).

c) Dose Response

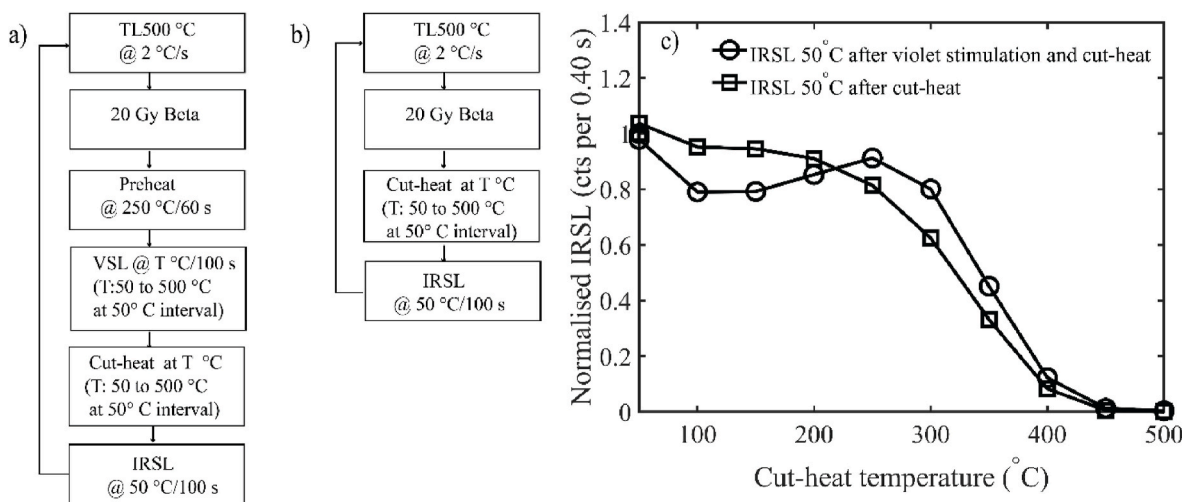


Fig. 3. a) Sequence used to explore the origin of IRSL signal after the violet stimulation of KF sample. The temperature of both violet stimulation and cut-heat was varied simultaneously. b) Measurements carried out to explore the origin of the IRSL signal. Both a) and b) sequences were performed on the same and single aliquot. c) Variation of IRSL and pVIRSL with different cut-heat and violet stimulation temperatures. The IRSL is obtained by subtracting the last 2s background from the initial 2 s signal. IRSL signal was normalised with respect to its maximum value. To test any sensitivity change data for IR 50 °C after all measurements is also presented.

Table 2
Measurement parameters for pVIR-SAR protocol after optimization for the equivalent dose estimation. The text in bold are optimized parameters for pVIR-SAR protocol.

Step	Optimized protocol	Remarks
1	Natural signal	
2	Preheat (250 °C, 60 s)	To remove unstable signal
3	VSL (50 °C, 100 s)	
4	IRSL (200 °C, 100 s)	L_n, L_x
5	Test Dose (50–80% D_e)	
6	Preheat (250 °C, 60 s)	To remove unstable signal
7	VSL (50 °C, 100 s)	
8	IRSL (200 °C, 100 s)	T_n, T_x
9	VSL (350 °C, 200 s)	Illumination
10	IRSL (350 °C, 200 s)	Illumination
11	Give dose and return to step 2	

To estimate the paleodoses using SAR protocol, optimization of the IR stimulation temperature after a violet bleach, preheat, and test dose was carried out on sample MHK-07-07, having a paleodose of 56 ± 7 Gy. The dose response of pVIRSL was constructed for optimized parameters, and the applicability of the protocol was further tested on all natural samples mentioned in Table 1.

The extent of pVIRSL bleaching under daylight and filtered sun-lamp

Table 3
Protocol used to explore the L_x and T_x correlation.

Steps	Protocol
1	Reader bleaching (VSL and IRSL @ 350 °C for 200 s at 70 % power)
2	Dose ^a (~530 Gy)
3	Preheat @250 °C for 60 s
4	VSL @50 °C for 100 s
5	IRSL @200 °C for 100 s
6	Test dose ^a (~350 Gy)
7	Preheat @250 °C for 60 s
8	VSL @50 °C for 100 s
9	IRSL @200 °C for 100 s
10	VSL @ 350 °C for 200 s
11	IRSL @ 350 °C for 200 s
12	Return to step 2 (Repeat up to 15 cycles)

a The mentioned doses are only for RSN-01-17 sample. For other samples, correlation was explored using a dose approximately equal to the expected dose, and test doses were about 50% of the expected doses.

Table 4

Estimated D_e , fading value, recuperation, residual dose, and dose recovery ratio for all samples using pVIR-SAR protocol. Recuperation observed in all the samples is <5% except for PRL0 (young sample) where it is less than 10%.

Sample name	pVIR D_e (Gy)	Expected D_e (Gy)	Dose rate (Gy/ka)	pVIR Age (ka)	Expected age (ka)	pVIR g-value (% per decade)	Maximum delay for fading (h)	pVIR Residual dose (Gy)	Dose recovery ratio	Remarks
PRL0	18 ± 1 ^a 21 ± 1	14 ± 2 ⁺ 11.1 ± 0.3 [§]	2.25 ± 0.17 1.84 ± 0.13 [§]	8 ± 1 ^a 9 ± 1	6 ± 1	1.9 ± 0.1	32	4.4 ± 0.2	0.97 ± 0.05	Quartz age (NCF-BSL-SAR)
PRL2	49 ± 3	46 ± 5 ⁺ 35.7 ± 0.1 [§]	1.87 ± 0.14 1.45 ± 0.09 [§]	24 ± 3	25 ± 2	-0.5 ± 0.3	41	5.4 ± 0.2	1.08 ± 0.04	Q: BSL-SAR
MHK-07-07	48 ± 1	56 ± 7 ⁺ 43.0 ± 0.1 [§]	1.82 ± 0.16 1.41 ± 0.12 [§]	25 ± 3	31 ± 3	-0.3 ± 0.2	41	5.3 ± 0.2	1.02 ± 0.02	Q: BSL-SAR
RTP-18-2	211 ± 7	234 ± 6	3.07 ± 0.21	69 ± 5	76 ± 6	0.1 ± 0.3	69	8 ± 1	0.97 ± 0.03	F: Youngest Toba Tuff sample
RSN-01-17	500 ± 30	511 ± 62	3.97 ± 0.16	126 ± 9	129 ± 16	-0.2 ± 0.3	95	19 ± 4	1.03 ± 0.03	F: pIRIR-SAR
HMP-18-5	340 ± 30	325 ± 12 ^a >511 ± 2	2.07 ± 0.12	164 ± 21	157 ± 11 ^a >247 ± 32	0.5 ± 0.3	106	12 ± 2	0.96 ± 0.05	F: pIRIR-SAR
MHD-02-17	484 ± 19 ^a >940 ± 4	505 ± 37 ^a >956 ± 2	3.35 ± 0.15	144 ± 13 >280 ± 13	151 ± 13 ^a >286 ± 13	2.8 ± 0.3	132	21 ± 1	1.06 ± 0.05	F: pIRIR-SAR

^a Represents the fading uncorrected feldspar doses and ages, + represents the quartz converted feldspar doses, and § represents the quartz D_e values and dose rates.

for exposure durations ranging from 0 to 300 min and 0 to 1200 min, respectively, was measured. Residual doses for all samples after 5 h of filtered sun-lamp exposure are provided in Table 4. For dose recovery tests, a known dose approximately equal to paleodose was given after a 5 h filtered sun-lamp bleach, and then the administered doses were recovered using the pVIR-SAR and pIRIR-SAR protocols. The pVIR-SAR paleodoses were compared with expected values based either on BSL-SAR of quartz (converted to the K-feldspar doses) or on pIRIR-SAR (pIRIRSL at 290 °C) of K-feldspar (Buylaert et al., 2011).

d) Changes in luminescence sensitivity

Change in luminescence sensitivity during repeated measurement cycles was investigated through a correlation between regenerative dose (L_x) and test dose luminescence (T_x) after laboratory bleach using sequential stimulation by violet and IR at 350 °C for 200 s (Table 3). This bleaching was carried out at the end of each L_x and T_x measurement cycle. A regeneration dose of ~530 Gy and a test dose of ~350 Gy were used for RSN-01-17 sample. The sequence in Table 3 was repeated for 16 cycles. The initial 2 s of pVIRSL decay curves were taken as the signal, and the final 2 s were considered the background. Fig. 9 provides the results.

4. Results and discussion

4.1. Source traps and pVIRSL mechanism

4.1.1. Post-violet TL/IRSL measurements

TL glow curve of the KF with 20 Gy dose comprises two peaks at 130 °C and 380 °C (Fig. S1). Fig. 2b shows TL glow curves after heating to 500 °C followed by a violet stimulation. These suggest photo-transfer of charges from traps deeper than 500 °C to shallower traps at 130 °C and 380 °C. Repetitive VSL and TL measurements without intervening irradiation produced TL signal above the background, suggesting that the deep traps served as a reservoir and supplied charges for post-violet TL (pVTL). Fig. 2b inset plots the integrated intensity of PTTL glow peaks with the cycles of violet stimulation and shows depletion in PTTL for repetitive VSL and TL measurements.

Similarly, over 20% IRSL of pVIRSL-1 was observed after repeated violet stimulations without any intervening radiation dose (Fig. 2c and d). At the end of each violet and IR stimulation, the IRSL was reduced to the background level. Like pVTL, pVIRSL intensity decreased with repetitive cycles of violet stimulation to an asymptotic value of about 20% of the initial value. VSL decay curves for each measurement cycle are shown in Fig. S2. After the third cycle, VSL residual was near background levels suggesting that the recombination centres responsible for emission in the narrow-UV window were depleted, although charges from deep reservoir traps were still being photo-transferred to IR traps (Fig. 2b).

4.1.2. Source of pVIRSL

The pVTL glow curve comprised TL glow peaks at 130 and 380 °C (Fig. 2b). Relation between pVTL and pVIRSL was examined through violet stimulation at increasing stimulation temperatures and cut-heat (Fig. 3a). The IRSL intensity of a sample was normalised to the IRSL after preheat, violet stimulation at 50 °C and a cut-heat at 50 °C. Fig. 3c provides normalised IRSL with increasing cut-heat temperatures after a violet exposure. The pVIRSL decreased by about 20% from 50 °C to 100 °C, followed by an increase of 15% up to 250 °C violet stimulation and cut-heat. At a cut-heat of 500 °C, pVIRSL reduced to 0.3% of the initial value (Fig. 3c). Similarly, variation of conventional IRSL with varying cut-heat temperatures was explored using the protocol in Fig. 3b. IRSL decreases by 15% up to the cut-heat of 200 °C and then a continuous decrease up to 500 °C was seen, where the signal was 0.01% of the initial value (Fig. 3c).

4.1.3. Mechanism for pVIRSL

Fig. 2b suggests that TL glow peaks <500 °C are populated through photo-transfer during a violet stimulation. The supply of charges and IRSL continues after repeated violet stimulation, suggesting that violet stimulation repopulates the IR traps each time. The efficiency of such a photo-transfer progressively diminishes with each cycle and reaches an asymptotic value of ~20% of the initial value (Fig. 2d). Based on Kalita and Chithambo (2022), Jain and Ankjærgaard (2011), Kumar et al. (2020), and the present observations, a plausible mechanism for pVIRSL is that charges in deep reservoir traps get stimulated to the conduction

band by violet stimulation. A fraction of these are then trapped at IR traps and give pVIRSL. Fortunately, the dose proportionality is retained in this complex process.

Fig. 3c shows the dependence of pVIRSL with temperature for violet stimulation and cut-heat. The initial decrease (up to 100 °C) is possibly due to reduction in a phosphorescence from glow peaks below 130 °C. An increase in IRSL with the temperature at which violet stimulation and cut-heat (up to 250 °C) are carried out suggests an increased thermal assistance to charges in deep traps, and this is seen through an increase in the slow component of VSL decay with stimulation temperature (Fig. S3). Consequently, charges recaptured in IRSL traps increase and lead to higher IRSL. At Stimulation temperatures >250 °C TL peaks sensitive to IR get depleted and result in a decrease in IRSL. Fig. 3c shows that IRSL has a slow decrease up to 200 °C followed by a faster decrease thereafter to up to a cut-heat of 500 °C. The initial decrease in IRSL reflects the depletion of the 130 °C peak. These results accord with Murray et al. (2009) that IR stimulation is related to the 140 °C and 410 °C TL glow peaks (130 °C and 380 °C in the present study). A rapid depletion of IRSL with increasing cut-heat and violet stimulation temperature (>250 °C) suggests a depletion of charges from TL peaks that provide IRSL.

Fig. 4 summarizes the mechanism of pVIRSL based on the band model of Jain and Ankjærgaard (2011). Transition-1 is the excitation of charges during violet stimulation, where charges from all traps get excited to the conduction band. Some of the charges get recaptured at the IR trap, while others produce VSL. Subsequent IR stimulation (Transition-2) probes the recaptured charges and provides pVIRSL. Violet stimulation also empties charges from IR traps acquired during geological antiquity and ensures that pVIRSL is exclusively due to photo-transferred charges from the deeper traps to the IR traps. As the measurements are made without any delay, post-violet IRSL yields a near zero fading (Devi et al., 2022).

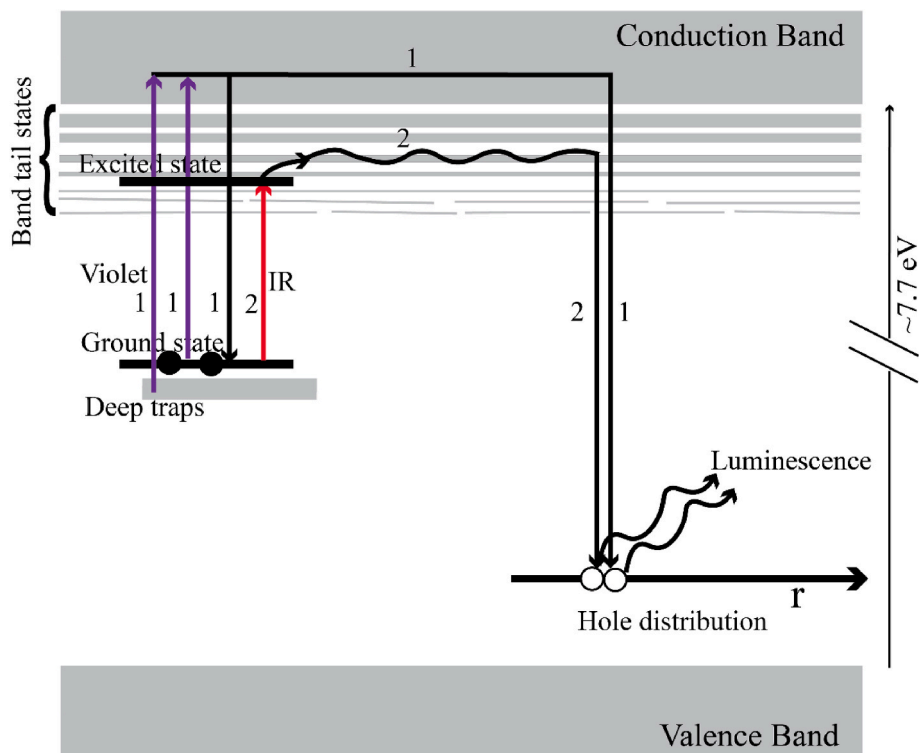


Fig. 4. Band model for post-violet IRSL signal (modified after Jain and Ankjærgaard, 2011). Transition-1 represents the excitation, recombination, and recapture pathway of violet stimulation. Electrons from deep reservoir traps are excited using violet stimulation. The excited electrons go to the conduction band, and some are recaptured to the unoccupied states of the principal trap. These recaptured charges are further probed using IR stimulation (Transition-2), resulting in pVIRSL in the blue window. (For interpretation of the references to colour in this figure legend, the reader is referred to the Web version of this article).

4.2. Dating using pVIRSL

A basic requirement for the applicability of pVIRSL for dating is that it should be bleachable by natural daylight. Therefore, the bleachability of the pVIRSL was explored.

4.2.1. Bleachability of the deep traps

The mean pVIR-SAR dose for a modern (zero age) desert dune DH1 sample was 0.09 ± 0.14 Gy ($n = 10$), which suggests that pVIRSL is bleached by daylight and can be used for geological dating.

Fig. 5a and b shows the protocol and the effect of bleaching of pVIRSL by violet and IR excitation with varied stimulation temperatures, respectively. The ratio of pVIRSL2/pVIRSL1 decreases with increasing stimulation temperatures of violet and IR excitation. Bleaching at 350 °C for 200 s reduces the residual signal to 4.5% of the initial value, and therefore, in the SAR protocol, 350 °C was used to bleach pVIRSL at the end of each dose measurement cycle.

Based on the foregoing, a regeneration protocol for the pVIRSL was developed (Table S4). This differs from the SAR protocol of Murray and Wintle (2000) in respect of stimulations and bleaching steps (steps 3, 4, 7, 8, 9, and 10). Here two step stimulation (violet (50 °C, 100 s) and IR (100 °C, 100 s)) and bleaching ((violet (350 °C, 200 s) and IR (350 °C, 200 s)) were used. A preheat of 250 °C for 60 s was used after each irradiation based on preheat plateau (Fig. 7b). The dose response curve (DRC) for an aliquot of MHK-07-07 gave a recycling ratio of 1.06 ± 0.04 and a paleodose of 50 ± 2 Gy (Fig. 6a) that concurred with the expected K-feldspar dose of 56 ± 7 Gy. This, however, gave a recuperation of 12%. Bleaching temperature above 350 °C reduced the recuperation to less than 5%, but to avoid luminescence sensitivity changes due to heat, it was set at 350 °C. Having settled these, optimization of the stimulation temperature of pVIRSL was examined.

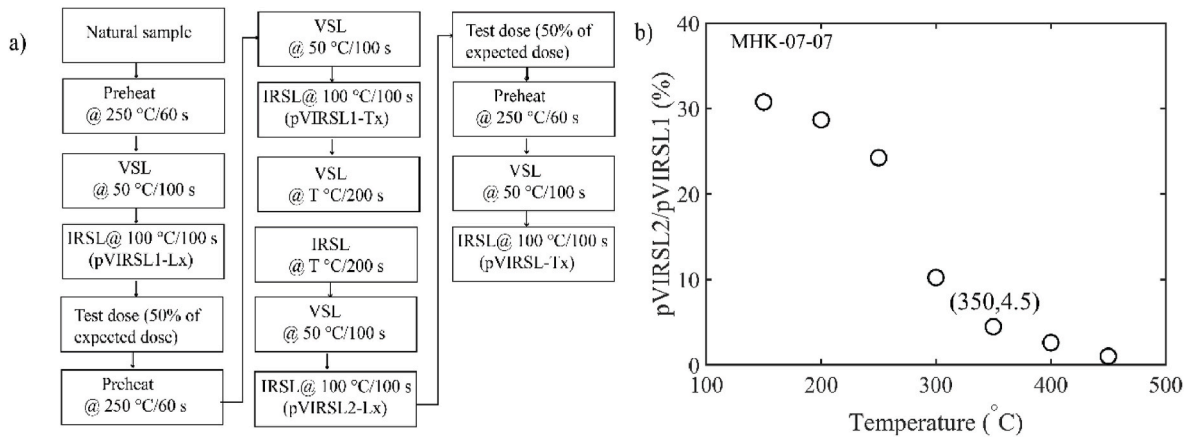


Fig. 5. a) Measurement protocol to test the bleachability of pVIRSL signal in the reader at the variable temperature of violet and IR stimulation (bleaching step). b) Percentage of residual pVIRSL signal (pVIRSL2/pVIRSL1; test dose normalised) at variable elevated temperature of violet and IR bleaching for MHK-07-07 sample. Each data point represents a single aliquot with a natural dose. At an illumination temperature of 350 °C, the residual pVIRSL signal is 4.5%.

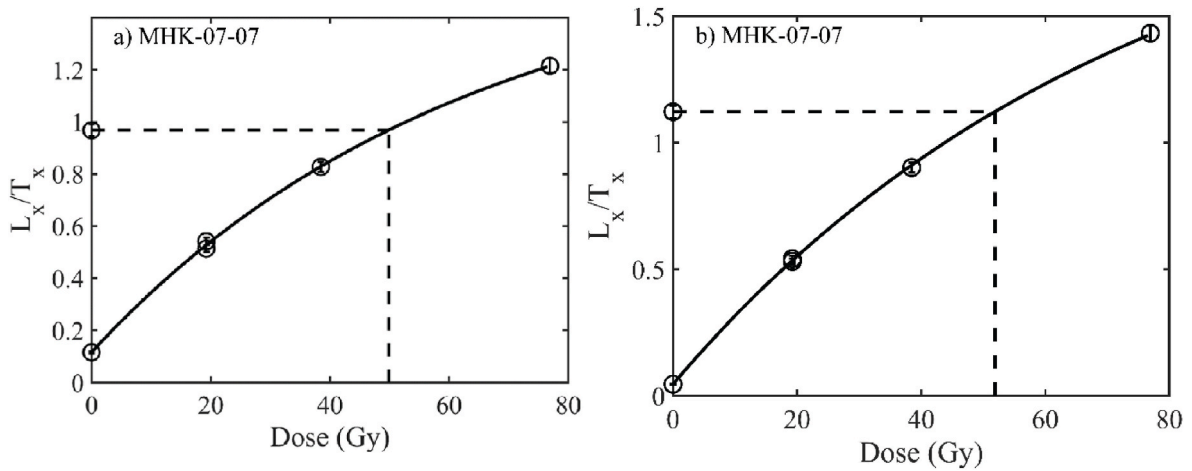


Fig. 6. a) DRC constructed using pVIR-SAR protocol (Table S4) for MHK-07-07 sample. The D_e , recycling ratio and recuperation are 50 ± 2 Gy, 1.06 ± 0.04 , and $12.0 \pm 0.5\%$, respectively. b) DRC constructed using an optimized pVIR-SAR protocol (Table 2) for the MHK-07-07 sample. The D_e , recycling ratio and recuperation are 52 ± 2 Gy, 1.02 ± 0.03 , and $4.1 \pm 0.1\%$, respectively.

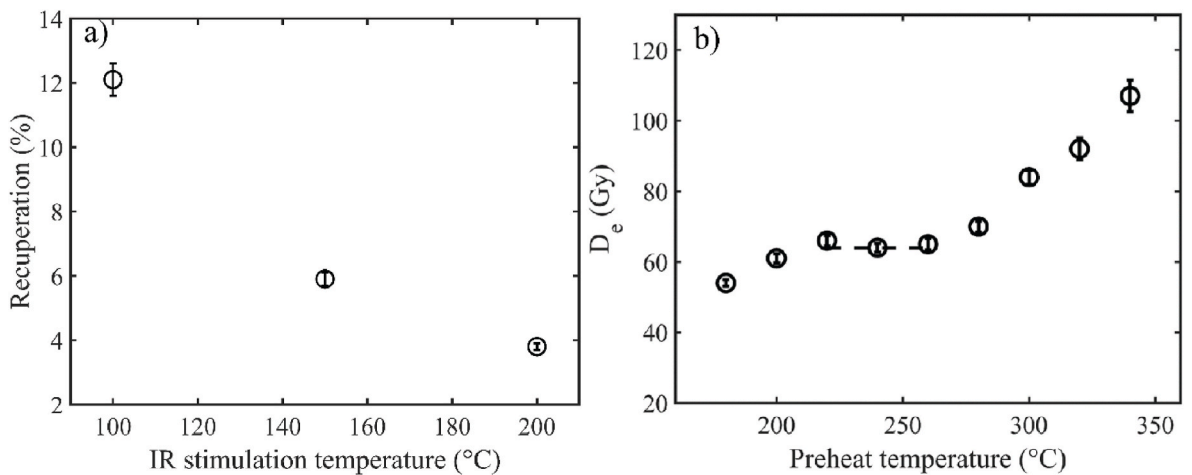


Fig. 7. a) Variation of recuperation for pVIR-SAR with IRSL stimulation temperature of the MHK-07-07 sample. Recuperation is <5% at IR 200 °C. b) D_e plateau with preheat temperature for PRL2 sample. Here D_e at each preheat temperature is the mean of three aliquots. All D_e values falls with 5% of each other in the preheat temperature range 220–260 °C.

4.2.2. Stimulation temperature for IRSL

Murray and Wintle (2000) suggested that higher stimulation temperatures reduce recuperation. In this study, the recuperation reduced from 12% to 4% for IR stimulations at 100–200 °C (step 4, 8; Table S4) (Fig. 7a). Thus, IRSL stimulation at 200 °C was used for paleodose estimation. DRC of MHK-07-07 for post-violet IRSL at 200 °C is shown in Fig. 6b. A recycling ratio of 1.02 ± 0.03 and recuperation of $4.1 \pm 0.1\%$ was obtained.

4.2.3. Preheat temperature

The preheat plateau for the natural dose of PRL2 gave a plateau of D_e values (within $\pm 5\%$) between 220 and 260 °C (Fig. 7b). A uniform preheat of 250 °C was therefore used.

4.2.4. Optimization of the test dose

Colarossi et al. (2018) reported that the magnitude of the test dose during pIRIR-SAR influences the growth curve. In their study, lower test doses (<15% of paleodose) led to the carryover of charges from the regeneration doses into test dose luminescence (T_x) and resulted in an early saturation of DRC. Higher test doses suppressed such a carryover of charges to the next SAR dose, and this led to a higher saturation dose of DRC, making it possible to date older samples. Therefore, these authors recommended the use of test doses in the range of 15–80% of D_e value, as was also suggested by Yi et al. (2016).

Dependence of pVIRSL D_e value on the test dose was explored on samples MHK-07-07 and RTP-18-02. Fig. 8a and c suggest that test doses less than 50% of the expected dose underestimate D_e , and test doses exceeding 50% of the anticipated D_e lead to paleodoses closer to the

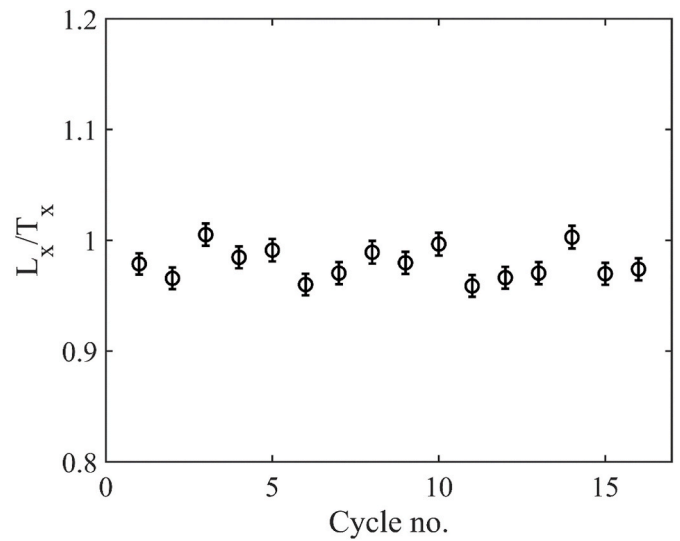


Fig. 9. a) Ratio of the pVIRSL signal for regeneration dose (L_x : initial signal minus background) to test dose (T_x : initial signal minus background) is plotted against measurement cycle number for the RSN-01-17 sample (Table 3).

expected doses. Fig. 8b and d plot the variation T_x/T_n with SAR cycles with test doses for pVIR-SAR and show that T_x follows regeneration dose luminescence (L_x). This indicates that T_x depends on L_x from the corresponding regeneration dose. Variation in T_x/T_n reduced from 76% to

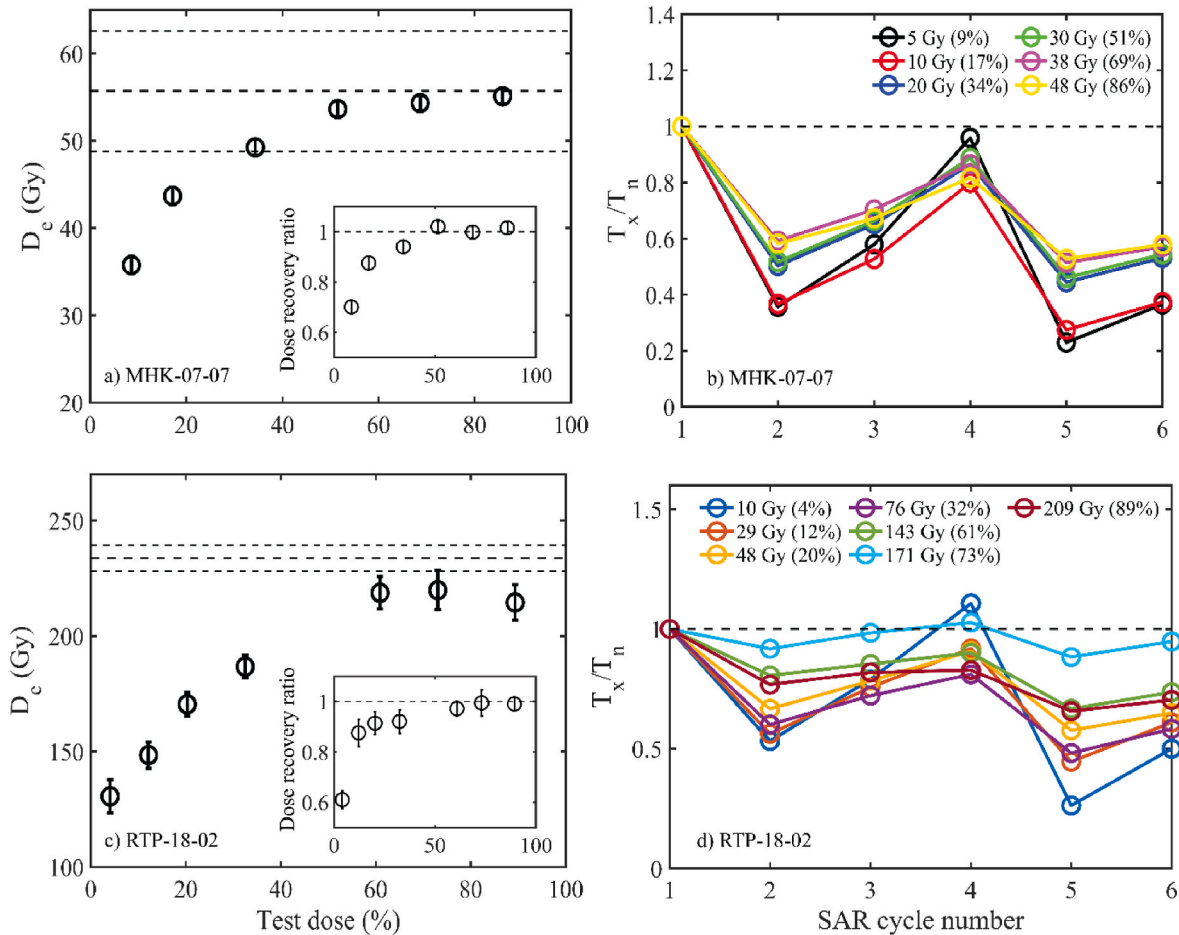


Fig. 8. Test dose dependency of dose for MHK-07-07 (a, b) and RTP-18-02 (c, d). At each test dose, D_e is an average of at least three aliquots. Test doses were varied from approximately 5 to 90% of the expected dose. Dose recovery ratios at variable test doses for MHK-07-07 and RTP-18-02 sample are shown in inset of (a) and (c).

47% when the test doses changed from 9% to 86% of the expected dose for MHK-07-07. For RTP-18-02, variation reduced from 76 to 25% for a change in test dose from 4 to 89% of the expected dose. The change in T_x/T_n is higher for low test doses, whereas for high test doses, T_x and T_n covary, suggesting that carryover of charges gets suppressed through the use of higher test doses. Therefore, test doses ranging from 50 to 80% of the expected doses were used.

Dose recovery tests also depend on the test dose. A known dose approximately equal to the expected dose was recovered using varied test doses. Inset in Fig. 8a and c shows that dose recovery ratios were less than unity for test doses <50% of the expected dose and near unity for test doses >50% for these samples. Therefore, in the future, it will be desirable to establish the test dose before proceeding with dating analysis.

The laboratory saturation doses ($2D_0$) of DRC also dependent on the test dose and ranged from 56 Gy to 300 Gy and from 148 Gy to 606 Gy for two independent samples for test doses ranging from 5 to 90% of the expected dose (Table S5). These results accord with Colarossi et al. (2018).

For HMP-18-5, the estimated D_e was in saturation for low test doses (i.e., <20% of the expected dose) (Fig. S4a), and at higher test doses (~55% of the expected dose), it was below saturation. The estimated dose was 580 ± 29 Gy (Fig. S4b). Variation of T_x/T_n reduced from 72 to 45% for test doses ranging from 15 to 55% of the expected dose (Figs. S4c and d). These results indicate that variation of D_e with test dose is sample dependent.

4.3. Optimized pVIRSL single aliquot regenerative (pVIR-SAR) dose protocol

The suggested pVIR-SAR protocol is shown in Table 2, with the test dose being 50–80% of anticipated D_e (step-5), preheat of 250 °C for 60 s, and bleaching using both violet and IR stimulation at 350 °C for 200 s. The pVIRSL at 200 °C was used for D_e estimations. A zero dose and recycling dose monitored recuperation and repeatability of sensitivity corrected signal. The results are discussed below:

4.3.1. Reproducibility and luminescence sensitivity changes

Reproducibility of sensitivity corrected pVIRSL signal was tested using the protocol mentioned in Table 3 for cycles of several repeated

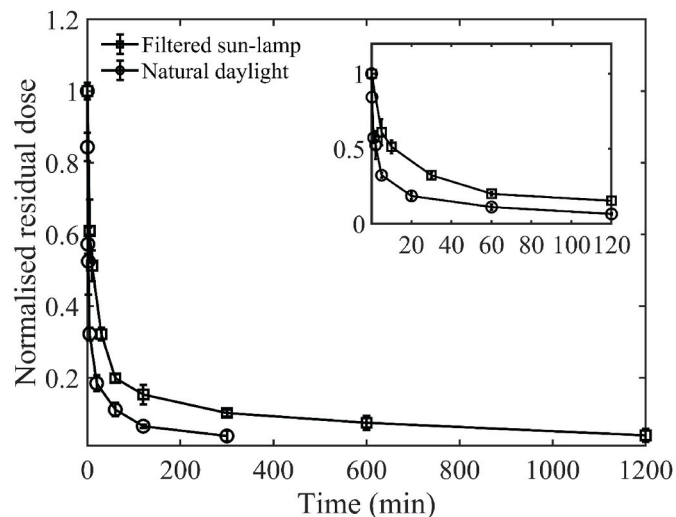


Fig. 10. Bleaching curves for a MHK-07-07 sample under UV filtered sun-lamp light and natural daylight exposure. Each point is an average of three aliquots. The pVIRSL signal reaches the residual level in ~60 min and ~100 min under daylight and solar lamp light exposure, respectively. For clarity data for the initial 2 h is shown in the inset.

measurements. Fig. 9 plots L_x/T_x values for 16 repeated cycles for RSN-01-17 sample. The regenerated pVIRSL (L_x) for a constant dose (~530 Gy) corrected by a test dose (T_x) (~350 Gy) remains unchanged. The variation is within 5% and suggests that pVIRSL is reproducible and that the test dose faithfully corrects for sensitivity changes during the measurements.

4.3.2. Residual doses of the pVIRSL

Normalised pVIRSL residual doses using natural daylight and filtered sun-lamp for different bleaching times are shown in Fig. 10. The residual levels are at 11% after ~60 min and at 15% after ~100 min under natural daylight and filtered sun-lamp, respectively. The mean of residual doses of five aliquots for different samples after 5 h of filtered sun-lamp bleach ranged from 4.4 ± 0.2 to 21 ± 1 Gy (Table 4), and these were subtracted from D_e values. The pIRIR-SAR residual doses measured after 5 h of bleach under filtered sun-lamp ranged from 10 ± 1 to 43 ± 8 Gy (Table S6). The pVIR-SAR residual doses were 23 to 67% lower than the pIRIR-SAR, suggesting that the pVIR-SAR protocol may provide a better option for dating young samples.

4.3.3. Athermal stability of the pVIRSL

Following the procedure mentioned in Table S3, the athermal fading rates of pVIRSL at 200 °C were measured with delays of 1–8 days after a preheat of 250 °C for 60 s. The t_c value was two days. Most samples had near zero athermal fading rates ($g \leq 0.5\%$ per decade, $n = 15$) (Table 4, Fig. 11). Sample PRL0 and MHD-02-17 had a g -value of 1.9 ± 0.1 and $2.8 \pm 0.3\%$ per decade, and the reason would need further investigations.

4.3.4. Dose recovery

Five aliquots per sample were measured for the dose recovery test, and the given doses were recovered using a pVIR-SAR protocol (Table 2). The residual doses were subtracted from the recovered doses. The ratios of the dose recovered to the dose given ranged between 0.96 and 1.08 for all samples (Table 4). The dose recovery ratios for pIRIR on the same set of samples ranged from 0.95 to 1.42 (Table S6).

4.3.5. Saturation dose

For laboratory saturation doses ($2D_0$), DRCs for regeneration doses up to 3500 Gy were constructed. A single saturating exponential function was used for DRC fitting (Fig. 12). The $2D_0$ values ranged from 295 to 970 Gy (Table S7). The best case example was of MHD-02-17 had $2D_0$ of ~1000 Gy, a recycling ratio of 1.00 ± 0.05 , and recuperation of $2.6 \pm$

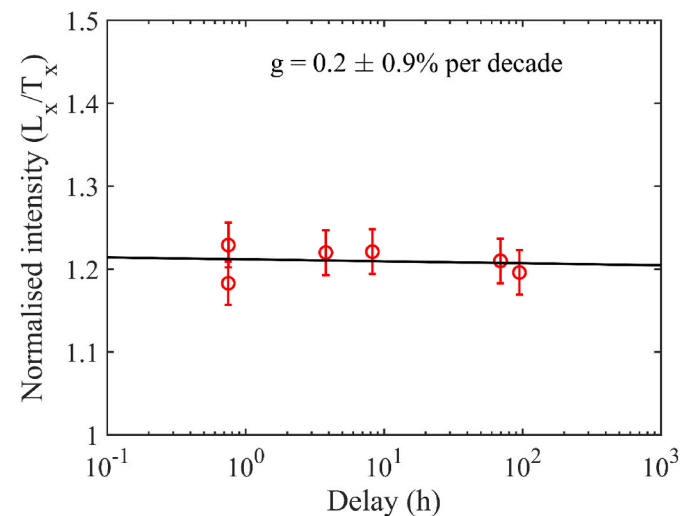


Fig. 11. Fading rate [g (% per decade)] results for RSN-01-17 sample for pVIRSL at 200 °C.

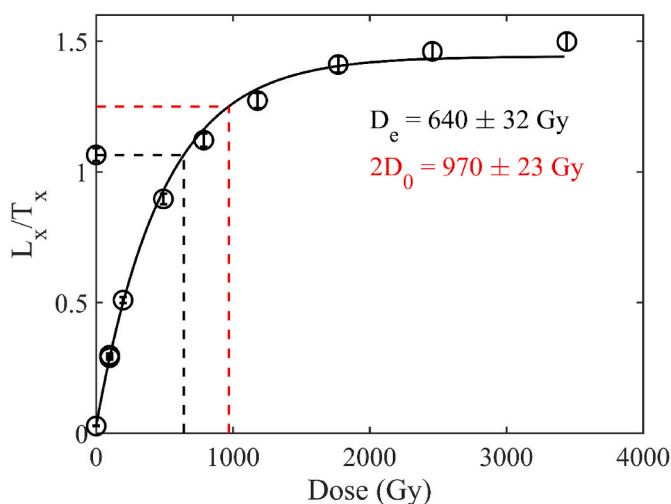


Fig. 12. Sensitivity corrected DRC constructed using pVIR-SAR protocol (Table 2) for MHD-02-17 sample along with the natural intensity. The single saturating exponential function as in analyst was used for the fitting. The recycling ratio and recuperation are 1.00 ± 0.05 and $2.6 \pm 0.1\%$, respectively. The estimated D_e is 640 ± 32 Gy, and saturation dose ($2D_0$) is 970 ± 23 Gy.

0.1% (Fig. 12). A dose rate of 3.35 ± 0.15 Gy/ka implies a dating age of 300 ka.

4.3.6. Comparison with expected ages

Table 4 compares pVIR-SAR ages with expected ages, which accord to within $\pm 2\sigma$ error with the expected ages. The pVIRSL age of sample RTP-18-02 which is immediately beneath the Youngest Toba Tuff (YTT) deposit, was 69 ± 5 ka, and this accords with 75 ka age of YTT (Table 1). The pVIRSL age of HMP-18-5 was 164 ± 21 ka and its pIRIRSL age was $>247 \pm 32$ ka. This needs further probing. For MHD-02-17, both the pVIRSL and pIRIRSL gave fading of 2.8 ± 0.3 and $2.7 \pm 0.6\%$ per decade, and ages agree with each other when corrected for fading using Kars and Wallinga (2009). For PRL0, pVIRSL age was corrected for fading rate ($g = 1.9 \pm 0.1\%$ per decade) using Huntley and Lamothe (2001). The ages agree within 2σ error.

4.4. Luminescence mechanism of pVIRSL at 200 °C

The pVIRSL at 200 °C passed all the criteria for a SAR based paleodose estimation. The luminescence production mechanism for pVIRSL at 200 °C was explored on KF using a protocol mentioned in Table 5. The pVIRSL (violet at 50 °C and IR at 50 °C or 200 °C for 100 s) signal was measured after the dose (20 Gy), preheat (250 °C for 60 s), and IR wash (50 °C or 200 °C for 100 s). This signal is named pVIRSL1. On the same aliquot, similar steps were repeated after the TL wash of 500 °C but without IR wash (step 4), and this signal was termed pVIRSL2. Two

separate measurements were conducted for IRSL at 50 °C and IRSL at 200 °C. The percentage difference in the two signals is estimated using the following expression:

$$\text{Difference (\%)} = \left(\frac{p\text{VIRSL2} - p\text{VIRSL1}}{p\text{VIRSL2}} \right) \times 100$$

This difference quantifies the re trapping from the principal trap during violet stimulation. Interestingly, both positive and negative values were obtained for measurements at 50 °C, but only positive values were obtained for IRSL at 200 °C measurements. Table 6 provides relevant results for all samples. For the museum KF sample, the difference was -22% for IRSL at 50 °C and 56% for IRSL at 200 °C. For natural samples, PRL2, MHK-07-07, RTP-18-02, RSN-01-17, and HMP-18-05, the re trapping from IR at 50 °C from principal trap to pVIRSL signal ranged from 0 to -20% considering errors. The near zero values suggest that IRSL at 50 °C from the principal trap gets depleted during violet stimulation. Therefore, for these samples, resulting pVIRSL at 50 °C has a single origin, i.e., photo-transfer from deep traps. The negative values in PRL2, MHK-07-07, and HMP-18-05 samples could be due to longer exposure to violet stimulation (50 °C, 200 s) in pVIRSL2 than in violet (50 °C, 100 s) stimulation in pVIRSL1. A longer exposure to violet stimulation resulted in a lower value for pVIRSL2 than pVIRSL1, leading to a negative percentage difference. However, for PRL0 and MHD-02-17, the percentage difference between pVIRSL2 and pVIRSL1 for IR at 50 °C was 30% and 45%, respectively. The positive values indicate that the pVIRSL at 50 °C contains a contribution from both the principal trap and the deep traps. This re trapping from the principal trap may be responsible for fading in these samples as IRSL (50 °C) originates from the recombination of proximal electron-hole pairs and is hence more prone to fading (Poolton et al., 1994). The results also indicate that re trapping from the principal trap for IR at 50 °C is sample dependent, and more complex trap dynamics are involved than currently understood. This could be linked to the nature of defect centres and crystal structure. A more specific spectroscopic study may be needed to understand the mechanism in detail. In the future, it may be of interest to include a step of IR stimulation at 50 °C prior pVIRSL measurement to eliminate the IR 50 °C contribution from the principal trap. This may facilitate the isolation of a more stable signal.

For pVIRSL at 200 °C, a significant contribution ($\geq 50\%$) from IRSL at 200 °C from principal traps to the pVIRSL at 200 °C was obtained for all samples, indicating that IRSL at 200 °C does not get depleted during violet stimulation and contributes to the pVIRSL. Therefore, pVIRSL at 200 °C arises from two sources: a) recapture of charges from the principal trap and b) photo-transfer of charges from deep traps as observed from all samples. The results indicate that the DRCs for the pVIR-SAR protocol are from photo-transfer from deep traps and re trapping from the principal trap.

An alternate explanation for fading in PRL0 and MHD-02-17 could be the instability of some of the recombination centres (Kumar et al., 2022). It may be possible that all the nearest recombination centres are not

Table 5
Protocol used to quantify the IRSL from principal trap contributing to the pVIRSL.

Steps	Protocol
1	TL 500 °C @ 2 °C/s
2	Dose (~20 Gy)
3	Preheat @250 °C for 60 s
4	IRSL @50 or 200 °C for 100 s
5	VSL @50 °C for 100 s
6	IRSL @50 or 200 °C for 100 s (pVIRSL1)
7	TL 500 °C @ 2 °C/s
8	Dose (~20 Gy)
9	Preheat @250 °C for 60 s
10	VSL @50 °C for 200 s
11	IRSL @50 or 200 °C for 100 s (pVIRSL2)

Table 6
Protocol used to quantify the IRSL from principal trap contributing to the pVIRSL.

Sample	IRSL contribution to pVIRSL at 50 °C	IRSL contribution to pVIRSL at 200 °C
KF	-22%	56%
PRL0	45%	74%
PRL2	-20%	68%
MHK-07-07	-20%	62%
RTP-18-02	2%	73%
RSN-01-17	-2%	79%
HMP-18-05	-8%	49%
MHD-02-17	30%	66%

consumed during violet stimulation, hence participating in the pVIRSL and leading to fading.

5. Conclusions

The present work probes the mechanism for pVIRSL, which exhibited nearly zero fading in most of the samples and very low fading in others. The work explores its potential for K-feldspar dating and following inferences are drawn:

1. Violet stimulation at 50 °C probes the TL peaks greater than 500 °C and causes photo-transfer of charges from the deeper traps to the shallower traps, and IR stimulation provides pVIRSL. Deep traps >500 °C serve as reservoir traps.
2. The pVIRSL at 50 °C results from the photo-transfer of charges from traps with TL peaks >500 °C except for PRL0 and MHD-02-17. In these two samples, IR 50 °C from the principal trap does not get depleted during the violet stimulation, and some of it gets retrapped to contribute to pVIRSL at 50 °C.
3. The pVIRSL at 200 °C originates from a) photo-transfer from deep traps and b) recapture from the principal trap,
4. Deep traps are sensitive to violet light and to daylight. This makes pVIRSL suitable for dating. Typically, 60 min of daylight exposure reduced the pVIRSL to a residual dose of a few Gy.
5. An augmented pVIR-SAR protocol is presented, and the suggested parameters for paleodose measurement are, a preheat at 250 °C for 60 s, pVIRSL at 200 °C for 100 s, bleaching using both violet and IR stimulation at 350 °C for 200 s, and test dose in the range of 50–80% of the expected dose. The pVIR-SAR provides doses with low recuperation (<5% and for PRL0 <10%), good recycling and dose recovery (within 10%), near zero fading, and low residual doses (<21 Gy), and provided reliable ages ranging from 8 to >280 ka. These accord with BSL-SAR or pIRIR-SAR estimates.
6. The pVIR-SAR dose response curve suggests a high laboratory saturation dose (2D₀ ~1000 Gy), implying the methodology can be used for higher doses.
7. Photo-transferred IRSL in most samples had near zero athermal fading. However, two samples, PRL0 and MHD-02-17, returned a g-value of 1.9 ± 0.1 and $2.8 \pm 0.3\%$ per decade, respectively.

Declaration of competing interest

The authors declare that they have no known competing financial interests or personal relationships that could have appeared to influence the work reported in this paper.

Data availability

Data will be made available on request.

Acknowledgement

The authors thank Mr. Devara Anil (MSU, Baroda) and Dr. Linto Alappat (Christ College, Kerala) for the K-feldspar samples. MD thanks Dr. Shivani Baliyan and Dr. Dwijesh Ray for the XRD characterization of KF sample. AKS thanks DST-SERB for a Year of Science Chair Professorship. The authors thank two anonymous reviewers for their constructive comments and valuable suggestions that improved the manuscript.

Appendix A. Supplementary data

Supplementary data to this article can be found online at <https://doi.org/10.1016/j.quageo.2023.101487>.

References

- Aitken, M.J., 1985. *Thermoluminescence Dating*, vol. 359. Academic Press, London, 0-12-046380-6.
- Anil, D., Chauhan, N., Ajithprasad, P., Devi, M., Mahesh, V., Khan, Z., 2022. An early presence of modern Human or Convergent Evolution? A 247 ka middle palaeolithic assemblage from Andhra Pradesh, India. *J. Archaeol. Sci. Reports* 45, 103565. <https://doi.org/10.1016/j.jasrep.2022.103565>.
- Anil, D., Devi, M., Blinkhorn, J., Smith, V., Sanghode, S., Mahesh, V., Khan, Z., Ajithprasad, P., Chauhan, N., 2023. Youngest Toba Tuff deposits in the Gundlakamma river basin, Andhra Pradesh, India and their role in Evaluating late pleistocene behavioural change in South Asia. *Quat. Res.* 1–12. <https://doi.org/10.1017/qua.2023.13>.
- Auclair, M., Lamothe, M., Huot, S., 2003. Measurement of anomalous fading for feldspar IRSL using SAR. *Radiat. Meas.* 37, 487–492.
- Biswas, R.H., Williams, M.A.J., Raj, R., Juyal, N., Singhvi, A.K., 2013. Methodological studies on luminescence dating of volcanic ashes. *Quat. Geochronol.* 17, 14–25. <https://doi.org/10.1016/j.quageo.2013.03.004>.
- Bøtter-Jensen, L., Thomsen, K.J., Jain, M., 2010. Review of optically stimulated luminescence (OSL) instrumental developments for retrospective dosimetry. *Radiat. Meas.* 45, 253–257. <https://doi.org/10.1016/j.radmeas.2009.11.030>.
- Buylaert, J.P., Murray, A.S., Thomsen, K.J., Jain, M., 2009. Testing the potential of an elevated temperature IRSL signal from K-feldspar. *Radiat. Meas.* 44, 560–565. <https://doi.org/10.1016/j.radmeas.2009.02.007>.
- Buylaert, J.P., Thiel, C., Murray, A.S., Vandenberghe, D.A.G., Yi, S., Lu, H., 2011. IrsI and post-ir IrsI residual doses recorded in modern dust samples from the Chinese loess plateau. *Geochronometria* 38, 432–440. <https://doi.org/10.2478/s13386-011-0047-0>.
- Buylaert, J.P., Jain, M., Murray, A.S., Thomsen, K.J., Thiel, C., Sohbati, R., 2012. A robust feldspar luminescence dating method for Middle and Late Pleistocene sediments. *Boreas* 41, 435–451.
- Colarossi, D., Duller, G.A.T., Roberts, H.M., 2018. Exploring the behaviour of luminescence signals from feldspars: implications for the single aliquot regenerative dose protocol. *Radiat. Meas.* 109, 35–44. <https://doi.org/10.1016/j.radmeas.2017.07.005>.
- Devi, M., Chauhan, N., Rajapara, H., Joshi, S., Singhvi, A.K., 2022. Multispectral athermal fading rate measurements of feldspar. *Radiat. Meas.* 156, 106804. <https://doi.org/10.1016/j.radmeas.2022.106804>.
- Duller, G.A.T., 1997. Behavioural studies of stimulated luminescence from feldspars. *Radiat. Meas.* 27, 663–694. [https://doi.org/10.1016/S1350-4487\(97\)00216-3](https://doi.org/10.1016/S1350-4487(97)00216-3).
- Duller, G.A.T., Wintle, A.G., 1991. On infrared stimulated luminescence at elevated temperatures. *Int. J. Radiat. Appl. Instrumentation. Part 18*, 379–384. [https://doi.org/10.1016/1359-0189\(91\)90003-Z](https://doi.org/10.1016/1359-0189(91)90003-Z).
- Goedicke, C., 1984. Microscopic investigations of the quartz etching technique for TL dating. *Nucl. Tracks Radiat. Meas.* 9, 87–93. [https://doi.org/10.1016/0735-245X\(84\)90026-7](https://doi.org/10.1016/0735-245X(84)90026-7).
- Huntley, D.J., Lamothe, M., 2001. Ubiquity of anomalous fading in K-feldspars and the measurement and correction for it in optical dating. *Can. J. Earth Sci.* 38, 1093–1106. <https://doi.org/10.1139/cjes-38-7-1093>.
- Hütt, G., Jaek, I., Tchonka, J., 1988. Optical dating: K-feldspars optical response stimulation spectra. *Quat. Sci. Rev.* 7, 381–385. [https://doi.org/10.1016/0277-3791\(88\)90033-9](https://doi.org/10.1016/0277-3791(88)90033-9).
- Jain, M., Ankjærgaard, C., 2011. Towards a non-fading signal in feldspar: insight into charge transport and tunnelling from time-resolved optically stimulated luminescence. *Radiat. Meas.* 46, 292–309.
- Jain, M., Singhvi, A.K., 2001. Limits to depletion of blue-green light stimulated luminescence in feldspars: implications for quartz dating. *Radiat. Meas.* 33, 883–892. [https://doi.org/10.1016/S1350-4487\(01\)00104-4](https://doi.org/10.1016/S1350-4487(01)00104-4).
- Jain, M., Sohbati, R., Guralnik, B., Murray, A.S., Kook, M., Lapp, T., Prasad, A.K., Thomsen, K.J., Buylaert, J.P., 2015. Kinetics of infrared stimulated luminescence from feldspars. *Radiat. Meas.* 81, 242–250. <https://doi.org/10.1016/j.radmeas.2015.02.006>.
- Kalita, J.M., Chithambo, M.L., 2022. Phototransferred thermoluminescence characteristics of microcline (KAlSi₃O₈) under 470 nm blue- and 870 nm infrared-light illumination. *Appl. Radiat. Isot.* 181, 110070. <https://doi.org/10.1016/j.apradiso.2021.110070>.
- Kars, R.H., Wallinga, J., 2009. IRSL dating of K-feldspars: modelling natural dose response curves to deal with anomalous fading and trap competition. *Radiat. Meas.* 44, 594–599. <https://doi.org/10.1016/j.radmeas.2009.03.032>.
- Kumar, R., Kook, M., Jain, M., 2022. Does hole instability cause anomalous fading of luminescence in feldspar? *J. Lumin.* 252, 119403. <https://doi.org/10.1016/j.jlumin.2022.119403>.
- Kumar, R., Kook, M., Jain, M., 2021. Sediment dating using infrared photoluminescence. *Quat. Geochronol.* 62, 101147. <https://doi.org/10.1016/j.quageo.2020.101147>.
- Kumar, R., Kook, M., Jain, M., 2020. Understanding the metastable states in K-Na aluminosilicates using novel site-selective excitation-emission spectroscopy. *J. Phys. D Appl. Phys.* 53. <https://doi.org/10.1088/1361-6463/aba788>.
- Kumar, R., Kook, M., Murray, A.S., Jain, M., 2018. Towards direct measurement of electrons in metastable states in K-feldspar: Do infrared-photoluminescence and radioluminescence probe the same trap. *Radiat. Meas.* 120, 7–13. <https://doi.org/10.1016/j.radmeas.2018.06.018>.
- Lapp, T., Kook, M., Murray, A.S., Thomsen, K.J., Buylaert, J.P., Jain, M., 2015. A new luminescence detection and stimulation head for the Risø TL/OSL reader. *Radiat. Meas.* 81, 178–184. <https://doi.org/10.1016/j.radmeas.2015.02.001>.

- Li, B., Li, S.H., 2011. Luminescence dating of K-feldspar from sediments: a protocol without anomalous fading correction. *Quat. Geochronol.* 6, 468–479. <https://doi.org/10.1016/j.quageo.2011.05.001>.
- Liu, J., Cui, F., Murray, A.S., Sohbati, R., Jain, M., Gao, H., Li, W., Li, C., Li, P., Zhou, T., Chen, J., 2018. Resetting of the luminescence signal in modern riverbed cobbles along the course of the Shiyang River, China. *Quat. Geochronol.* 49, 184–190. <https://doi.org/10.1016/j.quageo.2018.04.004>.
- Mishra, S., Chauhan, N., Singhvi, A.K., 2013. Continuity of microblade technology in the Indian Subcontinent since 45 ka: implications for the Dispersal of modern Humans. *PLoS One* 8, 1–14. <https://doi.org/10.1371/journal.pone.0069280>.
- Morthekai, P., Chauhan, P.R., Jain, M., Shukla, A.D., Rajapara, H.M., Krishnan, K., Sant, D.A., Patnaik, R., Reddy, D.V., Singhvi, A.K., 2015. Thermally redistributed IRSL (RD-IRSL): a new possibility of dating sediments near B/M boundary. *Quat. Geochronol.* 30, 154–160. <https://doi.org/10.1016/j.quageo.2015.05.018>.
- Murray, A.S., Wintle, A.G., 2000. Luminescence dating of quartz using an improved single-aliquot regenerative-dose protocol. *Radiat. Meas.* 32, 57–73. [https://doi.org/10.1016/S1350-4487\(99\)00253-X](https://doi.org/10.1016/S1350-4487(99)00253-X).
- Murray, A.S., Buylaert, J.P., Thomsen, K.J., Jain, M., 2009. The effect of preheating on the IRSL signal from feldspar. *Radiat. Meas.* 44, 554–559. <https://doi.org/10.1016/j.radmeas.2009.02.004>.
- Ninkovich, D., Shackleton, N.J., Abdel-Monem, A.A., Obradovich, J.D., Izett, G., 1978. K-Ar age of the late Pleistocene eruption of Toba, north Sumatra. *Nature* 276, 574–577. <https://doi.org/10.1038/276574a0>.
- Poolton, N.R.J., Bøtter-Jensen, L., Ypma, P.J.M., Johnsen, O., 1994. Influence of crystal structure on the optically stimulated luminescence properties of feldspars. *Radiat. Meas.* 23 (2–3), 551–554.
- Poolton, N.R.J., Kars, R.H., Wallinga, J., Bos, A.J.J., 2009. Direct evidence for the participation of band-tails and excited-state tunnelling in the luminescence of irradiated feldspars. *J. Phys. Condens. Matter* 21. <https://doi.org/10.1088/0953-8984/21/48/485505>.
- Porat, N., Faerstein, G., Medialdea, A., Murray, A.S., 2015. Re-examination of common extraction and purification methods of quartz and feldspar for luminescence dating. *Anc. TL* 33, 255–258.
- Prasad, A.K., Poolton, N.R.J., Kook, M., Jain, M., 2017. Optical dating in a new light : a direct, non-destructive probe of trapped electrons. *Sci. Rep.* 1–15. <https://doi.org/10.1038/s41598-017-10174-8>.
- Reimann, T., Ankjærgaard, C., Wallinga, J., 2015. Testing the potential of a transferred IRSL (T-IRSL) feldspar signal for luminescence dating. *Radiat. Meas.* 81, 275–281. <https://doi.org/10.1016/j.radmeas.2015.01.002>.
- Riedesel, S., King, G.E., Prasad, A.K., Kumar, R., Finch, A.A., Jain, M., 2019. Optical determination of the width of the band-tail states, and the excited and ground state energies of the principal dosimetric trap in feldspar. *Radiat. Meas.* 125, 40–51. <https://doi.org/10.1016/j.radmeas.2018.08.019>.
- Riedesel, S., Kumar, R., Duller, G.A.T., Roberts, H.M., Bell, A.M.T., Jain, M., 2021. Site-selective characterisation of electron trapping centres in relation to chemistry, structural state and mineral phases present in single crystal alkali feldspars. *J. Phys. D Appl. Phys.* 54, 385107 <https://doi.org/10.1088/1361-6463/ac10d7>.
- Spooner, N.A., 1994. The anomalous fading of infrared-stimulated luminescence from feldspars. *Radiat. Meas.* 23, 625–632.
- Spooner, N.A., 1992. Optical dating: preliminary results on the anomalous fading of luminescence from feldspars. *Quat. Sci. Rev.* 11, 139–145.
- Thalbitzer Andersen, M., Jain, M., Tidemand-Lichtenberg, P., 2012. Red-IR stimulated luminescence in K-feldspar: single or multiple trap origin? *J. Appl. Phys.* 112 <https://doi.org/10.1063/1.4745018>.
- Thomsen, K.J., Murray, A.S., Jain, M., Bøtter-Jensen, L., 2008. Laboratory fading rates of various luminescence signals from feldspar-rich sediment extracts. *Radiat. Meas.* 43, 1474–1486.
- Visocekas, R., 1979. La luminescence de la calcite apr'ès irradiation cathodique: thermoluminescence et luminescence par effet tunnel. Doctoral dissertation. Université P. et M. Curie, Paris.
- Visocekas, R., 1985. Tunnelling radiative recombination in labradorite: its association with anomalous fading of thermoluminescence. *Nucl. Tracks Radiat. Meas.* 10, 521–529.
- Wintle, A.G., 1973. Anomalous fading of thermo-luminescence in mineral samples. *Nature* 245, 143–144.
- Yi, S., Buylaert, J., Murray, A.S., Lu, H., Thiel, C., Zeng, L.I.N., 2016. A Detailed Post-IR IRSL Dating Study of the Niuyangzigou Loess Site in A Detailed Post-IR IRSL Dating Study of the Niuyangzigou Loess Site in Northeastern China. <https://doi.org/10.1111/bor.12185>.